eXPRESS Polymer Letters Vol.7, No.2 (2013) 106
Available online at www.expresspolymlett.com
DOI: 10.3144/expresspolymlett.2013.10

Editorial corner – a personal view
Improving fibre/matrix interface through nanoparticles

A. Pegoretti[*]

Department of Industrial Engineering, University of Trento, via Mesiano 77, 38123 Trento, Italy

It is widely recognized that fibre/matrix interfacial strength controls several mechanical properties of composite materials, in particular the matrix-dominated ultimate parameters. In the last thirty years an impressive number of experimental and modelling efforts have been focused on the understanding of fibre/matrix interfacial bond with the aim to improve it. Over the years, two main strategies emerged for polymer composites: i) the development of specific fibre sizings/coatings/treatments and/or ii) the addition of coupling agents to the matrix resin.

In the recent years new strategies came to light: in fact, the availability of various types of nanoparticles offered the possibility to tailor the fibre/matrix interactions at a nanoscale level. In particular, some recent investigations proved that nanoparticles homogeneously dispersed in a polymer matrix can play a beneficial role on the fibre/matrix interfacial adhesion in several types of structural composites. For example, the introduction of organo-modified clays in an epoxy matrix led to the formation of a stronger interface with E-glass fibres, with an increase of the interfacial shear strength of about 30% for a filler content of 5 wt% (DOI: 10.1177/0021998311420311). Concurrently, the evaluation of the fibre/matrix contact angle revealed an improved wettability when organo-modified clays were added, and a simultaneous enhancement of the fracture toughness of the resin matrix. This approach could be also adopted to add specific functional properties to composite materials, such as damage controlling capabilities (DOI: 10.1016/j.compositesa.2012.03.019).

Another approach relies on the possibility to confine nanoparticle in the interfacial region, with the advantage of localizing their presence in the area where stress transfer takes place, thus reducing the overall quantity of nanoparticle required. As an example, a sizing containing single or multi-walled carbon nanotubes has been used for coating glass fibres (DOI: 10.1016/j.compscitech.2007.10.009). Two simultaneous results have been reached, to 'heal' surface flaws and to enhance interfacial adhesion in a polypropylene matrix, indicating nanotube related interfacial toughening mechanisms.

An amazing amount of research has gone, and still goes, into the understanding of the properties of nanoscale particles and their usage to improve engineering materials. Development of polymer composites can surely benefit from this research, including the 'old issue' of fibre/matrix interface.

Prof. Dr. Alessandro Pegoretti
Member of International Advisory Board

[*]Corresponding author, e-mail: alessandro.pegoretti@unitn.it

eXPRESS Polymer Letters Vol.7, No.2 (2013) 107–119
Available online at www.expresspolymlett.com
DOI: 10.3144/expresspolymlett.2013.11

Chopped basalt fibres: A new perspective in reinforcing poly(lactic acid) to produce injection moulded engineering composites from renewable and natural resources

T. Tábi[1,2*], *P. Tamás*[1,2], *J. G. Kovács*[2]

[1]MTA–BME Research Group for Composite Science and Technology, Műegyetem rkp. 3., H-1111 Budapest, Hungary
[2]Department of Polymer Engineering, Faculty of Mechanical Engineering, Budapest University of Technology and Economics, Muegyetem rkp. 3., H-1111 Budapest, Hungary

Received 4 July 2012; accepted in revised form 11 September 2012

Abstract. This paper focuses on the reinforcing of Poly(lactic acid) with chopped basalt fibres by using silane treated and untreated basalt fibres. Composite materials with 5–10–15–20–30–40 wt% basalt fibre contents were prepared from silane sized basalt fibres using extrusion, and injection moulding, while composites with 5–10–15 wt% basalt fibre contents were also prepared by using untreated basalt fibres as control. The properties of the injection moulded composites were extensively examined by using quasi-static (tensile, three-point bending) and dynamic mechanical tests (notched and unnotched Charpy impact tests), dynamic mechanical analysis (DMA), differential scanning calorimetry (DSC), heat deflection temperature (HDT) analysis, dimensional stability test, as well as melt flow index (MFI) analysis and scanning electron microscopic (SEM) observations. It was found that silane treated chopped basalt fibres are much more effective in reinforcing Poly(lactic acid) than natural fibres; although basalt fibres are not biodegradable but they are still considered as natural (can be found in nature in the form of volcanic rocks) and biologically inert. It is demonstrated in this paper that by using basalt fibre reinforcement, a renewable and natural resource based composite can be produced by injection moulding with excellent mechanical properties suitable even for engineering applications. Finally it was shown that by using adequate drying of the materials, composites with higher mechanical properties can be achieved compared to literature data.

Keywords: *biodegradable polymers, polymer composites, poly(lactic acid), chopped basalt fibres, injection moulding*

1. Introduction

In the 21st century, due to the increasing environmental consciousness renewable resource based and inherently biodegradable polymers gain more and more role. These materials can be fully synthetized from biomass or previously not utilized agricultural feedstock and during their biodegradation harmless materials like water, carbon-dioxide and humus are produced, where the latter can be used to grow agricultural plants, so thus it can be easily seen that these materials fit into the life cycle of nature and also fit into the train of thoughts of sustainable development [1–3]. It is also believed that in the near future biodegradable polymers will be used for producing plastic products with short term applications, however nowadays in most cases for these applications still unnecessarily durable petrol-based plastics are used, what causes more and more waste management problems due to their not complete recyclability.

One of the most promising renewable resources to produce biopolymers is starch. Starch can be found all over the world in abundant amounts, because starch containing agricultural plants like corn, wheat, potato are grown extensively in a lot of countries. In the last few decades much research has

*Corresponding author, e-mail: tabi@pt.bme.hu

been made to make starch processable with conventional plastic processing equipment, and as a result thermoplastic starch (TPS) was developed and extensively researched [4–6]. Although TPS is cheap, its numerous drawbacks like low mechanical properties, high shrinkage, and water solubility retarded its widespread usage. Nowadays TPS together with Poly(ε-caprolactone) (PCL) is used as a compound and commercialised under trade name Mater-Bi (Novamont, Italy). Another possible way to utilise starch is its fermentation in the presence of sugar into lactic acid, what can be further polymerised into Poly(lactic acid) (PLA). In the last decade PLA was in the focus of interest, and it became the most promising biopolymers of all due to its excellent mechanical properties, easy processing by conventional equipment, low shrinkage, reasonable price and harmless biodegradation capability [7–9]. Although PLA is already commercialised and more and more PLA products are on the market, these products are still mainly related to packaging industry, even so the high strength and stiffness of PLA suggest it to be used as the matrix of a durable engineering composite material, but its low heat deflection temperature (HDT) and low impact strength still retards its usage as a high performance composite.

Lots of efforts have been made to further reinforce PLA with typically natural plant fibres [10–16] or even with glass fibres [17] to make a biocomposite for applications with higher demand then packaging. In most cases by adding natural plant fibres to PLA higher increase of mechanical properties occurred when solvent casting [10, 11], pultrusion [12], extrusion followed by compression [13], film-stacking [14, 15], compression followed by injection moulding [16] processes were used compared to the conventional and most productive extrusion followed by injection moulding process [17, 18]. This is probably due to the reduced length of the natural fibres in the latter technology. Furthermore, the increase of HDT due to the incorporation of various fibres is only a few times experienced. Iwatake *et al.* [10] demonstrated that by using solvent casting method and micro-fibrillated cellulose (MFC) fibres a cellulose fibre network interconnected by hydrogen bonds was developed which resisted the applied stress independently of the softening of PLA during dynamic mechanical analysis (DMA) tests. By using the above mentioned processes to increase HDT and impact strength it is crucial to have strong connection between the fibres and the PLA, and the adequate quantity and quality (according to stiffness and length) of reinforcing fibres is also important, which will prevent the well-known high stiffness loss of amorphous PLA products above glass transition temperature (T_g). However, by adding natural plant fibres to reinforce PLA, the real breakthrough did not occur because in order to gain significant reinforcing effect especially in the desired impact strength low productivity processes like solvent casting or film stacking method have to be used but to commercialise PLA based composites and make complicated 3D shaped, and accurate parts highly productive production technologies like injection moulding should be applied.

Besides natural fibres, a promising alternative may be the usage of basalt fibres, which is a novel reinforcement for composites. Although basalt fibres are not biodegradable but still considered as natural, because they can be produced by using basalt (volcanic) rocks, which can be found in nature and virtually in every country around the globe. Moreover, basalt is biologically inert, and the weathering of basalt rocks increase the mineral content of soil which further strengthens its natural character. Basalt fibres are typically produced by two different technologies: Junkers method and spinneret technology [19]. The shorter basalt fibres are prepared by the Junkers method and the continuous fibres are prepared by the spinneret technology [20]. Its mechanical properties and chemical composition is similar to the glass fibre, and it can be used between –200 and 600ºC without the significant loss of mechanical properties [21, 22]. Basalt fibres are biologically inert as well as environmentally friendly and can be used in very aggressive environments too [23, 24]. The surface of the basalt fibres can be modified easily, thus they can be used as reinforcement fibres for composites [25, 26]. Deák *et al*. [27] investigated the influence of different coupling agents on the mechanical and thermomechanical properties of basalt fibre reinforced Polyamide 6 (PA6). The tensile, flexural and impact strengths were improved in the highest level by the type of 3-glycidoxypropyltrimethoxysilane sizing. The suitability of that sizing material in a wide temperature range was proven by DMA tests.

Basalt fibres seem to be a good alternative to reinforce PLA, however, the number of papers in basalt

fibre reinforced PLA is very limited [28–30]. Liu *et al*. [28] demonstrated that basalt fibres with the adequate sizing can improve tensile, flexural and impact strength of PLA more significant as plant fibres. It was also found that by using 20 wt% of basalt fibres and 20 wt% of ethylene-acrylate-glycidyl methacrylate copolymer (EAGMA) the impact strength can be further increased up to 34 kJ/m^2 from the original value of PLA of 19 kJ/m^2 (unnotched Charpy test results). Finally the authors stated that the fibres are strongly bonded to the PLA because no gap was found at the fibre-matrix interface. Kurniawan *et al*. [29] used atmospheric pressure glow discharge plasma polymerization as surface treatment of basalt fibres and analysed the adhesion between the fibres and PLA in hot pressed composites. It was found that by increasing the plasma polymerisation time the tensile strength of the composites increased compared to PLA when the reaction time was higher than 3 minutes. Although the plasma polymerised fibres seem to be well wetted by the PLA, the tensile strength was lower compared to results from Liu *et al*. [28]. Finally Chen *et al*. [30] successfully produced PLA based scaffolds reinforced with basalt fibres. They proved that the basalt fibres retard degradation rate of the scaffold, thus most likely decrease inflammatory responses caused by acidification. Moreover, basalt fibres did not notably affect osteoblast viability and growth which means that basalt fibre reinforced PLA scaffolds can be potentially used in hard tissue repair.

According to these results basalt fibres seem to be a good selection to reinforce PLA, because PLA based composites with higher mechanical properties can be achieved compared to natural plant fibre reinforcement. However, the widespread analysis of the various mechanical, thermal, flow and dimensional stability properties of injection moulded basalt fibre reinforced PLA based composites can be only partly found in the literature. Thus, this paper focuses on the comprehensive usability analysis of chopped basalt fibres with and without silane treatment as potential reinforcing fibre for injection moulded, renewable and natural resource based PLA composites as high performance, durable engineering materials.

2. Materials, processing and experimental

Semi-crystalline PLA injection moulding grade resin was used for the measurements (type AI1001 from eSUN, Shenzhen, China, with a D-Lactide content of 4%). It was dried at 120°C for 6 hours prior to extrusion. A somewhat high drying temperature was chosen, because according to our previous research [31] simply by using adequate drying, significantly higher adhesion could be developed between the phases, because the residual moisture could induce degradation and it could also weaken the adhesion between the fillers or fibres and the matrix material. Chopped basalt fibres produced with Junkers method from Kameny Vek (Dubna, Russia) were obtained with the company's own silane treatment type KV-12 developed especially for strong adhesion with polyesters. The average diameter of the fibres was 13 μm, while the initial length was 10 mm. The fibres were also dried along with the PLA resin to remove residual moisture. Some of the basalt fibres were heated to 600°C to remove silane sizing. The PLA pellets and the treated and untreated (removed silane) basalt fibres were dry blended and extruded by using a LabTech Scientific twin screw extruder (Bangkok, Thailand) (screw diameter = 26 mm, L/D = 40) equipped with a 2 mm hole diameter die. A temperature profile of 175–180–185–190°C (from the hopper to the die) was used with a screw rotational speed of 30 rpm. 5–10–15–20–30–40 wt% basalt fibre composites were prepared with silane treatment (abbreviated as 5BS, 10BS, 15BS, 20BS, 30BS, 40BS) and 5–10–15 wt% basalt fibre composites with removed treatment for control (abbreviated as 5BN, 10BN, 15BN). The extrudates were pelletized and annealed (crystallised) prior to injection moulding to avoid processing problems (pellet sticking to the screw) caused by cold crystallisation as reported in our previous research [32]. The pellets were injection moulded with an Arburg Allrounder 370S 700–250 injection moulding machine (Lossburg, Germany) equipped with a 30 mm diameter, L/D = 25 screw. The applied injection moulding parameters can be seen in Table 1.

ISO standard dumbbell, three-point bending and Charpy specimens with a cross-section of 4 × 10 mm, and 80 × 80 mm area, 2 mm thick flat specimens were injection moulded for the tests.

Tensile and three-point bending tests were performed by using a Zwick Z020 universal testing machine equipped with Zwick BZ 020/TN2S force measuring cell with a force limit of 4 kN using a cross-head speed of 5 mm/min. Charpy tests were

Table 1. Injection moulding parameters

Injection moulding parameter	Value
Volume	50 cm^3 (flat specimen) 44 cm^3 (tensile specimen) 42 cm^3 (bending specimen)
Injection pressure	Variable according to basalt fibre content
Switch-over point	12 cm^3
Injection rate	50 cm^3/s
Holding pressure	600 bar
Holding time	20 s
Residual cooling time	30 s
Screw rotational speed	15 m/min
Backpressure	30 bar
Decompression volume	5 cm^3
Decompression rate	5 cm^3/s
Temperature of the first zone	165°C
Temperature of the second zone	175°C
Temperature of the third zone	180°C
Temperature of the fourth zone	185°C
Temperature of the fifth zone	190°C
Temperature of the mould	20°C

performed with a Ceast Resil Impactor impact testing machine equipped with a 15 J impact energy hammer and a DAS8000 data collector unit. Both notched (2 mm deep notch) and unnotched specimens were also prepared for the impact tests; 15 and 6.21 J impact energy was used for the unnotched and notched specimens respectively. All tests were executed at room temperature and at a relative humidity of 60%. 6 specimens were tested for each measurement.

Melt flow index (MFI) measurements were made by using a Ceast 7027.000 type melt flow indexer at 190°C with a load mass of 2.16 kg.

Differential Scanning Calorimetry (DSC) was made on a TA Q2000 type calorimeter by using 3–6 mg of the samples. Heat/cool/heat scans were registered from 0 to 180°C with a heating and cooling rate of 5°C/min and nitrogen gas flow was used. Crystallinity was calculated according to the theoretical enthalpy of fusion of 100% crystalline PLA (93.0 J/g) [33] by using Equation (1), where the basalt fibre content was also taken into consideration:

$$X = \frac{\Delta H_m - \Delta H_{cc}}{\Delta H_f \cdot (1 - \alpha)} \cdot 100 \quad (1)$$

where X [%] is the crystallinity, ΔH_m [J/g] and ΔH_{cc} [J/g] is the enthalpy of fusion and the enthalpy of cold-crystallisation, ΔH_f [J/g] is the enthalpy of fusion for 100% crystalline PLA and α [–] is the mass fraction of basalt fibres.

Dynamic Mechanical Analysis (DMA) was performed on a TA Q800 tester by using the injection moulded three-point bending specimens and dual cantilever. The dual cantilever was used in order to obtain storage modulus information above glass transition temperature (T_g). Amplitude of 20 μm with a span length of 35 mm and a frequency of 1 Hz were used from 0 to 160°C at a heating rate of 2°C/min.

Heat Deflection Temperature (HDT) was measured by using a Ceast 6505/000 HDT analyser. Injection moulded specimens with a cross-section of 4 × 10 mm and support distance of 100 mm were used. The specific load was 0.45 MPa and the heating rate was 2°C/min. The HDT value is obtained when the deflection reached 0.33 mm.

Dimensional stability of the injection moulded, 2 mm thick flat specimens were analysed by placing them into a heated oven and measuring the flow directional dimensional changes due to increasing temperature. The specimens were placed on a flat glass plate so as to get only dimensional changes and no deflection. The oven was heated to 40, 50, 60, 80, 100 and 120°C for 30 minutes and the dimensions of the specimens were recorded after cooling them to room temperature. These dimensions were compared with the dimensions recorded at room temperature prior to heating by using Equation (2):

$$D = \frac{L_b - L_a}{L_b} \cdot 100 \quad (2)$$

where D [%] is the dimensional change, L_b [mm] and L_a [mm] are the in-flow length of the specimens measured before and after the 30 minute heating process respectively.

The deflection of the specimens was also measured by using the flat specimens placed in the same oven, but in a cantilever to be loaded by their own weight.

Finally, scanning electron microscopy (SEM) was performed by a Jeol JSM 6380LA type electron microscope. The fracture surfaces of the tensile specimens were used for the observations. Prior to observation, Au/Pd alloy was sputtered onto the surface to avoid electrostatic charging.

3. Results and discussion

3.1. Melt flow index analysis

Prior to injection moulding, the melt flow index of the basalt fibre reinforced PLA composites was analysed (Figure 1).

It is found that by the incorporation of basalt fibres the MFI values decreased, what was expected, at the same time above 15 wt% the MFI values did not change essentially. This could be explained by the increased MFI of the PLA phase itself which compensated the MFI decreasing effect of the fibres. The increased MFI of PLA was possibly due to increased shear caused by the higher amount of fibres and due to higher residence times caused by lower output of the extruder during melt blending. It is also worth to note that by using silane treated basalt fibres the MFI values decreased more compared to untreated basalt fibre composites. This difference could be related to the adhesion between the fibres and the matrix and thus it suggest better compatibility between silane treated basalt fibres and PLA than between untreated basalt fibres and PLA presumably because the basalt fibres are distributed more uniformly – due to the silane treatment – in the melt, which thus becomes more viscous.

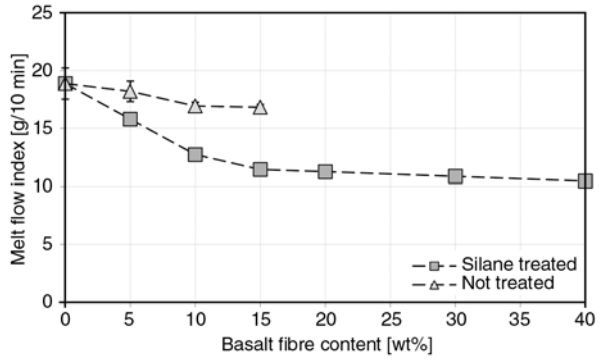

Figure 1. Melt flow index of the basalt fibre reinforced PLA composites

3.2. Mechanical properties

The mechanical properties of the injection moulded specimens were analysed by using quasi-static tensile and three-point bending tests and notched and unnotched Charpy impact tests. The tensile strength and the tensile modulus results can be seen in (Figure 2, Figure 3). Note that standard deviation is presented in all of the diagrams in the entire paper, however, in most cases it is so low, that the markings overlie it.

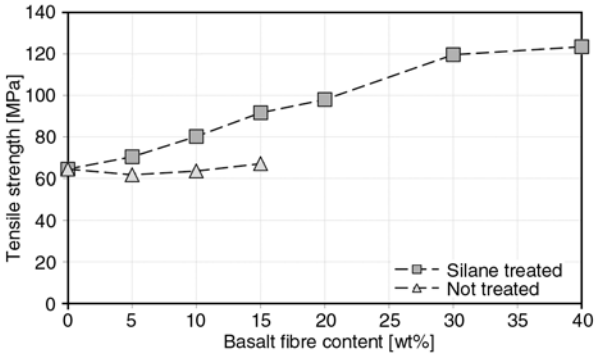

Figure 2. Tensile strength of the basalt fibre reinforced PLA composites

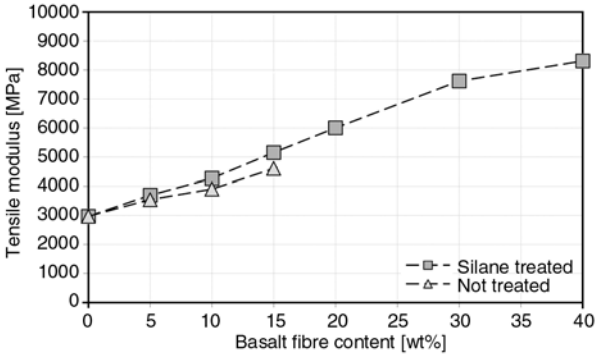

Figure 3. Tensile modulus of the basalt fibre reinforced PLA composites

It is obvious according to Figure 2 and Figure 3 that silane treated basalt fibre composites have superior mechanical properties (higher strength, the same order of magnitude of modulus) compared to the untreated basalt fibre composites, thus by using the silane treated basalt fibres, the composites reached a tensile strength of 123 MPa, a tensile modulus of over 8 GPa at the cost of minimal (0.6%) reduction of strain (measured but not presented). It was found that by increasing basalt fibre content both tensile strength and tensile modulus increased linearly in the 0–30 wt% basalt fibre content range. Moreover, it is also worth to note that there is low difference between the strength and modulus of 30 and 40 wt% silane treated basalt fibre reinforced PLA composites thus compared to 30 wt% basalt fibre content by adding another 10 wt% did not have significant reinforcing effect which suggest that at 40 wt% major fibre brakeage occurred probably caused by the fibre-fibre friction due to the increased amount of fibres.

The three-point bending tests show similar result compared to tensile tests (Figure 4, Figure 5).

The composites reached a flexural strength of 185 MPa and a flexural modulus of over 12 GPa.

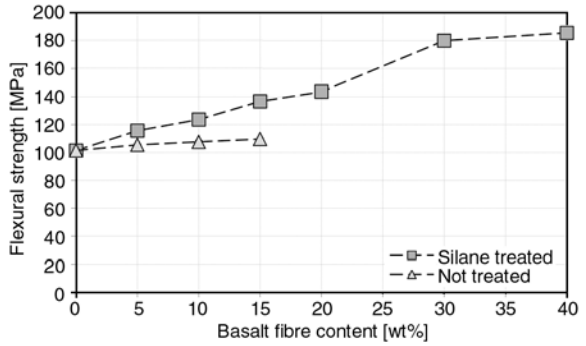

Figure 4. Flexural strength of the basalt fibre reinforced PLA compositesb

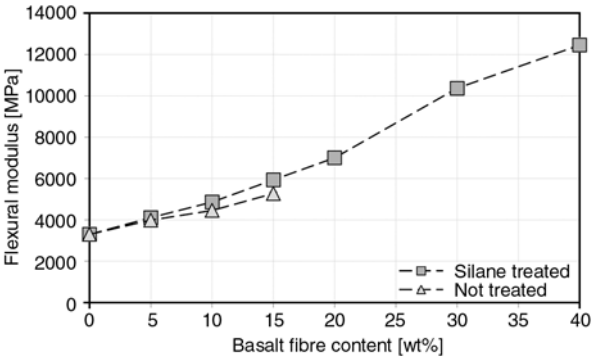

Figure 5. Flexural modulus of the basalt fibre reinforced PLA composites

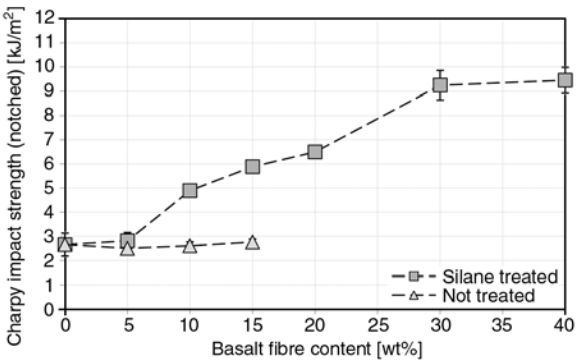

Figure 6. Charpy impact strength (notched) of the basalt fibre reinforced PLA composites

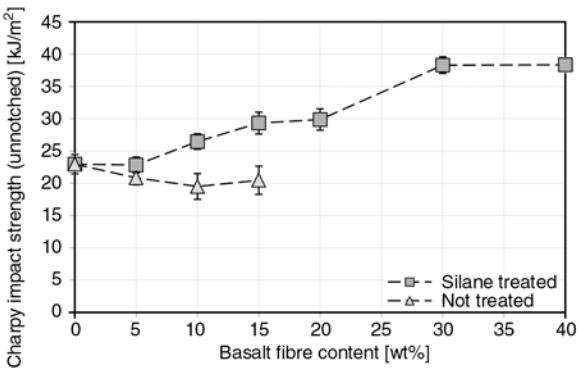

Figure 7. Charpy impact strength (unnotched) of the basalt fibre reinforced PLA composites

Correspondingly to tensile properties, the flexural properties were also linearly related to the basalt fibre content in the range of 0–30 wt% basalt, and the possible fibre breakage can also be observed in the flexural strength of the 40 wt% basalt fibre content composite, as it is almost the same as the flexural strength of the 30 wt% basalt fibre content composite. Finally, the notched (Figure 6) and unnotched (Figure 7) Charpy impact tests revealed that the critically low impact strength of PLA, especially for engineering applications can be significantly increased by the incorporation of basalt fibres.

By incorporating 30 wt% basalt fibres the notched and unnotched Charpy impact strength of PLA of 2.7 and 23.0 kJ/m^2 increased to 9.3 (by 244%) and 38.3 kJ/m^2 (by 67%) respectively. Charpy impact test results as well as tensile and bending test results also confirm that above 30 wt% basalt fibre content no significant reinforcing effect can be achieved due to probably increased fibre breakage.

All of the above mentioned mechanical properties increased more or less linearly to the basalt fibre content in the range of 0–30 wt% basalt fibre content range, which is demonstrated by using linear regression. The coefficients for the regression can be found in Table 2.

The mechanical properties of the injection moulded composites are better compared to results from Liu *et al*. [28] by 12, 25 and 53% according to tensile, flexural and Charpy impact strength respectively at same basalt fibre content (40 wt%) and also better compared to result from Kurniawan *et al*. [29] by 24 and 143% according to tensile strength and tensile modulus at same basalt fibre content (25 wt% (note that 25 wt% basalt fibre content composite was not fabricated in this research, but due to the highly linear relationship, the properties were determined by interpolation)). The reason for the better properties can be found in the higher drying tem-

Table 2. Linear regression coefficients for the mechanical properties between 0–30 wt% basalt fibre content

Mechanical property	Gradient	R^2
Tensile strength	1.77 MPa/basalt wt%	0.99
Tensile modulus	151.2 MPa/basalt wt%	0.99
Flexural strength	2.44 MPa/basalt wt%	0.98
Flexural modulus	209.5 MPa/basalt wt%	0.96
Charpy impact strength (notched)	0.227 [kJ/m^2]/basalt wt%	0.97
Charpy impact strength (unnotched)	0.518 [kJ/m^2]/basalt wt%	0.94

perature of PLA prior to processing as it is published in our former research [31]. Moreover, these results indicate that the basalt fibre reinforced PLA could be used as durable engineering composite materials, because the developed composite has similar mechanical properties to Polyamide 6 (PA6) reinforced with 15 wt% glass fibre. A further advantage of the developed composite is, that the above mentioned high mechanical properties can not only be achieved by using long fibres and slow technologies like film-stacking to produce only flat-like products (as is was mentioned in the introduction in the case of plant fibre reinforced biocomposites), but by injection moulding, which is the most versatile thermoplastic processing technology to produce complex, 3D shaped engineering parts with high dimensional accuracy and low cycle times.

3.3. Scanning electron microscopy

Scanning electron microscope (SEM) observations were made on the fracture surface of tensile specimens to evaluate the adhesion between the phases (Figure 8, Figure 9). On the fracture surface of the 15 wt% basalt fibre reinforced PLA composites without treatment basalt fibres with smooth surface can be observed, which represents inadequate fibre wetting, and moreover a gap between the matrix and the root of the fibres can also be seen in the untreated basalt fibre reinforced composites, which indicates weak adhesion as it could already be seen in the mechanical properties (Figure 8a). On the fracture surface of the composite with the same amount of basalt fibres but with silane treatment, much stronger adhesion can be observed which is denoted by the absence of gap between the fibres

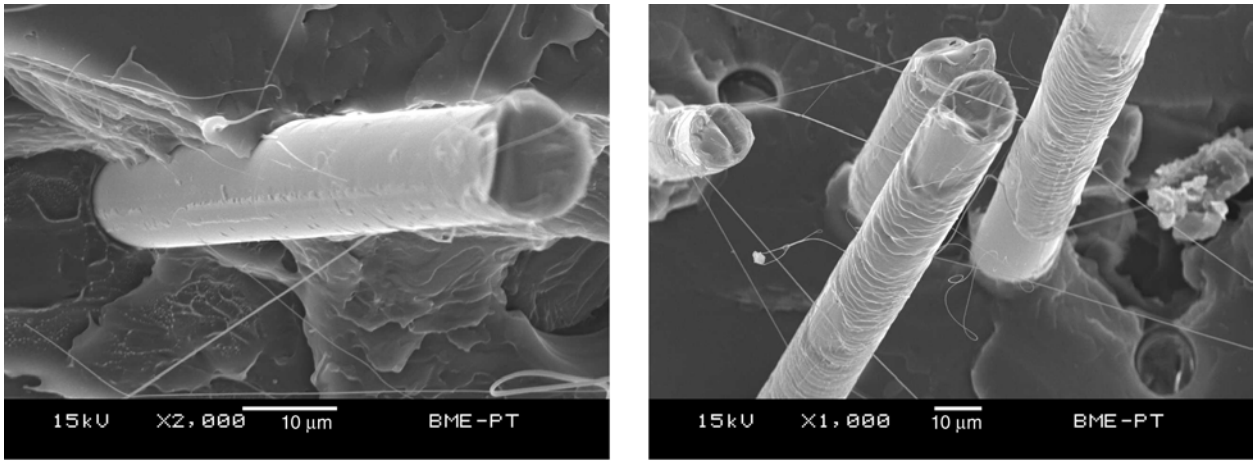

Figure 8. Cross-section of untreated (a) and treated (b), 15 wt% basalt fibre reinforced PLA composite

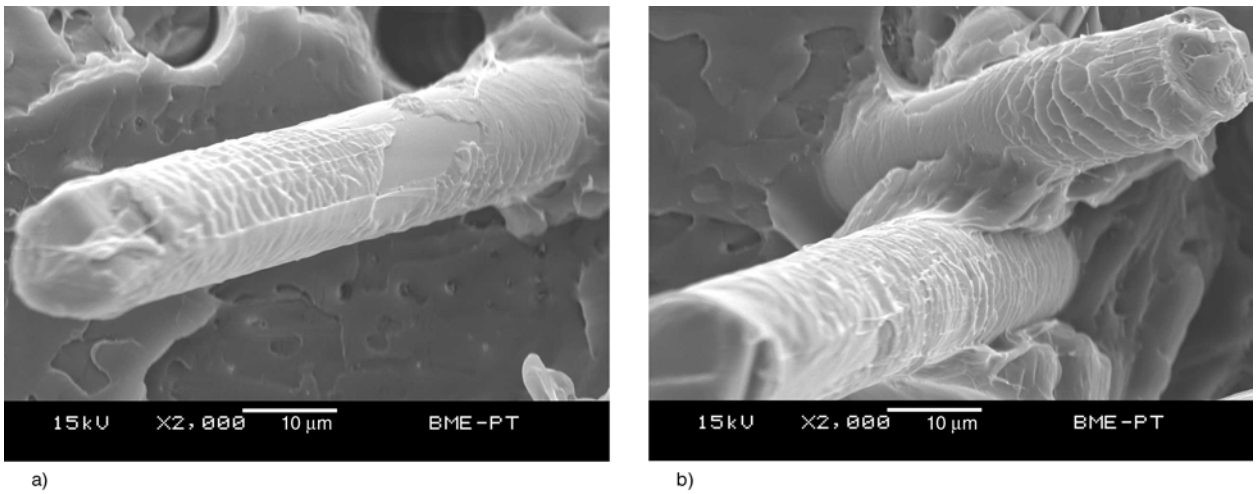

Figure 9. Cross-section of 20 wt% (a) and 40 wt% (b) silane treated basalt fibre reinforced PLA composite

and the matrix, and by the wetting of the fibre by PLA (Figure 8b).

For the 20, 30 and 40 wt% silane treated basalt fibre reinforced composites (Figure 9), also strong adhesion was found.

On the surface of the silane treated fibres a clear PLA layer can be found which represents excellent adhesion. These results are again better compared to literature data (Liu *et al*. [28]), where the surface of the basalt fibres were smooth and poorly wetted in spite of the reinforcing effect. Good quality wetting was achieved by Kurniawan *et al*. [29] by using plasma treatment of the basalt fibres, however only basalt fibre reinforced PLA composites were produced with lower mechanical properties compared to our results.

3.4. Differential scanning calorimetry

Differential scanning calorimetry (DSC) was performed by using 3–6 mg samples taken out from the middle of the cross section of the injection moulded specimens. The cooling DSC scans registered at a cooling rate of 5°C/min are presented in Figure 10.

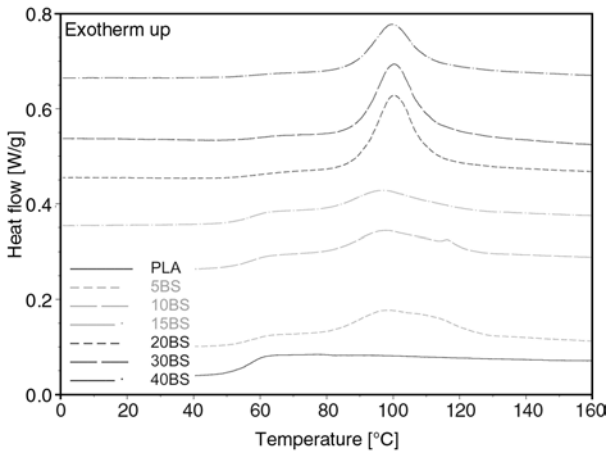

Figure 10. Cooling scan of 5–10–15–20–30–40 wt% basalt fibre reinforced composites

It can be seen that pure PLA only slightly crystallises and the specimens become transparent during cooling from melt what is a common phenomena according to its very slow crystallisation kinetics, especially when using high cooling rate technologies like injection moulding, thus the material of the pure PLA specimens are to be further referred in the paper as amorphous PLA. At the same time the silane treated and not treated basalt fibres both had nucleating effect which is represented by the higher and higher exothermic peak found around 100°C with increasing basalt fibre content. This statement is supported by the quantitative evaluation of the DSC results (Table 3). The crystallinity of the injection moulded samples was calculated by the first heating scan and by using Equation (1), while the crystallinity of the samples cooled at 5°C/min was calculated by using the second heating scan.

It is found that at and above 20 wt% basalt fibre content the nucleating effect of the fibres was enough to develop significant and at the same time the maximum possible crystallinity for PLA, which is around 40–45%. However, this statement is only valid for crystallinity values obtained from the cooling and second heating DSC scan where the cooling and heating rate was set to 5°C/min, while the crystallinity of the injection moulded specimens obtained from the first heating scan was naturally much lower, but still significant; around 19% due to the high cooling rates during processing. Nevertheless, the nucleating effect of basalt fibres suggest that by using further nucleating agents like talc and/or lower cooling rates during processing presumably basalt fibre reinforced semi-crystalline PLA can be produced which has an enormous advantage according to its crystallinity compared to amorphous PLA what is represented in the much higher heat deflec-

Table 3. Crystallinity of basalt fibre reinforced PLA composites

Material	Crystallinity of the injection moulded samples [%]	Crystallinity of the samples cooled at 5°C/min [%]	Crystallisation peak temperature [°C]
Amorphous PLA	1.1	3.0	–
5BN	8.5	21.6	96
5BS	4.0	25.6	99
10BN	10.6	20.9	96
10BS	14.0	24.4	97
15BN	17.2	23.1	97
15BS	17.5	21.1	97
20BS	18.7	42.9	100
30BS	19.0	44.2	100
40BS	18.5	44.8	100

tion temperature and thus it would be much more suitable for engineering applications.

3.5. Dynamic mechanical analysis

Dynamic mechanical analyses (DMA) were performed to examine the usability of the developed composites in the temperature range of 0–160°C and especially in the critical range above T_g. Due to the slow crystallisation of PLA, it remains mostly amorphous during injection moulding, thus the dramatic drop in storage modulus at T_g and the increase in storage modulus caused by cold-crystallisation in the temperature range of 80–120°C can be observed (Figure 11).

Naturally the basalt fibres increase the storage modulus; the silane treated basalt fibres increased it more significantly than the untreated ones due to the better adhesion proved previously by the SEM and mechanical test results. It can also be seen that the nucleating effect of basalt fibres at and above 20 wt% basalt fibre content observed by DSC was not enough to develop significant crystallinity in PLA during injection moulding to avoid the dramatic drop in storage modulus at T_g, thus this high storage modulus loss still can be observed for all of the basalt fibre reinforced composites (Figure 12).

For further analysis the DMA curve of semi-crystalline PLA (C-PLA) was also registered (semi-crystalline PLA sample was made by annealing at 120°C for 1 hour to gain maximum possible crystallinity). By using 40 wt% silane treated basalt fibres, the storage modulus above T_g was only reduced to the same order of magnitude as the storage modulus of semi-crystalline PLA (Figure 13), which is important because semi-crystalline PLA has a HDT value of 127°C and considered as heat resistant compared to amorphous PLA, which has a HDT value of 54°C.

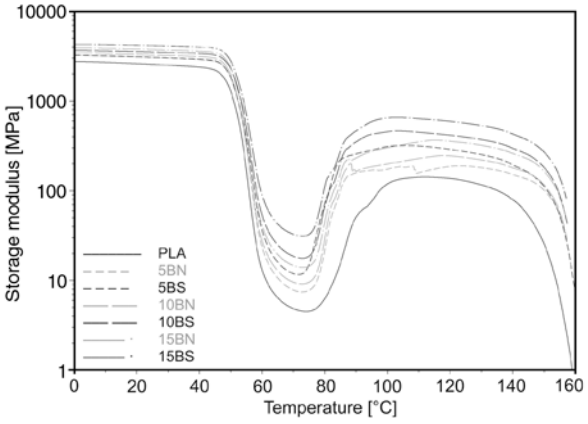

Figure 11. Storage modulus of amorphous PLA (PLA), and 5–10–15 wt% basalt fibre reinforced composites with and without silane treatment

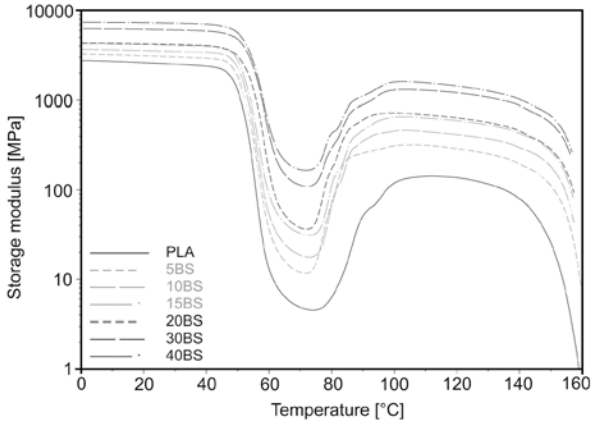

Figure 12. Storage modulus of amorphous PLA (PLA) and 5–10–15–20–30–40 wt% basalt fibre reinforced composites with silane treatment

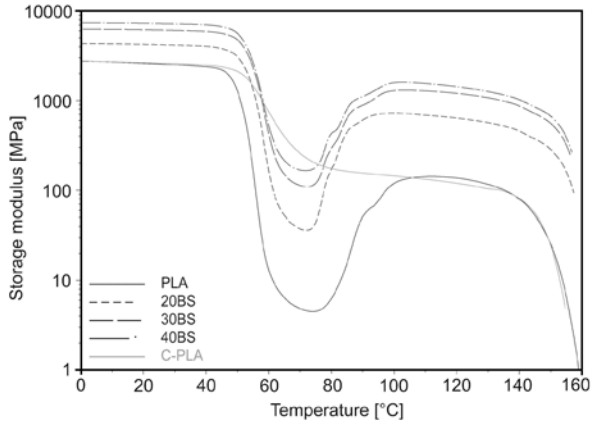

Figure 13. Storage modulus of amorphous PLA (PLA), semi-crystalline PLA (C-PLA) and 20–30–40 wt% basalt fibre reinforced composites with silane treatment

However, semi-crystalline PLA still has, but only slightly higher storage modulus in the range of 58–76°C than the 40 wt% basalt reinforced composite. The storage modulus values of PLA, semi-crystalline PLA and the basalt fibre reinforced PLA composites at 40, 120°C and the most critical and lowest storage modulus values between 70–80°C (above T_g but before cold-crystallisation) can be seen in Table 4.

It can be seen that by the incorporation of basalt fibres, the storage modulus increased linearly to reinforcement content and reached an around three-times higher modulus at 40°C and ten-times higher modulus at 120°C. By using linear regression it was found that the storage modulus at 40°C increased with a gradient of 114.0 MPa/basalt wt% content

Table 4. Storage modulus vales of amorphous PLA, semi-crysatlline PLA and basalt fibre reinforced PLA composites

Material	Storage modulus at 40°C [MPa]	Storage modulus at 120°C [MPa]	Lowest storage modulus between 70–80°C [MPa]
Amorphous PLA	2390	140	5 (at 74°C)
Semi-crystalline PLA	2490	130	250 (at 70°C)
5BN	2900	190	7 (at 73°C)
5BS	2920	290	12 (at 72°C)
10BN	3130	250	9 (at 72°C)
10BS	3380	420	18 (at 73°C)
15BN	3600	360	14 (at 73°C)
15BS	4000	590	31 (at 73°C)
20BS	4500	780	45 (at 72°C)
30BS	5900	1200	109 (at 72°C)
40BS	7030	1430	166 (at 71°C)

(R^2 = 0,99), while the storage modulus at 120°C increased with a gradient of 32.9 MPa/basalt wt% content (R^2 = 0,99) according to silane treated basalt fibres.

3.6. Dimensional stability

Dimensional stability of the basalt fibre reinforced PLA composites was examined by placing them into a heated oven and measuring the changes in flow directional (longitudinal) dimensions after heating by using Equation (2). Naturally, it is found that basalt fibres restrain deformation, and it can be observed that the main deformation occurs above T_g, which is caused by the specific volume change due to cold-crystallisation (Figure 14).

It is again found that basalt fibres with silane treatment are much more effective than untreated basalt fibres, this time in reducing deformation. With increasing silane treated basalt fibre content, the longitudinal deformation of PLA of 5.9% was reduced to 2.6, 1.6, 1.1, 0.7, 0.5 and 0.5% according to 5–10–15–20–30–40 wt% basalt fibre content respectively (Figure 15).

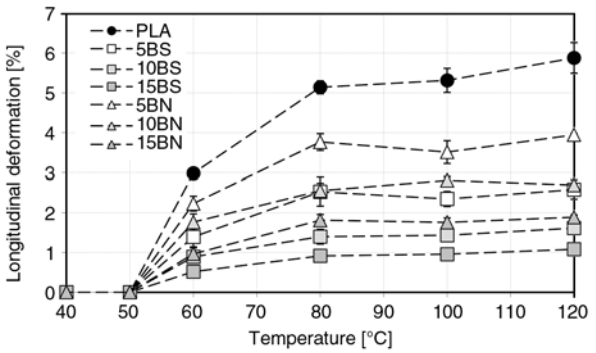

Figure 14. Longitudinal deformation of PLA and 5–10–15 wt% basalt fibre reinforced composites with and without silane treatment

The dimensional stability of the specimens was also analysed with another method by placing them in a cantilever and registering the deflection caused by the increasing heat and the own weight of the specimens. It was observed that the deflection of the pure PLA was significantly reduced (Figure 16), thus by incorporating basalt fires, the dimensional stability of the specimens highly increased.

It is again demonstrated that silane treated basalt fibres were much more effective than untreated fibres in reducing the deflection of the specimens. By using the same amount of basalt fibres, silane

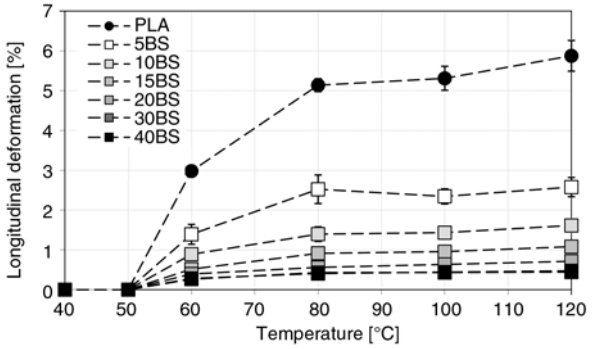

Figure 15. Longitudinal deformation of PLA and 5–10–15–20–30–40 wt% basalt fibre reinforced composites with silane treatment

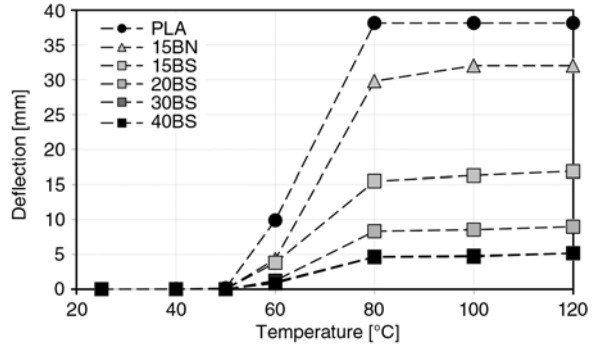

Figure 16. The deflection of the basalt fibre reinforced PLA composites

Figure 17. Deflection of the PLA, 15BN, 15BS specimens (from left to right) at 120°C

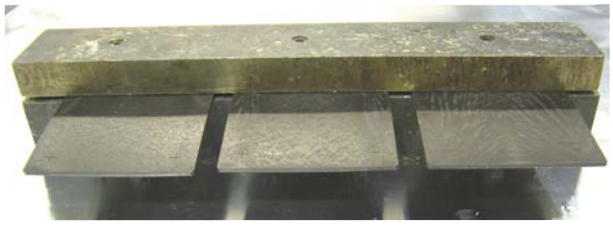

Figure 18. Deflection of the 20BS, 30BS, 40BS specimens (from left to right) at 120°C

treated basalt fibres reduced the deflection of PLA of more than 40 to 17 mm, while untreated basalt only reduced the deflection to 32 mm. 20, 30 and 40 wt% silane treated basalt reduced the deflection to 9, 5 and 5 mm respectively as it can be observed in Figure 17 and Figure 18.

As it can be seen, the PLA, 15BN and 15BS composites were highly deformed, while the deflection of the 30BS and 40BS composites was minimal; these latter can be considered as dimensionally stable up to 120°C.

3.7. Heat deflection temperature analysis

For further analysis of the dimensional stability standardised heat deflection temperature (HDT) tests were performed. The standardised HDT analysis with a support distance of 100 mm only allows 0.33 mm deflection of the specimens which puts up for much stricter requirements than our dimensional stability test discussed previously. Due to these strict requirements, HDT was only increased by from 54 to 59°C by using 40 wt% of silane treated basalt fibres. At the same time the DMA and dimensional stability test results confirm that 30–40 wt% basalt fibre reinforced PLA specimens were almost undeformed and nearly passed over the critical 60–80°C temperature range where the modulus drops and cold-crystallisation not yet commences. If the stiffness of the PLA can be kept above a certain level in the mentioned critical temperature range, then in the higher temperature range cold-crystallisation could ensure a HDT value of an at least 120°C.

4. Conclusions

In our work the usability of a novel natural fibre, the volcanic rock based basalt fibre was examined as a potential reinforcement for the most promising renewable resource based biodegradable polymer, the poly(lactic acid) (PLA) as well as the comprehensive analysis of basalt fibre reinforced PLA injection moulded composites was performed. 5–10–15–20–30–40 wt% silane treated and 5–10–15 wt% untreated basalt fibre reinforced composites were produced by using extrusion and injection moulding. According to our previous results on starch filled PLA, high drying temperature was used (120°C) to remove the smallest remnants of moisture, which could typically highly deteriorate the adhesion between the phases. As a result silane treated basalt fibre reinforced PLA composites were produced with higher mechanical properties compared to literature. By incorporating 40 wt% silane treated basalt fibres into PLA, a composite was fabricated with a tensile and flexural strength of 124 and 185 MPa, a tensile and flexural modulus of more than 8 and 12 GPa and a Charpy impact strength of 9.5 kJ/m^2 (notched) and 38.4 kJ/m^2 (unnotched) respectively. By using scanning electron microscopy strong adhesion was observed between the phases, and excellent wetting of the silane treated basalt fibres was seen, which is again much better compared to literature results. It was found by using differential scanning calorimetry that basalt fibres have nucleating ability on PLA, however, semi-crystalline PLA samples with the possible maximum crystallinity of 40–45% could only be made by using low cooling rate (5°C/min) and at least 20 wt% basalt fibre content. By using injection moulding, and thus high cooling rate, the crystallinity of the basalt fibre reinforced PLA composites reached a lower, but still significant value of 19%. Besides nucleating ability of the basalt fibres, they effectively reduced the deformation and deflection caused by increasing temperature making it a more or less dimensionally stable composite up to 120°C. According to the DMA results, by incorporating the basalt fibres the storage modulus at 40 and at 120°C became three-times higher and ten-times higher compared to the storage modulus of amorphous PLA respectively. Moreover the storage modulus of the 40 wt% basalt fibre reinforced PLA was in the same order of magnitude of a semi-crystalline PLA

in the critical temperature range of 60–80°C (where amorphous PLA products distort), which is a relevant result, because semi-crystalline PLA has a heat deflection temperature (HDT) of more than 120°C and considered as heat stable. At the same time, the storage modulus of semi-crystalline PLA (250 MPa) was still somewhat higher than 40 wt% basalt fibre reinforced PLA (166 MPa) at 70°C and as a result, by using basalt fibres the standard HDT value only increased from 54 to 59°C. This could be related to the strict HDT test condition requirement which allows only very small deflection, although the siginifcant impovement in dimensional stability in the case of 30 and 40 wt% basalt fibre reinforced composites compared to PLA was demonstrated. If the stiffness of the basalt fibre reinforced PLA composite can be kept above a certain level and it could pass over the mentioned critical temperature range undeformed, then in the higher temperature range cold-crystallisation could ensure a HDT value of an at least 120°C. Nevertheless, probably by using further nucleating agents like talc and/or slow cooling rate during processing basalt fibre reinforced semi-crystalline PLA composites with a heat deflection temperature of more than 120°C can be produced, which is much more suitable for engineering applications. Finally it was demonstrated that it is possible to produce basalt fibre reinforced PLA composites from renewable and natural resources with excellent mechanical properties not only by using low productivity technologies like film-stacking method not to damage the fibres but by using productive extrusion and injection moulding technologies suitable for manufacturing highly accurate, complex, 3D shaped and durable engineering parts with low cycle times.

Acknowledgements

The authors thank Arburg Hungária Kft. for the Arburg Allrounder 370C 700-290 injection moulding machine and Lenzkes GmbH for the clamping tool system. This work is connected to the scientific program of the 'Development of quality-oriented and harmonized R+D+I strategy and functional model at BME' project. This project is supported by the New Széchenyi Plan (Project ID: TÁMOP-4.2.1/B-09/1/KMR-2010-0002). The work reported in this paper has been developed in the framework of the project 'Talent care and cultivation in the scientific workshops of BME' project. This project is supported by the grant TÁMOP-4.2.2.B-10/1-2010-0009. This paper was supported by the János Bolyai Research Scholarship of the Hungarian Academy of Sciences.

References

[1] Avérous L.: Biodegradable multiphase systems based on plasticized starch: A review. Journal of Macromolecular Science Part C: Polymer Reviews, **44**, 231–274 (2004).
DOI: 10.1081/MC-200029326

[2] Yu L., Dean K., Li L.: Polymer blends and composites from renewable resources. Progress in Polymer Science, **31**, 576–602 (2006).
DOI: 10.1016/j.progpolymsci.2006.03.002

[3] Ren X.: Biodegradable plastics: A solution or a challenge? Journal of Cleaner Production, **11**, 27-40 (2003).

[4] Czigány T., Romhány G., Kovács J. G.: Starch for injection moulding purposes. in 'Handbook of engineering biopolymers: Homopolymers, blends and composites' Hanser, Munich, 81–108 (2007).

[5] Tábi T., Kovács J. G.: Examination of injection moulded thermoplastic maize starch. Express Polymer Letters, **1**, 804–809 (2007).
DOI: 10.3144/expresspolymlett.2007.111

[6] Tábi T., Tuba F., Oláh L.: Investigation of time-dependent behavior of starch-based, injection molded biodegradable polymer. Materials Science Forum, **589**, 281–286 (2008).
DOI: 10.4028/www.scientific.net/MSF.589.281

[7] Martin O., Avérous L.: Poly(lactic acid): Plasticization and properties of biodegradable multiphase systems. Polymer, **42**, 6209–6219 (2001).
DOI: 10.1016/S0032-3861(01)00086-6

[8] Yu L., Dean K., Li L.: Polymer blends and composites from renewable resources. Progress in Polymer Science, **31**, 576–602 (2006).
DOI: 10.1016/j.progpolymsci.2006.03.002

[9] Lim L-T., Auras R., Rubino M.: Processing technologies for poly(lactic acid). Progress in Polymer Science, **33**, 820–852 (2008).
DOI: 10.1016/j.progpolymsci.2008.05.004

[10] Iwatake A., Nogi M., Yano H.: Cellulose nanofiber-reinforced polylactic acid. Composites Science and Technology, **68**, 2103–2106 (2008).
DOI: 10.1016/j.compscitech.2008.03.006

[11] Suryanegara L., Nakagaito A. N., Yano H.: The effect of crystallization of PLA on the thermal and mechanical properties of microfibrillated cellulose-reinforced PLA composites. Composites Science and Technology, **69**, 1187–1192 (2009).
DOI: 10.1016/j.compscitech.2009.02.022

[12] Ganster J., Fink H-P., Pinnow M.: High-tenacity manmade cellulose fibre reinforced thermoplastics – Injection moulding compounds with polypropylene and alternative matrices. Composites Part A: Applied Science and Manufacturing, **37**, 1796–1804 (2006).
DOI: 10.1016/j.compositesa.2005.09.005

[13] Oksman K., Skrifvars M., Selin J-F.: Natural fibres as reinforcement in polylactic acid (PLA) composites. Composites Science and Technology, **63**, 1317–1324 (2003).
DOI: 10.1016/S0266-3538(03)00103-9

[14] Plackett D., Andersen T. L., Pedersen W. B., Nielsen L.: Biodegradable composites based on L-polylactide and jute fibres. Composites Science and Technology, **63**, 1287–1296 (2003).
DOI: 10.1016/S0266-3538(03)00100-3

[15] Bodros E., Pillin I., Montrelay N., Baley C.: Could biopolymers reinforced by randomly scattered flax fibre be used in structural applications? Composites Science and Technology, **67**, 462–470 (2007).
DOI: 10.1016/j.compscitech.2006.08.024

[16] Bax B., Müssig J.: Impact and tensile properties of PLA/Cordenka and PLA/flax composites. Composites Science and Technology, **68**, 1601–1607 (2008).
DOI: 10.1016/j.compscitech.2008.01.004

[17] Huda M. S., Drzal L. T., Mohanty A. K., Misra M.: Chopped glass and recycled newspaper as reinforcement fibers in injection molded poly(lactic acid) (PLA) composites: A comparative study. Composites Science and Technology, **66**, 1813–1824 (2006).
DOI: 10.1016/j.compscitech.2005.10.015

[18] Anuar H., Zuraida A., Kovács J. G., Tábi T.: Improvement of mechanical properties of injection-molded polylactic acid–kenaf fiber biocomposite. Journal of Thermoplastic Composite Materials, **25**, 153–164 (2012).
DOI: 10.1177/0892705711408984

[19] Gur'ev V. V., Neproshin E. I., Mostovoi G. E.: The effect of basalt fiber production technology on mechanical properties of fiber. Glass and Ceramics, **58**, 62–65 (2001).
DOI: 10.1023/A:1010901615857

[20] Czigány T.: Special manufacturing and characteristics of basalt fiber reinforced polypropylene composites: Mechanical properties and acoustic emission study. Composites Science and Technology, **66**, 3210–3220 (2006).
DOI: 10.1016/j.compscitech.2005.07.007

[21] Czigány T. Deák T. Tamás P.: Discontinuous basalt and glass fiber reinforced PP composites from textile prefabricates: Effects of interfacial modification on the mechanical performance. Composite Interfaces, **15**, 697–707 (2008).
DOI: 10.1163/156855408786778302

[22] Militký J., Kovačič V., Rubnerová J.: Influence of thermal treatment on tensile failure of basalt fibers. Engineering Fracture Mechanics, **69**, 1025–1033 (2002).
DOI: 10.1016/S0013-7944(01)00119-9

[23] Wei B., Cao H., Song S.: Tensile behavior contrast of basalt and glass fibers after chemical treatment. Materials and Design, **31**, 4244–4250 (2010).
DOI: 10.1016/j.matdes.2010.04.009

[24] Wei B., Cao H., Song S.: Environmental resistance and mechanical performance of basalt and glass fibers. Materials Science and Engineering: A, **527**, 4708–4715 (2010).
DOI: 10.1016/j.msea.2010.04.021

[25] Czigány T., Pölöskei K., Karger-Kocsis J.: Fracture and failure behavior of basalt fiber mat-reinforced vinylester/epoxy hybrid resins as a function of resin composition and fiber surface treatment. Journal of Materials Science, **40**, 5609–5618 (2005).
DOI: 10.1007/s10853-005-1273-8

[26] Matkó S., Anna P, Marosi G., Szép A., Keszei S., Czigány T., Pölöskei K.: Use of reactive surfactants in basalt fiber reinforced polypropylene composites. Macromolecular Symposia, **202**, 255–267 (2003).
DOI: 10.1002/masy.200351222

[27] Deák T., Czigány T., Tamás P., Németh Cs.: Enhancement of interfacial properties of basalt fiber reinforced nylon 6 matrix composites with silane coupling agents. Express Polymer Letters, **4**, 590-598 (2010).
DOI: 10.3144/expresspolymlett.2010.74

[28] Liu T., Yu F., Yu X., Zhao X., Lu A., Wang J.: Basalt fiber reinforced and elastomer toughened polylactide composites: Mechanical properties, rheology, crystallization, and morphology. Journal of Applied Polymer Science, **125**, 1292–1301 (2012).
DOI: 10.1002/app.34995

[29] Kurniawan D., Kim B. S., Lee H. Y., Lim J. Y.: Atmospheric pressure glow discharge plasma polymerization for surface treatment on sized basalt fiber/polylactic acid composites. Composites Part B: Engineering, **43**, 1010–1014 (2012).
DOI: 10.1016/j.compositesb.2011.11.007

[30] Chen X., Li Y., Gu N.: A novel basalt fiber-reinforced polylactic acid composite for hard tissue repair. Biomedical Materials, **5**, 044104/1–044104/8 (2010).
DOI: 10.1088/1748-6041/5/4/044104

[31] Kovács J. G., Tábi T.: Examination of starch preprocess drying and water absorption of injection-molded starch-filled poly(lactic acid) products. Polymer Engineering and Science, **51**, 843–850 (2011).
DOI: 10.1002/pen.21900

[32] Tábi T., Sajó I. E., Szabó F., Luyt A. S., Kovács J. G.: Crystalline structure of annealed polylactic acid and its relation to processing. Express Polymer Letters, **4**, 659–668 (2010).
DOI: 10.3144/expresspolymlett.2010.80

[33] Battegazzore D., Bocchini S., Frache A.: Crystallization kinetics of poly(lactic acid)-talc composites. Express Polymer Letters, **5**, 849–858 (2011).
DOI: 10.3144/expresspolymlett.2011.84

eXPRESS Polymer Letters Vol.7, No.2 (2013) 120–133
Available online at www.expresspolymlett.com
DOI: 10.3144/expresspolymlett.2013.12

Influence of the filler content on the free nanohole volume in epoxy-based composites

S. Tognana[1*], *W. Salgueiro*[1], *A. Somoza*[1], *A. J. Marzocca*[2]

[1]IFIMAT – Universidad Nacional del Centro de la Provincia de Buenos Aires, Pinto 399, (B7000GHG) Tandil, Argentina and Comisión de Investigaciones Científicas de la Provincia de Buenos Aires, calle 526 entre 10 y 11, La Plata, Argentina
[2]LPMP y MC, Departamento de Física, Facultad de Ciencias Exactas y Naturales, Universidad Nacional de Buenos Aires, Ciudad Universitaria, Pabellón I, C1428EGA Buenos Aires, Argentina

Received 29 June 2012; accepted in revised form 11 September 2012

Abstract. A study on free nanohole volumes in particulate epoxy matrix composites as a function of the aluminum particles content is presented. Specifically, the influence of the filler content in the epoxy matrix on the nanohole volume is analyzed in terms of the mechanical and morphological properties of the composites fabricated. Nanoholes data were measured using positron annihilation lifetime spectroscopy recently published by the authors. Applying the Park-Earmme micromechanical model, these data are interpreted in terms of the thermal stresses generated during the curing process applied during fabrication. Some input parameters of the model were experimentally obtained. In order to obtain a satisfactory description of the evolution of the free nanohole volume in the whole range of filler contents, a contribution due to the matrix-particle interphases is taken into account in the micromechanical model. To this aim, specific information on the interphases was obtained using atomic force microscopy (AFM), scanning electron microscopy (SEM), differencital scanning calorimetry (DSC) and a free-constraint analysis of the positron lifetime data.

Keywords: *polymer composites, epoxy, free volume, positron annihilation*

1. Introduction

The use of polymer matrix composites in different technological applications is of interest due to their very good mechanical properties, long life in service and optimization of cost. The different applications of a composite determin the different kinds and geometries of the inclusions (*i.e.*, fillers) as well as of the polymeric matrix. Specifically, many epoxy matrix composites filled with inorganic particles composites have been developed. These systems have been extensively studied in order to understand the influence of inorganic particles added to the matrix on properties of these composites (mechanical, thermal, optical, etc.) [1].

Epoxy matrix composites are fabricated performing a cure treatment at high temperature of the resin with the addition of a specific hardener and particles used as filler. This process mainly defines the network structure and, consequently, the final properties of a composite [2]. As an example, strong residual stresses can be generated during curing as a consequence of the thermal and mechanical mismatches between the constituent phases of the composite.

The residual stresses have been studied for some decades, using experimental and theoretical tools. In this last case, different theories and calculation methods have been developed. In particular, Eshelby [3] proposed a method to calculate the stress field

*Corresponding author, e-mail: stognana@exa.unicen.edu.ar

around an anisotropic particle embedded in a matrix of a general composite. Selsing reported [4] a simply equation for the residual stresses around a single inclusion in ceramic-based composites. Besides, a generalized self-consistent method was proposed and extensively used for the investigation of the physical properties of two-phase composites [5]. In particular, Park and Earmme [6] used some of these methods to investigate the residual stresses produced by a temperature variation during the manufacturing process of metal-matrix composites. These methods have also been applied to polymer-matrix composites [7, 8].

On the other hand, besides the residual stresses, the inclusion of particles in a polymeric matrix can generate other structural changes in the material. In composites, the filler-matrix interphases (*i.e.* a region around the surface between the constituent phases of the composites) have different characteristics with respect to the matrix. In fact, around the inclusion surface there is a region where the local properties are different of the bulk matrix properties [9]. In the interphase region from the matrix to the filler such differences become gradual. In polymers, these interphases can be formed during the curing process. However, the nature of the interphase remains as a field of research. The existence of this so-called third phase can influence in an important way the total properties of the composite. This concept was particularly developed in a three phase model that allowed the study of the mechanical properties in polymer matrix-metal particles composites [10]. In epoxy matrix composites, residual stresses and the interphase formation have experimentally been studied using different techniques [11]. However, it is difficult to find a proper technique that allows the study of both processes at the same time.

Some of the authors of the present work have studied the influence of the residual stresses on the free volume in polymer-matrix composites, taking advantage of the high specificity of Positron Annihilation Lifetime Spectroscopy (PALS) [8, 12, 13]. PALS is practically the only experimental technique that allows to directly measure the size of nanohole forming the free volume [14].

According to the common interpretation of PALS spectra in polymers, the nanoholes sizes V_H can be directly estimated using a well-recognized semi-empirical equation through the long-lived lifetime component, attributed to ortho-Ps (ortho-Positronium) annihilation by pick–off trapped in the free nanohole volumes [14, 15]. This lifetime τ_{o-Ps} component is usually used as the experimental input and by means of a simple quantum mechanical model the radius of the nanohole can be obtained from Equation (1) [14, 15]:

$$\tau_{o-Ps}=0.5\left[1-\frac{R}{R+\delta R}+\frac{1}{2\pi}sen\left(\frac{2\pi R}{R+\delta R}\right)\right]^{-1} \qquad (1)$$

in which δR is the thickness (0.166 nm) of the electron layer that constitutes the wall of the nanohole and can overlap with the o-Ps wave function. The nanohole volume can be computed as $V_H = 4\pi R^3/3$. It should be emphasized that the free volume is a concept used to explain the variation of several properties of a polymer under changes of temperature or pressure [16]. Also, it has been related to the structure and reticulation of the polymeric chains [17, 18]. However, the results obtained in those materials cannot be directly linked with the phenomena studied in the present work.

In this work, we go deeper into the analysis of experimental PALS results we reported in [13] on the variation of the free nanohole volume in particulate epoxy matrix as a function of the aluminum particles content. As a result, it was found that the free volume depends on the thermal residual stresses and the interphase formation in the fabricated composites containing different filler contents (from the blank epoxy resin to 30%). For the analysis of the experimental data, it was necessary to utilize different well-known micromechanical models as well as specific experimental techniques. The procedure we followed in approaching the objective of the present work was developed in different steps. Firstly, a micromechanical model, based on different approximations reported in the literature, allowed us to obtain the residual stresses generated into the composite matrix as a consequence of the addition of inclusions. In order to calculate the stresses values as a function of the filler content, previously reported values of the Young modulus, obtained by authors of the present work using the impulse excitation technique (IET), were used as input parameters into the micromechanical model. However, when the inclusion volumetric fraction was higher than 15% this model failed in describing the behavior of the experimental free nanohole volume data. Therefore, in a second step the influence of the inclusion-matrix interphases on the free nanohole

volume in the different composites fabricated was added to the model mentioned taking into account two contributions to the free nanohole volume; *i.e.* matrix and interphases. To this aim, experimental information regarding interphases was obtained using atomic force microscopy (AFM) and differential scanning calorimetry (DSC). These results were then used into a reformulated micromechanical model allowing a satisfactory description of the free nanohole volume in the whole range of the filler content. It is important to emphasize that a quantitative analysis on the contribution of the inclusion-epoxy matrix interphases to the free nanohole volumes is one of the most important contributions of this work to the literature, as well as a comprehensive discussion on the variation of the nanohole volume when different amounts of inorganic filler are added to the epoxy matrix of the composite.

2. Experimental

2.1. Sample preparation

The composites studied were prepared using as matrix diglycidyl ether of bisphenol A (DGEBA) epoxy resin, cured with an anhydride (MTHPA) and an accelerator (tertiary amine). DGEBA (100 pbw) and MTHPA (90 pbw) were mixed and stirred at room temperature in vacuum during 30 minutes. Then, the accelerator (0.7 pbw) was added and the mixture was stirred again during 5 minutes under vacuum. Finally, a required amount of aluminum particles was added and the mixture was stirred under vacuum until to reach a good dispersion of the particles in the resin. The compound was poured in a Pyrex tubular mold and kept in horizontal position in a tubular oven.

With the help of a device especially developed a rotation was imposed to the molds in order to avoid the settling down of the aluminum particles during the curing. In the curing process, the mixture was heated up to 393 K with a 0.8 K/min rate, and at the end of the heating process, the samples were kept at a constant temperature (393 K) for 14 h. The composites were prepared using aluminum powder with particle diameters between 106 and 125 μm and with a filler volume fraction, ϕ, ranging from 0 to 30% in 5% steps. More details about the preparation process are given in [8, 12].

For microscopy measurements, the samples were cut using a low speed diamond saw and then polished in several steps, starting with 1200 grit grinding paper followed by 3 and 1 μm diamond particles and 0.3 and 0.05 μm alumina particles/water suspensions.

2.2. Atomic force and scanning electron microscopies

SEM images were taken with a FE-SEM, Zeiss DSM 982 Gemini microscope.

AFM tests were carried out in tapping mode in a Digital Instruments Nanoscope III. The tests were performed using a single beam cantilever provided by an etched silicon nitride probe, in a nitrogen atmosphere. During the scanning, the topography and phase shifts, *i.e.*, changes in the phase angle of vibration respect to the phase angle of the freely oscillating cantilever, were simultaneously recorded. The phase image allows revealing differences in surface properties of the material which in nature are currently qualitative. The AFM data were analyzed by using the WSxM 3.0 software [19].

3. Results and discussion

3.1. PALS

In Figure 1, the variation of the average free nanohole volume as a function of the filler volume fraction is shown. Though these data were already published in a previous work [13], in order to facilitate the reading and put major emphasis in the key issues of the present work, we decided to present them and to give a brief analysis of the experimental data again. As can be seen, there is a complex and non-monotonic behavior of V_H when ϕ increases. To analyze it, the plot was divided into three regions: in the first, when the filler content is lower than

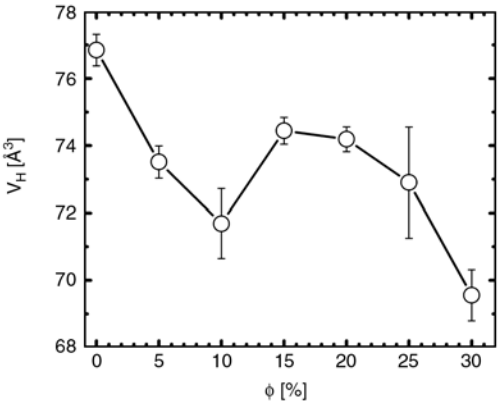

Figure 1. Average free nanohole volume as a function of the filler content measured, using positron annihilation lifetime spectroscopy (after [13])

10%, V_H rapidly decreases when the filler content increases; in the second region, an increment of V_H until ϕ reaches a value around 15%; and for higher volume fractions (third region) the average free nanohole volume decreases, initially in a slight way and then in a more noticeably mode.

A similar behavior has been previously reported and discussed by some authors of the present work. In that paper, Goyanes *et al.* [8] discussed the results obtained in terms of the average thermal stresses occurring in the matrix as a consequence of the thermal mismatch due to the presence of filler particles. However, the authors could only explain the V_H decreasing behavior for the first region (*i.e.*, till ϕ values up to 10–15%) of the curve above described. To go further into the analysis of the data presented in Figure 1 and taking as a starting point the previous work of Goyanes *et al*. [8] and Tognana *et al*. [13], it was necessary to obtain additional experimental evidences. Besides, a deeper analysis of the data using well-known micromechanical models was carried out. Specifically, experimental information obtained using calorimetric and mechanical properties measurements was used as input parameters in such models.

In the following sections, different contributions to solve the same original problem, specifically to explain the behavior of the free nanohole volume against the filler content in the whole volume fraction range, are given.

3.2. Thermal residual stresses around a particle

It is well-known that during the fabrication process of the composites, strong residual stresses are produced when cooling the material from the cure temperature to that of service. These residual stresses are caused by the difference between the coefficients of thermal expansion (CTE) of the matrix and the inclusion as well.

Selsing [4] calculated the residual stresses, induced by a change in the temperature (ΔT), produced around a single spherical inclusion of radius r_f imbedded within an infinite isotropic elastic matrix. In order to analyze the stresses above mentioned, the radial stress in the matrix is can be calculated by Equation (2):

$$\sigma_{rr}^{M} = -P\cdot\left(\frac{r_f}{r}\right)^3 \tag{2}$$

where P is the hydrostatic pressure in the inclusion and r is the distance since the center of the inclusion. The value of P can be obtained using the following Equation (3) [4]:

$$P = \frac{(CTE_M - CTE_F)\Delta T}{\frac{1+\nu_M}{2E_M} + \frac{1-2\nu_F}{E_F}} \tag{3}$$

where *CTE* is the coefficient of thermal expansion, and the subscripts *M* and *F* refer to the matrix and the particle, respectively. In the inclusion, the radial stress is independent of the r parameter (see Equation (4)), so Selsing [4] concluded that:

$$\sigma_{rr}^{F} = -P \tag{4}$$

On the other hand, the tangential component of the residual stresses in the matrix as well as in the inclusion can be calculated as shown by Equations (5) and (6) (for details see [4]):

$$\sigma_{\theta\theta}^{M} = \sigma_{\phi\phi}^{M} = \frac{P}{2}\left(\frac{r_f}{r}\right)^3 \tag{5}$$

$$\sigma_{\theta\theta}^{F} = \sigma_{\phi\phi}^{F} = -P \tag{6}$$

In a composite containing a high amount of particles in the matrix, if the stress fields around each particle do not overlap each other both components of the residual stresses are used. In such a sense, from a study on ceramic matrix composites [20] it was reported that the above expressions for the residual stresses were valid for composites containing up to approximately 15% of filler volume fraction. Taking into account that result, we could conclude that the use of a simple model like that proposed by Selsing [4] is not enough to obtain reliable information on the evolution of the residual stresses in our composites. The filler content is higher than a limit given by the overlapping of the stress fields of the individual particles we have found to be around 15%. For this reason, from the micromechanical point of view we have used other models which allowed us to obtain a satisfactory description of the realistic problem we were dealing with. In the next two Sections they are discussed in detail.

3.3. Average thermal stresses

To go further into the analysis of the thermal stresses present in a composite, in this Section we will dis-

cuss them in terms of the existence of a higher amount of inclusions into the materials.

Park and Earmme [6] modeled the thermal residual stresses using the generalized self-consistent method proposed by Christensen and Lo [5] to study other properties of a general kind of particulate materials. Basically, a spherical inclusion is considered to be perfectly bounded to a spherical shell which is embedded in an effective medium. The radius of the inclusion and the shell are r_f and r_b, respectively. Then, $(r_f/r_b)^3$ represents the filler content, ϕ. In the model, it is assumed that the mechanical and thermal properties of the effective medium are in-between that corresponding to the matrix and that of the inclusion. As a result, Park and Earmme estimated the stresses in the three regions (*i.e.*, matrix, particles and effective medium). In particular, they reported that the stress into the matrix is given by Equations (7) and (8):

$$\sigma_{rr}^{M}=\frac{12K_F\varepsilon_{ij}^{F}}{D}\left(I-II\left(\frac{r_f}{r}\right)^3\right)+\frac{12K_M\varepsilon_{ij}^{M}}{D}\left(III+IV\left(\frac{r_f}{r}\right)^3\right) \tag{7}$$

$$\sigma_{\theta\theta}^{M}=\sigma_{\phi\phi}^{M}=\frac{12K_F\varepsilon_{ij}^{F}}{D}\left(I+II\left(\frac{r_f}{r}\right)^3\right)+$$

$$+\frac{12K_M\varepsilon_{ij}^{M}}{D}\left(III-IV\left(\frac{r_f}{r}\right)^3\right) \tag{8}$$

(other components = 0), where:

$I = 3K_M\phi(G_M - G_C)$

$II = G_M(3K_M + 4G_C)$

$III = 3K_F\phi(G_C - G_M) - G_C(3K_F + 4G_M)$

$IV = G_M(3K_F + 4G_C)$

$D = (3K_F + 4G_M)(3K_M + 4G_C) -$
$- 12\phi(G_C - G_M)(K_F - K_M)$

$\varepsilon_{ij}^{F} = (CTE_F - CTE_C)\Delta T\delta_{ij}$

$\varepsilon_{ij}^{M} = (CTE_M - CTE_C)\Delta T\delta_{ij}$

K being the bulk modulus and G the shear modulus. The subscripts M, F and C refer to the matrix, particle and effective medium, respectively. In our case, we have assumed that the properties of the effective medium are those of the composite. In this work, it was considered that the temperature change ΔT was 100 K.

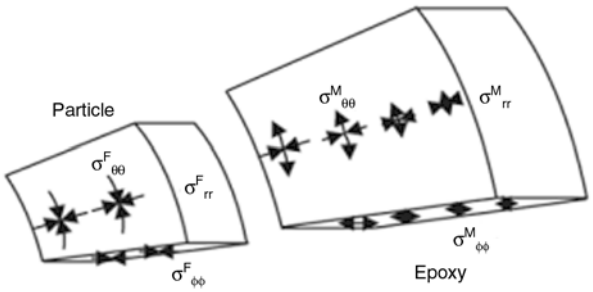

Figure 2. Schematic description of the stress fields acting on the filler and the matrix in a particulate composite

Specifically, for aluminum microparticles as used in the present work $K_F > K_M$, $G_F > G_M$ and $CTE_M > CTE_F$, and, then, a particle is subjected to a compression radial stress σ_{rr}^{F} from the epoxy matrix. On the other hand, the shell of the matrix suffers two kinds of stresses: one representing the radial compression of the effective medium; and another corresponding to the radial tensile caused by the particle. A schematic description of the nature of each stress fields acting on the particle (aluminum inclusions in this work) and in the epoxy matrix is presented in Figure 2. During the cooling process from the cure temperature of the composite, compressive stresses operate on the particle. This kind of stress is homogeneous for all particles. Conversely, the strength of stresses present in the matrix diminishes when the distance to the particle increases.

It is known that the chemical shrinkage a polymer suffers during the cure process can also produce residual stresses; however, this contribution is usually neglected since at this stage of the cure process the elastic properties of the matrix are poor. So, to analyze and discuss the data in the present work we only have taken into account the contribution to the stresses coming from the thermal properties of the phases forming the different composites.

Equations (7) and (8) were parameterized in terms of the distance to the center of the particle r. In this way, those radial and the tangential stress components which are independent of r (terms I and III in the equations above mentioned) have the same sign. Conversely, those terms depending on r (terms II and IV) have an opposite sign. It must also be noted that the terms independent of r take into account the influence of the effective medium; *i.e.*, the remainder inclusions into the composite.

On the other hand, when considering that ϕ goes to zero and G_C and CTE_C tend to G_M and CTE_M respec-

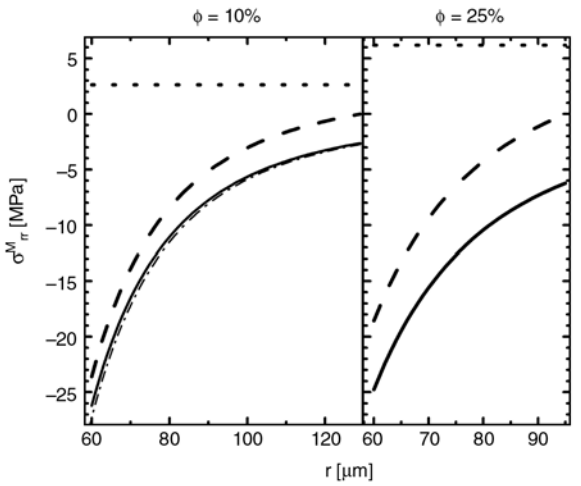

Figure 3. Component σ^{M}_{rr}, represented by (— —), of the stress tensor into the matrix as a function of distance to the particle and for different filler contents. In the different plots, the contributions of the terms depending, or not, on *r* are presented separately, e.g.; the term of σ^{M}_{rr} that depends on *r* was represented by (——) and that independent of *r* by (· ·). In the case of ϕ = 10%, the stress calculated using the Selsing's equation is also presented by (— · —).

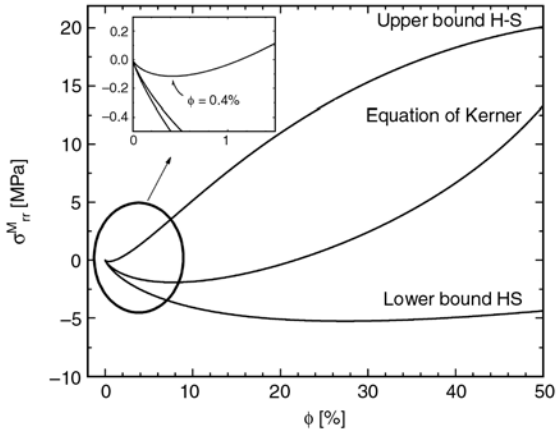

Figure 4. Average volumetric radial stress σ^{M}_{rr} as a function of the filler content. To this aim, the upper and lower bounds of the Hashin and Shtrikman equation were calculated (see text). Other approximation given by the Kerner equation was also plotted (see section 3.4).

tively, the σ^{M}_{rr} reduces to the Selsing's equation above discussed.

In Figure 3, the solid line represents the evolution of σ^{M}_{rr} as a function of *r* and for different filler contents ϕ. The particle radius selected was of 60 μm, chosen taking into account the typical sizes of the aluminum particles used in our composites. In the figure, the different terms contributing to the stress tensor are also plotted. It must be pointed out that for the lower filler content (ϕ = 10%), the Selsing's equation is also presented. As can be seen in the figure, there is a very good agreement with the tensor term dependent on *r*.

In a second step, on the basis of the results presented above, to calculate the average volumetric radial stresses acting on the matrix as well as the particle we have followed the ideas of Park and Earmme [6]. However, in the present work we focused our analysis on the average volumetric radial stress into the matrix ($<\sigma^{M}_{rr}>$) where the matrix is characterized by a volume (V^{M}). As mentioned, $\phi = (r_f/r_b)^3$; besides the volume of the matrix can be calculated as $V^{M} = 4/3\pi(r_b^3 - r_f^3)$, then according to Equation (9):

$$\langle \sigma^{M}_{rr} \rangle = \frac{1}{V^{M}} \int \sigma^{M}_{rr} \, dV \tag{9}$$

and using Equation (7) Equation (10) is obtained:

$$\langle \sigma^{M}_{rr} \rangle = \frac{12}{D}(K_F \varepsilon^{F}_{ij} I + K_M \varepsilon^{M} III) + \\ + \frac{36}{D}(-K_F \varepsilon^{F}_{ij} II + K_M \varepsilon^{M}_{ij} IV) \frac{1}{\frac{1}{\phi} - 1}(-\ln\sqrt[3]{\phi}) \tag{10}$$

The constants CTE_C, K_C and G_C in the effective medium were assumed to be those corresponding to the composite. To calculate these constants, a model developed for particulate composites by Hashin [21] was used. This model allows calculating the bulk (*K*) and the shear modulus (*G*) of a particulate composite. Specifically, the model predicts for the different particle content an upper and a lower value (both named bounds) for *K* and *G*. In Figure 4, the two bounds of $<\sigma^{M}_{rr}>$ as a function of the filler content were plotted. As can be observed, the lower bound of $<\sigma^{M}_{rr}>$ decreases when the filler content increases. After $\phi \approx 25\%$; $<\sigma^{M}_{rr}>$ shows a slight increase with the increment of ϕ. In the case of the Hashin and Shtrikman (H-S) upper bound and around a filler content of 0.4%, a small minimum in the average volumetric radial stress can be seen; then $<\sigma^{M}_{rr}>$ rapidly increases when ϕ increases.

3.4. Young's modulus variation due to filler content

The models discussed in the previous Sections did not give the detailed information we needed to obtain reliable results on the thermal stresses operating in the particulate epoxy composites we are dealing

Table 1. Young's modulus as a function of filler content of aluminum particles ([22])

ϕ [%]	Modulus E_C [GPa]
5	4.3 (±0.2)
10	4.9 (±0.2)
15	5.8 (±0.2)
20	6.2 (±0.3)
25	7.1 (±0.2)

with. To this aim, we have used experimental values of the resonance frequencies measured by using the impulse excitation technique (IET) that we recently reported in [22]. From the mentioned frequencies, the different Young's moduli (E) were calculated. Since it is of utmost importance to understand the different approximations discussed in the present work, we summarize here some of the main results reported in [22]. It is worth remembering that in the case of pure epoxy, a value of E_M = 3.9±0.2 GPa was found. The corresponding results for the composites are reported in Table 1. As can be seen, E_C increases when the filler content (ϕ) increases.

To fit the experimental data of the Young's modulus, the Kerner equation, generalized by Lewis and Nielsen and Landel [1], was used. It should be noted that the Kerner's equation results from the ratio between the Young's moduli of the composite (E_C) and the matrix (E_M), respectively. It is given by Equation (11):

$$\frac{E_C}{E_M} = \frac{1 + AB\phi}{1 - B\psi\phi} \tag{11}$$

where A is a constant that takes into account factors as the geometry of the particles and the Poisson's ratio of matrix, B is a constant depending on the relative E_F and E_M values of the filler and matrix phases, respectively. This parameter is defined by Equation (12):

$$B = \frac{\frac{E_F}{E_M} - 1}{\frac{E_F}{E_M} + A} \tag{12}$$

Besides, the factor ψ depends on the maximum packing fraction ϕ_m of the filler. ψ can be obtained by using an empirical function as given by Equation (13):

$$\psi = 1 + \frac{1 - \phi_m}{\phi_m^2}\phi \tag{13}$$

where the factor ϕ_m was taken from the literature ϕ_m = 0.637 ([22]). This parameter is independent of the materials forming the composite.

The experimental data of E_C as a function of the filler content were fitted using Equation (11) and the constant A = 1.72 was obtained from the best fit of E versus ϕ curve.

Successively, the volumetric radial stress into the matrix given was calculated by means of Equation (10) and using the experimental data obtained by IET. Besides, Equation (14) describing the relationship between the bulk (K) and E_C moduli was used [1]:

$$E_C = 3K_C(1 - 2\mu) \tag{14}$$

where μ the Poisson's ratio. There is an analogous expression for the shear modulus G.

On the other hand, the CTE_C value was calculated using the Hashin-Shtrikman model for each composite.

The evolution of $<\sigma_{rr}^M>$ obtained as a function of ϕ is depicted in Figure 4. The estimation of the average volumetric radial stress using the Kerner's equation is also shown. As can be seen, there qualitatively exists a good agreement of the resulting curve with that calculated using the lower Hashin-Shtrikman bound; but, from the comparison the curve corresponding to the Kerner's equation shows a sharper minimum located about a filler content of 8%.

The results presented in the previous sections on the models used to analyze the composites will be used as an input to the analysis of the free nanohole volumes behavior as a function of the filler content into the epoxy matrix composites studied in the present work.

3.5. Average free nanohole volume variation due to filler content

The epoxy matrix composites are subjected to a thermal treatment during curing process. Then, if the composite is considered in thermal equilibrium at the high temperature stage, thermal stresses are developed when the samples are cooled to ambient temperature due to the different thermomechanical properties between the matrix and the inclusion. Under this scenario, it is reasonable to expect that the residual stresses have a strong influence onto the average free nanohole volume. Precisely, this assumption allowed Goyanes *et al.* [8] to satisfacto-

rily explain the decrease in the V_H versus ϕ for aluminum powder contents up to about 15%. However, an explanation regarding highest filler contents is still an open issue.

In order to go deeper into the analysis of the experimental data reported in Figure 1, as a first attempt we assumed a spherical geometry for the aluminum particles. In the above sections, it was found that there is a compressive radial stress around an inclusion.

On the other hand, it has been reported that in polymers the o-Ps lifetime [23] is dominated by the smaller length of the nanohole. Then, in our composites it could be expected that $\tau_{o\text{-}Ps}$ decreases as a consequence of a diminution of the radial characteristic length of the nanoholes around the particles used as filler.

In a previous paper, authors of the present work [8] used a simple relationship between the free volume fraction and the average hydrostatic pressure P, given by Equation (15):

$$f = f^0 + \beta \cdot P \tag{15}$$

where f^0 is the free volume fraction into the pressure-free state and β is the free volume compressibility.

The free volume fraction and the average volume of the nanoholes are related by $f = N_h \cdot V_H$ where N_h is the number of nanoholes per volume unit. If N_h does not change with the filler content, then the change of V_H is proportional to the pressure with a constant of the order of β/N_h. However, there has not been reported a relation between the average radial stress in the matrix $<\sigma_{rr}^M>$ and V_H. In such a way, assuming the linear relation between f and P we propose the following relationship (Equation (16)) that allows calculating the free nanohole volume as a function of the average volumetric radial stress:

$$V_H = V_H^0 + C\langle\sigma_{rr}^M\rangle \tag{16}$$

where C is a constant and V_H^0 the free nanohole volume in the stress free state. As already mentioned, the different V_H can be directly obtained from the $\tau_{o\text{-}Ps}$ experimental values.

Taking into account Equation (16), V_H and $<\sigma_{rr}^M>$ should have the same dependence of the filler content ϕ. Then, the experimental data of Figure 1 were fitted in the ϕ range from 0 to about 15% using

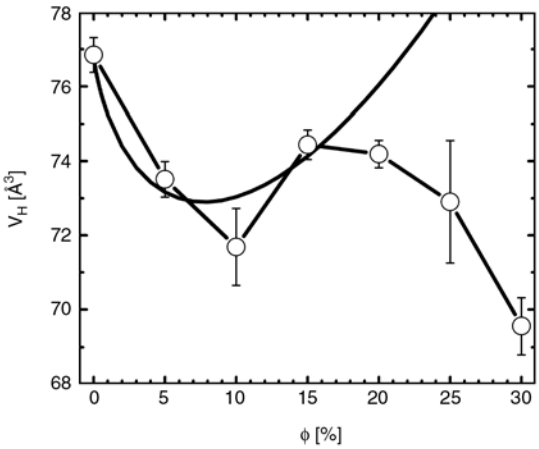

Figure 5. Dependence of the average free nanohole volume as a function of the filler content: (—o—) experimental values and (——) calculated data obtained using Equation (16)

Equation (16) with C as a free parameter. The $<\sigma_{rr}^M>$ values were calculated by means of Equation (10). From the fit, the parameter C results $2.06 \cdot 10^{-6}$ Å^3·Pa^{-1}. In Figure 5, the mentioned function is presented with a solid line. As can be seen, qualitatively there exists a reasonable agreement between the fitting curve and that representing the experimental data in the ϕ range from 0 to about 15%. For higher ϕ values, the fitting function overestimates the experimental V_H values. In fact, for $\phi > 15\%$ the average free nanohole volume predicted shows a strong increase while the experimental data decrease.

Summarizing, it is clear that the model used is not good enough to satisfactorily fit the whole behavior of the V_H experimental data as a function of the filler content. As a consequence, we considered necessary to introduce other elements in order to explain the whole behavior of the V_H versus ϕ curve. Therefore, in the next section other contributions to the average free nanohole volume, especially those that take into account the inclusion-matrix interphases are analyzed.

3.6. Characterization of the inclusion-matrix interphases using microscopy techniques

In this Section, information regarding the inclusion-matrix interphases present in the composites is analyzed.

3.6.1. A scanning electron microscopy study

The composites studied were microstructurally characterized using Scanning Electron Microscopy (SEM). In Figure 6, as an example some SEM

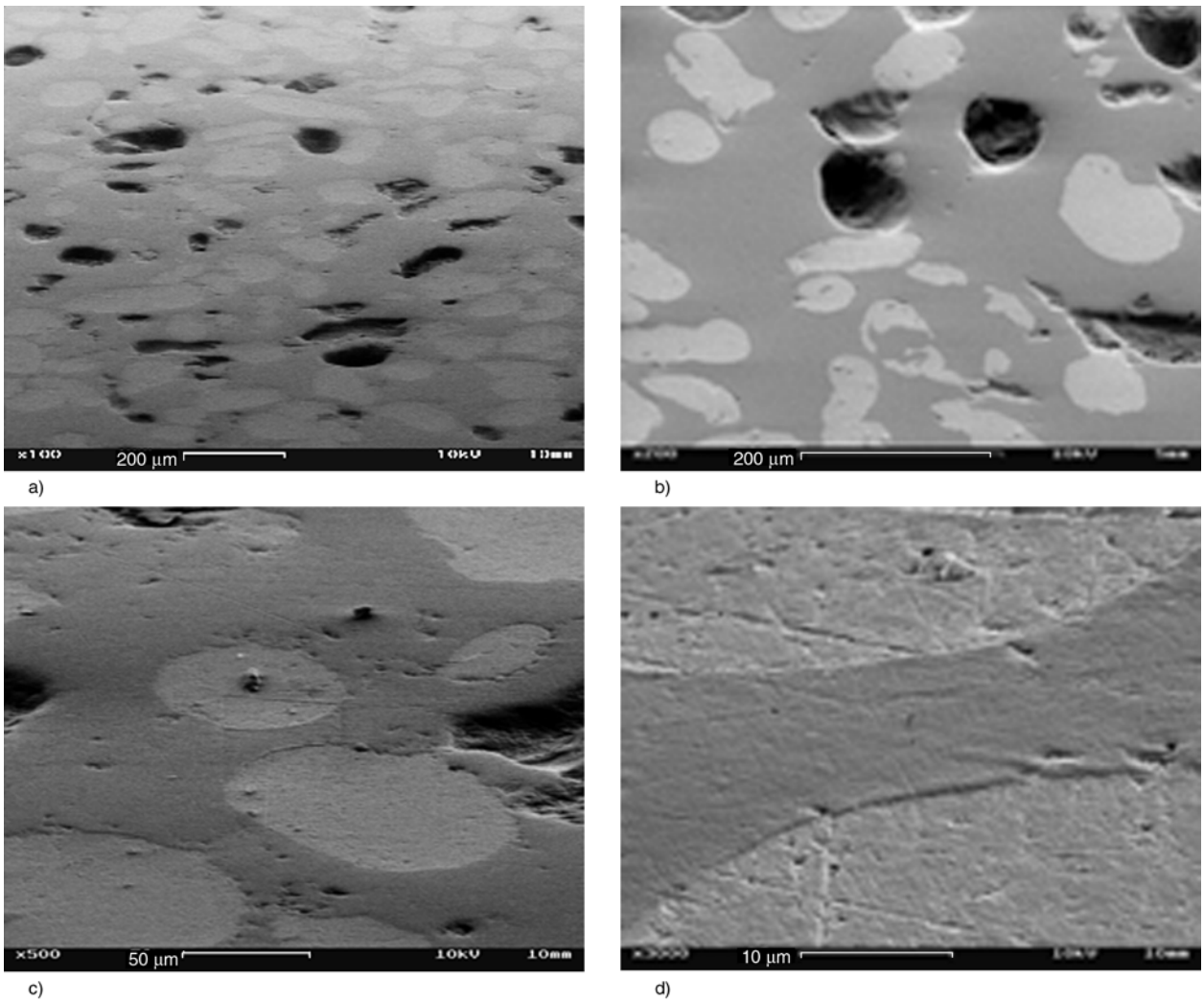

Figure 6. SEM micrographs of an epoxy composite (30% aluminum particle content). The images were obtained using different magnifications: 100, 200, 500 and 3000.

micrographs obtained for a sample containing 30% of aluminum particles are shown. In these images, the surface of aluminum particles is clearer than the matrix one. Dark holes correspond to particles removed from the matrix during the surface polishing. In the images, it can be observed that the matrix presents a surface smoother than that of the inclusion. This is a consequence that the matrix is softer than the particle. Besides, it seems that the particles are slightly deeper than the level of the matrix. To explore in detail this behavior, atomic force microscopy was used. The results are presented in the next section.

3.6.2. An atomic force microscopy study

Atomic force microscopy was used to study the topography of the composites. The use of this technique allowed us to go further into the analysis of differences between the surface levels of the particles with respect to the matrix. In this Section, we present AFM results obtained for the samples filled with 30% of particles. In Figure 7, images of the topography and shift phase, taken along the dashed line drawn in the images, obtained for the samples mentioned above are shown.

Analyzing the topographic mapping, it results that the bright zones in the images represent a surface level higher than that of the dark zones. As can be observed, in both samples the inclusion presents an image darker than that corresponding to the matrix surrounding the filler. Therefore, it can be concluded that the inclusions are located at a deeper level than that of the matrix. This behavior is in total agreement with the SEM results presented in the previous Section.

On the other hand, in the figure the profile of height Z as a function of the x length parameter, considered along the dashed line drawn in the image, show that

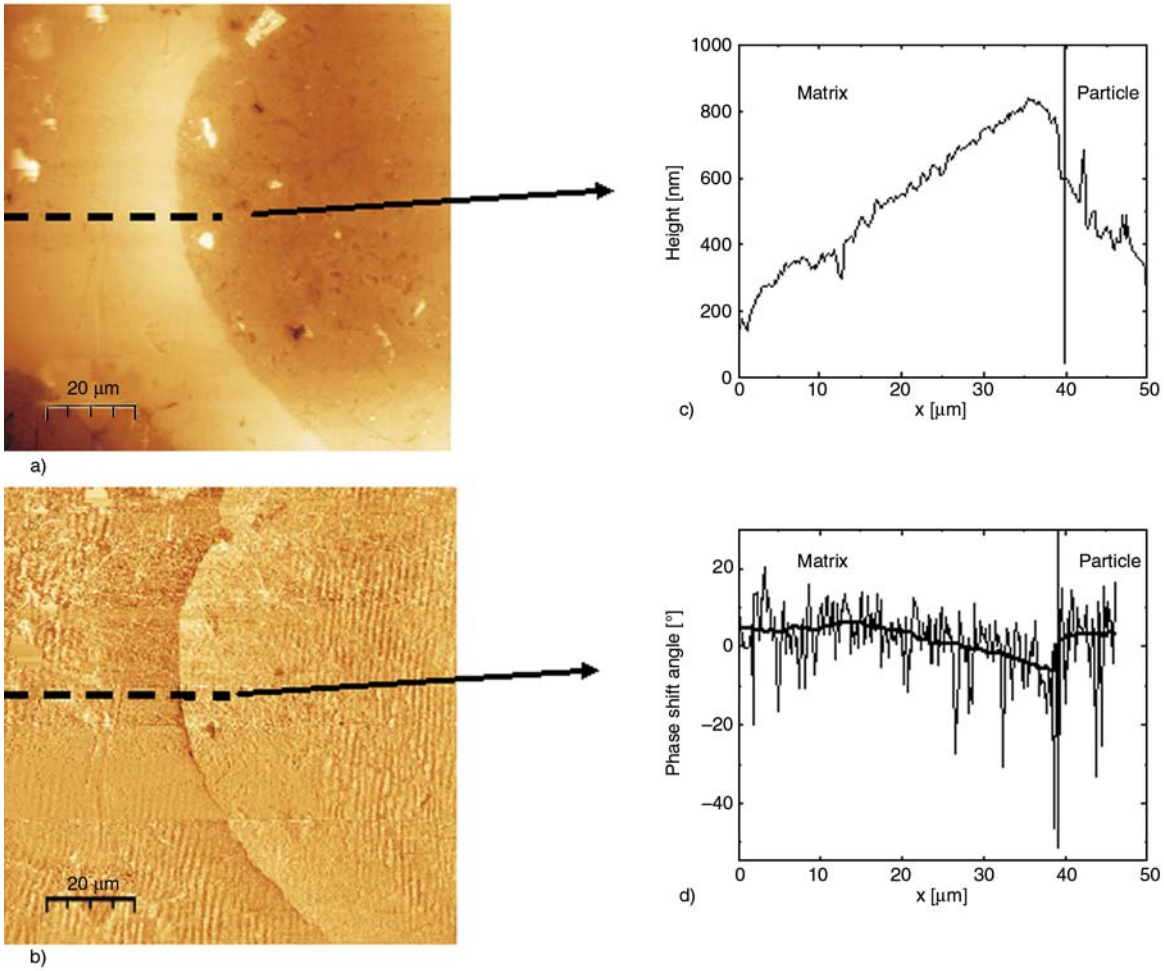

Figure 7. AFM measurements of an epoxy composite (30% filler content). a) topographic mapping. b) phase shift mapping around an aluminum particle. In c) and d) the profile of height *Z* and the phase shift, along the axis *x* represented by the dashed lines drawn in the images, are respectively shown. The solid line in d) was obtained smoothing the experimental data.

the maximum values of *Z* are reached around the inclusion. When moving outside the particle towards the matrix, a systematic decrease of *Z* is observed. Into the particle, *Z* rapidly decreases in about 500–600 nm. This behavior seems abnormal and must be carefully analyzed. In fact, as the inclusion is harder than the matrix, it would be expected that this last one would be located in a deeper level than that corresponding to the particle. We consider that such a difference could be explained in terms of the relaxation induced in the matrix by the cutting procedure. Specifically, when a composite sample is cut the stresses around a particle are relaxed. Therefore, a relaxation of the tangential stresses around a particle would cause an 'expansion' of the matrix in the direction normal to the surface, *i.e.*, a relative change in the level of the surfaces corresponding to the inclusion and the matrix. This analysis is compatible with the scheme of the stresses operating in a composite represented in Figure 2, and with the contraction of the radial dimension of the nanohole. On the other hand, the phase image (Figure 7b) clearly shows that matrix and particle have different phase angles. Although the profile (phase angle versus *x*) obtained from the respective images are very noisy, after smooth experimental data when moving outside the particle towards the matrix (up to 20 µm) a small but significant variation of the phase shift around the inclusion is observed.

It is known that the phase shifts depend on the energy dissipated in the tapping interaction of probe and the specimen explored [24]. Differences in the phase shifts are usually associated with differences in surface or in underlying properties (stiffness, viscosity and adhesion). Hence, the phase shift is sensitive to variations in materials local properties and it can be an important tool for surface analysis [25].

3.7. Evidence on the inclusion-matrix interphases from DSC measurements

In order to completely explain the behavior of V_H as a function of the filler content plotted in Figure 1, we have taken into account an additional element from which some information had been obtained using AFM: the inclusion-matrix interphase. On the basis of previous results, it was assumed that around the filler particles there exists a region with different properties from those of the matrix. This interphase region was characterized using differential scanning calorimetry (DSC). Specifically and following ideas reported in the literature, the interphase volumetric fraction was estimated from the DSC curves [10, 26, 27].

To simplify our study, the geometry of the particles used as filler of the epoxy-based composites was assumed to be spherical with a characteristic radius r_f. It was also supposed that each particle was surrounded by an interphase with an associated thickness Δr_i. On the basis of the experimental techniques used to study the characteristics of the interphases, we have not considered chemical factors like the presence of oxides onto the inclusion surfaces. Work in progress is addressed to the study of the chemical and physical characteristics that should be considered into the inclusion-matrix interphases contribution.

In a previous work, we reported the different Δr_i values as well the volumetric fraction of the interphases v_i as a function of the filler content for the same composites studied here [13]. Additionally, in the mentioned paper we already obtained the glass transition temperatures T_g for each composite sample. Experimentally, DSC data were obtained using a heating rate of 10 K/min, in a temperature range between 293 and 453 K. Specifically, the glass transition temperature was determined of the onset temperature for the step observed in the thermograms.

Table 2. Thickness, volumetric fraction of interphase and glass transition temperature for different filler content of particles of aluminum in the epoxy-resin composite ([13])

ϕ [%]	Δr_i [μm]	v_i^{DSC} [%]	T_g [K]
0	0	0	391 (±1)
5	0.2 (± 0.1)	0.05 (± 0.03)	392 (±1)
10	0.3 (± 0.1)	0.16 (± 0.05)	392 (±2)
15	0.4 (± 0.1)	0.30 (± 0.08)	393 (±1)
20	2.18 (± 0.08)	2.26 (± 0.08)	393 (±1)
25	2.9 (± 0.6)	3.8 (± 0.8)	393 (±1)
30	6.3 (± 0.7)	10 (± 1)	395 (±2)

In Table 2, the results of the parameters above mentioned are presented.

As useful for the general discussion on the whole data reported in this work, we briefly analyze the data reported in Table 2. As can be seen, Δr_i and its associated volume v_i increase when the filler content increases. For $\phi \leq 15\%$ both parameters show a small increment but for higher filler contents they strongly increase. It is important to point out that the highest value of Δr_i (~6 μm) approximately represents 10% of a typical radius of an inclusion. Furthermore, the maximum value of v_i is equivalent to 15% ca. of the total volume of the epoxy matrix. In addition, the glass transition temperature systematically increases with the increment of ϕ.

From the DSC results shown in Table 2, we can conclude that the effect of the interphase becomes significant for filler contents higher than 15%. At this point, it is worth remembering that in this ϕ region the V_H versus ϕ behavior cannot be described using the thermal stress model. Therefore, an additional term in Equation (16) should be considered; *i.e.*, a contribution to V_H related to the inclusion-matrix interphase. Recently, from PALS measurements on the same samples studied in the present work we reported quantitative information on this term [13]. Specifically, studying a sample containing 15% of filler, a bimodal-like distribution of the free nanohole volume was obtained. So, nanohole volume values of 76 Å^3 (representing the free volume in the epoxy resin) and 32 Å^3 (assigned to the free volume in the interphase region) were reported.

3.8. Influence of the inclusion-matrix interphases on the average free nanohole volumes

In this Section, the different results previously obtained on the aluminum inclusion-epoxy resin matrix interphases are used in order to analyze the behavior of the average free nanohole volume in the whole range of the filler content used to charge the matrix of the different composites. As already shown, the free nanohole volume associated with the interphase is lower than that of the bulk matrix. Therefore, the average free nanohole volume of a composite V_H (e.g., that corresponding to the matrix) should diminish with the increase of the interphase contribution as a consequence of a progressive increase of the filler content.

To evaluate the interphase influence on V_H, as a first approximation a homogeneous number of holes distributed into the matrix of the composite, independently of the position of the inclusion, was considered. Then, we have modeled the average free nanohole volume as follows: a contribution due to the average of free nanohole volume of the matrix outward the interphase (*i.e.* bulk) $V_{H\,bulk}$ and another coming from the average free nanohole volume corresponding to the interphase $V_{H\,Int}$.

In the case of $V_{H\,bulk}$, as described in Section 4.4 the value of this parameter was estimated using the average radial stress. On the other hand, as a first approximation $V_{H\,Int}$ was considered to be constant and its value was that coming from the analysis of bimodal distribution of the PALS data (specifically 32 Å^3). Then, the average free nanohole volume was calculated as a combination of the two free nanohole volume terms above mentioned according to Equation (17):

$$V_H = \frac{V_{H\,Int} \cdot v_i + V_{H\,bulk} \cdot v_{bulk}}{v_i + v_{bulk}} \qquad (17)$$

In this equation, v_i is the volume fraction associated with the inclusion-matrix interphases and v_{bulk} volume fraction of the bulk. To link both parameters, we have used the following relationship $v_{bulk} = 1 - \phi - v_i$, which is a reasonable one.

The volume fraction values associated with the inclusion-matrix interphases were obtained from the DSC data reported in Table 2. But, to use them into the general model developed to fit the V_H versus ϕ data presented in Figure 1, a scale constant factor which allowed matching the data was used. This factor was obtained from a free parameter fitting.

Finally, using the model simply expressed by Equation (17) the experimental values of V_H obtained from PALS measurement as a function of the filler content in the different composites studied could be satisfactorily described in the whole volume range of aluminum particles contained in the different composites (see Figure 8). Undoubtedly, for $\phi > 15\%$ the contribution of the inclusion-matrix interphases becomes very important but, as we have discussed in detail along the present work, $\phi \leq 15\%$ the average free nanohole volume was mainly due to the contribution of the radial thermal stresses.

Though we have analyzed our data under the assumption that all metallic particles used as filler of the epoxy matrix were spherical and had the same size, the results predicted by the model used allowed us to satisfactory fit the experimental behavior of the free nanohole volume as a function of the filler content. Work in progress will allow us to evaluate the influence of the real geometry of the particles and their distribution of sizes on the free nanohole volume.

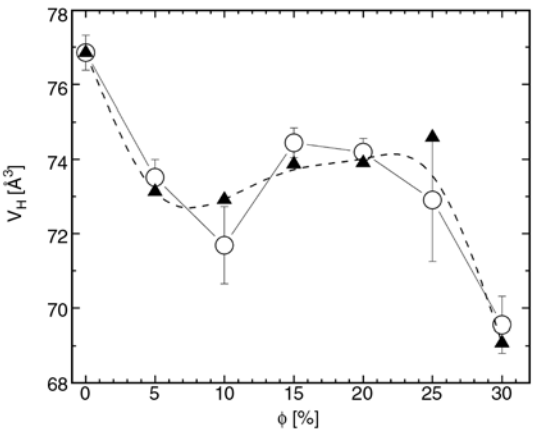

Figure 8. Dependence of average free nanohole volume as a function of the filler content: (—○—) experimental values obtained from PALS; (—▲—) data obtained from Equation (17) in which the contribution of the average thermal stresses and that of the inclusion-matrix interphases were considered. The dashed line is an eye guide

4. Conclusions

In the present work and on the basis of previous studies on the particulate epoxy matrix composites recently published [13, 22], we have made a systematic study on the evolution of the free nanohole volumes in particulate epoxy matrix composites with the filler content ranging from 0 to 30% of volumetric fraction. Specifically, as filler we have used aluminum particles with characteristic sizes of about 100 μm.

As a starting point of the present work, experimental free nanohole volume data directly measured using positron annihilation lifetime spectroscopy recently reported, were used. In a second step, these data were interpreted in the frame of different well-known micromechanical models.

As a first approximation, when considering only the contribution of the thermal stresses acting into the composite as a consequence of the fabrication process and the further curing treatments applied to the resulting composites, we could only satisfactory explain the evolution of the free nanohole volume

in the range of filler content between 0% and approximately 15%. For highest filler contents, the approach used failed. For this reason, from the different micromechanical models available in the literature that allow to calculate the thermal stresses in composites, in the present work we choose the Park-Earmme model which we specifically adapted to take into account the contribution of the different stresses coming from the phases present in the epoxy composite.

To go further, in some cases it was necessary to use experimental data as input parameters into the model used. While values of the Young's modulus used here were taken from our recently published paper on the same composites studied in this work [22]. There is no available quantitative information on matrix-particle interphases. Therefore, we obtained specific experimental information using atomic force and scanning electronic microscopies, differential scanning calorimetry and a refined analysis of the positron annihilation lifetime data. It is worth mentioning that in the present work the concept of interphase was used in a general context; thus, chemical and physical properties of the interphases did not are separately evaluated.

Among the information reported in the present work on particulate metal-epoxy matrix composites, a contribution to the knowledge of these materials that deserves special consideration is the study about the influence of the matrix-particle interactions on the nanohole sizes in epoxy-based composites.

Summarizing, the present work allowed to completely describe the behavior of the free nanohole volume as a function of the inclusion content into the composites. In fact, when considering the joint contribution of the radial stresses in epoxy matrix and the particle-matrix interphase, the reformulated micromechanical Park and Earmme model allowed us to give a satisfactory description of the free nanohole volume behavior in the whole range of the filler content.

Acknowledgements

This work was partially supported by Agencia Nacional de Promoción Científica y Tecnológica (PICT 2011-1088), Comisión de Investigaciones Científicas de la Provincia de Buenos Aires, Universidad Nacional del Centro de la Provincia de Buenos Aires (Argentina) and Universidad de Buenos Aires (Argentina) (Research Project 2006–2009 X808).

References

[1] Nielsen L. E., Landel R. F: Mechanical properties of polymers and composites. Marcel Dekker, New York (1994).

[2] Harsch M., Karger-Kocsis J., Holst M.: Influence of fillers and additives on the cure kinetics of an epoxy/anhydride resin. European Polymer Journal, **43**, 1168–1178 (2007).
DOI: 10.1016/j.eurpolymj.2007.01.025

[3] Eshelby J. D.: The determination of the elastic field of an ellipsoidal inclusion, and related problems. Proceedings of Royal Society of London A, **241**, 376–396 (1957).
DOI: 10.1098/rspa.1957.0133

[4] Selsing J.: Internal stresses in ceramics. Journal of the American Ceramic Society, **44**, 419 (1961)
DOI: 10.1111/j.1151-2916.1961.tb15475.x

[5] Christensen R. M., Lo K. H.: Solutions for effective shear properties in three phase sphere and cylinder models. Journal of the Mechanics and Physics of Solids, **27**, 315–330 (1979).
DOI: 10.1016/0022-5096(79)90032-2

[6] Park S. J., Earmme Y. Y.: Bound solution for residual stress due to thermal mismatch in particle reinforced composites. Journal of Composite Materials, **33**, 1205–1221 (1999).
DOI: 10.1177/002199839903301303

[7] Low I. M.: Toughening of epoxies by thermal expansion mismatch. Journal of Applied Polymer Science, **39**, 759–762 (1990).
DOI: 10.1002/app.1990.070390324

[8] Goyanes S., Rubiolo G., Salgueiro W., Somoza A.: On the free volume evolution in a deformed epoxy composite. A positron annihilation study. Polymer, **46**, 9081–9087 (2005).
DOI: 10.1016/j.polymer.2005.07.020

[9] Gao S-L., Mäder E.: Characterisation of interphase nanoscale property variations in glass fibre reinforced polypropylene and epoxy resin composites. Composites Part A: Applied Science and Manufacturing, **33**, 559–576 (2002).
DOI: 10.1016/S1359-835X(01)00134-8

[10] Theocaris P. S.: The unfolding model for the representation of the mesophase layer in composites. Journal of Applied Polymer Science, **30**, 621–645 (1985).
DOI: 10.1002/app.1985.070300214

[11] Pérez-Pacheco E., Moreno-Chulim M. V., Valadez-González A., Rios-Soberanis C. R., Herrera-Franco P. J.: Effect of the interphase microstructure on the behavior of carbon fiber/epoxy resin model composite in a thermal environment. Journal of Materials Science, **46**, 4026–4033 (2011).
DOI: 10.1007/s10853-011-5331-0

[12] Goyanes S., Rubiolo G., Marzocca A., Salgueiro W., Somoza A., Consolati G., Mondragon I.: Yield and internal stresses in aluminum filled epoxy resin. A compression test and positron annihilation analysis. Polymer, **44**, 3193–3199 (2003).
DOI: 10.1016/S0032-3861(03)00229-5

[13] Tognana S., Salgueiro W., Somoza A.: On the matrix-particle interphase in epoxy-based composites. Journal of Alloys and Compounds, **495**, 588–591 (2010).
DOI: 10.1016/j.jallcom.2009.10.058

[14] Jean Y.: Characterizing free volumes and holes in polymers by positron annihilation spectroscopy. in 'Positron spectroscopy of solids' (eds.: Dupasquier A., Mills Jr A. P.) IOS Press, Amsterdam, 563–580 (1995).

[15] Mallon P. E.: Applications to polymers. in 'Principles and application of positron and positronium chemistry' (eds.: Jean Y. C., Mallon P. E., Schrader D. M.) World Scientific, Singapore, 253–280 (2003).

[16] Ferry J. D.: Viscoelastic properties of polymers. John Wiley and Sons, New York (1980).

[17] Dlubek G., Stejny J., Alam M. A.: Effect of cross-linking on the free-volume properties of diethylene glycol bis(allyl carbonate) polymer networks: A positron annihilation lifetime study. Macromolecules, **31**, 4574–4580 (1998).
DOI: 10.1021/ma971801y

[18] Salgueiro W., Marzocca A., Somoza A., Consolati G., Cerveny S., Quasso F., Goyanes S.: Dependence of the network structure of cured styrene butadiene rubber on the sulphur content. Polymer, **45**, 6037–6044 (2004).
DOI: 10.1016/j.polymer.2004.05.008

[19] Horcas I., Fernández R., Gómez-Rodríguez J. M., Colchero J., Gómez-Herrero J., Baro A. M.: WSXM: A software for scanning probe microscopy and a tool for nanotechnology. Review of Scientific Instruments, **78**, 013705/1–013705/8 (2007).
DOI: 10.1063/1.2432410

[20] Mastelaro V. R., Zanotto E. D.: Residual stresses in a soda-lime-silica glass-ceramic. Journal of Non-Crystalline Solids, **194**, 297–304 (1996).
DOI: 10.1016/0022-3093(95)00509-9

[21] Hashin Z.: Analysis of composite materials – A survey. Journal of Applied Mechanics, **50**, 481–505 (1983).
DOI: 10.1115/1.3167081

[22] Tognana S., Salgueiro W., Somoza A., Marzocca A.: Measurement of the Young's modulus in particulate epoxy composites using the impulse excitation technique. Materials Science and Engineering: A, **527**, 4619–4623 (2010).
DOI: 10.1016/j.msea.2010.04.083

[23] Soles C. L., Yee A. F.: A discussion of the molecular mechanisms of moisture transport in epoxy resins. Journal Polymer Science Part B: Polymer Physics, **38**, 792–802 (2000).
DOI: 10.1002/(SICI)1099-0488(20000301)38:5<792::AID-POLB16>3.0.CO;2-H

[24] Cleveland J. P., Anczykowski B., Schmid A. E., Elings V. B.: Energy dissipation in tapping-mode atomic force microscopy. Applied Physics Letters, **72**, 2613–2615 (1998).
DOI: 10.1063/1.121434

[25] Babcock K. L., Prater C. B.: Phase imaging: Beyond topography. Veeco, Santa Barbara (1995).

[26] Theocaris P. S., Stavroulakis G. E., Panagiotopoulos P. D.: Calculation of effective transverse elastic moduli of fiber-reinforced composites by numerical homogenization. Composites Science and Technology, **57**, 573–586 (1997).
DOI: 10.1016/S0266-3538(97)00018-3

[27] Lombardo N.: Effect of an inhomogeneous interphase on the thermal expansion coefficient of a particulate composite. Composites Science and Technology, **65**, 2118–2128 (2005).
DOI: 10.1016/j.compscitech.2005.05.006

eXPRESS Polymer Letters Vol.7, No.2 (2013) 134–145
Available online at www.expresspolymlett.com
DOI: 10.3144/expresspolymlett.2013.13

Development and characterisation of injection moulded, all-polypropylene composites

Á. Kmetty[1,2*], *T. Tábi*[1,2], *J. G. Kovács*[1], *T. Bárány*[1]

[1]MTA–BME Research Group for Composite Science and Technology, Műegyetem rkp. 3., H-1111 Budapest, Hungary
[2]Department of Polymer Engineering, Faculty of Mechanical Engineering, Budapest University of Technology and Economics, Műegyetem rkp. 3., H-1111 Budapest, Hungary

Received 16 July 2012; accepted in revised form 16 September 2012

Abstract. In this work, all-polypropylene composites (all-PP composites) were manufactured by injection moulding. Prior to injection moulding, pre-impregnated pellets were prepared by a three-step process (filament winding, compression moulding and pelletizing). A highly oriented polypropylene multifilament was used as the reinforcement material, and a random polypropylene copolymer (with ethylene) was used as the matrix material. Plaque specimens were injection moulded from the pellets with either a film gate or a fan gate. The compression moulded sheets and injection moulding plaques were characterised by shrinkage tests, static tensile tests, dynamic mechanical analysis and falling weight impact tests; the fibre distribution and fibre/matrix adhesion were analysed with light microscopy and scanning electron microscopy. The results showed that with increasing fibre content, both the yield stress and the perforation energy significantly increased. Of the two types of gates used, the fan gate caused the mechanical properties of the plaque specimens to become more homogeneous (i.e., the differences in behaviour parallel and perpendicular to the flow direction became negligible).

Keywords: *polymer composites, all-polypropylene composites, injection moulding*

1. Introduction

Recently, environmental protection and recycling issues have become important. Environmentally conscious and new materials are spreading widely. Development of self-reinforced materials and composites (matrix and reinforced materials belonging to the same polymer family) began in the 1970s and now are intensively researched [1]. Originally, *in situ* self-reinforcing parts were made from a single-component material. These techniques, e.g., self-reinforced extrusion and self-reinforced injection moulding (both shear-controlled orientation in injection moulding (SCORIM) [2–3] and vibration injection moulding (VIM) [4]), were used successfully. The essence of these techniques was the orientation of the molecular chain relative to the shear load to produce a shish-kebab structure [5]. The main disadvantage of these techniques was the difficulty in designing the reinforcement structure. From the 1990s until present, multi-step production of self-reinforcing parts has become widespread. Three methods were used to produce self-reinforced materials/composites [6]: hot compaction (single-component self-reinforced materials (SRM)) [7–9], consolidation of coextruded tapes [10] and film-stacking methods (multi-component SRM) [11–18]. The geometries of the products prepared with these techniques are limited because only sheet pre-product can be manufactured, and thereafter it can be shaped by thermoforming. However, large-scale production of SRPCs has become highly preferred in the last 1–3 years.

*Corresponding author, e-mail: kmetty@pt.bme.hu

The aim of this paper is to demonstrate that it is possible to injection mould all-polypropylene composites and to determine the effects of the reinforcing fibre content and the type of gate on static tensile and dynamic mechanical properties and shrinkage of the composite plaque.

2. Preliminary tests

To produce products with complex 3D geometry, injection moulding is a suitable technique. To process all-polypropylene composites by injection moulding, intensive preliminary tests have been performed. Matrix and reinforcement materials, pellets for injection moulding and a processing method were developed. Random ethylene-polypropylene copolymer (rPP) and highly oriented polypropylene homopolymer (hPP) reinforcement were characterised by mechanical and morphological tests. First, the matrix and the reinforcement were mixed in a powder mixer. The mix was subsequently injection moulded with an Arburg Allrounder 320C 700-290 machine. The preliminary results showed that the hPP multifilament became roughened and formed agglomerates (due to electrostatic charge), and a cold slug formed that blocked the standard flat nozzle, which had 2 mm diameter hole. The reinforcement fibre content could not be guaranteed, and even distribution of reinforcement fibres could not be achieved. The standard flat nozzle has been replaced with a heated flat nozzle with 4 mm-diameter hole to avoid cold slug formation. Next, to avoid agglomeration of reinforcing fibres, extrusion coating was applied prior to injection moulding; one or two bobbins of hPP multifilament were used, and these were continuously coated in a special extrusion die by molten matrix material made of rPP. The coated multifilament was granulated into 4, 10 mm long cylindrical pellets and used for injection moulding. This pre-product can be injection moulded at different temperature between 150–180°C. 160°C was the lowest temperature where stable technology (without cold slug) can be achieved. At this temperature the thermoplastic reinforcement did not melt during manufacturing. The mechanical tests revealed that a slight reinforcing effect can be detected. The microscopy images showed that neither the distribution of the single fibres nor the impregnation of matrix material was perfect. These problems must arise from the improper impregnation of the coated pre-product; the impregnation process required improvement. Hence, the goal of this paper is to demonstrate the improved processability of all-polypropylene composites by injection moulding, including preparation of the pre-product and the injection moulding.

3. Materials, processing and testing

3.1. Materials

Highly oriented polypropylene homopolymer (hPP) multifilament (Stradom S. A., Czestochowa, Poland) was used as reinforcement. This reinforcing multifilament has a melting temperature of 173°C (as determined by DSC from the first melting curve with a heating rate of 10°C/min); a yield stress of 581±30 MPa; tensile modulus of 6432±490 MPa (measured by single-fibre tensile tests) and the single fibre diameter of 40.1±1.8 μm. The multifilament was sized with carboxylic acid by the producer. Random ethylene-polypropylene (rPP) copolymer (Tipplen R959A, TVK Nyrt., Tiszaújváros, Hungary) was used as the matrix material. From the initial rPP granules, a 50 μm thick film was produced using an extrusion film blowing technique. The melting temperature of the matrix was 150°C (as determined by DSC from the first melting curve with a heating rate of 10°C/min).

3.2. Pre-impregnated material preparation

The matrix film and the reinforcing hPP multifilament were laminated pretensioned onto an aluminium core in a filament winding process using the film-stacking method, which resulted in unidirectionally aligned (UD) fibres, shown in Figure 1a. All-polypropylene composite (all-PPC) sheets with thicknesses of 1.7 mm and varying nominal reinforcing multifilament content (50, 60, 70 and 80 wt%) were produced by compression moulding, shown in Figure 1b. For the sandwich structure 9 layers were applied. The nominal reinforcement was controlled by the number of the applied matrix foils. For 50 wt% four layer matrix foil and one layer reinforcement was used. To increase the reinforcement content number of the matrix foils was decreased one by one. A temperature of 180°C was applied during the consolidation process. The filament-wound, film-stacked package was inserted in between the preheated moulds and held for 240 s without pressure, was compressed for 240 s under a pressure of 5.26 MPa and finally was cooled to 45°C (under pressure). Actually the processing temperature was

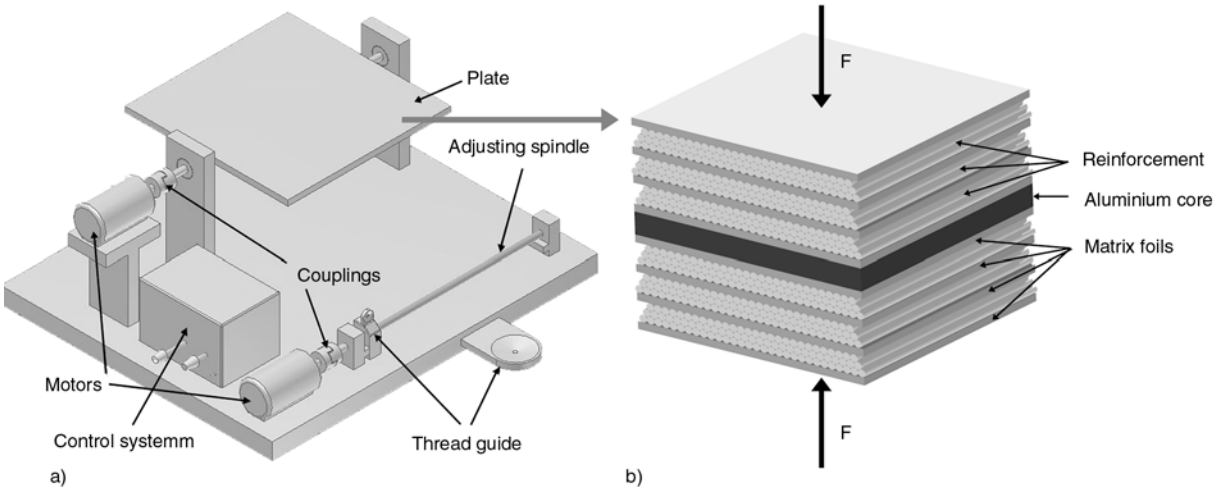

Figure 1. Preparation of unidirectional all-PP composite, with filament winding (a) and with subsequent compression moulding (b) (theoretical lay-up)

higher than the melting temperature of the reinforcement but, due to the high pressure, this value shifted towards higher value (similar the self-reinforced extrusion technique [19]) and the thermoplastic reinforcement did not melt. The consolidated plates were cut into 5 (wide) × 5 (length) mm^2 sections for injection moulding. The length dimension of these cut pieces determined the length of the reinforcing fibres.

3.3. Injection moulding

From pre-impregnated pellets plaque specimens measuring 80 × 80 × 2 mm in dimension were injection moulded with varying amounts of reinforcing multifilament (50, 60, 70 and 80 wt%). The production occurred on an Arburg Allrounder 370S 700-290 injection moulding machine with a heated, flat nozzle with holes measuring 4 mm in diameter (parameters listed in Table 1). In the mould, both a conventional film gate measuring 1 mm in thickness and a fan gate (FG) measuring 2 mm in thickness were used (Figure 2).

Table 1. Injection moulding parameters

Injection moulding parameters	Value
Injection volume [cm^3]	50
Injection rate [cm^3/s]	50
Injection pressure [bar]	800±200
Switch over point [cm^3]	10
Holding pressure [bar]	500
Holding time [s]	10
Residual cooling time [s]	15
Screw rotational speed [m/min]	15
Back pressure [bar]	20
Decompression volume [cm^3]	5
Decompression rate [cm^3/s]	5
Melt temperature [°C]	160
Mould temperature [°C]	40

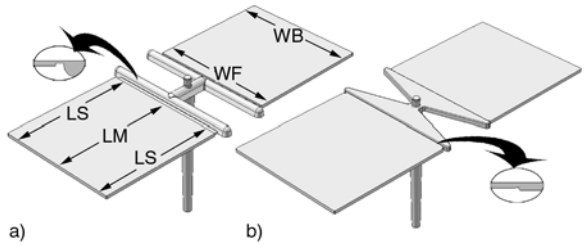

Figure 2. Plaque specimens with a conventional film gate along with shrinkage measurement positions (a) and a fan gate (FG) (b). Dimensional abbreviations [mm] are as follows: LM – length dimension at the middle; LS – length dimension at the side; WE – width dimension at the front; WB – width dimension at back.

3.4. Specimens and their testing

Static tensile tests

Static tensile tests were performed on compression-moulded sheets (20 × 150 mm; in parallel to the fibre direction) and injection moulding plaque specimens. Dumbbell-shaped specimens (EN ISO 8256 Shape 3) were cut from injection moulding plaque specimens by water jet cutting parallel and perpendicular to the flow direction (Figure 3). The tensile tests were carried out by a universal ZWICK Z020 tensile machine according to the standard EN ISO 527. The cross-head speed was set to 5 mm/min, and each test was performed at room temperature (24°C); at least 5 specimens from each material were tested.

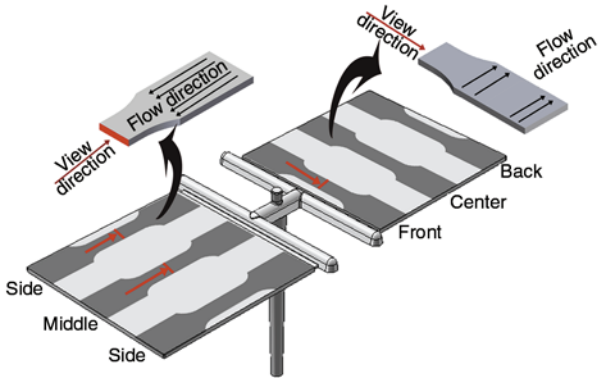

Figure 3. Preparation of dumbbell specimens from the plaque specimens in the parallel and perpendicular to the flow directions. The red lines show the positions at which the cross-sections of the injection moulding specimens were analysed by light microscopy.

Instrumented falling weight impact tests

Instrumented falling weight impact (IFWI) tests were performed on a Fractovis 3789 (Ceast, Italy) machine with the following settings: 131.84 J maximal energy; 20 mm dart diameter; 40 mm support rig diameter; 13.62 kg dart weight; and 1 m drop height. The samples were tested at room temperature (24°C) and at –30°C; at least 10 specimens were tested.

Dynamic mechanical analysis

Dynamic mechanical analysis (DMA) tests were performed on a DMA Q800 machine in a 3-point bending arrangement with the following parameters: frequency: 1 Hz; temperature range: –100 to 150°C; amplitude: 0.16 mm; heating rate: 5°C/min. Specimens 60 × 10 × 2 mm in dimension, which were cut in the flow direction from the plaque specimens (Figure 3 'Side'), were used for these tests.

Shrinkage tests

To describe the effect of the thermoplastic reinforcement on the shrinkage of the injection moulded products shrinkage tests were performed. Shrinkage was measured at different times (1, 4, 24, 48, and 168 h) and positions on the plaque specimens by digital calliper after injection moulding (cf. Figure 2).

Light microscopy

Light microscopy (LM) images were taken from the polished cross sections of injection moulding specimens in parallel and perpendicular to the flow directions by an Olympus BX51M machine. Cross sections were cut from injection moulding specimens and were embedded in epoxy resin (Figure 3). After the samples were prepared, they were polished in a Struers polisher in four steps using 320-, 1000-, 2400- and 4000-grit SiC papers and water as a lubricant.

Scanning electron microscopy (SEM)

Scanning electron microscopy micrographs were taken from fracture surfaces with a Jeol JSM-6380LA microscope. The samples were sputter-coated with gold alloy.

4. Results and discussion

4.1. Static tensile tests

The mechanical properties of the compression-moulded sheets (parallel to the fibres) are shown in Figure 4.

Based on the results in Figure 4, it is obvious that using this filament winding and compression moulding technique can significantly increase the tensile properties. The yield stress and tensile modulus values increase linearly with increasing nominal fibre content. These results are in close agreement with previously published results for all-polypropylene composites produced by a film-stacking process [5].

The yield stress (related to maximum tensile force) of injection moulding all-PP composite is shown in Figure 5.

Yield stress increases in the flow direction with increasing nominal fibre content of the composites until the fibre content reaches 70 wt%. Composites with 70 wt% fibre reinforcement produced the largest yield stress value, ~38 MPa, which corresponds to a 52% improvement compared to the matrix material. At 80 wt% nominal fibre content, the yield stress is

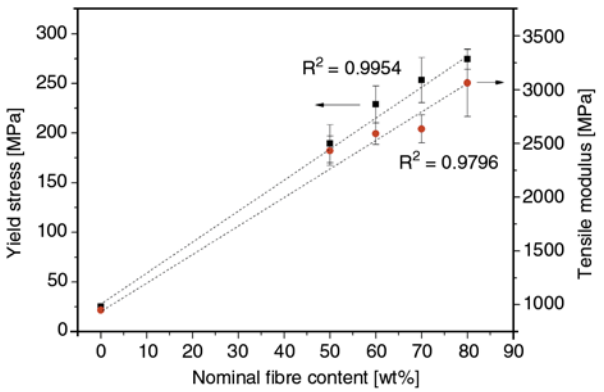

Figure 4. Yield stress and the tensile modulus of the compression-moulded all-PP composite sheets as a function of nominal fibre content

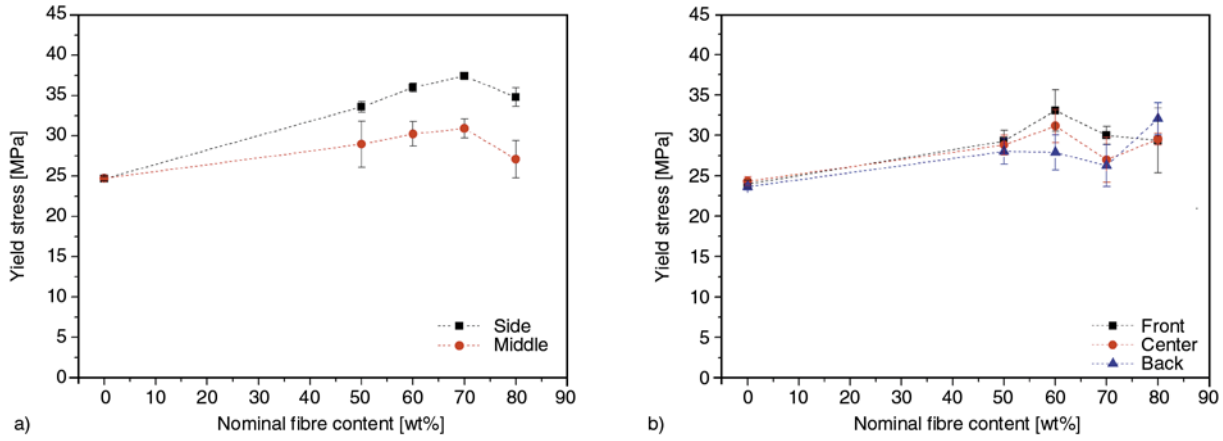

Figure 5. Yield stress of the all-PP composite parallel (a) and perpendicular (b) to the flow direction

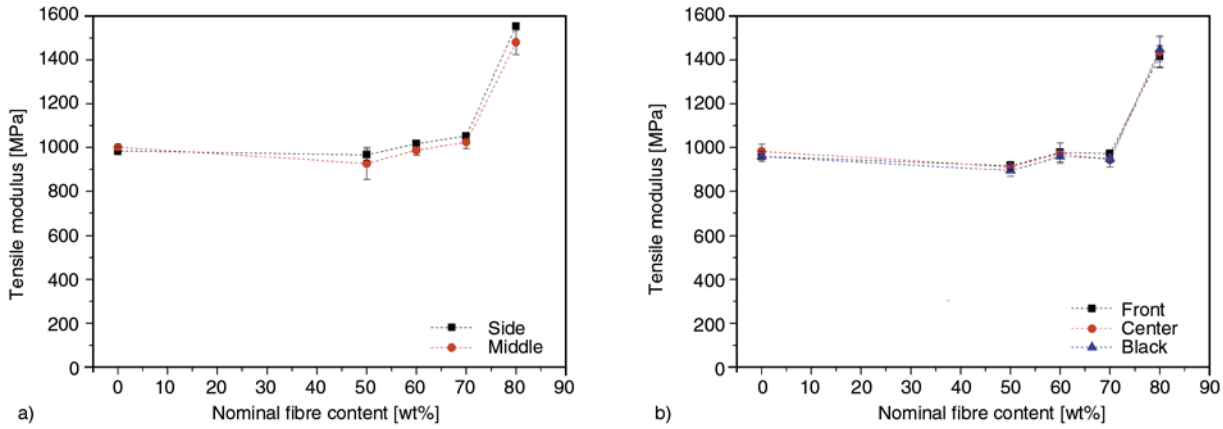

Figure 6. Tensile modulus of the all-PP composite in parallel (a) and perpendicular (b) to the flow directions

slightly lower, which is attributed to the improper consolidation of the composite structure. If analysing the filling pattern mechanical test results followed the expectations. Samples taken from the middle of the plaques had a lower yield stress than those taken from the side. This effect is caused by the orientation of the fibres inside the specimens. A slight deviation in yield stress is observed in perpendicular to the flow direction.

The tensile modulus remained constant with increasing nominal fibre content of the composites until the fibre content reached 70 wt%, after which the modulus increased markedly (Figure 6). Increased tensile modulus is due to considerably more single fibres being aligned parallel to the load direction. This observation is also confirmed by LM (cf. Figure 11 and 12) and SEM micrographs (cf. Figure 14).

Table 2 lists the effect of the gate types on the mechanical properties. With a fan gate, the deviation in properties across the three zones of specimens decreased, i.e., the mechanical behaviours became more similar. Using the fan gate, the filling patterns became more even. In perpendicular to the flow direction, the yield stress increased compared to the one injected with film gate.

The tensile modulus in the flow direction did not change, but perpendicular to the flow direction, it

Table 2. Effect of the gate type on the yield stress and tensile modulus of all-PP composite in parallel (a) and perpendicular (b) to the flow directions (FG: fan gate)

Section	Yield stress [MPa]				Tensile modulus [MPa]			
	Matrix	Matrix (FG)	80 wt%	80 wt% (FG)	Matrix	Matrix (FG)	80 wt%	80 wt% (FG)
SIDE	24.7±0.2	26.3±0.1	34.8±1.1	34.8±1.3	984.6±17.4	939.4±194.9	1554.4±11.5	1518.9±12.1
MIDDLE	24.7±0.4	25.5±1.1	27.1±2.3	30.4±1.8	1000.8±16.3	880.0±127.0	1479.6±55.5	1456.2±44.3
FRONT	24.0±0.5	26.0±0.3	29.4±4.0	36.6±3.7	959.4±23.5	905.4±104.4	1415.8±49.1	1635.5±125.8
CENTER	24.3±0.6	26.0±0.4	29.5±0.7	36.2±2.7	982.6±32.9	1096.1±117.5	1437.1±72.8	1594.5±43.1
BACK	23.6±0.4	26.4±0.4	32.0±2.0	34.9±2.4	958.4±12.8	1154.5±33.5	1447.7±55.5	1624.7±39.4

increased up to 1600 MPa, due to lower friction heat in the gate zone.

4.2. Instrumented falling weight impact tests

To analyse the effect of reinforcing fibre content and gate type on the energy-absorbing capacity of the injection moulding plaque specimens, instrumented falling weight impact tests were performed. Typical force-time curves of the composites are shown in Figure 7a.

These results show that the maximum of the force-time curves increase with increasing fibre content of the composites. Figure 7b shows the perforation energy (impact energy related to the thickness) of all-PP composite and matrix specimens. These results show that with increasing fibre content of up to 60 wt%, the perforation energy increases. Above that value, the perforation energy (~3.5 J/mm) remains constant. Using a fan gate led to higher perforation energy (above 6 J/mm) compared to the conventional film gate which assumed to the better filling patterns. Analysing the effect the testing temperature, significant difference can be seen between the results at 24 and –30°C than the matrix materials. It seems that the all-PP composites are more sensitive to the temperature. The perforation energy of all-PP composite was compared to the conventional polypropylene homopolymer material (Tipplen PP H388F, TVK Nyrt., Tiszaújváros, Hungary,); value obtained is in accordance with the literature [20]. It can be concluded that fibre reinforcement increases the perforation energy significantly compared to the matrix. The perforation energy can be increased by up to 1200% compared to the conventional raw material.

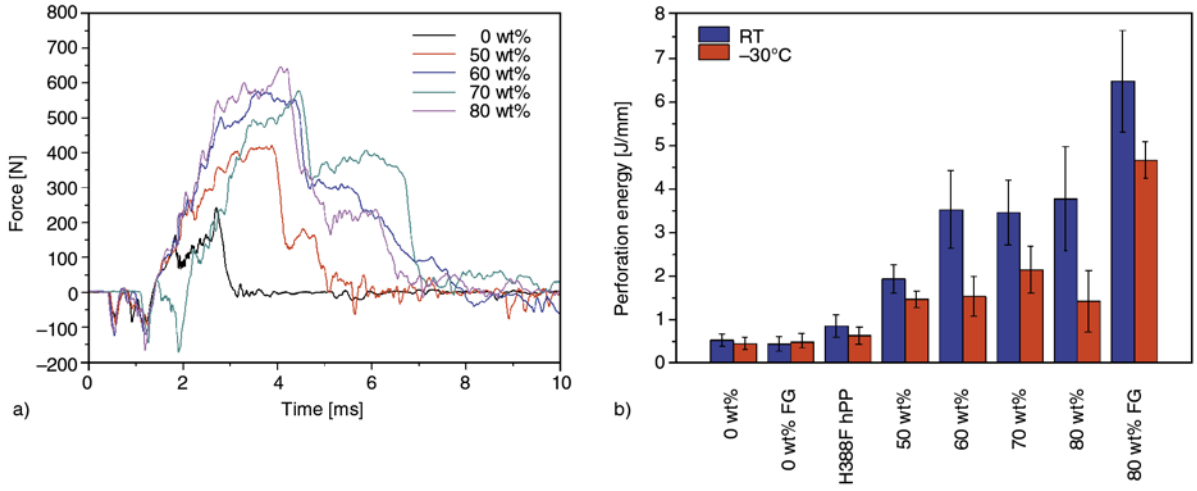

Figure 7. Force-time curves of the all-PP composites at 24°C (a) and perforation energy of all-PP composite, matrix and a PP homopolymer (H388F) (FG: fan gate)

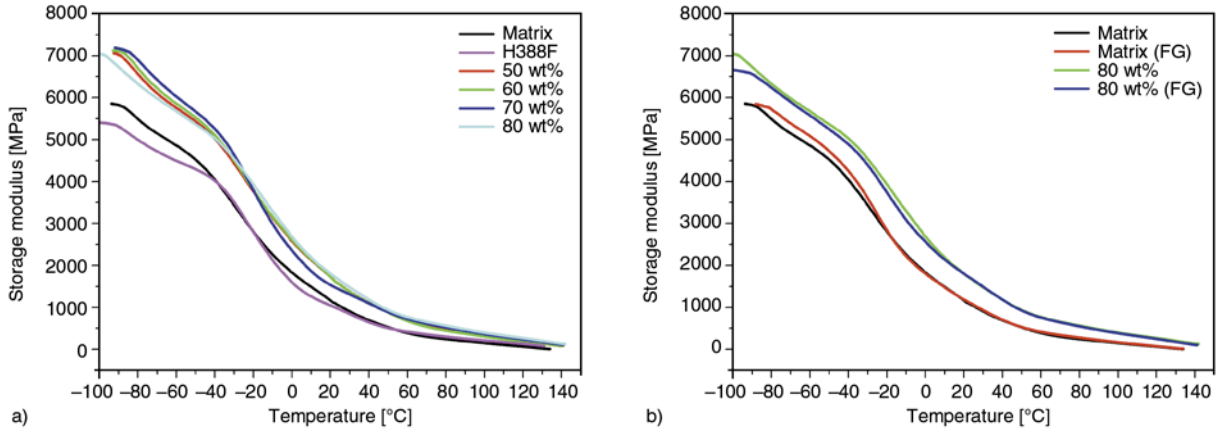

Figure 8. Storage modulus of raw materials and composites with varying fibre content with a conventional film gate (a) and a fan gate (FG) (b)

4.3. Dynamic mechanical analysis

Dynamic mechanical analysis was also used to show the reinforcing effect of the fibres. The storage modulus (E') curves are shown in Figure 8.

The composites have a higher storage modulus compared to those of the matrix and commercially available PP homopolymer. While fibre reinforcement typically leads to a higher storage modulus, increasing the fibre content did not significantly affect this parameter. Replacing the conventional film gate with a fan gate did not affect the storage modulus. Upon analysis of the glass transition temperature (T_g, derived from the maximum peak of $\tan\delta$ curves), a slight shift to higher temperature can be observed (from –14.3°C (matrix) to –8.1°C (80 wt%)) with increasing reinforcing fibre content (i.e., increasing homopolymer content).

4.4. Shrinkage tests

Shrinkage of the injection moulding specimens is shown in Figure 9.

Shrinkage of thermoplastic fibre-reinforced composite increased in all directions compared to the matrix material, which is in contrast to the shrinkage behaviour of conventional fibre-reinforced composites (e.g., glass fibre) where the reinforcement in flow direction decreased the shrinkage. This effect is attributed to the relaxation of the thermoplastic fibre. Shrinkage of the matrix material is approximately 1%, which is in agreement with the literature [21]. Increasing the thermoplastic reinforcing fibre content increased the shrinkage. The greatest shrinkage occurred parallel to the flow direction at the middle of the specimen. As expected, the least shrinkage was observed near the gate due to the local pressure. Despite increased technological shrinkage (measured 1 h after injection) in fibre-reinforced composites, subsequent post shrinkage does not differ from that in unreinforced composites. Thus, calculating the proper shrinkage for the mould construction could make the part dimensions stable over time. Plotting the results an exponential relation between technological shrinkage and fibre content can be deduced (Figure 10). One can see that the technological shrinkage is different parallel and perpendicular to the flow direction.

The shrinkage of the all-polypropylene composites used in this study can be calculated by the following Equation (1):

$$S(t) = C_1 \cdot e^{-C_2\left(1-\frac{\Phi}{100}\right)} + m \cdot \log(t) \qquad (1)$$

where $S(t)$ is the shrinkage of the composite in time and direction, C_1 is a constant which is proportional to the relaxation of the fibres, C_2 is a constant which is proportional to the fibre orientation in the speci-

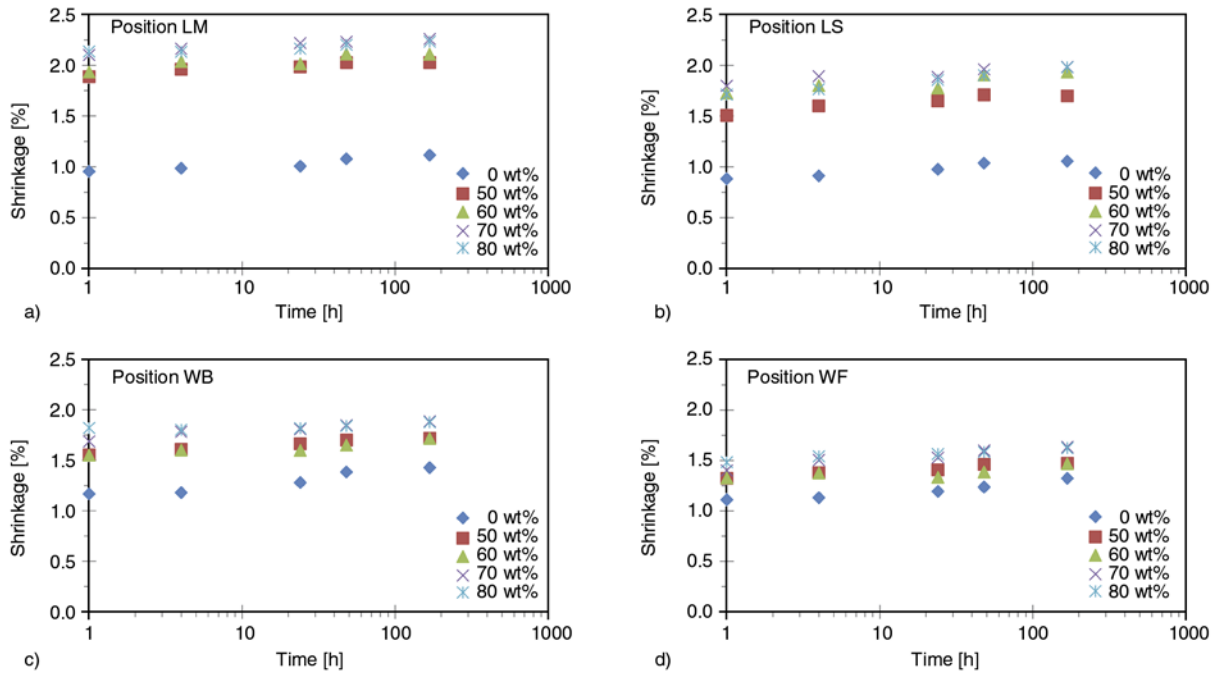

Figure 9. Shrinkage of all-PP composite specimens in different directions LM: Length Middle (a), LS: Length Side (b), WB: Width Back (c), WF: Width Front (d)

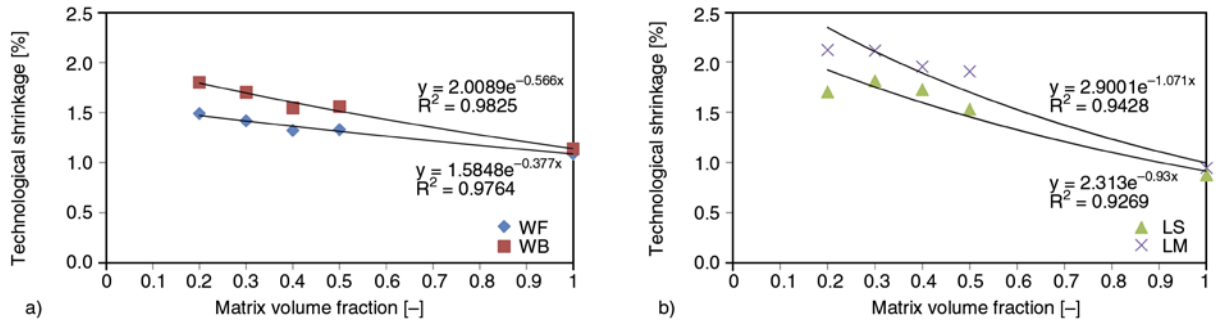

Figure 10. Technological shrinkage of the all-PP composite as a functional of matrix volume fraction perpendicular (a) and parallel (b) to the flow direction

men, Φ is the fibre content of the composite, and *m* is the slope of the post shrinkage (time factor), *t* [1;168 h].

4.5. Light microscopy

Figure 11 shows the single-fibre distributions in the specimens perpendicular to the flow direction (Front) near the gate. The distribution of single fibres is imperfect, and a skin-core structure formed. For 80 wt% fibre content, many more single fibres are aligned perpendicular to the flow direction, which significantly increased the tensile modulus (cf. Figure 6b).

LM images taken from the specimen cut in the flow direction (Side) are shown in Figure 12. A skin-core layer can also be found with a thickness that is similar to that of specimens cut perpendicular to the flow direction. For 80 wt% fibre content, there is

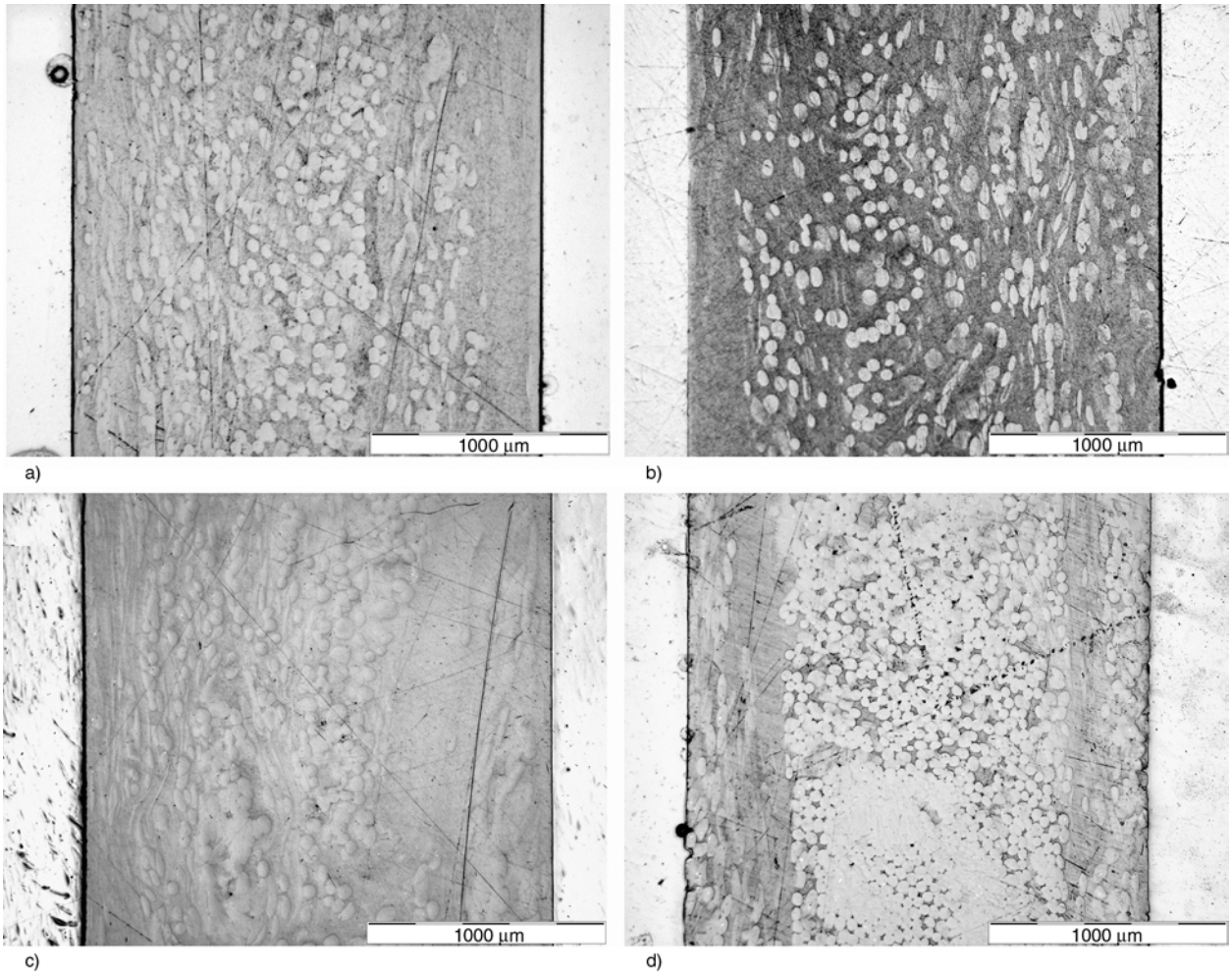

Figure 11. LM micrographs of all-PP composites perpendicular to the flow direction (Front) a) 50 wt%; b) 60 wt%; c) 70 wt%; d) 80 wt%

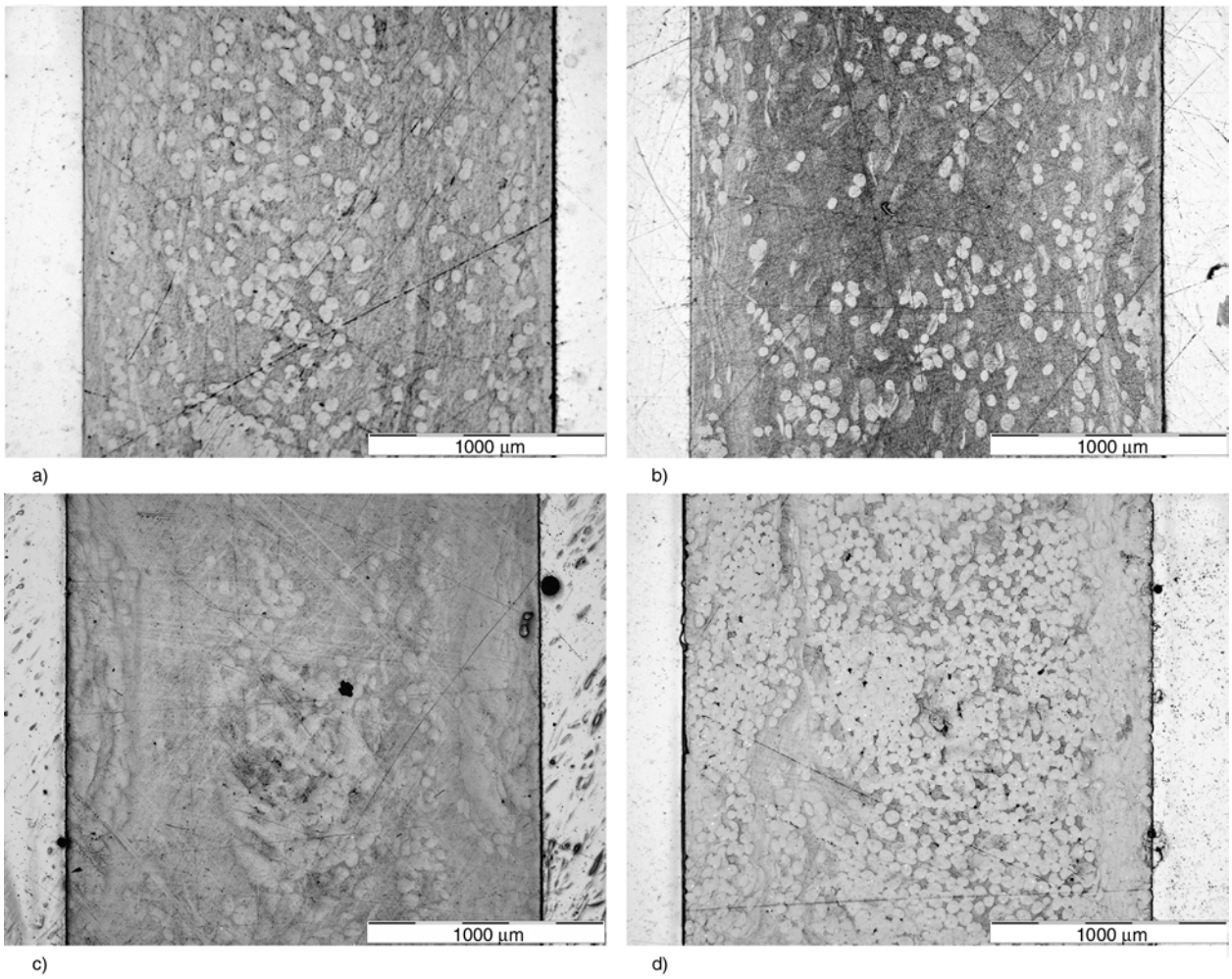

Figure 12. LM micrographs of the all-PP composites in the flow direction (Side) a) 50 wt%; b) 60 wt%; c) 70 wt%; d) 80 wt%

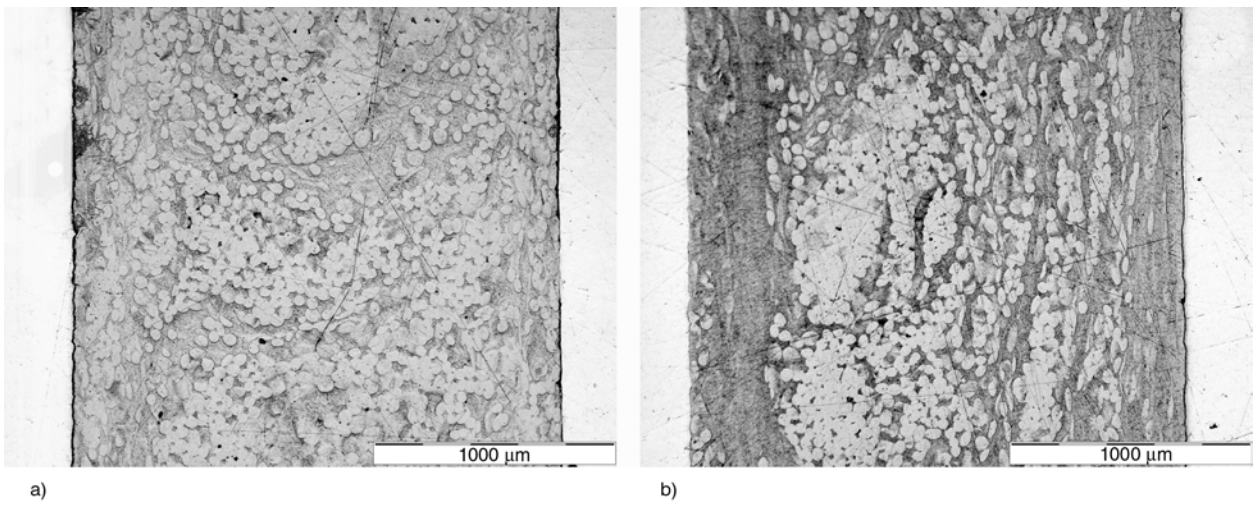

Figure 13. LM micrographs of the all-PP composites (80 wt%) with fan gate perpendicular (a) and parallel (b) to the flow direction

better fibre distribution (Figure 12d) than for other composites, a trend similar to that in Figure 11d.

Perpendicular to the flow direction of the 80 wt% all-PP composites with a fan gate is presented in Figure 13. There is no skin layer formed perpendicular to the flow direction. Furthermore, the fibre distribution is better than that for the conventional film gate, which explains the improved mechanical properties.

4.6. Scanning electron microscopy (SEM)

SEM micrographs were taken from the fracture surface of the all-PP composite specimens (Figure 14). The consolidation and fibre distribution worsened with increasing fibre content. Voids formed among the fibres because the matrix material could not impregnate the fibres. Moreover, for the 80 wt% sample, there is poor adhesion between the matrix and fibres in the core region (Figure 14d).

Figure 15 shows the effect of the gate type used. With a fan gate, perpendicular to the flow direction of the specimen became more homogeneous, and the core could not be distinguished from the skin region.

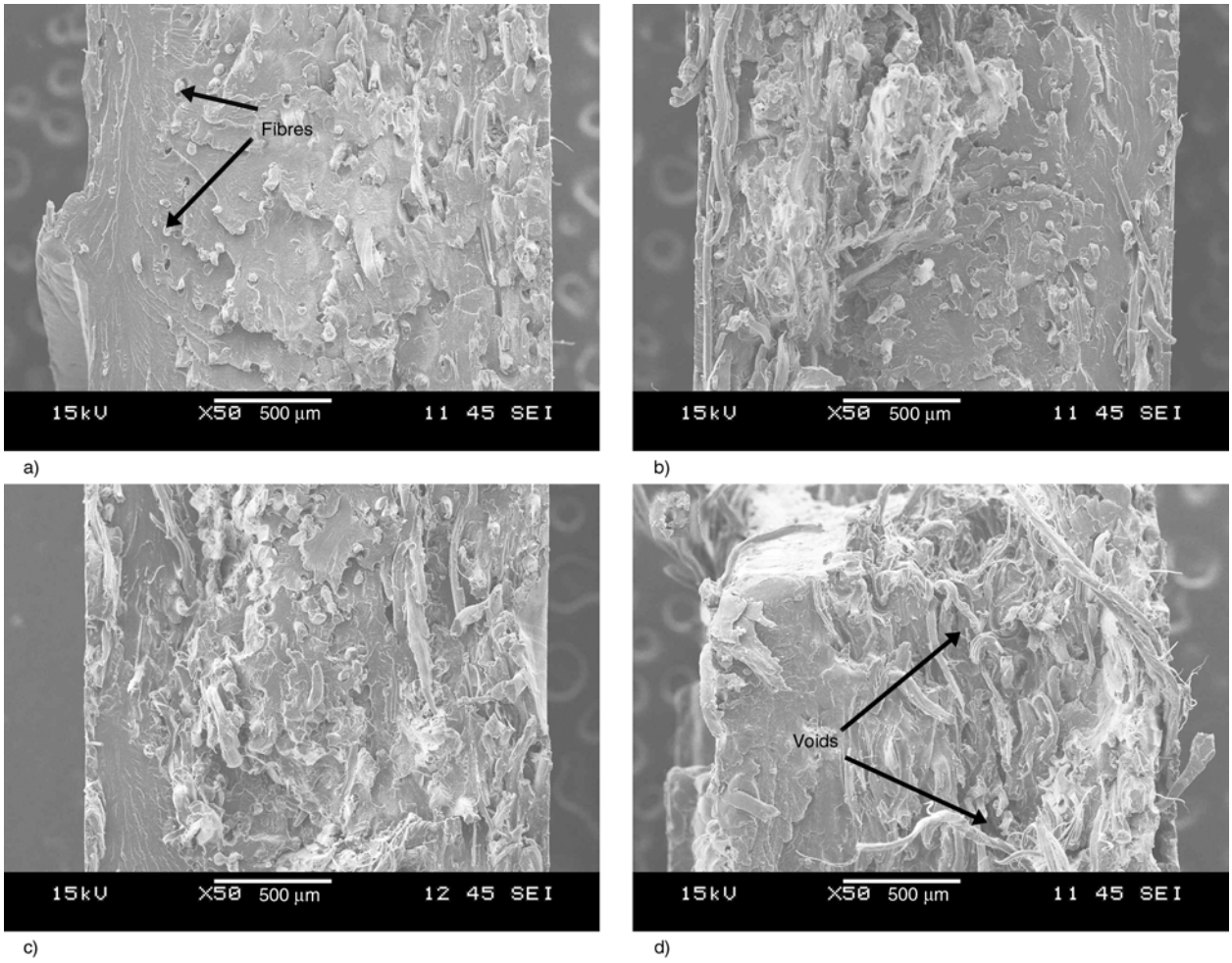

Figure 14. Fracture surface of the all-PP composites a) 50 wt%; b) 60 wt%; c) 70wt%; d) 80wt%

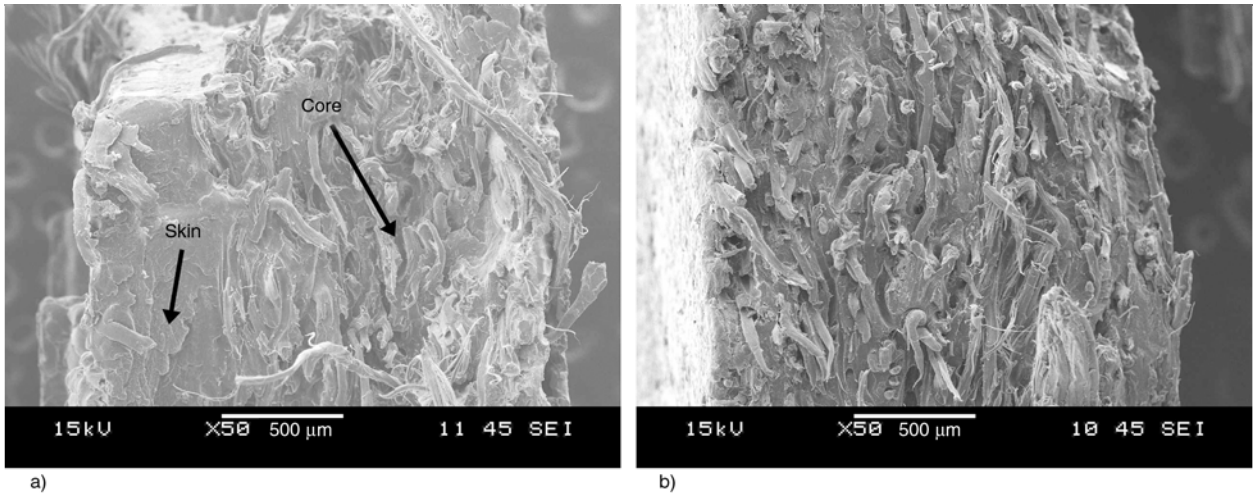

Figure 15. Fracture surface of a composite prepared by a conventional film gate (a) and a fan gate (b)

5. Conclusions

The goal of this paper was to study all-polypropylene composites that were produced by injection moulding. Static tensile tests, IFWI tests, DMA tests, shrinkage analysis, optical microscopy and scanning electron microscopy were carried out. The mechanical tests showed that increasing the fibre content (50–70 wt%) of the pre-product the yield stress and perforation energy significantly increased. The applied fan gate resulted in more homogeneous tensile properties and greater perforation energy. Based on the results, all-PP composite showed greater shrinkage than the rPP matrix and the reinforcement did not decrease the shrinkage contrast to the conventional fibre reinforcement. This effect assumed to the relaxation of the thermoplastic reinforcement.

Acknowledgements

The authors are grateful to the Hungarian Scientific Research Fund (OTKA K75117).

T. Bárány is thankful for the János Bolyai Research Scholarship from the Hungarian Academy of Sciences. The work reported in this paper has been developed within the framework of the 'Talent care and cultivation in the scientific workshops of BME' project. This project is supported by the grant TÁMOP-4.2.2.B-10/1-2010-0009. This work is connected to the scientific program of the 'Development of quality-oriented and harmonized R+D+I strategy and functional model at BME' project. This project is supported by the New Széchenyi Plan (Project ID: TÁMOP-4.2.1/B-09/1/KMR-2010-0002). The authors are grateful to Arburg Hungary Ltd. for the Arburg Allrounder 370S 700-290 machine.

References

[1] Capiati N. J., Porter R. S.: The concept of one polymer composites modelled with high density polyethylene. Journal of Materials Science, **10**, 1671–1677 (1975). DOI: 10.1007/BF00554928

[2] Allan S. P., Bevis I. M., Zadhoush A.: The development and application of shear controlled orientation technology. Iranian Journal of Polymer Science and Technology, **4**, 50–55 (1995).

[3] Ogbonna C. I., Kalay G., Allan P. S., Bevis M. J.: The self-reinforcement of polyolefins produced by shear controlled orientation in injection molding. Journal of Applied Polymer Science, **58**, 2131–2135 (1995). DOI: 10.1002/app.1995.070581126

[4] Li Y., Chen J., Shen K.: Self-reinforced isotactic polypropylene prepared by melt vibration injection molding. Polymer-Plastics Technology and Engineering, **47**, 673–677 (2008). DOI: 10.1080/03602550802129551

[5] Kmetty Á., Bárány T., Karger-Kocsis J.: Self-reinforced polymeric materials: A review. Progress in Polymer Science, **35**, 1288–1310 (2010). DOI: 10.1016/j.progpolymsci.2010.07.002

[6] Pegoretti A.: Trends in composite materials: The challenge of single-polymer composites. Express Polymer Letters, **1**, 710 (2007). DOI: 10.3144/expresspolymlett.2007.97

[7] Hine P. J., Ward I. M.: Hot compaction of woven nylon 6,6 multifilaments. Journal of Applied Polymer Science, **101**, 991–997 (2006). DOI: 10.1002/app.22771

[8] Hine P. J., Ward I. M.: Hot compaction of woven poly(ethylene terephthalate) multifilaments. Journal of Applied Polymer Science, **91**, 2223–2233 (2004). DOI: 10.1002/app.13343

[9] Ward I. M.: Developments in oriented polymers, 1970–2004. Plastics Rubber and Composites, **33**, 189–194 (2004). DOI: 10.1179/174328904x4864

[10] Alcock B., Cabrera N. O., Barkoula N-M., Loos J., Peijs T.: The mechanical properties of unidirectional all-polypropylene composites. Composites Part A: Applied Science and Manufacturing, **37**, 716–726 (2006). DOI: 10.1016/j.compositesa.2005.07.002

[11] Chen J. C., Wu C. M., Pu F. C., Chiu C. H.: Fabrication and mechanical properties of self-reinforced poly (ethylene terephthalate) composites. Express Polymer Letters, **5**, 228–237 (2011). DOI: 10.3144/expresspolymlett.2011.22

[12] Izer A., Bárány T., Varga J.: Development of woven fabric reinforced all-polypropylene composites with beta nucleated homo- and copolymer matrices. Composites Science and Technology, **69**, 2185–2192 (2009). DOI: 10.1016/j.compscitech.2009.06.002

[13] Pegoretti A., Zanolli A., Migliaresi C.: Flexural and interlaminar mechanical properties of unidirectional liquid crystalline single-polymer composites. Composites Science and Technology, **66**, 1953–1962 (2006). DOI: 10.1016/j.compscitech.2006.01.015

[14] Dorigato A., Pegoretti A.: Biodegradable single-polymer composites from polyvinyl alcohol. Colloid and Polymer Science, **290**, 359–370 (2012). DOI: 10.1007/s00396-011-2556-z

[15] Wu C. M., Chang C. Y., Wang C. C., Lin C. Y.: Optimum consolidation of all-polyester woven fabric-reinforced composite laminates by film stacking. Polymer Composites, **33**, 245–252 (2012). DOI: 10.1002/pc.22146

[16] Matabola K. P., de Vries A. R., Luyt A. S., Kumar R.: Studies on single polymer composites of poly(methyl methacrylate) reinforced with electrospun nanofibers with a focus on their dynamic mechanical properties. Express Polymer Letters, **5**, 635–642 (2011). DOI: 10.3144/expresspolymlett.2011.61

[17] Bhattacharyya D., Maitrot P., Fakirov S.: Polyamide 6 single polymer composites. Express Polymer Letters, **3**, 525–532 (2009).
DOI: 10.3144/expresspolymlett.2009.65

[18] Pegoretti A., Zanolli A., Migliaresi C.: Preparation and tensile mechanical properties of unidirectional liquid crystalline single-polymer composites. Composites Science and Technology, **66**, 1970–1979 (2006).
DOI: 10.1016/j.compscitech.2006.01.012

[19] Prox M., Pornnimit B., Varga J., Ehrenstein G. W.: Thermoanalytical investigations of self-reinforced polyethylene. Journal of Thermal Analysis, **36**, 1675–1684 (1990).
DOI: 10.1007/BF01913414

[20] Karger-Kocsis J., Wanjale S. D., Abraham T., Bárány T., Apostolov A. A.: Preparation and characterization of polypropylene homocomposites: Exploiting polymorphism of PP homopolymer. Journal of Applied Polymer Science, **115**, 684–691 (2010).
DOI: 10.1002/app.30624

[21] Karian H. G.: Part shrinkage behavior of polypropylene resins and polypropylene composites. in 'Handbook of polypropylene and polypropylene composites' (eds.: H. G. Karian) Marcel Dekker, New York, Vol 19, 675–706 (2003).

eXPRESS Polymer Letters Vol.7, No.2 (2013) 146–160
Available online at www.expresspolymlett.com
DOI: 10.3144/expresspolymlett.2013.14

Photodegradation profiles of PVC compound and wood/PVC composites under UV weathering

K. Chaochanchaikul[1], *V. Rosarpitak*[2], *N. Sombatsompop*[1*]

[1]Polymer PROcessing and Flow (P-PROF) Group, School of Energy, Environment and Materials, King Mongkut's University of Technology Thonburi (KMUTT), Bangmod, Thungkru, 10140 Bangkok, Thailand
[2]V.P. Wood Co., Ltd., 25/5 Moo 4, Soi Suksawad 66, Bangmod, Thungkru, 10140 Bangkok, Thailand

Received 3 July 2012; accepted in revised form 19 September 2012

Abstract. This work aimed to study the effect of different ultraviolet (UV) weathering conditions (natural and accelerated) on the photodegradation of polyvinyl chloride (PVC) and wood/polyvinyl chloride (WPVC) composites by considering the structural and physical changes of PVC and WPVC samples as well as examining the photodegradation profiles at different depths from the sample surfaces. The photodegradation of PVC and WPVC composites under natural weathering conditions were lower than those under accelerated weathering conditions. The addition of Tinuvin P stabilizer at 2 phr was sufficient to stabilize PVC and WPVC composites, whereas the presence of wood appeared to accelerate the photodegradation of PVC under both natural and accelerated weathering conditions. When considering the photodegradation profiles at different depths of the samples, it was found that the polyene and carbonyl sequences of PVC and WPVC composites were high at the sample surfaces and tended to decrease rapidly with increasing depth from the specimen surface before stabilizing at a depth of 60 μm for PVC and 80 μm for WPVC composites. The differences in specimen depths for the stabilization of polyene and carbonyl sequences in PVC and WPVC samples implied that the presence of wood particles enhanced the absorption of UV radiation by the WPVC composite samples.

Keywords: *polymer composites, wood, material testing, environmental degradation*

1. Introduction

The use of WPC has been rapidly growing in several key market segments, such as outdoor decorations, and also building and construction products [1, 2]. Therefore, evaluation of changes in the properties of WPC under service conditions has become a significant issue, as this indicates the durability of WPC products. Environmental factors – such as UV radiation from sunlight, and also moisture, temperature, and biological decay – result in chemical and physical changes to the structure of the material components in WPC.

Studies on the factors affecting on the properties of WPC under weathering conditions have focused on various aspects, such as weathering conditions (e.g. moisture, temperature, and biological decay) [3–20], wood content, processing method, weathering condition, and type and content of UV absorbers and pigments [3–14]. The presence of wood has been found to accelerate the photodegradation of WPC. Works by Stark and Matuana [3, 4] showed that wood particles accelerated the oxidation reaction at the surface of wood/high density polyethylene (WPE) composite, to a greater extent than that of neat high density polyethylene (HDPE). In the case of wood/polyvinyl chloride (WPVC) composites, the presence of wood strongly accelerated the photodegradation of PVC [5–7] and interfered with the function of a UV absorber [7]. The chromophore groups or carbonyl groups in lignin as a component

*Corresponding author, e-mail: narongrit.som@kmutt.ac.th

of wood accelerated the photodegradation of polymer matrix with enhancing absorption of UV light on the WPC surface. Stark and Matuana [8] showed that WPC specimens processed by an extrusion method degraded more than the WPC specimen processed by an injection method. This was because the surface of the injection molded WPC have more of polymer rich layer when compared with that of the extruded WPC. A report by Wang *et al*. [9] indicated that a smooth WPC surface was more durable in terms of mechanical properties than a sawn WPC surface. The works of Stark and Matuana [8] and Wang *et al*. [9] implied that the emerged wood particles on the WPC surface accelerated the degradation in WPC.

Stark [10] studied the effect of weathering cycles on changes in color and mechanical properties of WPE composites, and found that exposure of WPE composites to water spray in combination with radiation in a xenon arc weathering apparatus was more severe than exposure to radiation alone. Filson *et al*. [11] studied the effect of weathering on chemical and color changes of WPVC composites, and found that the conjugated ketones and lignin were reduced by weathering, whereas the cellulose part was unaffected. The use of a UV absorber and/or pigment could improve the stabilization of the polymer matrix in WPC, which prevent or retard the photodegradation [7, 12–14]. In addition to UV radiation, moisture and temperature are classified as effective variables affecting the property changes in WPC. Moisture or water can accelerate photooxidation in WPC by causing swelling of the wood cell wall, thus facilitating light penetration into the wood [10]; this results in decreases in both strength and modulus of WPC due to the deterioration of interfacial bonding between natural fiber and matrix, and the softening of amorphous regions of microfibrils of wood fiber [10, 15, 16]. Bledzki *et al*. [17] found that the decrease of mechanical properties of wood/polypropylene (WPP) composites, after cyclic conditions of temperature and moisture, was partially reversible. However, cyclic conditions showed less effect than static conditions. The work of Wang *et al*. [18] indicated that the flexural strength and modulus of WPC tended to decrease significantly after freeze-thaw cycling treatment. Higher temperature was also found to increase the water absorption of WPC [17, 18].

Available literature indicates that there is very little information comparing the property changes of WPC under accelerated and natural conditions [21, 22]. Abu-Sharkh and Hamid [21] revealed that the photostability of maleic anhydride-grafted polypropylene (MAPP)-compatibilized palm fiber/PP composites under artificial weathering was higher than that under natural weathering. This was because the difference in light spectrum was produced by solar radiation, and that the accelerated weathering of MAPP was susceptible to degradation by radiation frequencies that were more abundant in solar radiation. The work of Fabiyi and McDonald [22] also reported on the effects of three weathering regimes – xenon-arc, UVA, and natural weathering – on the photodegradation of WPVC composites; they found that the carbonyl and polyene contents of weathered WPVC composites under xenon-arc and UVA weathering increased with increasing weathering time and then decreased after 1200 h, whereas those under natural weathering progressively increased throughout the natural weathering times used.

Several studies have indicated that the degradation pattern of WPC under natural weathering might differ from that of WPC under accelerated weathering, based on laboratory conditions [21, 22]; also, a previous study [7] reported on the effect of the type and content of a UV stabilizer on the photostabilization of WPVC composites using a QUV weatherometer only. Therefore, it would be interesting to investigate the photodegradation pattern of WPVC composites under natural weathering compared to that of WPC under accelerated weathering. In addition, the photodegradation level of WPVC composites at different depths from the specimen surface may differ; this was investigated in order to clarify the magnitude of photodegradation in WPVC composites.

Thus, this work was divided into two parts. The first part was to compare the photodegradation of WPVC composites under both natural and QUV weathering, while the second part was to study the magnitude of photodegradation in WPVC composites at different depths from the specimen surface. Photodegradation of WPVC composites was mainly evaluated by discoloration and chemical and structural changes.

2. Experimental

2.1. Raw materials

The ingredients of the PVC compound and composites are shown in Table 1.

2.1.1. Suspension PVC

Suspension PVC (trade name, SIAMVIC 258RB) was supplied by V.P. Wood Co., Ltd. (Bangkok Thailand). The PVC powder was dry-blended with various necessary additives as listed in Table 1, this being referred to as PVC compound.

2.1.2. Wood flour particles

Wood flour particles were supplied by V.P. Wood Co., Ltd. and were chemically treated with N-(2-aminoethyl)-3-aminopropyl trimethoxysilane of 1.0 wt% wood flour. For silane treatment, the wood flour was dried in oven for 24 h at 80°C or until the weight of wood flour was constant to remove the moisture. The silane solution was prepared by dropping *N*-(2-aminoethyl)-3-aminopropyl trimethoxysilane slowly into mixture of deionized water and 1% acetic acid. And then the silane solution was sprayed onto wood flour, with a better mixing obtained with a high speed mixer for 5 mins. Thereafter, the treated wood flour was oven-dried for 6 h at 100°C until a constant weight was achieved for the removal of the solvent. In this work, the content of wood flour in the PVC compounds varied: 0, 50 or 100 parts per hundred resin [phr] of PVC powder.

2.1.3. UV stabilizers

From our previous work [7], 2-(2H-benzotriazol-2-yl)-p-cresol (trade name, Tinuvin P; Ciba Specialty Chemicals, Basel, Switzerland) at 2 phr was recommended as the most effective UV stabilizer for both PVC and WPVC composites. Therefore, formulations of PVC and WPVC composites with 2 phr of Tinuvin P were chosen to compare the effects of weathering regimes and the magnitude of photodegradation at different depths from the specimen surface. After weathering, changes in chemical structure and color of PVC and WPVC composites with 2 phr of Tinuvin P were examined.

2.2. Sample preparation

PVC and WPVC composites were produced by an industrial-scale twin-screw extruder (D-521; Reifenhäuser Extrusion GmbH, Troisdorf, Germany) with counter-rotating screws. The experimental procedure and instruments used for the sample preparation are detailed in our previous work [7]. The processing temperature profiles on the extruder from hopper to die zones were 170, 160, 150, 140, 135 and 170°C. The screw rotating speed was 16 rpm. A slit die, whose dimensions (width × height × length) were $40 \times 4 \times 180$ mm^3, was used to produce slit extrudates. The extrudates were then solidified by passing through a water cooling-system before collection for preparing specimens.

Table 1. Materials formulations for PVC compound and WPVC composites

Ingredients	Concentration [phr]
Suspension PVC grade SIAMVIC® 258RB (*K* value = 58)	100.0
External lubricant (Finalux® G-741)	0.6
Internal lubricant (Ca-St)	0.6
Acrylic Processing aids (Kane Ace® PA-20)	6.0
One pack heat stabilizer (PF608)	3.6
Natural filler (wood flour)	Varied (0, 50, 100)
UV Stabilizers (Tinuvin P)	Varied (0, 1.0, 2.0)

2.3. Effects of natural and accelerated weathering conditions

2.3.1. QUV weathering testing

PVC and WPVC specimens were cut from extrudates whose dimensions were dependent on the standard testing methods used. The prepared PVC and WPVC specimens were weathered in a QUV weatherometer (Q-Lab, Cleveland OH, USA) operated according to ASTM G154 (2006). PVC and WPVC specimens were UV-weathered under cyclic UV/condensation exposures: 8 h of UV light exposure at 60°C under 313 nm fluorescent UV (UVB) lamps, followed by 4 h of condensation temperatures at 50°C in dark condition (without UV exposure). The weathered PVC and WPVC specimens were evaluated for changes in chemical structure and color after UV weathering times of 0 to 720 h.

2.3.2. Natural weathering testing

PVC and WPVC specimens were exposed on a roof deck at the School of Energy, Environment and Materials building at King Mongkut's University of Technology Thonburi, Bangkok, Thailand, for 365 days (from April 2010 through March 2011). The typical weather conditions in Bangkok for the duration of exposure are illustrated in Table 2. Data regarding average weather conditions were provided by the Thai Metrological Department. PVC and WPVC

Table 2. Average weather conditions in Bangkok for April 2010 to March 2011

Weather condition	April – June 2010	July – September 2010	October – December 2010	January – March 2011
Temperature [°C]	31.03	28.93	27.86	27.47
Relative humidity [%]	72.68	79.33	70.64	68.56
UV-B intensity [W/m^2]	0.36	0.33	0.24	0.24
Rainfall [mm]	5.44	11.97	2.30	2.29

specimens were placed on aluminum exposure racks according to ASTM D1435 (2005). The specimens were mounted on the racks at a 45° angle, facing in a southerly direction, and were later taken for characterization after 90, 180, 270 and 365 days.

2.4. Photodegradation profiles at different depths from the specimen surface

PVC and WPVC specimens weathered by a QUV weatherometer at UV weathering times of 0 and 720 h were studied for their photo-degradation level at different depths from the specimen surface, using an abrasion tester to remove the weathered PVC and WPVC surface layers to the desired depth. Standard curves relating to the thickness of the removed specimen bulk and the number of abrasions were established for determination of the number of abrasions. The magnitude of photodegradation at different depths from the specimen surface were investigated based on structural changes, in terms of polyene and carbonyl sequences and color changes, as well as from visual photographs.

Standard curves were established as a plot of the number of abrasions against the thickness of the removed specimen surface. Removal of the specimen surface was performed using an abrasion tester (Taber Abraser model 5130; Testing Machines Inc., Ronkonkoma NY, USA). Sandpaper (P12) with an average grit size of 1815 μm was used for abrasion of specimen surfaces in the abrasion tester. The number of abrasions was varied from 50, 100, 150, 200 and 250 rounds and the thickness of the removed specimen was measured using a micrometer. During abrasion, each specimen was pressed with a 250 g steel load. The standard curves for PVC and for WPVC composites with wood contents of 50 and 100 phr are given in Figure 1. The calculated number of abrasions for removing each 20 μm of specimen surface is shown in Table 3. The chemical structure and color of weathered PVC and WPVC composites at 720 h UV weathering time were evaluated as a function of depth from specimen surface ranging from 0 to 100 μm as compared to those of un-weathered PVC and WPVC composites.

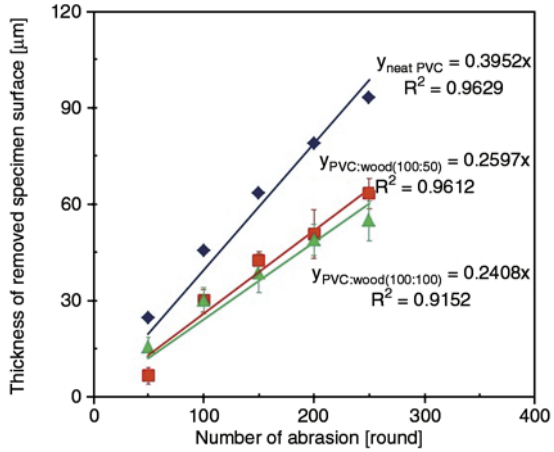

Figure 1. Standard curves between removed thickness of specimen surface and number of abrasions

Table 3. Number of abrasion for removing specimen surface at every 20 μm

Formula	Number of abrasion [round]
PVC	51
PVC with wood flour at 50 phr	77
PVC with wood flour at 100 phr	83

2.5. Characterizations

It should be noted that all reported data for all tests were averaged from at least three independent specimens and each specimen was measured from at least three different positions.

2.5.1. Contact angle measurement

Contact angles of unweathered and weathered WPVC samples were measured using a contact angle goniometer (model 100-00; Ramé-Hart, Succasunna NJ, USA) equipped with an automated camera and image analysis software. Distilled water was used as the wetting liquid. Further details of the experimental procedure can be obtained elsewhere [23].

2.5.2. Structural change analysis

Polyene and carbonyl indices were determined using attenuated total reflectance–Fourier transform

infrared (ATR-FTIR) analysis to assess the extent of degradation of the PVC and WPVC. A Nicolet 6700 FT-IR spectrometer (Thermo Scientific, Waltham MA, USA) was used to measure the reflectance spectra of specimens, as well as changes in their absorbance. Polyene and carbonyl indices were calculated in accordance with our previous work [7]. The wavenumbers of interest were 2920, 1650 and 1730 cm^{-1}, representing C–H stretching, polyene sequences and carbonyl groups, respectively.

2.5.3. Discoloration testing

Color changes of unweathered and weathered PVC and WPVC specimens were determined using two different color systems: Munsell and CIELAB. In the Munsell color system, the yellowness index (*YI*) was estimated using a UV-Vis spectrophotometer (model 3100; Shimadzu, Kyoto, Japan) under the standard source C. The *YI* values of unweathered and weathered specimens were calculated in accordance with our previous work [24].

In addition, a UV-Vis spectrophotometer was used to measure color changes of PVC and WPVC samples before and after weathering, using the CIELAB color system. $L^*a^*b^*$ coordinates of unweathered and weathered PVC and WPVC specimens were calculated based on a D65 light source. L^* represents the lightness, whereas a^* and b^* are the chromaticity coordinates. The total color changes or discolorations of the weathered specimens were calculated from differences of lightness and chromatic coordinates (ΔE) of unweathered and weathered PVC and WPVC specimens [25].

3. Results and discussion

3.1. Effects of natural and accelerated weathering conditions

3.1.1. Contact angle analysis

Figure 2 shows contact angle values of PVC and WPVC composites with and without Tinuvin P at 2 phr under natural and QUV weathering conditions. It was found that the initial contact angle of PVC was slightly different from that of WPVC composites, suggesting that wood particles had no significant effect on the contact angle value. After weathering, the contact angle for PVC and WPVC composites generally decreased with increasing weathering time under both natural and QUV weathering conditions except for WPVC with wood content of 100 phr under natural weathering, suggesting that the specimen surfaces of the PVC and WPVC composites became more hydrophilic. The decreases in contact angle with weathering time were more obvious in the case of QUV weathering, indicating that photodegradation of PVC and WPVC composites under QUV weathering became more severe than under natural weathering.

3.1.2. Structural changes

Figure 3 shows the effects of weathering conditions on the polyene index of PVC and WPVC composites with and without Tinuvin P at 2 phr. The polyene contents of PVC and WPVC composites under natural and QUV weathering conditions were found to increase with increasing weathering time. The change in the polyene index in the case of QUV weathering, however, was more pronounced than in the case of natural weathering. It is known that radi-

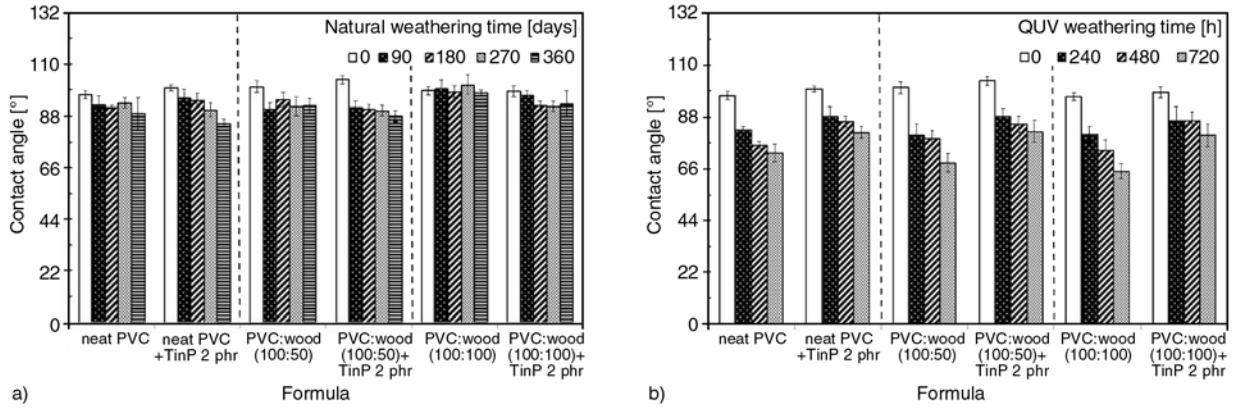

Figure 2. Effect of weathering condition on contact angle in PVC and WPVC composites with and without Tinuvin P at 2 phr: (a) natural weathering condition, (b) QUV weathering condition

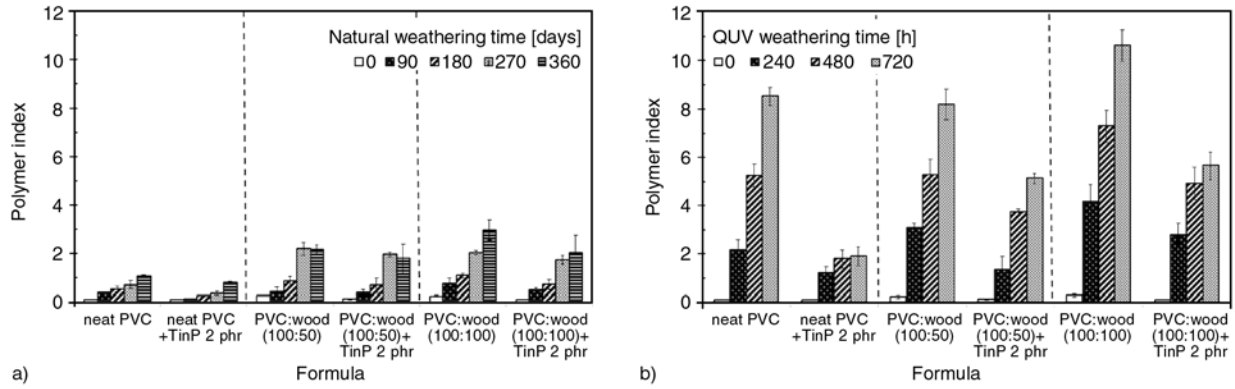

Figure 3. Polyene index in PVC and WPVC composites with and without Tinuvin P at 2 phr: (a) natural weathering condition, (b) QUV weathering condition

ation from sunlight under natural weathering conditions includes visible light, UV and infrared radiation, whereas the radiation from a UVB lamp under QUV weathering conditions contains only UV radiation (280–380 nm) [26]. In general, radiation in UV wavelengths is primarily responsible for PVC degradation [27]. In this case, UV radiation under natural weathering was much lower than that under QUV weathering. This was the reason for greater PVC degradation under QUV weathering as compared with natural weathering. The addition of Tinuvin P could stabilize PVC and WPVC composites, as seen by a decrease in polyene content; whereas the presence of wood appeared to accelerate the photodegradation of PVC under both natural and QUV weathering conditions. This was evidenced by an increase in polyene content with increasing wood content (from 50 to 100 phr). Figure 4 shows the carbonyl index as a function of weathering time of PVC and WPVC composites, with and without Tinuvin P, under different weathering conditions. The carbonyl index of both PVC and WPVC composites tended to increase with weathering time under both natural and QUV weathering conditions – except for WPVC under natural weathering, and WPVC with wood content of 100 phr under QUV weathering. The increase in the carbonyl index was probably caused by the oxidation reaction of PVC, in both PVC compound and WPVC composites [22, 28]. In WPVC composites, the carbonyl content could increase and then decrease at longer weathering times, this being associated with the photodegradation of lignin, which reversibly transformed the paraquinone to hydroquinone structures [12]. In addition to the cause of photodegradation in lignin, the decrease of carbonyl index for the WPVC specimen under natural weathering may be because the outer layer of the weathered specimens was washed away by rain. For the effect of weathering conditions, it was observed that the changes of carbonyl content under natural weathering was lower than those under QUV weathering, the explanation being similar to the polyene results. The addition of Tinuvin P at 2 phr was found to reduce the photooxidation of PVC and WPVC composites under both natural and QUV weathering conditions, as evidenced by a decrease in the carbonyl index as compared with the specimens without Tinuvin P.

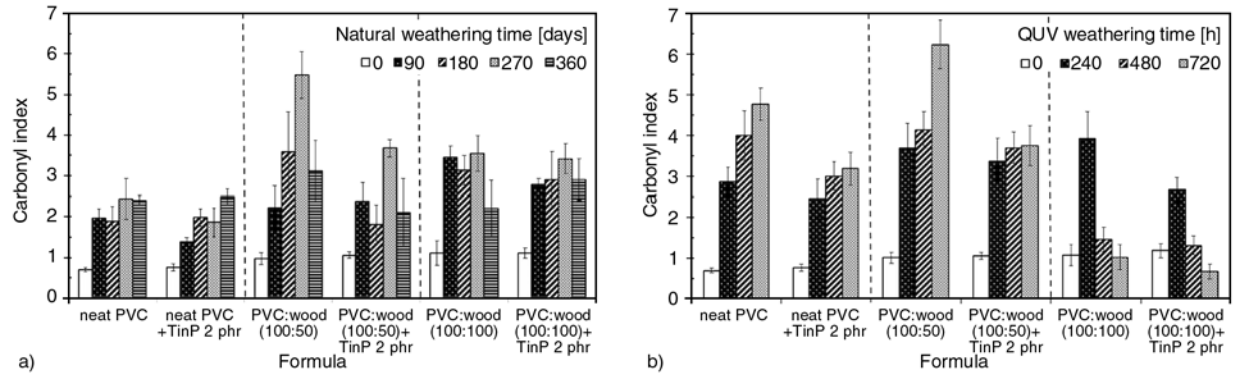

Figure 4. Carbonyl index in PVC and WPVC composites with and without Tinuvin P at 2 phr: (a) natural weathering condition, (b) QUV weathering condition

3.1.3. Discoloration

Figure 5 shows *YI* of PVC and WPVC composites with and without Tinuvin P under different weathering conditions. The effect of natural and QUV weathering conditions on *YI* of PVC and WPVC specimens was found to be different. For natural weathering, *YI* of PVC without Tinuvin P did not change with increasing weathering time, whereas that of PVC with Tinuvin P tended to decrease at 90 days after that did not change. The decrease of *YI* of PVC was probably because the coloration of PVC changed from yellow-white to light gray; this is known as the 'whitening effect', which is caused by visible radiation at wavelengths above 400 nm [29]. A similar whitening effect of PVC was also mentioned in the report by Real *et al*. [30]. The whitening effect of PVC was because the attack of oxygen on long polyenes molecules, resulting in the reduction in polyene length [31]. However, the unchanged *YI* values in case of PVC without Tinuvin P and PVC with Tinuvin P after weathering time of 90 days may be a result photoyellowing of PVC caused by UV radiation that compensated for the photobleaching of PVC by visible radiation. For WPVC composite under natural weathering, *YI* values increased at weathering time of 90 days and then decreased at 180 days and increased again at 270 days. The increase of *YI* at initial weathering time was probably affected by wash-away by rain, which led to a color change from brown to yellow shade. The decrease of *YI* at 180 days might be attributed to photobleaching of PVC as discussed for neat PVC. The increase of *YI* at 270 days was again caused by an obvious photoyellowing of PVC. For QUV weathering, *YI* of both PVC and WPVC composites increased with increasing QUV weathering time *except for* that of PVC adding Tinuvin P did not change after weathering time of 240 h. The increase of *YI* of both PVC and WPVC composites under QUV weathering resulted from the photoyellowing of PVC caused by intense UV radiation. The addition of Tinuvin P could diminish the change in *YI* under both natural and QUV weathering especially for PVC. This explanation of YI corresponds well to the visual photographs of PVC and WPVC composites under natural and QUV weathering conditions (Figure 6).

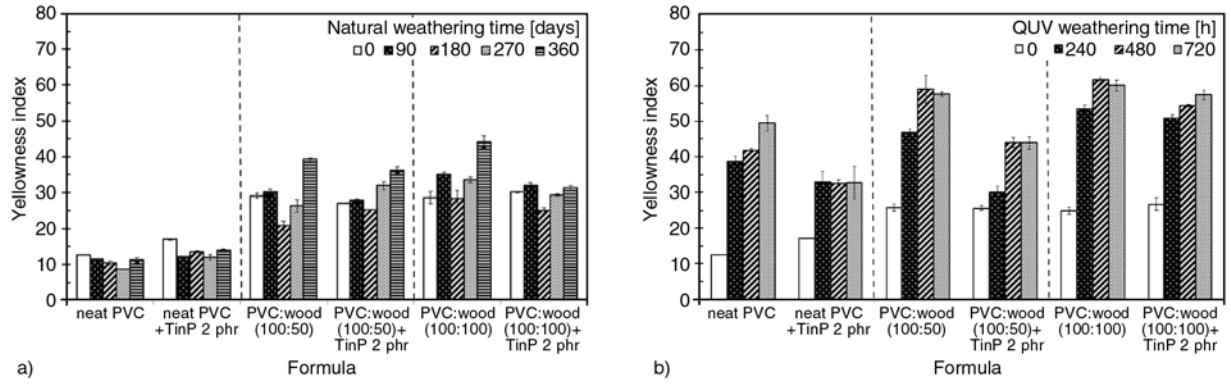

Figure 5. Effect of weathering condition on yellowness index in PVC and WPVC composites with and without Tinuvin P at 2 phr: (a) Natural weathering condition, (b) QUV weathering condition

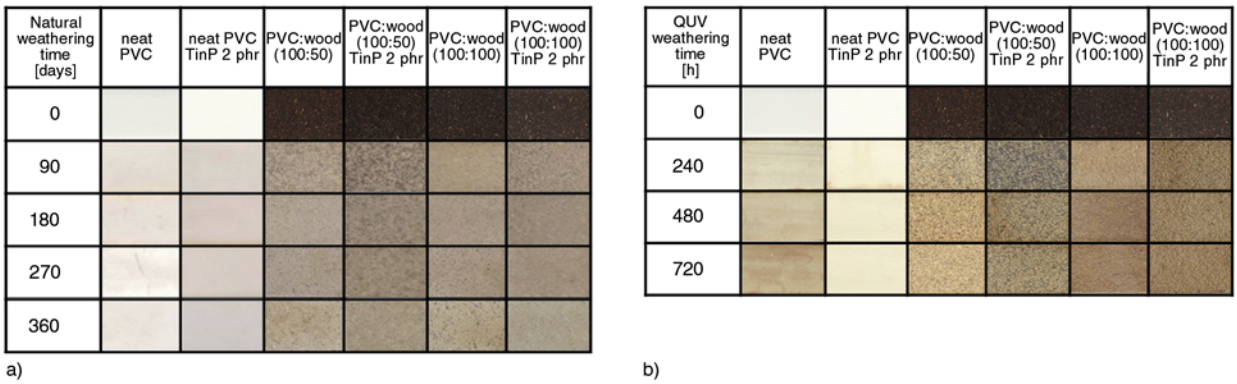

Figure 6. Digital photographs of PVC and WPVC composites with and without Tinuvin P at 2 phr: (a) natural weathering condition, (b) QUV weathering condition

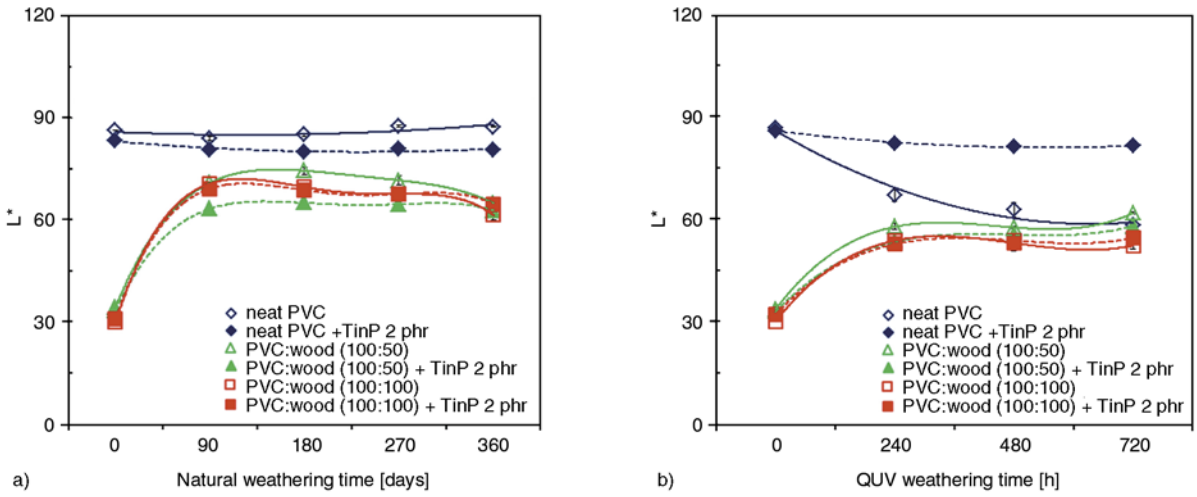

Figure 7. Effect of weathering condition on lightness in PVC and WPVC composites with and without Tinuvin P at 2 phr: (a) natural weathering condition, (b) QUV weathering condition

Figure 7 shows L^* as a function of weathering time for PVC and WPVC composites, with and without Tinuvin P at 2 phr, under natural and QUV weathering conditions. It was observed that L^* of PVC, with and without Tinuvin P, slightly changed with weathering time under natural and QUV weathering conditions – except for PVC without Tinuvin P under QUV weathering, in which L^* tended to decrease when subjected to UV weathering. This resulted from photoyellowing of PVC under severe UV conditions and without a UV stabilizer. L^* for WPVC composites, with and without Tinuvin P, and under both natural and QUV weathering, increased at initial weathering time and leveled off after 90 days and 240 h for natural and QUV weathering, respectively. The increases of L^* for WPVC composites indicated that the photobleaching effect of lignin was more predominant than the photodegradation effect of PVC in WPVC composites. L^* values for weathered WPVC composites under natural weathering conditions were higher than those of weathered WPVC composites under QUV weathering conditions. This was because natural rainwater removes some water-soluble extractives that impart color to wood flour [8]. In addition, chromophores in lignin enhance the absorption of visible light on the specimen surface [32]; this may lead to the whitening effect of the PVC in WPVC composites.

The total discoloration (ΔE) values under natural and QUV weathering conditions are given in Figure 8. It was found that the ΔE values of PVC under natural weathering were lower than those of PVC under accelerated weathering, whereas those of the WPVC composites exhibited the opposite trend. The lower ΔE values of PVC under natural weathering occurred because the degradation of PVC

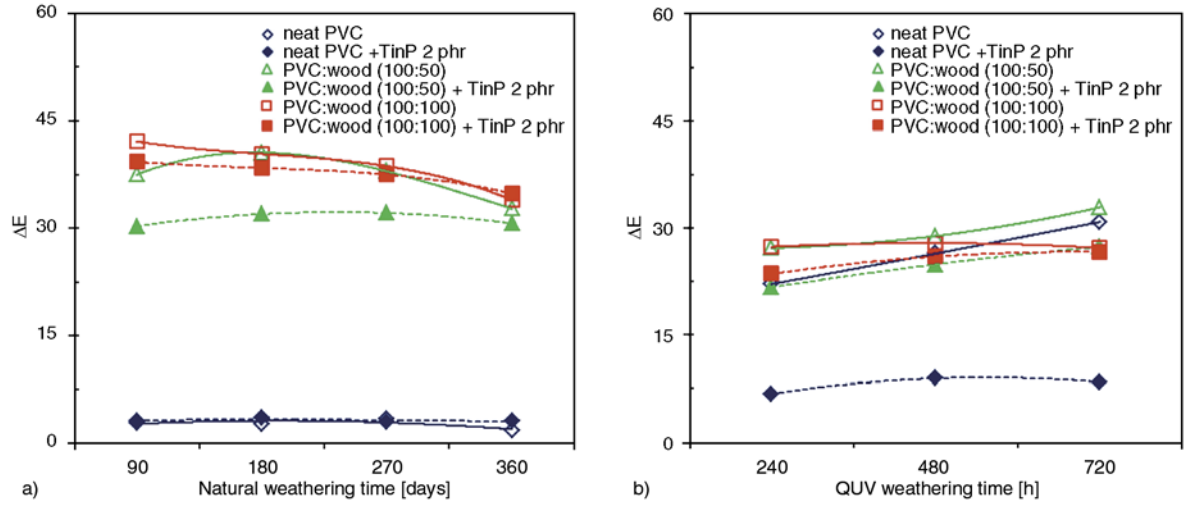

Figure 8. Effect of weathering condition on discoloration in PVC and WPVC composites with and without Tinuvin P at 2 phr: (a) natural weathering condition, (b) QUV weathering condition

caused by solar radiation was much lower than that caused by UV radiation in a QUV weatherometer. Higher ΔE values of WPVC composites under natural weathering might be attributed to the photobleaching of both PVC and wood flour during natural weathering tests, whereas those of WPVC composites under QUV weathering were affected by photobleaching of lignin and photoyellowing of PVC. The photobleaching of lignin in WPVC composites under QUV weathering was partially compensated by the photoyellowing of PVC during QUV weathering testing.

In regard to the effect of Tinuvin P, it was found that Tinuvin P could improve the photostability of both PVC and WPVC composites under both natural and QUV weathering conditions, as seen by a reduction of ΔE values with the addition of Tinuvin P. However, the differences in ΔE values of PVC with and without Tinuvin P under natural weathering conditions were not evident over the natural weathering time of 365 days due to the small amount of PVC degradation. In WPVC composites, the differences in ΔE values of WPVC composites with and without Tinuvin P under natural weathering conditions were greater than those under QUV weathering conditions; this was because Tinuvin P could stabilize PVC in WPVC composites under natural weathering, resulting in a reduction of photobleaching (less color fading) of the PVC. The addition of Tinuvin P under QUV weathering conditions also led to a reduction in photoyellowing of PVC in WPVC composites.

3.2. Photodegradation profiles at different depths from specimen surface

3.2.1. Structural changes

The profiles of polyene and carbonyl indices at various depths from the specimen surfaces for unweathered and QUV-weathered PVC and WPVC composites with and without 2 phr Tinuvin P are shown in Figures 9 and 10, respectively. The depth from the specimen surface was contingent on the abrasion number of sandpaper. The polyene and carbonyl contents of weathered PVC and WPVC composites

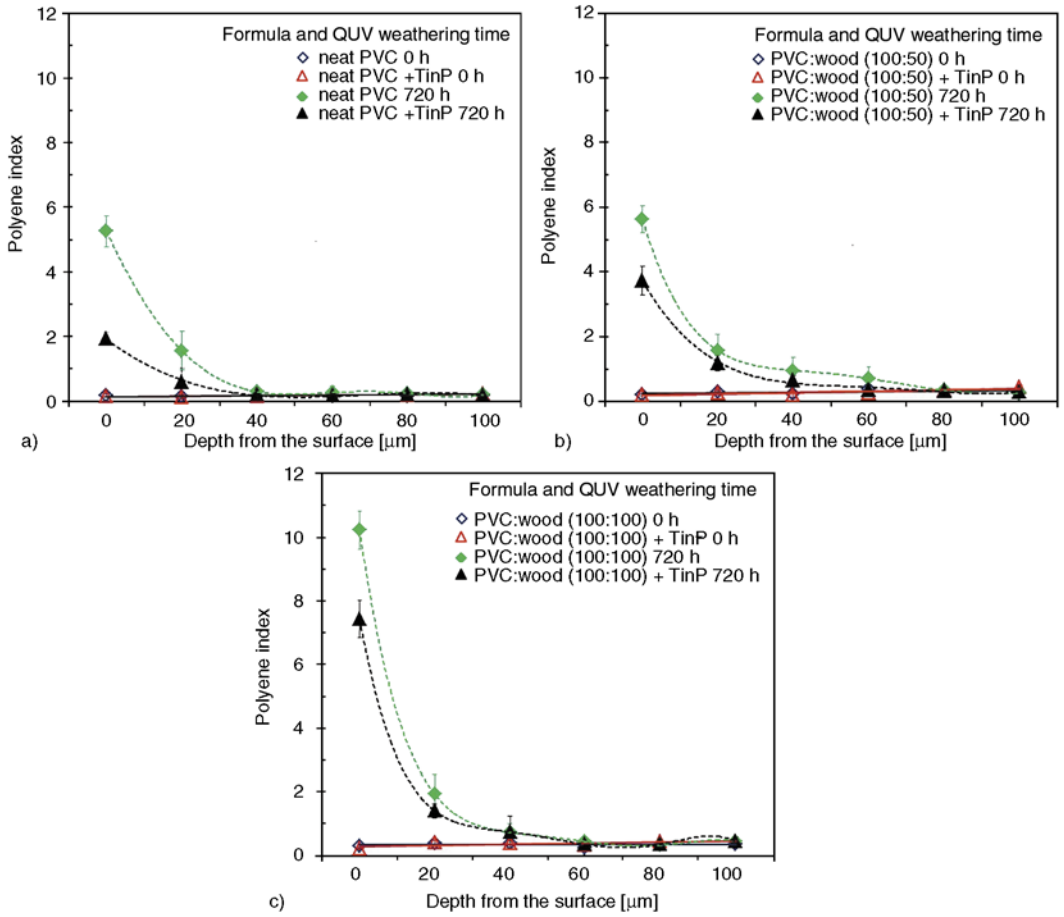

Figure 9. Polyene index as a function of depth from the surface for PVC and WPVC composites with and without 2 phr Tinuvin P at weathering times of 0 and 720 h: (a) neat PVC, (b) PVC with wood flour at 50 phr, (c) PVC with wood flour at 100 phr

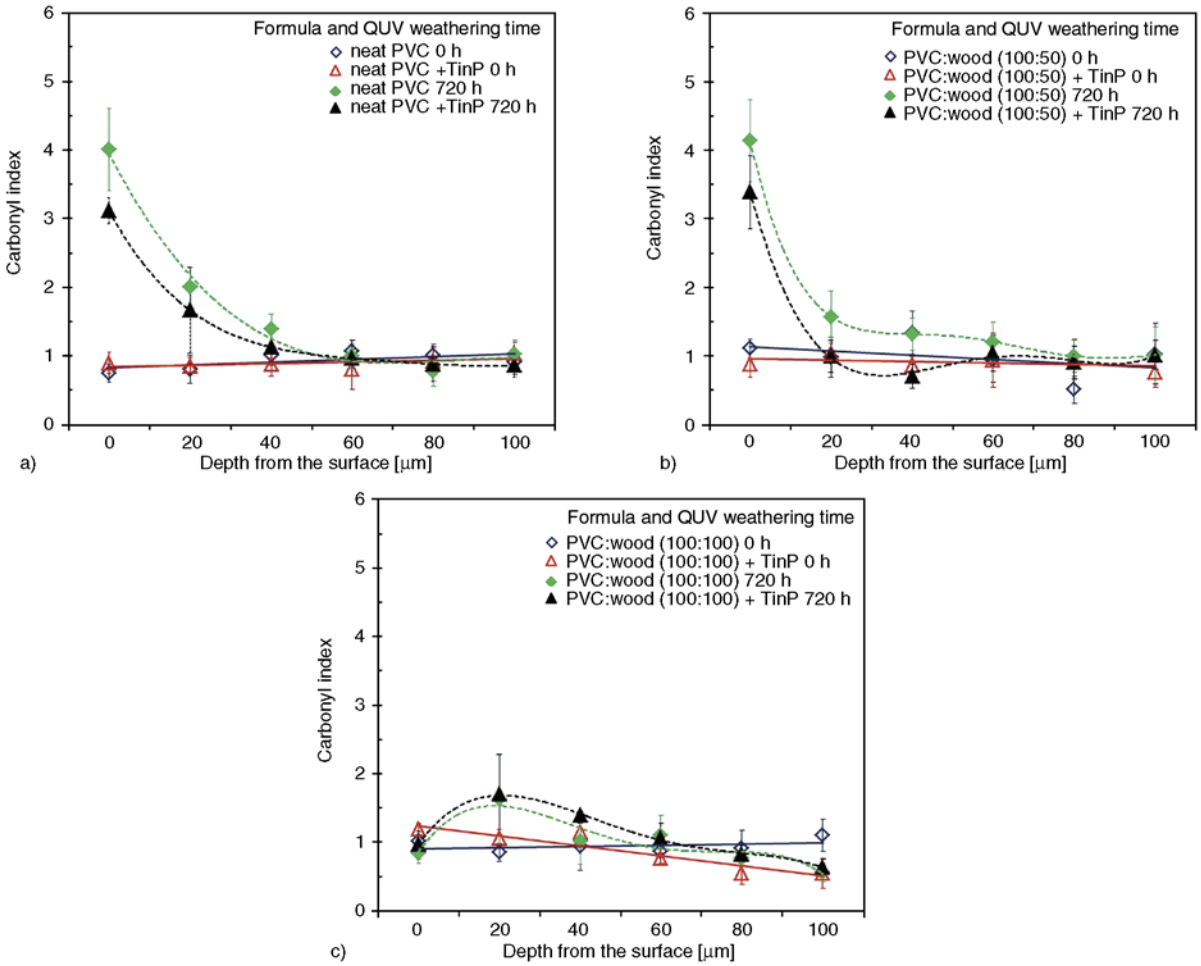

Figure 10. Carbonyl index as a function of depth from the surface for PVC and WPVC composites with and without 2 phr Tinuvin P at QUV weathering times of 0 and 720 h: (a) neat PVC, (b) PVC with wood flour at 50 phr, (c) PVC with wood flour at 100 phr

at 720 h significantly decreased with increasing depth from the specimen surface, except for carbonyl content in WPVC with wood content of 100 phr; whereas those of unweathered PVC and WPVC composites remained unchanged. The polyene and carbonyl contents for weathered specimens significantly decreased at a depth of 20 μm from the specimen surface, and then slightly decreased at further depths until stabilizing to an extent similar to those of unweathered PVC and WPVC composites, at 40–60 and 60–80 μm, respectively. This result indicated that UV radiation could not penetrate PVC and WPVC specimens at thicknesses beyond 60 and 80 μm, respectively, and also that the presence of wood enhanced the absorption of UV radiation onto the WPVC surface resulting from increasing depth of UV penetration. However, the contents of polyene and carbonyl decreased with increasing depth from the specimen surface, and were more pronounced when the wood content was increased. The addition of Tinuvin P could improve the photostability of PVC in neat PVC and WPVC composites, as evidenced by decreases in the polyene and carbonyl indices of weathered PVC and WPVC composites. The polyene content of WPVC composites resulted from the photodegradation of PVC in WPVC composites, whereas the carbonyl contents for WPVC composites may have been caused by photooxidation of both PVC and lignin in WPVC composites.

3.2.2. Discoloration

YI profiles at various depths from the specimen surfaces of unweathered and QUV- weathered PVC and WPVC composites, with and without Tinuvin P at 2 phr, are shown in Figure 11. *YI* values of unweathered PVC remained unchanged despite increasing depth from the specimen surface, whereas those of unweathered WPVC composites with wood content of 50 and 100 phr decreased at a depth up to 20 μm. The decreases in *YI* of WPVC composites at depths

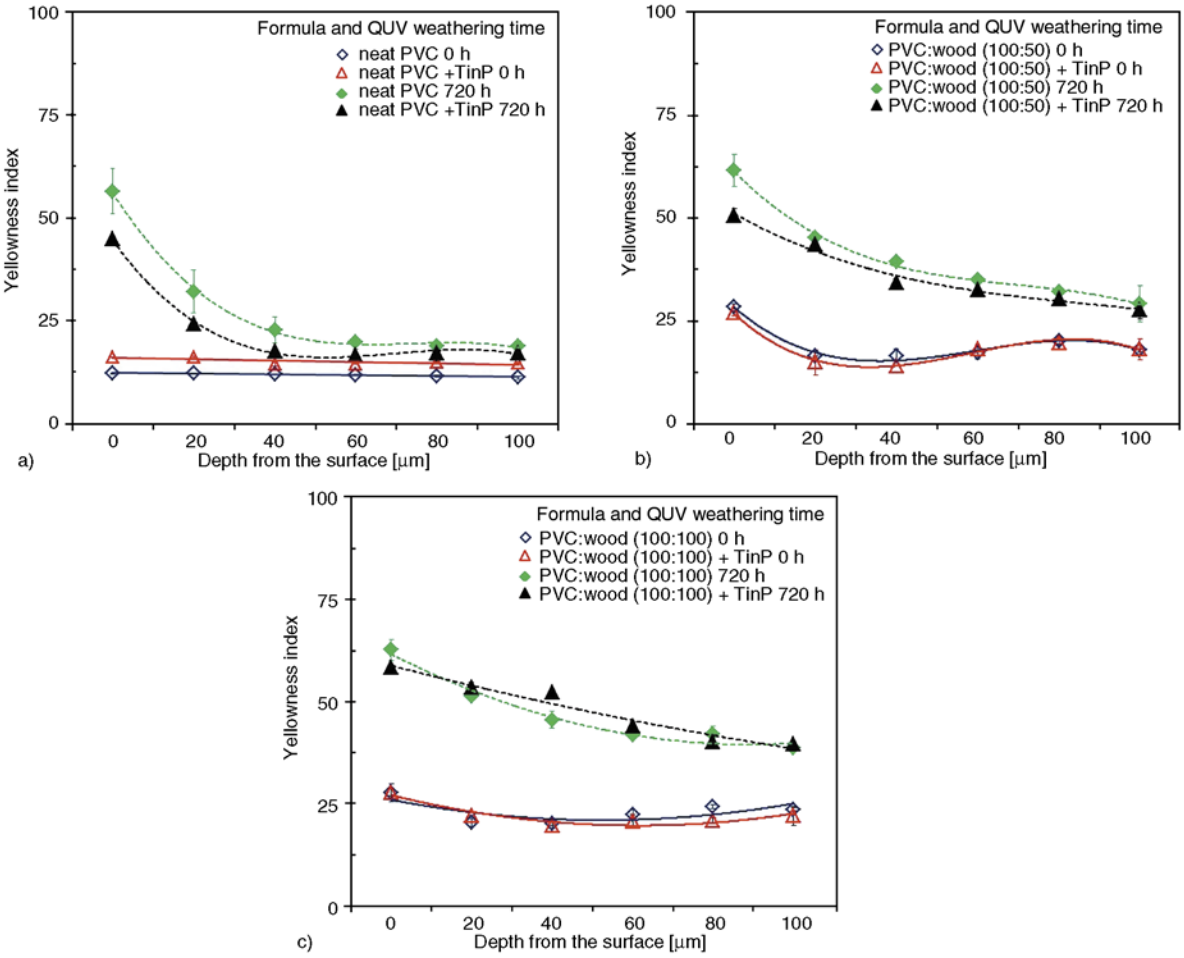

Figure 11. Yellowness index as a function of depth from the surface for PVC and WPVC composites with and without 2 phr Tinuvin P at QUV weathering times of 0 and 720 h: (a) neat PVC, (b) PVC with wood flour at 50 phr, (c) PVC with wood flour at 100 phr

between 0 and 20 μm were caused by a white scratch occurring as a result of physical abrasion from sandpaper during the experiment, as shown in Figure 12. For QUV-weathered specimens, the *YI* values for both PVC and WPVC composites decreased with increasing depth from the specimen surface, and then slightly changed at depths between 40 and 60 μm, respectively. However, the *YI* values of

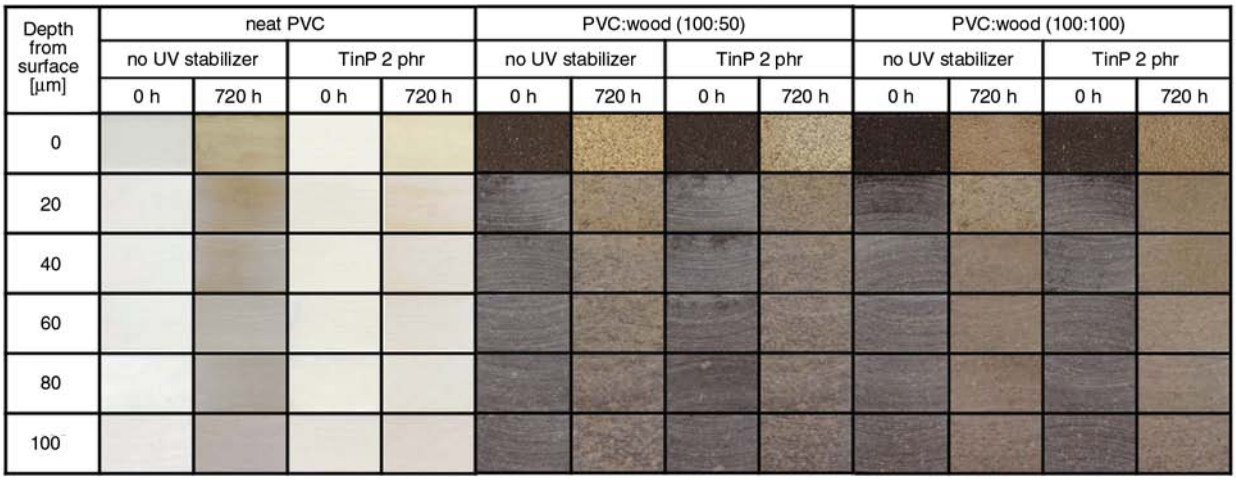

Figure 12. Digital photographs of PVC and WPVC composites with wood contents of 50 and 100 phr, at QUV weathering times of 0 and 720 h, at different depths from the specimen surface

weathered specimens after abrasion still differed from those of unweathered specimens, especially in the case of WPVC composites. The difference in *YI* of PVC might be attributed to the thermal degradation of PVC caused by heat during QUV testing; whereas the difference for WPVC composites was mainly due to moisture, which removed some water-soluble extractives that imparted color to the wood flour [8]. Visual photographs of unweathered and weathered PVC and WPVC composites at various depths from the specimen surface are shown in Figure 12. It was found that color changes of PVC and WPVC specimens at different depths from the specimen surface corresponded well to the *YI* results. The *L** profiles at different depths from the specimen surface for PVC and WPVC composites, with and without Tinuvin P and before and after QUV weathering of 720 h, are shown in Figure 13. Similar to the *YI* values in Figure 11, the *L** values of unweathered PVC remained unchanged with increasing depth from the specimen surface, whereas those of unweathered WPVC composites increased at initial depth and then remained unchanged beyond 40 μm depth. In the case of weathered specimens, the *L** values of weathered PVC and WPVC specimens after abrasion differed from those of unweathered specimens. The differences in *L** values can be explained in similar fashion, as given in Figures 11 and 12. The discolorations or total color changes (ΔE) in Figure 14 were determined from the differences of *L**, *a** and *b** values between unweathered and QUV-weathered specimens at identical depths from the specimen surface. It was found that the lower the ΔE values, the higher the depth from the specimen surface for both PVC and WPVC composites. The ΔE values of PVC and WPVC composites slightly changed beyond depths of 40 and 60 μm, respectively. Based on ΔE results, Tinuvin P appeared to be more effective in the stabilization of PVC as compared with WPVC composites.

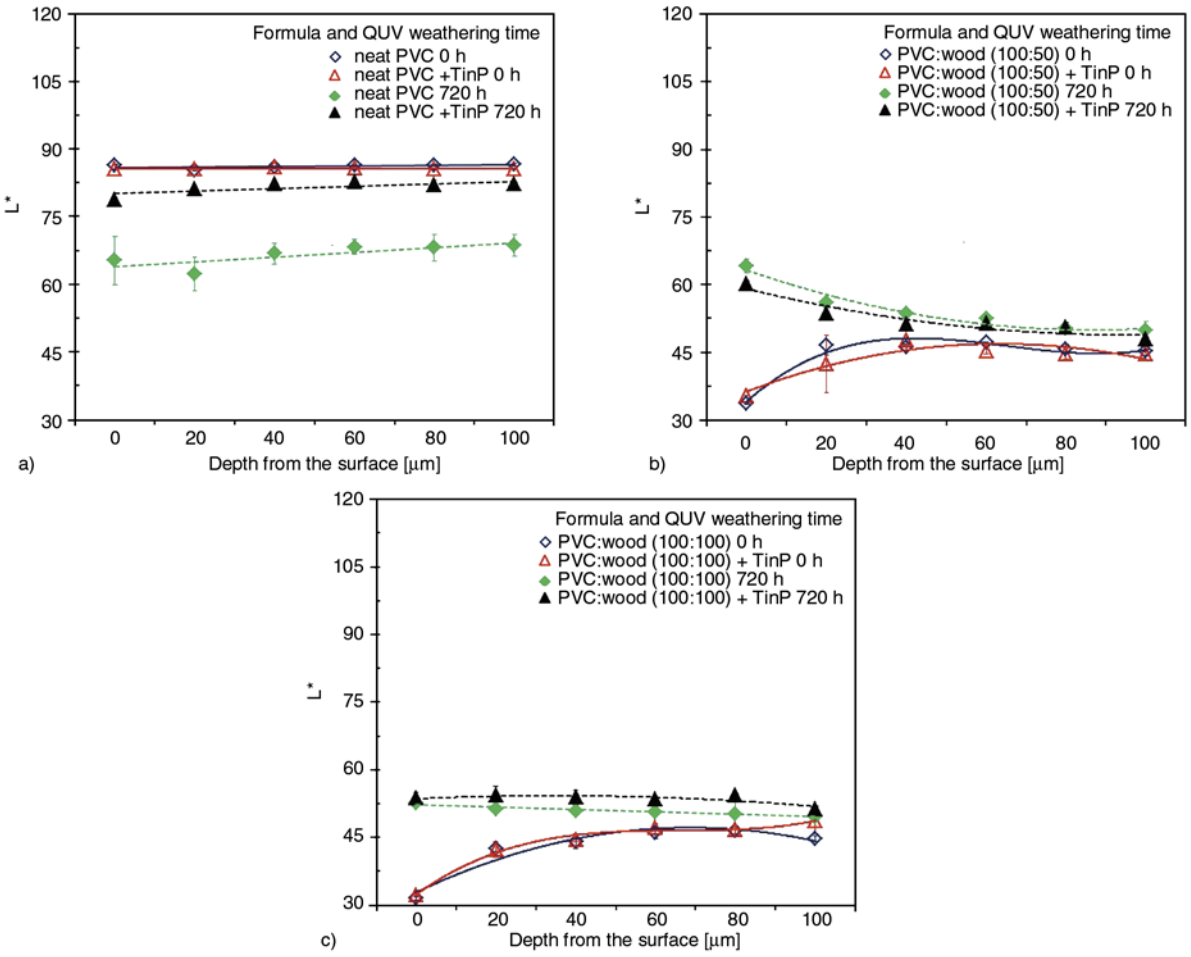

Figure 13. Lightness as a function of depth from the surface for PVC and WPVC composites with and without 2 phr Tinuvin P at QUV weathering times of 0 and 720 h: (a) neat PVC, (b) PVC with wood flour at 50 phr, (c) PVC with wood flour at 100 phr

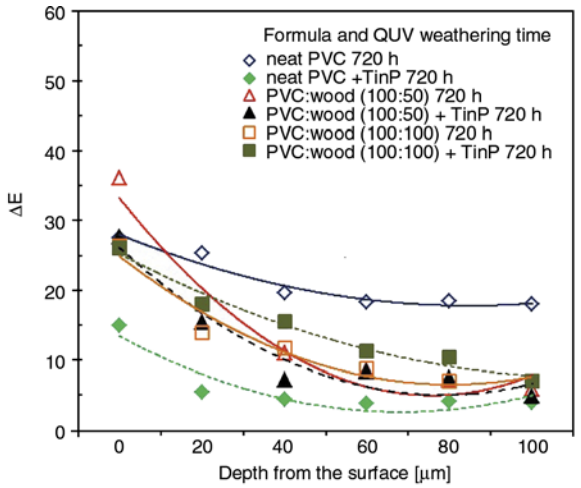

Figure 14. Discoloration levels of QUV-weathered PVC and WPVC composites, with and without 2 phr Tinuvin P, compared with unweathered specimens at various depths from the specimen surface

4. Conclusions

The effects of different UV weathering conditions (natural and accelerated) on the photodegradation behavior of PVC and wood/polyvinyl chloride (WPVC) composites were studied and the following conclusions were noted.

- Changes in the polyene and carbonyl sequences and contact angle of PVC and WPVC composites under accelerated UV weathering were more pronounced than those under natural weathering. The addition of Tinuvin P could stabilize PVC and WPVC composites, whereas the presence of wood appeared to accelerate the photodegradation of PVC under both natural and QUV weathering conditions.
- The yellowness index of PVC and WPVC composites under natural weathering decreased with weathering time, but the opposite was observed for accelerated weathering conditions due to photobleaching of PVC under visible radiation.
- The lightness of WPVC composites under natural weathering conditions significantly increased as compared with accelerated weathering conditions due to the photobleaching effect on both PVC and wood parts.
- The polyene and carbonyl sequences of PVC and WPVC composites were high at the sample surfaces and then reduced significantly with increasing depth from the specimen surface before leveling off at the depth of 60 μm for PVC and at 80 μm for WPVC composite. The differences in the specimen depths to the stabilizations of polyene and carbonyl sequences in PVC and WPVC samples implied that the presence of wood particles enhanced the absorption of UV radiation onto the WPVC composite samples.
- The colors of PVC and WPVC composites after abrasion were different from unweathered specimens due to thermal degradation of PVC and color fading of the wood.

Acknowledgements

The authors would like to express their thanks to the Thailand Research Fund (TRF) under Senior Scholar Grant (RTA 5580009) for financial support of this work. The authors also are grateful to the Office of the Higher Education Commission (OHEC) for additional funding under the National Research University (NRU) program.

References

[1] Deng Y., Tang Y.: Increasing load-bearing capacity of wood-plastic composites by sandwiching natural and glass fabrics. Journal of Reinforced Plastics and Composites, **29**, 3133–3148 (2010).
DOI: 10.1177/0731684410367535

[2] Fabiyi J. S., McDonald A. G.: Effect of wood species on property and weathering performance of wood plastic composites. Composites Part A: Applied Science and Manufacturing, **41**, 1434–1440 (2010).
DOI: 10.1016/j.compositesa.2010.06.004

[3] Stark N. M., Matuana L. M.: Surface chemistry changes of weathered HDPE/wood-flour composites studied by XPS and FTIR spectroscopy. Polymer Degradation and Stability, **86**, 1–9 (2004).
DOI: 10.1016/j.polymdegradstab.2003.11.002

[4] Stark N. M., Matuana L. M.: Surface chemistry and mechanical property changes of wood-flour/high-density-polyethylene composites after accelerated weathering. Journal of Applied Polymer Science, **94**, 2263–2273 (2004).
DOI: 10.1002/app.20996

[5] Matuana L. M., Kamdem D. P., Zhang J.: Photoaging and stabilization of rigid PVC/wood-fiber composites. Journal of Applied Polymer Science, **80**, 1943–1950 (2001).
DOI: 10.1002/app.1292

[6] Abu Bakar A., Hassan A., Mohd Yusof A. F.: Effect of accelerated weathering on the mechanical properties of oil palm empty fruit bunch filled UPVC composites. Iranian Polymer Journal, **14**, 627–635 (2005).

[7] Chaochanchaikul K., Sombatsompop N.: Stabilizations of molecular structures and mechanical properties of PVC and wood/PVC composites by Tinuvin and TiO_2 stabilizers. Polymer Engineering and Science, **51**, 1354–1365 (2011).
DOI: 10.1002/pen.21893

[8] Stark N. M., Matuana L. M.: Characterization of weathered wood–plastic composite surfaces using FTIR spectroscopy, contact angle, and XPS. Polymer Degradation and Stability, **92**, 1883–1890 (2007).
DOI: 10.1016/j.polymdegradstab.2007.06.017

[9] Wang W., Wang Q., Dang W.: Durability of a rice-hull–polyethylene composite property change after exposed to UV weathering. Journal of Reinforced Plastics and Composites, **28**, 1813–1822 (2009).
DOI: 10.1177/0731684408090574

[10] Stark N. M.: Effect of weathering cycle and manufacturing method on performance of wood flour and high-density polyethylene composites. Journal of Applied Polymer Science, **100**, 3131–3140 (2006).
DOI: 10.1002/app.23035

[11] Filson P., Dawson-Andoh B. E., Matuana L.: Colorimetric and vibrational spectroscopic characterization of weathered surfaces of wood and rigid polyvinyl chloride–wood flour composite lumber. Wood Science and Technology, **43**, 669–678 (2009).
DOI: 10.1007/s00226-009-0254-5

[12] Muasher M., Sain M.: The efficacy of photostabilizers on the color change of wood filled plastic composites. Polymer Degradation and Stability, **91**, 1156–1165 (2006).
DOI: 10.1016/j.polymdegradstab.2005.06.024

[13] Du H., Wang W., Wang Q., Zhang Z., Sui S., Zhang Y.: Effects of pigments on the UV degradation of wood-flour/HDPE composites. Journal of Applied Polymer Science, **118**, 1068–1076 (2010).
DOI: 10.1002/app.32430

[14] Zhang Z-M., Du H., Wang W-H., Wang Q-W.: Property changes of wood-fiber/HDPE composites colored by iron oxide pigments after accelerated UV weathering. Journal of Forestry Research, **21**, 59–62 (2010).
DOI: 10.1007/s11676-010-0009-z

[15] Bledzki A. K., Letman M., Viksne A., Rence L.: A comparison of compounding processes and wood type for wood fibre–PP composites. Composites Part A: Applied Science and Manufacturing, **36**, 789–797 (2005).
DOI: 10.1016/j.compositesa.2004.10.029

[16] Bengtsson M., Stark N. M., Oksman K.: Durability and mechanical properties of silane cross-linked wood thermoplastic composites. Composites Science and Technology, **67**, 2728–2738 (2007).
DOI: 10.1016/j.compscitech.2007.02.006

[17] Bledzki A. K., Letman-Sakiewicz M., Murr M.: Influence of static and cyclic climate condition on bending properties of wood plastic composites (WPC). Express Polymer Letters, **4**, 364–372 (2010).
DOI: 10.3144/expresspolymlett.2010.46

[18] Wang W. H., Wang Q. W., Xiao H., Morrell J. J.: Effects of moisture and freeze-thaw cycling on the quality of rice-hull-PE composite. Pigment and Resin Technology, **36**, 344–349 (2007).
DOI: 10.1108/03699420710831764

[19] Schirp A., Wolcott M. P.: Influence of fungal decay and moisture absorption on mechanical properties of extruded wood-plastic composites. Wood and Fiber Science, **37**, 643–652 (2005).

[20] Fabiyi J. S., McDonald A. G., Morrell J. J., Freitag C.: Effects of wood species on durability and chemical changes of fungal decayed wood plastic composites. Composites Part A: Applied Science and Manufacturing, **42**, 501–510 (2011).
DOI: 10.1016/j.compositesa.2011.01.009

[21] Abu-Sharkh B. F., Hamid H.: Degradation study of date palm fibre/polypropylene composites in natural and artificial weathering: Mechanical and thermal analysis. Polymer Degradation and Stability, **85**, 967–973 (2004).
DOI: 10.1016/j.polymdegradstab.2003.10.022

[22] Fabiyi J. S., McDonald A. G.: Physical morphology and quantitative characterization of chemical changes of weathered PVC/pine composites. Journal of Polymers and the Environment, **18**, 57–64 (2010).
DOI: 10.1007/s10924-009-0152-9

[23] Pattamasattayasonthi N., Chaochanchaikul K., Rosarpitak V., Sombatsompop N.: Effects of UV weathering and a CeO_2-based coating layer on the mechanical and structural changes of wood/PVC composites. Journal of Vinyl and Additive Technology, **17**, 9–16 (2011).
DOI: 10.1002/vnl.20246

[24] Sombatsompop N., Taptim K., Chaochanchaikul K., Thongpin C., Rosarpitak V.: Improvement of structural and thermal stabilities of PVC and Wood/PVC composite by Zn and Pb stearates, and zeolite. Journal of Macromolecular Science Part A: Pure and Applied Chemistry, **45**, 534–541 (2008).
DOI: 10.1080/10601320802100572

[25] Xiang X., Chen S., Zhang J., Chai R.: Effect of the combination of a benzophenone-type ultraviolet absorber with thermal stabilizers on the photodegradation of poly(vinyl chloride). Journal of Vinyl and Additive Technology, **16**, 23–32 (2010).
DOI: 10.1002/vnl.20222

[26] ASTM G154: Standard practice for operating fluorescent light apparatus for UV exposure of nonmetallic materials (2006).

[27] Rabek J. F.: Photostabilization of polymers: Principles and applications. Elsevier, New York (1990).

[28] Anton-Prinet C., Dubois J., Mur G., Gay M., Audouin L., Verdu J.: Photoageing of rigid PVC–II. Degradation thickness profiles. Polymer Degradation and Stability, **60**, 275–281 (1998).
DOI: 10.1016/S0141-3910(97)00077-3

[29] Andrady A. L., Hamid S. H., Hu X., Torikai A.: Effects of increased solar ultraviolet radiation on materials. Journal of Photochemistry and Photobiology B: Biology, **46**, 96–103 (1998).
DOI: 10.1016/S1011-1344(98)00188-2

[30] Real L. P., Gardette J-L., Rocha A. P.: Artificial simulated and natural weathering of poly(vinyl chloride) for outdoor applications: The influence of water in the changes of properties. Polymer Degradation and Stability, **88**, 357–362 (2005).
DOI: 10.1016/j.polymdegradstab.2004.11.012

[31] Rabek J. F., Rånby B., Östensson B., Flodin P.: Oxidation of polyene structures in poly(vinyl chloride) by molecular oxygen and singlet oxygen. Journal of Applied Polymer Science, **24**, 2407–2413 (1979).
DOI: 10.1002/app.1979.070241209

[32] Chaochanchaikul K., Jayaraman K., Rosarpitak V., Sombatsompop N.: Influence of lignin content on photodegradation in wood/HDPE composites under UV weathering. BioResources, **7**, 38–55 (2012).

eXPRESS Polymer Letters Vol.7, No.2 (2013) 161–171
Available online at www.expresspolymlett.com
DOI: 10.3144/expresspolymlett.2013.15

Synthesis and characterization of phenylethynylcarbonyl terminated novel thermosetting imide compound

H. Kimura[1*], *K. Ohtsuka*[1], *A. Matsumoto*[1], *H. Fukuoka*[2], *Y. Oishi*[3]

[1]Thermosetting Resin Lab., Organic Materials Research Division, Osaka Municipal Technical Research Institute, 1-6-50 Morinomiya, Joto-ku, 536-8553 Osaka, Japan
[2]Research & Development Division, Mitsubishi Gas Chemical Company, Inc., 2-5-2 Marunouchi, Chiyoda-ku, 100-8324 Tokyo, Japan
[3]Department of Chemistry and Bioengineering, Faculty of Engineering, Iwate University, 3-18-8 Ueda, Morioka, 020-8550 Iwate, Japan

Received 17 July 2012; accepted in revised form 22 September 2012

Abstract. Phenylethynyl terminated novel imide compound based on 1,3-bis(3-aminophenoxy)benzene (APB) and phenylethynyl trimellitic anhydride (PETA) were prepared. The curing behavior of phenylethynyl terminated imide compound was investigated by differential scanning calorimetry and Fourier transform infrared spectrometry. The curing reaction of phenylethynylcarbonyl end group completed at 220°C, and proceeded much faster than that of phenylethynyl end group. Glass transition temperature of the thermosetting resin from phenylethynylcarbonyl terminated novel imide compound determined by dynamic mechanical analysis was almost the same as that of *o*-cresolnovolac type epoxy resin. In addition, the thermosetting resin from phenylethynylcarbonyl terminated novel imide compound exhibited excellent thermal and dimensional stabilities. These excellent properties of these phenylethynyl terminated imide compound might be due to the incorporation of alkene group or aromatic ring substitutes in the backbones, which might enhance the chain interaction (molecular packing) and reduce the molecular chain mobility.

Keywords: *thermosetting resins, imide, phenylethynylcarbonyl*

1. Introduction

Aromatic polyimides are well known as high-performance polymer materials widely used in aerospace and electronics fields. They have some excellent properties such as high thermal stability, good mechanical properties and superior chemical resistance. However, their rigid polymer backbones and the strong chain interactions result in poor solubility and high softening or melting temperature for most of aromatic polyimides, which limit their use for commercial purposes.

Therefore, for molding compounds or matrix resins of fiber reinforced plastics, many addition-type (thermosetting) polyimides (imide oligomers terminated with reactive groups) have been developed [1–2]. These imide oligomers terminated with reactive groups could be thermally cured at high temperatures providing good processibility. Namely, due to their oligomeric nature, these materials exhibit excellent processability during fabrication of neat resin moldings and composites under pressure.

The recently best known reactive group among the addition-type polyimides is the phenylethynyl group. The phenylethynyl reactive group has high-cure temperature and a good processing window can be obtained. Upon thermal cure for ~1 h at 350–370°C, the phenylethynyl group undergoes a complex reaction involving chain extension, branching and

*Corresponding author, e-mail: kimura@omtri.or.jp

crosslinking to afford a pseudo three dimensional network. The networks exhibit high thermal stability, good mechanical properties and superior chemical resistance as well as aromatic polyimides [1].

A system based on this, namely, phenylethynyl-terminated imide, PETI-5 shown in Figure 1, has been formulated by the group at the NASA Langley Research Center. The material is a random copolymer prepared from 3,4′-oxydianiline, 1,3-bis(3-aminophenoxy)benzene and 3,3′,4,4′-biphenyltetracarboxylic dianhydride and end-capped with 4-phenylethynylphthalic anhydride at a calculated number average molecular weight (M_n) of 5000 g/mol. This material has displayed good processability and excellent mechanical properties in adhesive and composite forms. The cured PETI-5 has high fracture toughness, high thermo-oxidative stability, and good processability. However, the cured resin has a relatively low T_g of 270°C because flexible diamines are introduced for the purpose of high melt fluidity [3].

Yokota and coworkers [4-5] have developed an amorphous, asymmetric, and addition-type polyimide 'TriA-PI' shown in Figure 2. TriA-PI is prepared from asymmetric monomer, 2,3,3′,4′-biphenyltetracarboxylic dianhydride (a-BPDA), 4,4′-diaminodiphenyl ether (4,4′-ODA), and PEPA. Both the imide oligomer and cured polymer have irregular and asymmetric structures that are derived from a-BPDA, resulting in a low melting temperature and a low melt viscosity for the imide oligomer, and a high T_g value of 343°C for the cured polymer. Along with good processability, TriA-PI has high heat resistance, high thermooxidative stability, and good fracture toughness [3].

However, phenylethynyl terminated imide oligomers require high temperature (about 350–370°C) treatment to completely remove solvent and to convert the oligomeric precursor into cured polyimide, which limit their use for commercial all purposes except for the special use of aerospace field.

In this report, we synthesized phenylethynylcarbonyl terminated imide compound and investigated the curing behavior and the properties of the cured thermosetting resin.

The phenylethynylcarbonyl group may be more flexible than the phenylethynyl group because of the adjacent carbonyl group. And, due to the electron withdrawing groups, such as ketone on acetylene bond, phenylethynylcarbonyl group terminated imide compound might enhance the rate of cure. In this way, by the introduction of the carbonyl group adjacent of phenylethynyl group, the high cure temperature (about 350–370°C) of phenylethynyl terminated polyimide could be lowered.

In this study, we investigated the synthesis and characterization of phenylethynylcarbonyl terminated novel thermosetting imide compound. The novel phenylethynylcarbonyl-terminated imide compound has only two imide groups in the molecular structure, and so differs from polyimide resins. And the curing condition of the new imide compound may be completely different from polyimide. The properties of thermosetting resin are influenced by the curing condition, especially maximum curing temperature. Therefore, we think this novel compound as the new thermosetting resin, and compare the new imide compound to an epoxy resin which has almost similar curing condition. We selected higher performance o-cresol novolac type epoxy

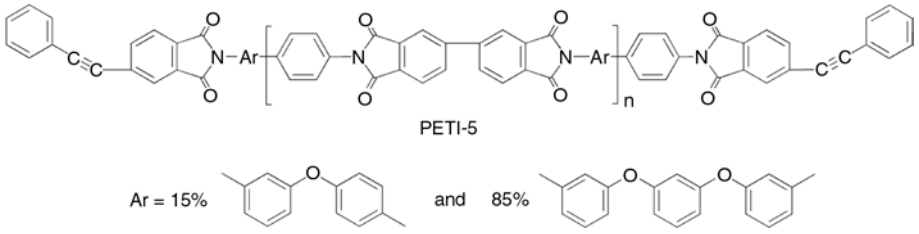

Figure 1. Chemical structure of PETI-5

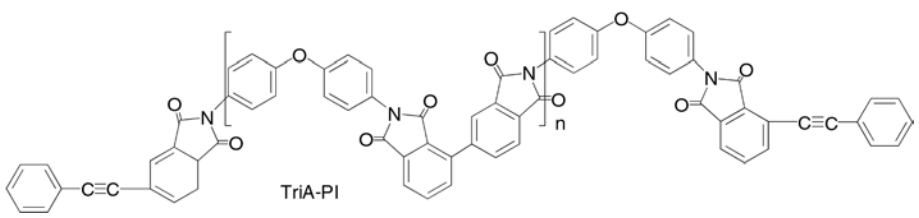

Figure 2. Chemical structure of TriA-PI

resin which was used as encapsulating material for semiconductors of epoxy resins.

2. Experimental

2.1. Materials

1,3-bis(3-aminophenoxy)benzene (APB) was supplied by Mitsubishi Gas Chemical Company, Inc. (Tokyo, Japan). Phenylethynyl trimellitic anhydride (PETA) was supplied by Nexam chemical AB (Lund, Sweden). Pyridine, acetic anhydride and N-methyl-2-pyrrolidone were purchased from Nacalai Tesuque, Inc. (Kyoto, Japan). All chemicals were used without further purification. The chemical structures of APB and PETA are shown in Figure 3. *O*-cresol novolac type epoxy resin (EP, epoxy equivalent, 211) and 2-ethyl-4-methylimidazole as a curing accelerator were supplied by Mitsubishi Chemical Corp. (Tokyo, Japan). Phenol novolac (phenolic hydroxyl equivalent, 94) as a curing agent was supplied by Asahi Organic Chemicals Industry Co. Ltd. (Tokyo, Japan).

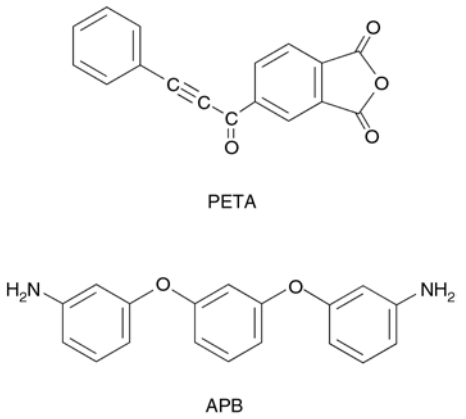

Figure 3. Chemical structures of PETA and APB

2.2. Synthesis of phenylethynylcarbonyl terminated imide compound

The synthesis of phenylethynylcarbonyl terminated imide compound was conducted by chemical imidization method [6–7]. 1,3-bis(3-aminophenoxy) benzene APB (5.84 g, 20 mmol) and N-methyl-2-pyrrolidone (NMP, 40 ml) were placed in a three necked flask, equipped with a magnetic stirrer and calcium chloride drying tube. The glass flask was dried or removed from a hot oven to prevent water from interfering with the reaction. Phenylethynyl trimellitic anhydride PETA (11.06 g, 40 mmol) was added to the solution. The reaction was allowed to stir for 24 h at room temperature under air. Subsequently, pyridine (6.32 g, 80 mmol) and acetic anhydride (8.16 g, 80 mmol) was added slowly to the solution; the solution was stirred for 30 min at room temperature under air. The solution was then poured into water. The product was washed with water, filtered, and then dried at 60°C in vacuo. The scheme for synthesis of phenylethynylcarbonyl terminated imide compound (PECI-APB) is shown in Figure 4. The structure of the obtained compound (PECI-APB) was analyzed by ^{1}H-NMR measurement. ^{1}H-NMR measurement was carried out on Japan Electron Company (Tokyo, Japan) JMN-GSX-270 instrument operating at 270 MHz. Deuterated dimethyl sulfoxide was used as a solvent and tetramethylsilane was used as an internal standard.

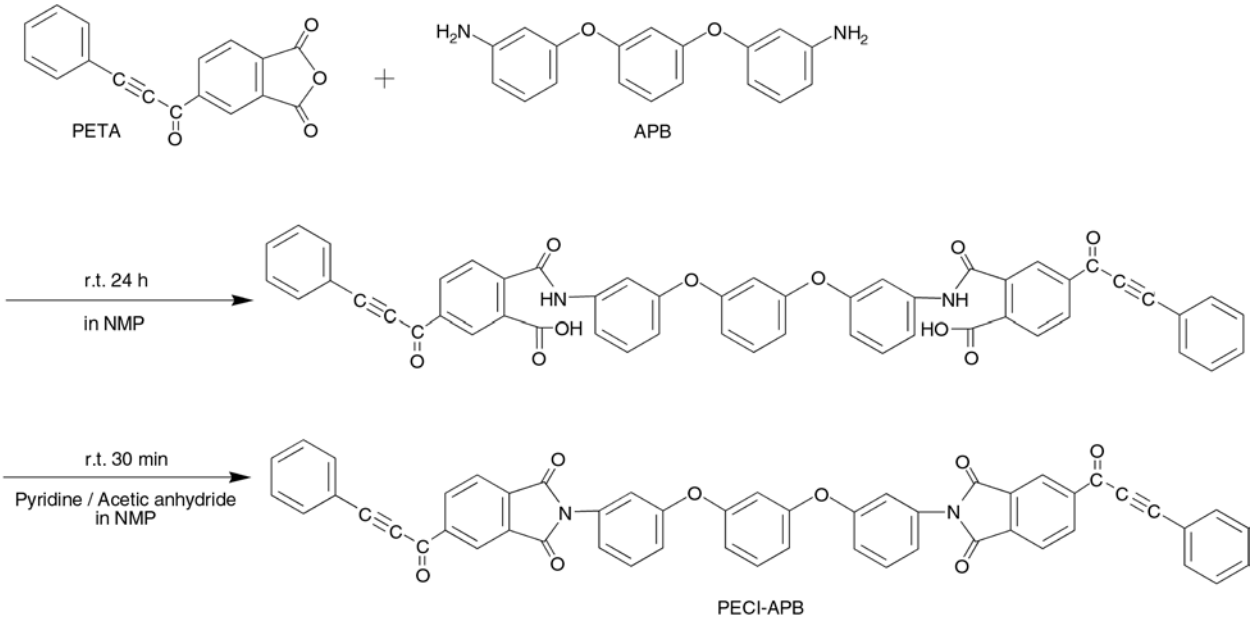

Figure 4. Synthesis of phenylethynylcarbonyl terminated imide compound (PECI-APB)

^{1}H-NMR (PECI-APB, DMSO-d6, δ); 8.60–8.62 ppm (d, 2H, CH), 8.37 ppm (s, 2H, CH), 8.08–8.12 ppm (d, 2H, CH), 7.82–7.88 ppm (d, 4H, CH), 7.10–7.70 ppm (m, 15H, CH), 6.85–6.95 ppm (d, 2H, CH), 6.65–6.82 ppm (s, 1H, CH).

2.3. Curing condition of phenylethynylcarbonyl terminated imide compound

Phenylethynylcarbonyl terminated imide compound was cured in a mold using a programmed oven cycle. The curing condition was determined as 200°C/3 h + 220°C/3 h from the results of differential scanning calorimetry (DSC). The molded sample contained a small amount of voids, but the sample was cut to use the void-free sample for each measurement.

To compare the characteristics of phenylethynylcarbonyl terminated imide compound with other resins, *o*-cresol novolac type epoxy resin, which was used as encapsulating material for semiconductors, was cured in a mold using a programmed oven cycle. Epoxy resin compositions were prepared by uniformly melt mixing the components (*o*-cresol novolac epoxy resin 211 parts per hundred parts [phr], phenol novolac 94 phr, 2-ethyl-4-methylimidazole 2.1 phr) in a hot twin-roll, followed by cooling and grinding. The curing reaction of epoxy resin was carried out under the same condition as that of the phenylethynylcarbonyl terminated imide compound (200°C/3 h + 220°C/3 h) to evaluate the characteristics.

2.4. Characterization of phenylethynylcarbonyl terminated imide compound and the cured thermosetting resin

The structures of phenylethynylcarbonyl terminated imide compound and the cured thermosetting resin were analyzed by Fourier Transform Infrared Spectrophotometer (FT-IR). FT-IR measurement was carried out on Nicolet Impact 420 instrument (Thermo Fisher Scientific K.K, Yokohama, Japan). The spectral range was 4000–400 cm^{-1}. One hundred twenty-eight scans were averaged at a resolution of 4 cm^{-1}. Samples were prepared as KBr pellets.

FT-IR (PECI-APB, KBr); 1780 cm^{-1} (s, imide C=O asymmetric stretching), 1725 cm^{-1} (vs, imide C=O symmetric stretching), 2213 cm^{-1} (m, phenylethynyl stretching), 1600 cm^{-1} (s, aromatic C=C), 1370 cm^{-1} (s, imide C–N stretching), 739 cm^{-1} (s, imide C–N bending).

Differential scanning calorimetry (DSC) was applied to evaluate the cure behavior of phenylethynylcarbonyl terminated imide compound. DSC was measured with heating rate of 10°C/min under N_2 atmosphere on a Seiko Instruments Co., Ltd., (Chiba, Japan) STI EXSTAR 6000.

The properties of the cured thermosetting resin were characterized by dynamic mechanical analysis (DMA), thermal gravimetric analysis (TGA) and thermal mechanical analysis (TMA).

Dynamic mechanical analysis (DMA) was applied to evaluate the glass transition temperature (T_g). Dynamic mechanical analysis was measured by a three points bending method at 1 Hz, amplitude of 10 μm, with a heating rate of 2°C/min on a Seiko Instruments Co., Ltd (Chiba, Japan). DMS-110 Dynamic Mechanical Analysis Spectrometer. The test specimen consists of 50 mm long and 15 mm wide with a thickness of 2–3 mm. The peak temperature of tan δ by dynamic mechanical analysis was considered as T_g [8].

Thermal gravimetric analysis (TGA) was applied to evaluate the thermal stability. TGA was measured with heating rate of 10°C/min under N_2 atmosphere on a Seiko Instruments Co., Ltd. (Chiba, Japan) TGA 5200 Thermal Gravimetric Analyzer. The values of 5% mass loss temperature were evaluated.

Thermal mechanical analysis (TMA) was applied to evaluate the dimensional stability. TMA was measured with heating rate of 2°C/min under N_2 atmosphere on a Seiko Instruments Co., Ltd. (Chiba, Japan) TMA/SS 6100 Thermal Mechanical Analyzer. The oblong specimen measuring 3–4 mm in length and usually 10–15 mm in height was subjected to a loading 5 g force via a vertically adjustable quartz glass probe. The value of coefficient of thermal expansion (CTE, 40–60°C) was evaluated.

3. Results and discussion

3.1. Synthesis of phenylethynylcarbonyl terminated imide compound

The synthesis of phenylethynylcarbonyl terminated imide compound was conducted by chemical imidization method [6–7]. The formation of poly (amic acid)s is achieved via the reaction of a dianhydride and a diamine in a dry aprotic solvent at room temperature. The reaction mechanism involves

the nucleophilic attack of the amino group on the carbonyl carbon of the anhydride group, followed by the opening of the anhydride ring to form an amic acid group. The second pathway of cyclodehydration of amic acid to imide involves the use of a chemical dehydrating agent to promote ring closure reactions, which is effective for either soluble or insoluble polyimides. Commonly used reagents include acid anhydrides in dipolar aprotic solvents or in the presence of tertiary amines. Among the dehydrating agent used were acetic anhydride, benzoic anhydride, as well as others. The amine catalysts used include pyridine, N-methylmorpholine, trialkylamines and others. For this work, acetic anhydride and pyridine were used, although other chemical combinations may be equally amenable to this system.

In several instances, the product yield was found to be about 90%. And it was found that phenylethynylcarbonyl terminated imide compound could be easily dissolved in DMSO, to afford a homogeneous solution. But the imide compound was insoluble in other solvents such as acetone, methanol, chloroform, ethyl acetate and tetrahydrofuran.

^{1}H-NMR spectrum of raw materials (PETA and APB) and the product (phenylethynylcarbonyl terminated imide compound, PECI-APB) is shown in Figure 5. As a result, a peak (z, 4.78 ppm) assigned to the primary amine groups of APB were not detected. All peaks assigned to the aromatic ring proton were detected. The structure of phenylethynylcarbonyl terminated imide compound (PECI-APB) was confirmed by NMR. The small peaks at 2.1, 2.3 and 2.7 ppm come from acetic anhydride and N-metyl-2-pyrrolidone used as the raw material or reaction solvent. And the peak at 2.2 ppm comes from acetic acid arising from acetic anhydride. The peak at 3.4 ppm comes from water used for purification after synthesis of phenylethynylcarbonyl terminated imide compound. There was not significant indication of side reaction in the NMR, and the purity of PECI-APB was almost 100% from ^{1}H-NMR.

The FT-IR spectra of raw materials (PETA and APB), phenylethynylcarbonyl terminated amic acid and phenylethynylcarbonyl terminated imide compound (PECI-APB) are shown in Figure 6.

In Figure 6c, it can be seen that the amic acid compound exhibited the characteristic absorption near 2900–3200 cm^{-1}, which was attributed to COO–H and HN–H. The absorption at ca. 1710 cm^{-1}, which was related to amic acid C=O (COOH) was observed.

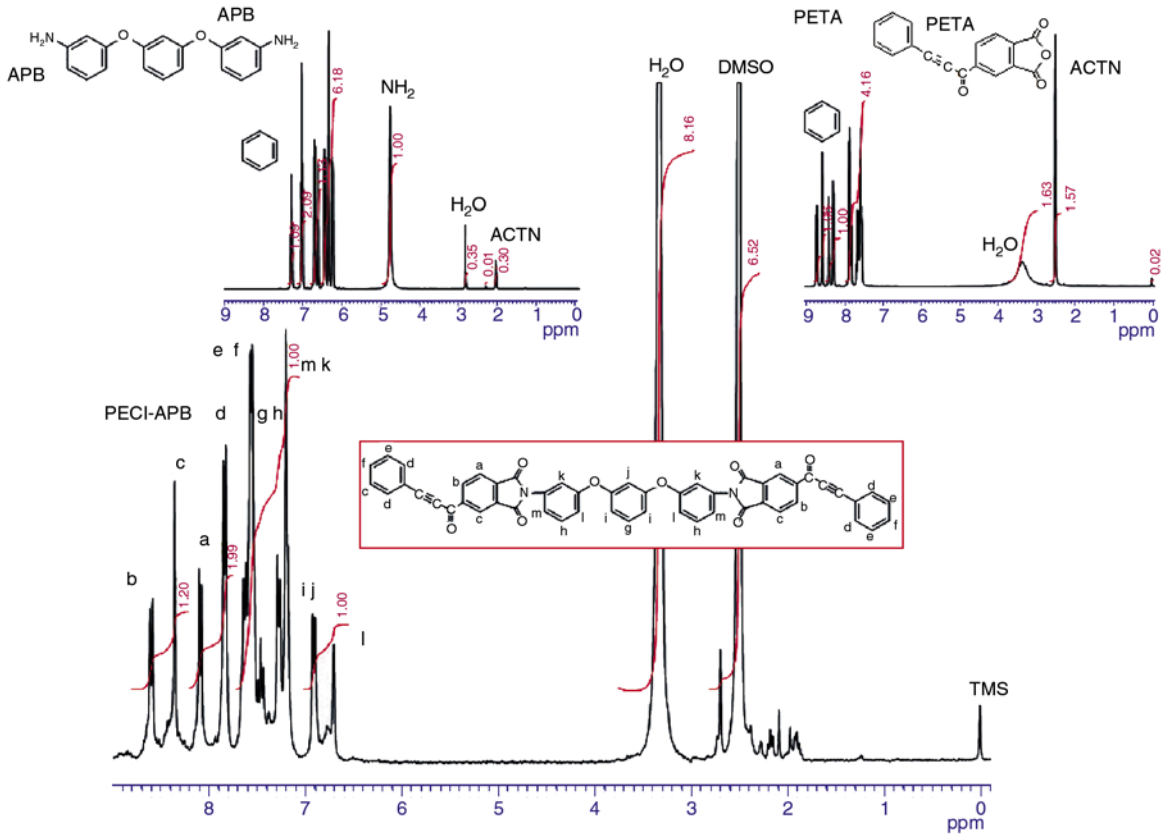

Figure 5. ^{1}H-NMR spectrum of phenylethynylcarbonyl terminated imide compound (PECI-APB) in DMSO-d6

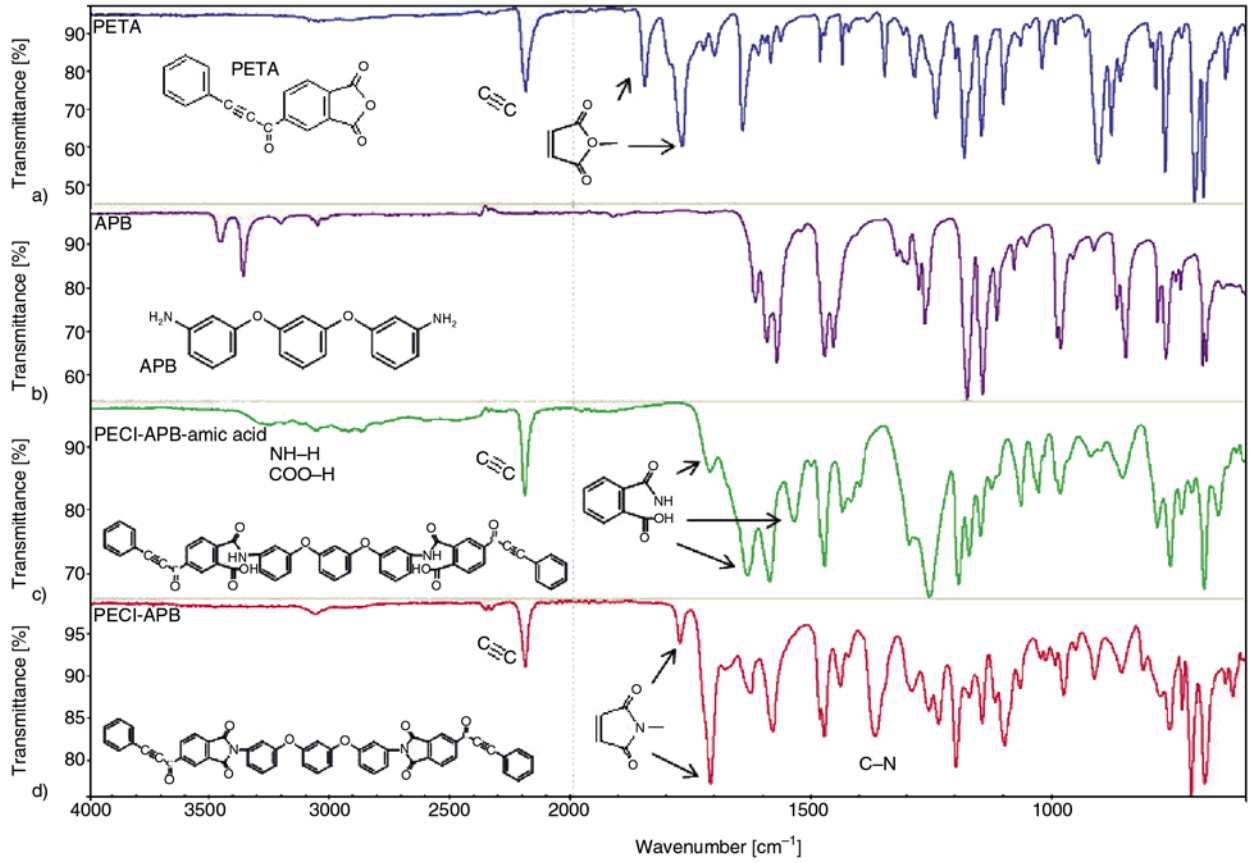

Figure 6. FT-IR spectra of (a) PETA, (b) APB, (c) phenylethynylcarbonyl terminated amic acid and (d) phenylethynylcarbonyl terminated imide compound (PECI-APB)

The absorptions at ca. 1660 and 1550 cm^{-1}, which were related to amide groups of amic acid C=O (amide CONH) and C–NH, were also observed.

In Figure 6d, it can be seen that the imide compound exhibited the characteristic absorption around 2213 cm^{-1}, which was attributed to the stretching vibration of ethynyl C≡C. The absorptions at ca. 1780 and 1725 cm^{-1}, which were related to the asymmetric and symmetric stretching vibrations of imide C=O, were also observed. Moreover, the absorptions around 1600 cm^{-1} (aromatic C=C), 1370 cm^{-1} (imide C–N), were also detected. Additionally, the lack of near 2900–3200 cm^{-1} which was attributed to COO–H and HN–H, the absorption at ca. 1710 cm^{-1} which was related to amic acid C=O (COOH) and the absorptions at ca. 1660 and 1550 cm^{-1} which were related to amide groups of amic acid C=O (amide CONH) and C–NH indicated that the polyimide did not contain significant amounts of amic-acid functional groups.

By these results of NMR and FT-IR, it was found that the synthesis of phenylethynylcarbonyl terminated imide compound by chemical imidization method was conducted effectively, and the objective phenylethynylcarbonyl terminated imide compound (PECI-APB) was obtained.

3.2. DSC analysis of phenylethynylcarbonyl terminated imide compound

DSC thermogram of phenylethynylcarbonyl terminated imide compound (PECI-APB) is shown in Figure 7. From the first DSC heating scan, it is found that phenylethynylcarbonyl terminated imide compound exhibited a weak glass transition around 156°C and a broad exothermic peak with the onset and maximum around 180 and 212°C, respectively. The exothermic peak is assigned to the curing reaction of the phenylethynyl groups, which is accompanied with heat release. As a result, it was found that phenylethynylcarbonyl terminated imide group could react more rapidly than phenylethynyl terminated imide group which needed the high cure temperature (about 350–370°C) [1]. This is because the phenylethynylcarbonyl group might be more flexible than the phenylethynyl group because of the adjacent carbonyl group, and electron withdrawing

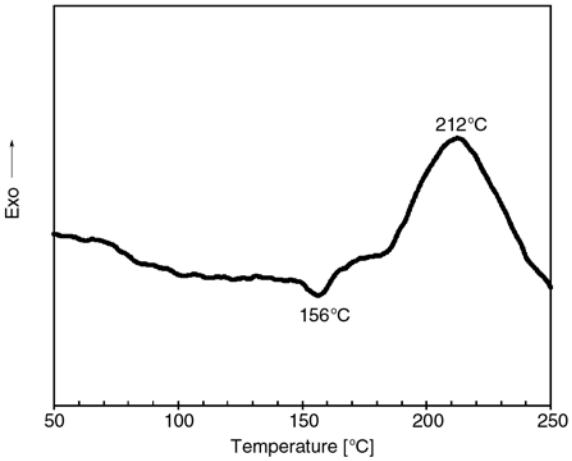

Figure 7. DSC curve of phenylethynylcarbonyl terminated imide compound (PECI-APB)

groups such as ketone on acetylene bond; phenylethynyl group terminated imide compound might enhance the rate of cure.

From the result of DSC measurement, the curing condition was determined as follows: after phenylethynylcarbonyl terminated imide compound (PECI-APB) softened at 160°C to remove any bubbles containing in it sufficiently, curing reaction was carried out at 200°C/3 hr. Finally, at 220°C/3 hr the cured thermosetting resin was postcured so that the curing reaction could proceed completely. In this way, the curing condition of phenylethynylcarbonyl terminated imide compound was determined as 200°C/3 hr + 220°C/3 hr.

DSC thermogram of the cured resin from phenylethynylcarbonyl terminated imide compound (PECI-APB) is shown in Figure 8. DSC curve of the cured resin showed no exothermic peaks, implying that PECI-APB resin had been completely cured. And glass transition temperature of the cured resin was observed around 164°C.

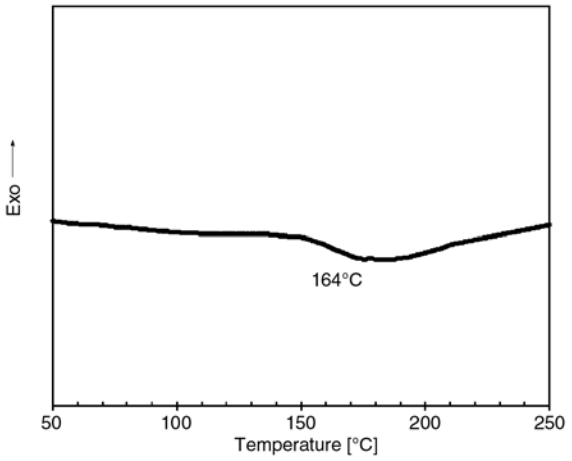

Figure 8. DSC curve of the cured resin from phenylethynylcarbonyl terminated imide compound (PECI-APB)

3.3. Curing reaction of phenylethynylcarbonyl terminated imide compound

To investigate the curing reaction of phenylethynylcarbonyl terminated imide compound, FT-IR measurement was carried out. FT-IR spectra of the compound before and after the curing reaction of phenylethynylcarbonyl terminated imide compound (PECI-APB) are shown in Figure 9. As a result, the characteristic absorption around 2213 cm^{-1}, which was attributed to the stretching vibration of ethynyl C≡C, disappeared after curing reaction (Figure 9b). The absorptions at ca. 1780 and 1725 cm^{-1}, which were related to the asymmetric and symmetric stretching vibrations of imide C=O, were also observed. Moreover, the absorptions around 1600 cm^{-1} (aromatic C=C), 1370 cm^{-1} (imide C–N), were also detected.

The new absorption of alkene C=C at 1635 cm^{-1} appeared after curing reaction (Figure 9b). It was found that the curing reaction of phenylethynylcarbonyl terminated imide compound occurred, and then the alkene groups or aromatic groups (the absorptions around 1600 cm^{-1}) might be generated by the curing reaction.

Based on the investigations on the thermal curing of phenylethynyl terminated imide oligomers it has been suggested that a polyene initially began to form in the curing reaction, which then participated in more complex reactions to yield crosslinked aromatic structures and condensed polycyclic unsaturated structures [9–13].

3.4. TGA analysis of phenylethynylcarbonyl terminated imide compound

Figure 10 shows the TGA curves of the cured thermosetting resin from phenylethynylcarbonyl terminated imide compound (PECI-APB) and that from *o*-cresol novolac type epoxy resin (EP). As for phenylethynylcarbonyl terminated imide compound, the initial decomposition temperature, defined as the temperature at which 5 wt% mass loss occurred, was 432°C. And the cured resin achieved char yields above 75% under nitrogen at 600°C, which exhibited the cured thermosetting resin had good thermal stability. In contrast, the decomposition temperature and the char yield at 600°C of epoxy resin was 384°C and 37% respectively (Table 1). As a result,

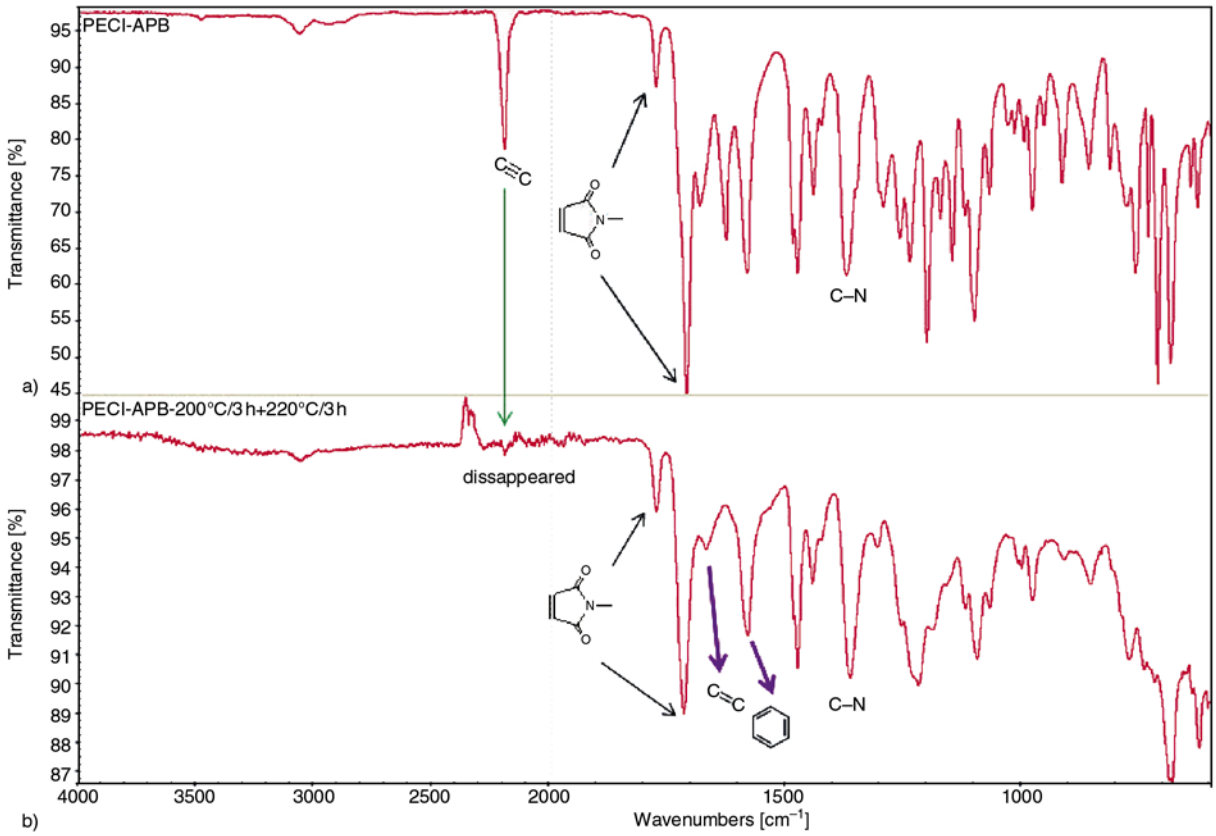

Figure 9. FT-IR spectra of (a) before, (b) after curing reaction of phenylethynylcarbonyl terminated imide compound (PECI-APB)

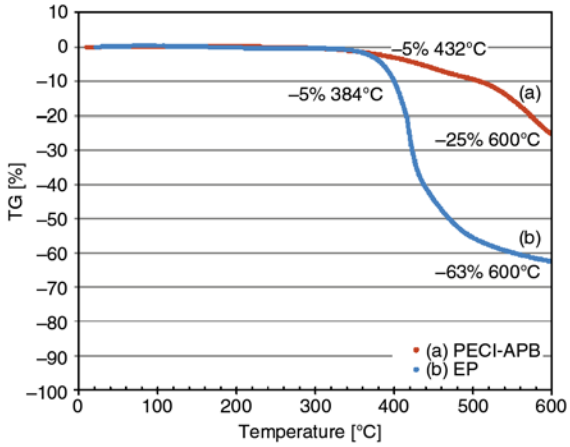

Figure 10. TGA curves of (a) phenylethynylcarbonyl terminated imide compound (PECI-APB) and (b) epoxy resin (EP)

the thermosetting resin from phenylethynylcarbonyl terminated imide compound showed more superior thermal stability to that of epoxy resin. The improvement of thermal stability is due to the incorporation of alkene group or aromatic ring substitutes in the backbones, which might enhance the chain interaction and reduce the molecular chain mobility.

Table 1. Properties of the cured thermosetting resins

Sample	T_g[a] [°C]	T_d[b] [°C]	Char yield[c] [%]	ρ(E′) [mol/m^3]	CTE[d] [ppm/°C]
PECI-APB	201	432	75	$1.5 \cdot 10^2$	44
Epoxy resin	205	384	37	$1.6 \cdot 10^4$	57
PETI-5	270	503	–	–	–

[a]Peak temp. of tan δ by DMA.
[b]Temperature at which 5 wt% mass loss occurred.
[c]At 600°C.
[d]The value (40–60°C) by TMA.

And 5% decomposition temperature of other imide oligomer (PETI-5) [14] was also shown in Table 1. The thermosetting resin from phenylethynylcarbonyl terminated imide compound showed lower thermal stability to other imide oligomer (PETI-5).

3.5. DMA analysis of phenylethynylcarbonyl terminated imide compound

The curves of Dynamic Mechanical Analysis (DMA) are shown in Figure 11. As a result, glass transition temperature (T_g) of the thermosetting resin from phenylethynylcarbonyl terminated imide compound (PECI-APB) was 201°C. And T_g of the cured epoxy resin (EP) was 205°C (Table 1).

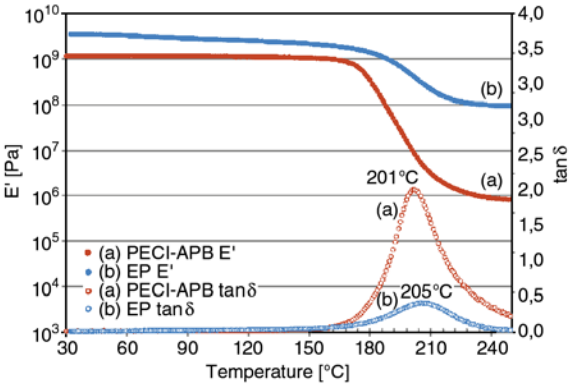

Figure 11. DMA curves of (a) phenylethynylcarbonyl terminated imide compound (PECI-APB) and (b) epoxy resin (EP)

The crosslink density $\rho(E')$ can be calculated using the equation of state for rubbery elasticity (see Equation (1)) [15]:

$$\rho(E') = \frac{E'}{3\Phi RT} \tag{1}$$

where Φ is the front factor, T is the absolute temperature, R is the gas constant, and E' is the storage modulus of the sample at temperature T. This equation is applicable to polymer networks that have a rubbery plateau region [15]. Though the adoption of this equation to the highly crosslinked system is beyond the applicability of the rubber elasticity theory, there is no theoretical equation to calculate crosslink density for highly crosslinked polymers. Therefore, in our study, the value of $\rho(E')$ of the samples was calculated at $T_g + 40$°C according to this equation to compare the crosslink density of each sample [16–17]. The results are shown in Table 1, under the assumption that Φ is equal to 1 [18]. The value of $\rho(E')$ of the cured resins from phenylethynylcarbonyl terminated imide compound (PECI-APB) was much smaller (one hundredth) than that of the cured epoxy resin (EP). As a result, the thermosetting resin from phenylethynylcarbonyl terminated imide compound showed almost the same T_g as that of epoxy resin. The reason of the good heat resistance of phenylethynylcarbonyl terminated imide compound is due not to high crosslink density, but to the incorporation of alkene group or aromatic ring substitutes in the backbones, which might enhance the chain interaction and reduce the molecular chain mobility. Namely, contrasting the chemical composition of epoxy resin to phenylethynylcarbonyl terminated imide compound, the epoxy does not have the functionalities that are reducing chain mobility.

And T_g of other imide oligomer (PETI-5) [14] was also shown in Table 1. The thermosetting resin from phenylethynylcarbonyl terminated imide compound showed lower glass transition temperature to other imide oligomer (PETI-5).

3.6. TMA analysis of phenylethynylcarbonyl terminated imide compound

The coefficient of thermal expansion (CTE, 40–60°C) of the thermosetting resin from phenylethynylcarbonyl terminated imide compound (PECI-APB) was evaluated by Thermal Mechanical Analysis (TMA). The CTE is another important property with regard to the electronic package applications. Unfortunately, most organic polymers have much higher CTEs (about 40–200 ppm/°C) than those of the inorganic substrates (for example, fused silica 0.55 ppm/°C) and conductors (for example, copper 17–20ppm/°C) used in electronics. Additionally, CTE of the printed circuit board is 13–18 ppm/°C, 80 to 90 ppm/°C in the plate thickness Z-axis direction. This CTE mismatch results in residual stress buildup in the electronic materials following thermal processing. It is of interest to determine the CTEs of the thermosetting resin from phenylethynylcarbonyl terminated imide compound.

As a result, CTE of the thermosetting resin from phenylethynylcarbonyl terminated imide compound (PECI-APB) was 44 ppm/°C, which showed relatively lower CTE values. In contrast, CTE of the cured epoxy resin was 57 ppm/°C (Table 1). As a result, the thermosetting resin from phenylethynylcarbonyl terminated imide compound showed much lower coefficient of thermal expansion than that of epoxy resin. The improvement of CTE might be due to the incorporation of alkene group or aromatic ring substitutes in the backbones, which might enhance the chain interaction (molecular packing) and reduce the molecular chain mobility. Namely, the reduction in CTE may be attributed to the segmental motions of the chains that are restricted. Phenylethynylcarbonyl terminated imide compound showed lower CTE than epoxy resin, even though the T_g of epoxy resin was a little higher than that of phenylethynylcarbonyl terminated imide compound. It seems that the chain structure of phenylethynylcarbonyl terminated imide compound which

has more planar shape than epoxy resin affected the CTE more than the glass transition temperature of the polymer [19].

4. Conclusions

In this study, we investigated the synthesis and characterization of phenylethynylcarbonyl terminated novel thermosetting imide compound. As a result, it was found that the curing reaction of phenylethynylcarbonyl terminated imide group proceeded much faster than that of phenylethynyl terminated imide group. This is due to the phenylethynylcarbonyl group might be more flexible than the phenylethynyl group because of the adjacent carbonyl group, and electron withdrawing groups such as ketone on acetylene bond might enhance the rate of cure. From the results of Fourier transform infrared spectrometry measurement, the new absorption of alkene groups (C=C) at 1635 cm^{-1} and aromatic groups at 1600 cm^{-1} appeared after curing reaction. It was found that the curing reaction of phenylethynylcarbonyl terminated imide compound occurred, and then the alkene groups or aromatic groups might be generated by the curing reaction. The cured thermosetting resin from phenylethynylcarbonyl terminated imide compound exhibited had good thermal decomposition stability. From the results of dynamic mechanical analysis and thermal mechanical analysis, the thermosetting resin from phenylethynylcarbonyl terminated imide compound showed almost the same T_g as that of epoxy resin, and the coefficient of thermal expansion of the thermosetting resin from phenylethynylcarbonyl terminated imide compound was 44 ppm/°C, which showed relatively lower CTE values. The improvement of these excellent thermal properties might be due to the incorporation of alkene group or aromatic ring substitutes in the backbones, which might enhance the chain interaction and reduce the molecular chain mobility. These excellent properties of the phenylethynyl terminated imide compound demonstrate a promising potential for future use of commercial all purposes except for the special use of aerospace field.

References

[1] Connell J. W., Smith J. G. Jr., Hergenrother P. M.: Oligomers and polymers containing phenylethynyl groups. Journal of Macromolecular Science Part C: Polymer Reviews, **40**, 207–230 (2000).
DOI: 10.1081/MC-100100585

[2] Hergenrother P. M.: The use, design, synthesis, and properties of high performance/high temperature polymers: An overview. High Performance Polymers, **15**, 3–45 (2003).
DOI: 10.1177/0954008303015001O1

[3] Ishida Y., Ogasawara T., Yokota R.: Development of highly soluble addition-type imide oligomer and polyimide/carbon fiber composite prepared by imide solution prepreg. in '16th International Conference on Composite Materials, Kyoto, Japan' p4 (2007).

[4] Yokota R., Yamamoto S., Yano S., Sawaguchi T., Hasegawa M., Ozawa H., Sato R.: Molecular design of heat resistant polyimides having excellent processability and high glass transition temperature. High Performance Polymers, **13**, S61–S72 (2001).
DOI: 10.1088/0954-0083/13/2/306

[5] Ogasawara T., Ishikawa T., Yokota R., Ozawa H., Taguchi M., Sato R., Shigenari Y., Miyagawa K.: Processing and properties of carbon fiber reinforced triple-A polyimide (tri-A PI) matrix composites. Advanced Composite Materials, **11**, 277–286 (2002)
DOI: 10.1163/156855102762506317

[6] Volksen W.: Condensation polyimides: Synthesis, solution behavior, and imidization characteristics. Advances in Polymer Science, **117**, 111–164 (1994).
DOI: 10.1007/BFb0021198

[7] Kailani M. H., Sung C. S. P.: Chemical imidization study by spectroscopic techniques. 1. model amic acids. Macromolecules, **31**, 5771–5778 (1998)
DOI: 10.1021/ma980095d

[8] Kwei K. T.: Viscoelasticity of crosslinked epoxy polymer in the transition region. Journal of Polymer Science A2: Polymer Physics, **4**, 943–949 (1966).
DOI: 10.1002/pol.1966.160040609

[9] Sun H., Huo H., Nie H., Yang S., Fan L.: Phenylethynyl terminated oligoimides derived from 3,3′,4,4′-diphenylsulfonetetracarboxylic dianhydride and their adhesive properties. European Polymer Journal, **45**, 1169–1178 (2009).
DOI: 10.1016/j.eurpolymj.2009.01.004

[10] Fang X. M., Rogers D. F., Scola D. A., Stevens M. P.: A study of the thermal cure of a phenylethynyl-terminated imide model compound and a phenylethynyl-terminated imide oligomer (PETI-5). Journal of Polymer Science Part A: Polymer Chemistry, **36**, 461–470 (1998).
DOI: 10.1002/(SICI)1099-0518(199802)36:3<461::AID-POLA10>3.0.CO;2-L

[11] Nakamura K., Ando S., Takeichi T.: Thermal analysis and sof Thermal analysis and solid lid-state ^{13}C NMR study of crosslink in polyimides containing acetylene groups in the main chain. Polymer, **42**, 4045–4054 (2001).
DOI: 10.1016/S0032-3861(00)00827-2

[12] Holland T. V., Glass T. E., McGrath J. E.: Investigation of the thermal curing chemistry of the phenylethynyl group using a model aryl ether imide. Polymer, **41**, 4965–4990 (2000).
DOI: 10.1016/S0032-3861(99)00578-9

[13] Takekoshi T., Terry J. M.: High-temperature thermoset polyimides containing disubstituted acetylene end groups. Polymer, **35**, 4874–4880 (1994).
DOI: 10.1016/0032-3861(94)90746-3

[14] Smith Jr. J. G., Connell J. W., Hergenrother P. M.: The effect of molecular weight on the composite properties of cured phenylethynyl terminated imide oligomers. NASA Langley Research Center, Technical Report (1998).

[15] Murayama T., Bell P. J.: Relation between the network structure and dynamic mechanical properties of a typical amine-cured epoxy polymer. Journal of Polymer Science Part A2: Polymer Physics, **8**, 437–445 (1970).
DOI: 10.1002/pol.1970.160080309

[16] Hasegawa K., Fukuda A., Tonogai S.: Structure and viscoelastic properties of epoxy resins prepared from four-nuclei novolacs. Journal of Applied Polymer Science, **37**, 3423–3435 (1989).
DOI: 10.1002/app.1989.070371213

[17] Matsumoto A., Hasegawa K., Fukuda A.: Studies on modified phenolic resin. Iv: Properties of phenolic resin modified with 4-hydroxyphenyl- maleimide/*n*-butylacrylate copolymers. Polymer International, **30**, 65–72 (1993).
DOI: 10.1002/pi.4990300110

[18] Kamon T., Saito K., Miwa Y. Saeki K.: Dynamic mechanical analysis of diamine cured epoxy resin (in Japanese). Kobunshi Kagaku, **30**, 279–282 (1973).
DOI: 10.1295/koron1944.30.279

[19] Choi H., Chung I. S., Hong K., Park C. E., Kim S. Y.: Soluble polyimides from unsymmetrical diamine containing benzimidazole ring and trifluoromethyl pendent group. Polymer, **49**, 2644–2649 (2008).
DOI: 10.1016/j.polymer.2008.04.019

eXPRESS Polymer Letters Vol.7, No.2 (2013) 172–185
Available online at www.expresspolymlett.com
DOI: 10.3144/expresspolymlett.2013.16

Isocyanate toughened pCBT: Reactive blending and tensile properties

T. Abt[1], *A. Martínez de Ilarduya*[2], *J. J. Bou*[2], *M. Sánchez-Soto*[1*]

[1]Department of Materials Science, Centre Català del Plàstic, Universitat Politècnica de Catalunya, BarcelonaTech. C/Colom 114, 08222 Terrassa, Spain
[2]Department of Chemical Engineering, ETSEIB, Universitat Politècnica de Catalunya, BarcelonaTech, Diagonal 647, 08028 Barcelona, Spain

Received 22 July 2012; accepted in revised form 29 September 2012

Abstract. Cyclic butylene terephthalate oligomers (CBT) were reacted in a ring-opening polymerization with three types of isocyanates: a bifunctional aromatic type, a bifunctional aliphatic type and a polymeric aromatic isocyanate. All reactions took place in a batch mixer. The use of 0.5 to 1 wt% isocyanate led to a dramatic increase in elongation at break of polymerized cyclic butylene terephthalate (pCBT), from 8 to above 100%. The stiffness and strength of the modified pCBT, however, were found to slightly decrease. Proton nuclear magnetic resonance (NMR) analysis shows that the formation of thermally stable amide groups is the dominant chain extension reaction mechanism. Gel content measurements suggest a linear structure for samples containing bifunctional isocyanates while pCBT modified with polyfunctional isocyanate exhibited some gel formation at higher isocyanate content. Melting and crystallization temperatures as well as degree of crystallinity were found to decrease with increasing isocyanate content. No phase separation was detected by scanning electron microscopy (SEM) analysis. Moreover, a high degree of polymerization is deduced due to the absence of CBT oligomer crystals.

Keywords: *mechanical properties, cyclic butylene terephthalate, pCBT, isocyanate, toughening*

1. Introduction

The *in situ* ring-opening polymerization of cyclic butylene terephthalate oligomers is a promising route to replace thermosetting polymers in composites and has become of great interest. CBT oligomers melt at low temperatures (120–160ºC) and exhibit a water-like viscosity prior to polymerization. Due to this very low initial viscosity, fiber reinforcements can be readily impregnated. After impregnation, the molten CBT oligomers quickly polymerize in an entropically driven, athermal ring-opening polymerization (ROP) without releasing volatile organic compounds. This process yields pCBT, a thermoplastic polyester with high molecular weight [1–3]. So far, continuous fiber reinforced composites made from CBT and glass fibers [3–8], basalt fibers [9], and carbon fibers [10–13] have been reported. Moreover, a hydrogenated nitrile rubber (HNBR) was modified with CBT and the HNBR/CBT hybrids exhibited improved mechanical and triblogical properties compared to pristine HNBR [14]. CBT has also been extensively used in nanocomposites due to the low melt viscosity prior to ROP which is advantageous for a good dispersion of the reinforcement. Nanocomposites with nanosilica [15], multiwalled carbon nanotubes [16–19], graphene [20] and organically modified montmorillonite [21–24] have been prepared. Various researchers obtained an improved dispersion or intercalation/exfoliation in the case of organoclays compared to conventional melt blended PBT nanocomposites. The good dispersion and exfoliation of nanoparticles in pCBT resulted

*Corresponding author, e-mail: m.sanchez-soto@upc.edu

in improved thermomechanical properties [15, 17, 20, 21] and better thermal stability [18, 20, 24].

However, pCBT was found to be brittle [4, 5, 7, 9, 13, 25]. This brittleness is caused by the formation of large perfect crystals with a lack of intercrystalline tie molecules [3, 13, 26]. Another reason for brittleness is a low molecular weight, which can be caused by hydrolysis if moisture is present during the ROP. Moreover, water can negatively affect the catalyst, which also leads to a lower molecular weight [9, 27]. Several researchers have addressed this problem by copolymerizing CBT with poly (ethylene-*co*-vinyl acetate) [28], poly(vinyl butyral) [29], ε-caprolactone [30] and polycaprolactone [4, 31]. This leads to a decreased crystallinity with less perfect crystals and an increased elongation at break together with a deep decrement of other relevant mechanical properties such as stiffness and strength.

Recently, we showed that reactive chain extension of pCBT with a bifunctional epoxy resin is a useful way to increase the molecular weight and to toughen pCBT without considerably affecting other properties [25]. The bifunctional epoxide groups react with the terminal carboxyl groups of two or more pCBT chains, increasing molecular weight and causing an improvement in toughness. However, the chain extension reaction of pCBT and epoxy resin is rather slow and requires high reaction temperatures. Additionally, it can result in considerable gel formation when there is an excess of epoxy resin. Therefore an addition-type chain extender with no by-products, higher reactivity and capable of yielding a linear macromolecular structure is desirable. Of the available groups of chain extenders for polyesters, isocyanates (NCO) are promising. They show higher reactivity than epoxides and readily react at moderate temperatures with active hydrogen containing compounds [27, 32, 33]. The reaction can be promoted by metals in the form of organometallics and/or salts of organic acids. Tin compounds such as dibutyl tin dilaurate and tin (II) octoate are particularly effective, so the reaction can even be conducted at room temperature [34, 35]. This high reactivity and versatility make isocyanates an important group of chemicals and they are used as building blocks, e.g. as hard segments in polyurethane chemistry. Linear, branched and crosslinked structures can be obtained with isocyanates, depending on functionality and stoichiometry. Isocyanates can be used as compatibilizers for partially miscible polymer blends [36] as well as chain extenders or toughening agents to improve the properties; particularly the toughness of recycled poly(ethylene terephthalate) [33, 36], polylactide [37], and poly(butylene terephthalate) [38]. These properties render isocyanates a useful group of chain extender and toughening agents for pCBT. To the best of our knowledge, there has been no publication on this subject.

In the present work we have studied the role of different isocyanates on the ring-opening polymerization and the properties of CBT. The resultant structure and properties have been analyzed and discussed.

2. Experimental section

2.1. Materials

Cyclic butylene terephthalate oligomers were used in this study, namely one-component CBT 160®, containing butylchlorotin dihydroxide as a catalyst and were provided in granule form from Cyclics Europe GmbH (Schwarzheide, Germany). The CBT was ground into a fine powder using a mortar and pestle.

Three different types of isocyanates were used; their chemical structures are depicted in Figure 1. Hexamethylene diisocyanate (referred to as HDI) is a liquid aliphatic diisocyanate and 4,4′-methylenebis(phenyl isocyanate) (referred to as MDI) is a solid aromatic diisocyanate. Both types were analytical grades from Sigma-Aldrich and used as received. A polymeric methylene diphenyl diiso-

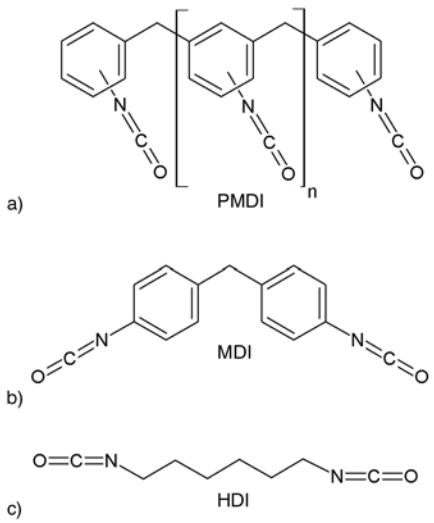

Figure 1. Chemical structures of polymeric isocyanate (a), aromatic 4,4′-methylenebis(phenyl isocyanate) (b) and aliphatic hexamethylene diisocyanate (c)

cyanate (referred to as PMDI) was purchased from BASF Poliuretanos Iberia S.A., Rubí, Spain and used as received. The PMDI is a brown, viscous liquid of grade IsoPMDI 92410. According to the material data sheet the PMDI was based on 4,4′-methylenebis(phenyl isocyanate) and contained oligomers with an average functionality of ~2.7 and a NCO content of 31.8%.

2.2. Sample preparation

CBT and the corresponding amount of each isocyanate (0.25, 0.5, 0.75 and 1 wt%) were blended using mortar and pestle and vacuum dried at 80°C for 8 h. The blends were stored in a desiccator over silica gel prior to in-situ polymerization and simultaneous reactive blending in a batch mixer. After polymerization the polymer was collected, ground into granules and vacuum dried at 80°C for 8 h. An IQAP LAP PL-15 hot plate press was used to compression mould the dried granules at 250°C for 5 min between two PTFE films in ambient atmosphere. The samples were then rapidly cooled to room temperature in the cold stage of the press. The resulting pCBT/NCO films had dimensions of ca. 150 × 150 × 0.5 mm^3 and were used to extract samples for further characterization. Neat CBT was equally processed for comparison.

2.3. Characterization

2.3.1. Torque versus time measurements

The CBT/NCO blends were in-situ polymerized in a Brabender Plasti-Corder W50EHT (Duisburg, Germany), equipped with a torque measuring system. Around 40 g of the CBT/NCO blends were polymerized in the mixing chamber of the Brabender batch mixer at 230°C and 60 min^{-1} rotor speed under a blanket of nitrogen to minimize hydrolysis. The preheated mixing chamber was purged with nitrogen for 5 min and the predried CBT/NCO blend was introduced. Then the nitrogen blanket was introduced again and after a predetermined time the mixing was stopped. The material was collected from the mixing chamber and allowed to cool to room temperature.

2.3.2. Gel content

The insoluble content of the isocyanate-modified pCBT samples was determined by dissolving around 50 mg of sample in 5 mL of a mixture of $CHCl_3$/TFA (9/1) at ambient temperature with agitation for 30 min. The solution was subsequently centrifuged and the soluble part was removed. The insoluble fraction was washed with 5 mL of the same solvent mixture two additional times and finally with $CHCl_3$. It was then dried in an oven at 80°C for 12 h and weighted. The gel content was calculated by insoluble fraction weight over sample weight expressed in percent.

2.3.3. Nuclear magnetic resonance spectroscopy (NMR)

Proton NMR spectroscopy was used to determine the chemical structures of the NCO-modified pCBT samples. Spectra were collected on a Bruker AMX-300 spectrometer operated at 300.1 MHz at 363.1 K. Sample concentrations were 1% (w/v) and a 1,1,2,2-tetrachloroethane-d_2 solvent was used. A total of 640 scans with 32k data points were recorded with a relaxation delay of 2 s.

2.3.4. Differential scanning calorimetry (DSC)

The thermal properties of neat pCBT and NCO-modified pCBT samples were determined by differential scanning calorimetry using a Perkin Elmer Pyris 1 device under nitrogen atmosphere. Compression moulded samples were heated from 30 to 250ºC at a heating rate of 10ºC/min, followed by an isothermal step of 3 minutes and then cooled from 250 to 30ºC at a rate of 10ºC/min. The sum of both melting enthalpies ΔH_{m1+2} of the second heating run was used to calculate the degree of crystallinity $\chi_{\Delta H}$ of the samples according to Equation (1):

$$\chi_{\Delta H} = \frac{\Delta H_m}{\Delta H_m^0} \cdot 100\ [\%] \qquad (1)$$

The melting enthalpy ΔH_m^0 of fully perfect crystalline PBT is found in to be 142 J/g according to literature [13, 16].

2.3.5. Tensile tests

The tensile properties were determined according to ISO 527 at room temperature and at a crosshead speed of 10 mm/min on a Galdabini Sun 2500 (Galdabini, Italy) tensile testing machine. The strain was measured using a video extensometer. Type 1BA specimens were die cut from the above described compression moulded pCBT/NCO films. Presented values were averaged from a minimum of five spec-

imens. The toughness in terms of strain energy was determined by integrating the area under the stress-strain curve from the origin until rupture.

2.3.6. Scanning electron microscope (SEM)

The morphologies of unmodified and NCO-modified pCBT were analyzed by SEM. Tensile test specimens were submerged in liquid N_2 and equilibrated for 15 min. The specimens were quickly extracted and cryo-fractured by bending. The fracture surfaces were then sputter coated with a thin gold layer using a Bal-Tec SCD005 Sputter Coater. SEM analysis was performed on a Jeol JSM-5610 scanning electron microscope and an acceleration voltage of 10 kV was used.

3. Results and discussion

Isocyanates are well known to readily react with compounds that bear active hydrogen. The classical reaction in polyurethane chemistry is the reaction of an isocyanate group with an alcohol group where a urethane group is formed. The reactivity depends mainly on the chemical structure of the employed isocyanate and it was found that aromatic isocyanates are more reactive than aliphatic ones [33, 39]. Urethane bonds are thermally unstable and can dissociate at high temperatures. The decomposition temperature depends on the structures of the isocyanate and alcohol used. Generally, the higher the reactivity of the isocyanate-alcohol system, the lower the thermal stability of the formed urethane. The thermal stabilities of urethanes as reaction products of different isocyanate-alcohol systems are as follows: alkyl isocyanate-alkyl alcohol (250ºC) > aryl isocyanate-alkyl alcohol (200ºC) > alkyl isocyanate aryl alcohol (180ºC) > aryl isocyanate-aryl alcohol (120ºC) [40]. According to this sequence, the thermal stabilities of pCBT-isocyanate systems are

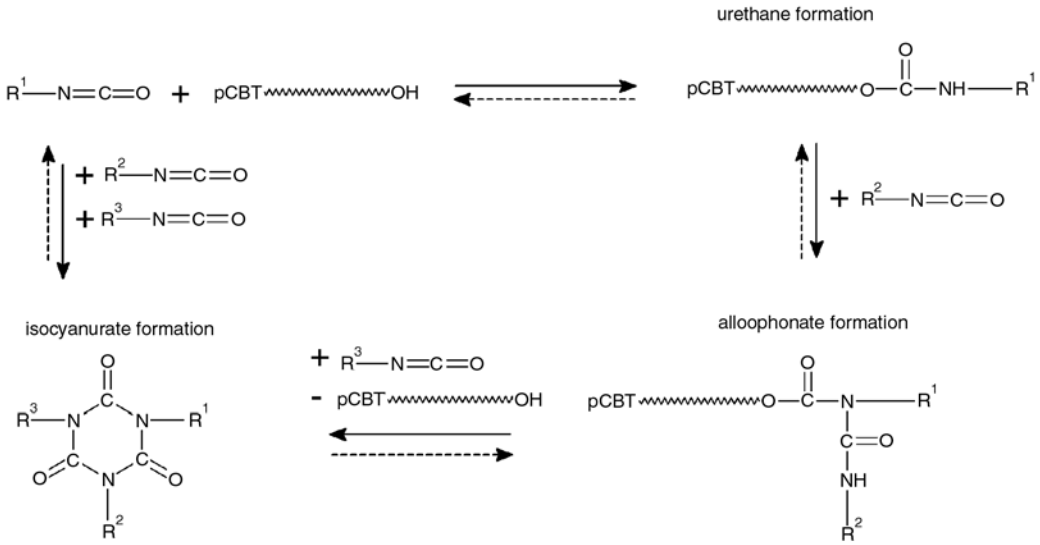

Figure 2. Possible reaction mechanisms of pCBT hydroxyl end groups and isocyanate functional groups

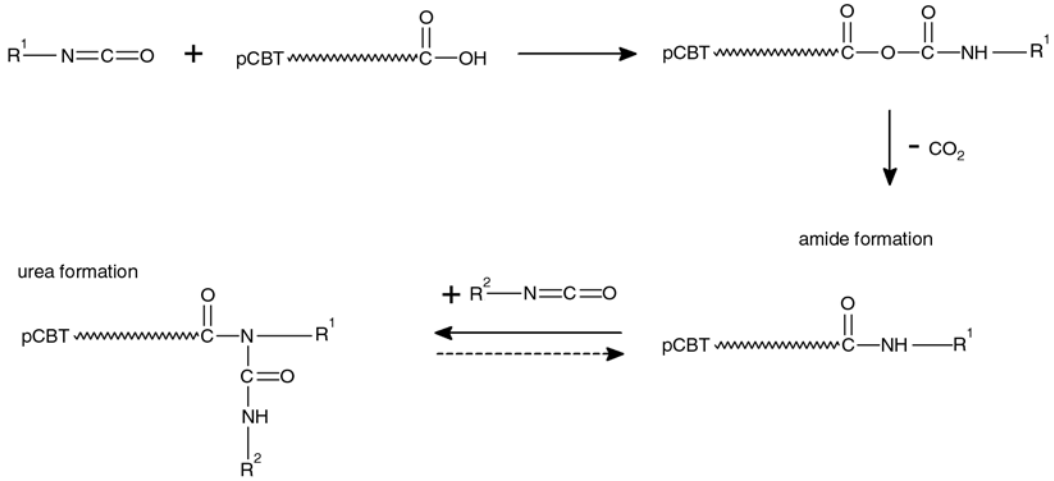

Figure 3. Possible reaction mechanisms of pCBT carboxyl end groups and isocyanate functional groups

expected to be in the range of 200–250ºC. Due to their high reactivity, the isocyanate groups can also react with carboxyl end groups leading to amide groups and carbon dioxide as by-product. Amide bonds are thermally more stable than urethane or ester bonds due to their partial double bond character [41].

Secondary reactions with excess isocyanate and the previously formed urethane and amide groups can occur, resulting in allophanates (Figure 2) and ureas (Figure 3), respectively. Additionally, isocyanurates can arise from trimerization of isocyanate as well as from the reaction of allophanate and excess isocyanate. These secondary reactions lead to branching and finally to crosslinking of the polymer [27, 33, 36, 39, 40, 42]. The kinetic rate constants of allophanate, urea and isocyanurate formation are much smaller than the ones of urethane and amide formation [39], and it is well known that these reactions are only favored at higher concentrations of isocyanate groups.

3.1. Torque versus time measurements

A chain extension reaction of (growing) pCBT chains and a bi- or polyfunctional chain extender causes an increase in molecular weight due to the coupling of multiple pCBT chains onto a chain extender molecule. This results in an increase in viscosity with reaction time. The ring-opening polymerization and the chain extension reaction were initially carried out in a Brabender batch mixer for a prolonged time (60 min) in order to visualize the torque/time signal, which is taken as an indicator for the viscosity evolution. The torque evolution is only shown for 15 min. The optimum polymerization times were chosen from these graphs, as will be explained below. The torque curves are depicted in Figure 4; the maximum torque values and the corresponding times to reach the maximum torque are given in Table 1. The torque signal of neat CBT was first detected after 2 min which was considered to be the onset of the ROP. Before this time the melt viscosity of the molten CBT was below the detection limit of the measuring system. The torque curve reached a plateau after 9 min at ca. 6 Nm. Then it slowly increased and reached a maximum of 8 Nm after ~41 min. After reaching the maximum, the torque decreased to 7 Nm after 60 min probably due to thermo-mechanical degradation.

Regarding the CBT/NCO blends, apparently all three types of isocyanates act as promoters for the ring-opening polymerization when they are used in small concentrations (until 0.5 wt%,) because the onset of the torque signal appears earlier (Figure 4). The aliphatic HDI was the most effective promoter when 0.5 wt% was used, showing an onset of only 30 s (c.f. Figure 4b). However, higher isocyanate contents (> 0.5 wt%) result in an increase of the onset time as well as of the time to reach the maximum torque value (Table 1).

A remarkable increase in torque can be seen for all blend compositions, confirming the chain extension reaction. The highest torque value was observed with aromatic MDI at a concentration of 0.75 wt%, probably due to the higher reactivity of aromatic isocyanates compared to aliphatic ones.

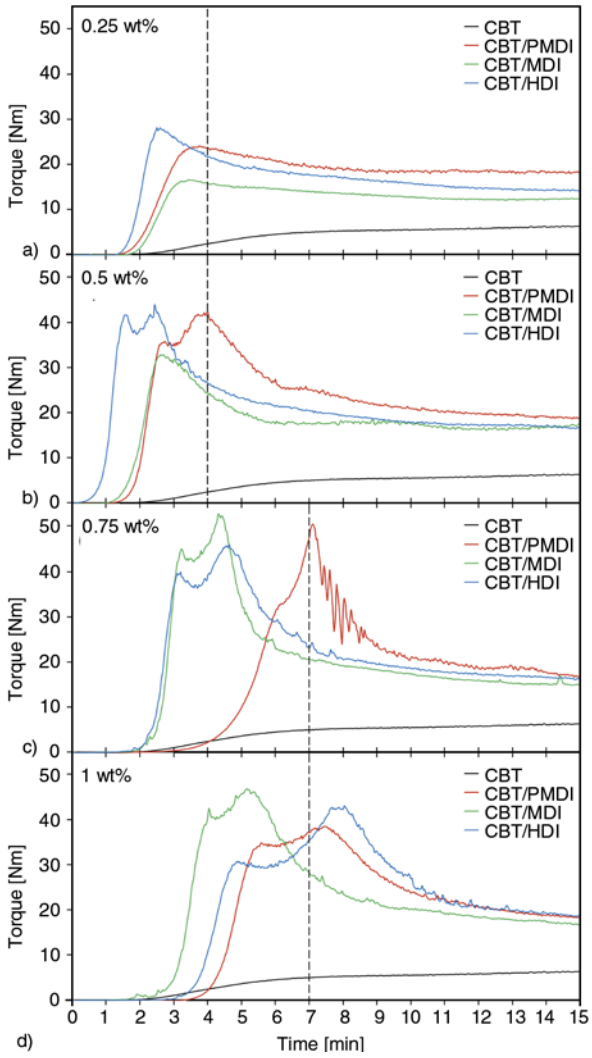

Figure 4. Torque vs. time plots of CBT/NCO blends with an isocyanate content of (a) 0.25 wt%, (b) 0.5 wt%, (c) 0.75 wt% and (d) 1 wt% at 230°C and 60 rpm under nitrogen atmosphere

Table 1. Maximum torque values during ring-opening polymerization in the batch mixer, times to reach the maximum torque and gel contents prior to compression moulding. Tensile properties of compression moulded pCBT and pCBT/NCO samples.

Chain extender	Content [wt%]	Polymerization[a]		Gel content	Tensile properties			
		Torque max. [Nm]	Time[b] [min]	[%]	Tensile modulus [GPa]	Tensile strength [MPa]	Elongation at break [%]	Strain energy [MJ/m^3]
–	0	7.7	40.7	–	2.9±0.3	60±2	8±1	4.2±0.5
PMDI	0.25	24.0	3.7	–	2.8±0.3	57±1	30±4	13.5±1.7
	0.5	42.4	4.0	2.2	2.6±0.3	55±3	184±94	77.9±41.1
	0.75	50.4	7.1	1.2	2.6±0.2	55±1	167±84	70.9±38.3
	1	38.5	7.5	31.5	2.6±0.2	51±1	215±28	87.1±11.7
MDI	0.25	16.6	3.4	–	2.6±0.4	56±1	25±18	8.7±4.3
	0.5	32.9	2.6	–	2.7±0.4	55±1	141±71	57.0±29.9
	0.75	52.7	4.3	–	2.6±0.1	55±1	174±68	71.9±30.0
	1	46.8	5.2	–	2.7±0.2	55±1	79±11	30.5±4.6
HDI	0.25	28.1	2.5	–	2.4±0.2	60±1	24±9	9.9±4.9
	0.5	43.9	2.4	–	2.8±0.3	55±1	143±85	61.2±28.7
	0.75	46.1	4.6	–	2.7±0.7	54±1	227±35	95.4±18.4
	1	43.0	8.0	–	2.8±0.2	54±1	109±21	44.9±9.0

[a]Polymerization conditions: 230°C, 60 rpm, N_2 atmosphere
[b]Time to reach maximum torque

When only 0.25 wt% chain extender was used, a single torque maximum was observed. At higher isocyanate concentrations a second maximum appeared. This may be due to intermediate reactions, i.e. an initial urethane formation corresponding to the first maximum, subsequently followed by urethane dissociation into isocyanates and hydroxyl groups, leading to a torque decrease and finally amide formation, resulting in the second torque maximum. This urethane dissociation during processing will be discussed in detail in the NMR section.

After prolonged processing times (>10 min), all curves decreased to an average value of ~17 Nm after 15 min. This suggests that an equilibrium was reached and all blends, regardless of their isocyanate content, exhibited a similar molecular weight. Raffa *et al*. [32] came to a similar conclusion working with recycled PET and its chain extension with di- and multifunctional isocyanates. They found a plateau value of both molecular weight and melt viscosity above a threshold amount of isocyanate and ascribed this stationary condition to a mutual compensation of chain extension and degradation processes.

It is apparent from Figure 4 that higher isocyanate concentrations require a longer time to fully react. The peak of the torque curve was considered as the highest molecular weight of the formed pCBT/NCO. Therefore a polymerization time of 4 min was chosen for blends containing 0.25 and 0.5 wt% isocyanate, whereas neat CBT and blends with isocyanate concentrations of 0.75 and 1 wt% were polymerized for 7 min. The two dashed vertical lines in Figure 4 represent these selected polymerization times 4 and 7 min.

Fresh CBT/NCO blends were polymerized in the batch mixer under the same conditions for 4 and 7 min, respectively. A gel-like texture was noticed in pCBT/PMDI samples with higher isocyanate concentrations when the materials were collected from the mixing chamber, therefore the gel content was determined.

3.2. Gel content

The insoluble part of the NCO-modified pCBT samples was determined by dissolution, centrifugation, washing and filtration; the results are compiled in Table 1. Samples modified with bifunctional MDI or HDI were completely soluble, suggesting a linear chain structure. Only samples containing polyfunctional PMDI showed gel formation, namely 2.2 and 1.2% insoluble content for 0.5 and 0.75 wt% PMDI concentration. The highest insoluble content of 31.5% was observed for 1 wt% PMDI content. Note that gelling was only observed in samples after in-situ polymerization in the batch mixer. All compression moulded samples were completely soluble for NMR analysis. This leads to the assumption that

these crosslinked structures in pCBT/PMDI samples changed to linear or branched structures during compression moulding.

3.3. NMR

Proton NMR analysis was used to determine the chemical structures of pCBT and chain extended pCBT obtained from compression moulding. The structures and corresponding spectra are shown in Figure 5.

In the spectrum of neat pCBT, the signal at 1.9 ppm is assigned to shielded methylene protons, the triplet at 3.7 ppm corresponds to methylenes attached to terminal hydroxyl groups (–CH_2OH), the peak at 4.4 ppm is assigned to oxymethylene protons and the one at 8.0 ppm is assigned to the aromatic protons.

The spectra of the pCBT/NCO samples revealed several additional peaks. Samples chain extended with aromatic isocyanate (i.e. MDI and PMDI) exhibited new peaks at 4.0, 7.2, 7.5 and 7.8 ppm. The peaks at 4.0 ppm are due to methylene protons of the reacted MDI, the doublets at 7.2 and 7.5 ppm are assigned to aromatic protons of the reacted MDI whereas the doublet at 7.9 ppm is assigned to aromatic protons of the terephthalic moiety which are linked to one ester group and one amide group in para position.

In the case of samples containing aliphatic isocyanates (i.e. HDI), new peaks at 3.1, 3.4, 4.1, 6.2 and 7.8 ppm arose. The weak peaks at 3.1 and 4.1 ppm are assigned to urethane formation of pCBT hydroxyl end groups and HDI [42]. More pronounced peaks at 3.4, 6.2 and 7.8 ppm are due to amide formation. Furthermore, no signal of remaining unreacted isocyanates could be detected, suggesting a complete reaction of the isocyanates. Moreover, no crosslinked structures such as allophanates, ureas or biurets have been detected in compression moulded samples by NMR which is also concordant with gel content measurements. It can be also seen that the number of terminal hydroxyl groups (c.f. triplet at 3.7 ppm) is similar for all samples. A possible explanation is that the isocyanate reacted with terminal hydroxyl groups in the first stage but due to the low thermal stability of urethane at the processing temperature the formed urethane groups dissociated back into –NCO and –OH groups. The liberated

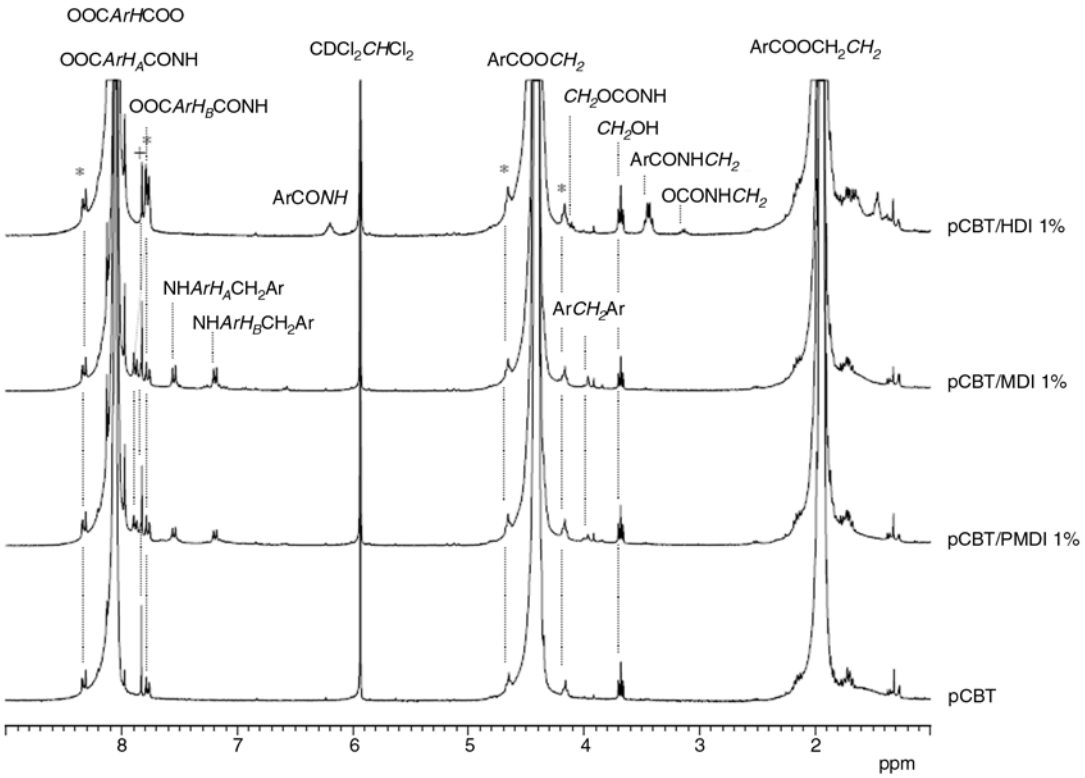

Figure 5. [1]H NMR spectra of pCBT and chain extended pCBT samples with peak assignments. (*) Satellite signals; (+) Unreacted pCBT; (Ar) Aromatic ring.

isocyanate reacted then with the pCBT terminal – COOH groups, forming thermally stable amide groups and liberating CO_2.

Further proton NMR experiments were performed to clarify this assumption and to see the influence of the compression moulding step on the chain extension reaction. Two chain extended samples which contained 1 wt% HDI were analyzed, before and after compression moulding. The corresponding spectra with peak assignments are depicted in Figure 6.

It can be seen that the sample before compression moulding showed higher intensity for the peaks at 3.1 and 4.1 ppm assigned to urethane, compared to the sample after compression moulding. Moreover, the triplet at 3.7 ppm assigned to hydroxyl end groups and the peaks assigned to amide groups (3.4, 6.2 and 7.8 ppm) increased after compression moulding. This supports the assumption that during compression moulding the urethane groups dissociated into isocyanate and hydroxyl end groups, the former subsequently reacting with pCBT carboxyl end groups. Apart from the above mentioned effect, the increase in hydroxyl end groups is believed to be also caused by hydrolysis to a certain degree during compression moulding in ambient atmosphere.

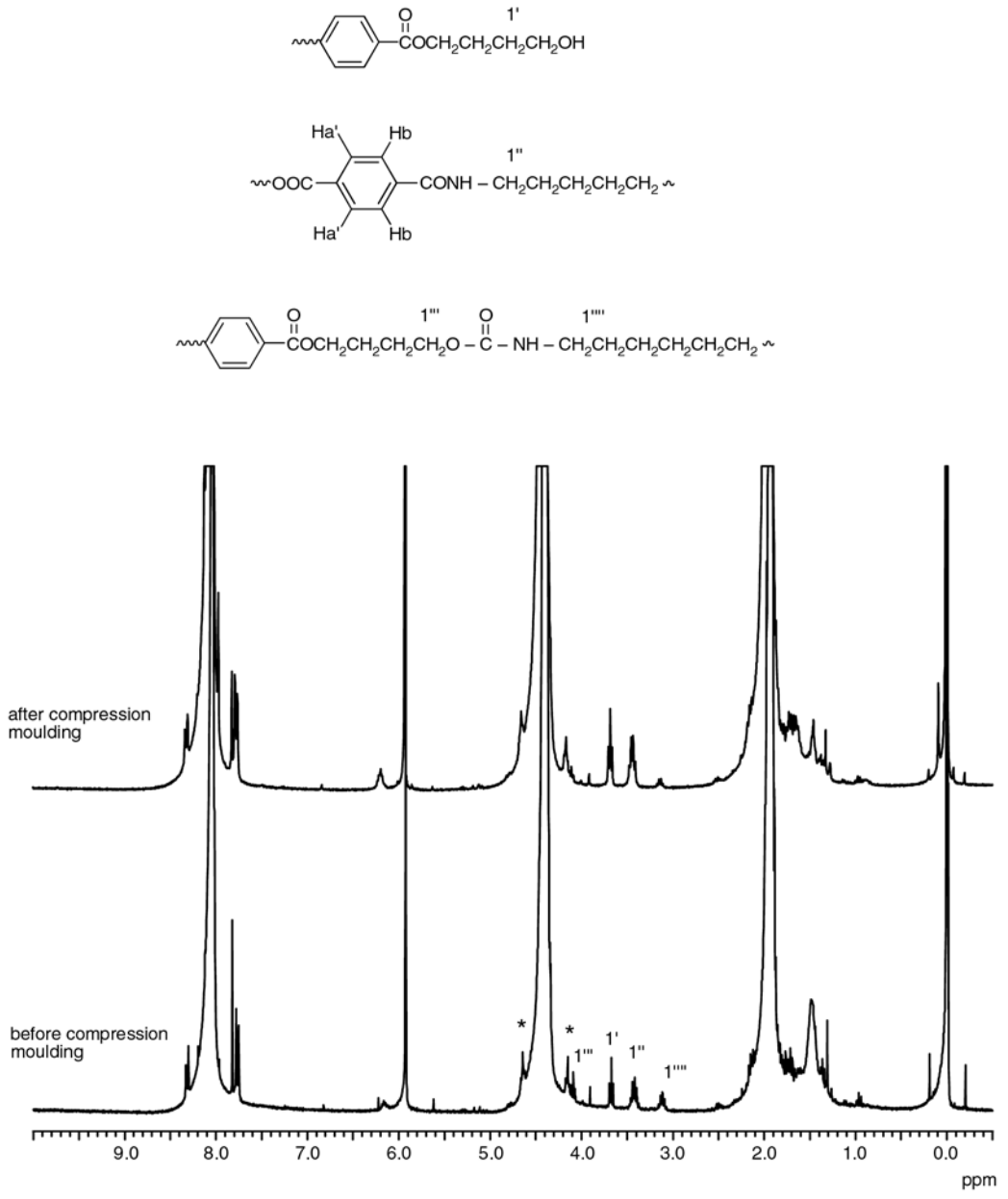

Figure 6. ^{1}H NMR spectra of pCBT/HDI 1% before and after compression moulding with peak assignments. (*) Satellite signals.

Therefore it can be concluded that the predominant reaction mechanism of pCBT and isocyanate is amide formation, although some urethane groups were detected in pCBT/HDI samples. The amount of formed urethane is less than 10% for pCBT/HDI but this is difficult to quantify for samples containing aromatic isocyanate due to signal overlapping.

3.4. Thermal properties

The thermal properties of compression moulded pCBT and pCBT/NCO samples were assessed by DSC analysis; the results are depicted in Figure 7 and Table 2. The observed trends are similar for all three types of used isocyanates, thus only the second heating scans of pCBT/PMDI are shown as representative sample series. Unmodified pCBT shows a minor melting peak at 215°C and a major peak at 224°C, typical for polyesters and ascribed to the recrystallization and melting of imperfect crystal structures [22]. The degree of crystallinity was calculated from the sum of both melting enthalpies and was found to be 36%. During the cooling scan the crystallization peak was observed at 193°C.

Regarding isocyanate modified pCBT samples, a general depression of crystallization and melting temperatures and their corresponding enthalpies can be observed (Table 2). Both melting temperatures decreased up to 3°C and crystallization temperatures reduced up to 6°C. The crystallinity was most effectively decreased (about 7%) when 0.75 wt% PMDI was used. Torres *et al*. [33], Zhang and coworkers [43] and Raffa *et al*. [32] modified recycled PET with di- and polyfunctional isocyanates

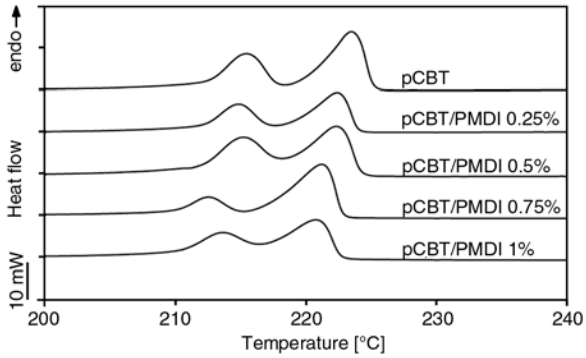

Figure 7. DSC second heating scan of compression moulded pCBT and pCBT/PMDI samples, heating and cooling rate of 10°C/min

and observed a similar tendency. This depression is due to the amide and urethane groups which form in the isocyanate reaction. These groups along the pCBT backbone disturb the chain symmetry and regularity and hence the crystallization rates are decreased, resulting in a decreased crystallinity and hence a higher toughness. Another consequence of the disturbed chain symmetry is a reduced lamellar thickness which leads to a decrease in melting temperature [33, 43]. No obvious tendency of the isocyanate modification on the glass transition of pCBT can be found, although most samples exhibited a slightly decreased T_g (1– 2°C), indicating an increased chain mobility.

3.5. Tensile properties

The mechanical properties of compression moulded samples were assessed by tensile tests and the results are shown in Table 1 and Figure 8. Unmodified pCBT is brittle and fails at ~8% elongation at

Table 2. Thermal properties of compression moulded pCBT and pCBT/NCO samples

Chain extender	Content [wt%]	1. Cooling		2. Heating			Crystallinity	Glass transition*
		T_c [°C]	ΔH_m [J/g]	T_{m1} [°C]	T_{m2} [°C]	ΔH_{m1+2} [J/g]	$X_{\Delta H}$ [%]	T_g]°C]
–	0	193.1	–50.6	215.4	223.5	50.7	35.7	66.4
PMDI	0.25	191.0	–49.3	214.8	222.4	47.9	33.7	66.5
	0.5	190.7	–47.8	215.1	222.3	46.9	33.0	67.0
	0.75	189.7	–47.3	212.5	221.3	40.8	28.7	63.9
	1	187.0	–44.4	213.5	220.8	42.5	29.9	65.3
MDI	0.25	192.1	–46.7	215.5	223.6	44.1	31.1	64.0
	0.5	189.8	–44.9	213.5	221.0	43.9	30.9	65.2
	0.75	190.4	–49.3	213.4	221.7	43.1	30.3	64.7
	1	188.9	–48.8	213.2	221.2	45.0	31.7	63.4
HDI	0.25	189.7	–44.9	214.0	221.8	45.2	31.8	65.6
	0.5	188.7	–42.8	213.0	221.1	41.3	29.1	65.6
	0.75	189.6	–48.2	214.4	222.5	46.3	32.6	63.0
	1	189.4	–47.7	214.0	222.0	46.2	32.5	62.7

*As determined by DMTA in tensile mode in the temperature range T = 30–220°C, f = 1 Hz, ε = 0.05%

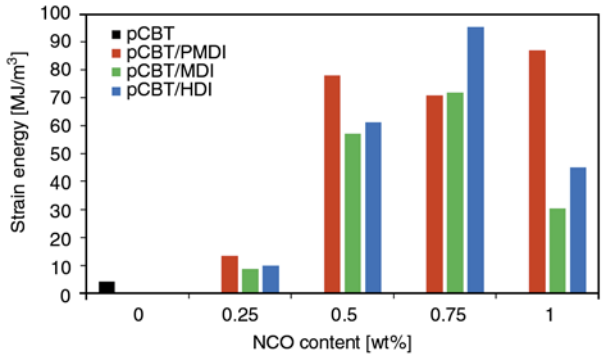

Figure 8. Strain energy versus NCO content for isocyanate-modified pCBT

break without yielding. By contrast, all isocyanate-modified samples showed a ductile behavior with an increased elongation at break. It can be seen that only 0.25 wt% isocyanate, regardless of type, results in a three-fold increase in failure strain although some samples failed in a brittle manner. All samples showed neck formation when the NCO content was increased to 0.5 wt%. The maximum failure strain for MDI- (22-fold increase) and HDI- (28-fold increase) modified samples was observed at 0.75 wt% NCO content see Table 1). In the case of polymeric isocyanate a maximum failure strain (27-fold increase) was found for 1 wt% PMDI. Toughness is better described by the strain energy calculated from tensile curves than by ultimate strain. Regarding the toughening effect by means of strain energy, the best result was obtained with 0.75 wt% HDI. But since PMDI was more effective over a wide NCO concentration range (0.5–1 wt%, see Figure 8), it appears to be the better toughening agent. Stiffness and strength decreased about 10% when samples contained the optimum amount of 0.5 to 1 wt% isocyanate. This decrease is small compared to other toughening methods like copolymerization and consistent with the marginal amount of isocyanate added. When these NCO-modified materials are employed, for instance in continuous fiber reinforced composites, the decrease in matrix stiffness will be compensated by the fibers. Additionally, the excellent toughness of isocyanate-modified pCBT may considerably increase the impact strength of composites.

3.6. SEM

In comparison to neat pCBT, pCBT/NCO samples were more difficult to break cryogenically. Therefore, small notches of ca. 2 mm depth were inserted with a razor blade on both sides of these specimens prior to cryo-fracture in order to ensure a brittle fracture. The micrographs of neat pCBT and pCBT/NCO 0.75 wt% are depicted in Figure 9. In all cases a single phase was observed and no signs of phase separation or incomplete reaction between pCBT and isocyanate could be found, indicating that the isocyanate had fully reacted with CBT which was also demonstrated by NMR. Moreover, no micron-sized plate- or prism-like crystals of unpolymerized CBT were detected, indicating a high degree of conversion of CBT to pCBT [14, 25]. Unmodified pCBT shows a smooth and uniform fracture surface. The small crests that are visible in Figure 9a are attributed to the rapid propagation of the crack during the fracture at low temperature that caused the crack front to oscillate. The detail at higher magnification (×10 000) clearly shows the absence of localized plastic deformation, indicating the brittle nature of unmodified pCBT (see detail of Figure 9a). Similarly, all modified samples fractured in a brittle manner (c.f. Figures 9b–9d), as expected due to the presence of notches and the low temperature used. Nevertheless, a somewhat rougher fracture surface compared to neat pCBT can be observed. This granular, rough structure is the result of the fracture of localized stretched matrix, as can be well observed at higher magnification [44]. This may indicate a certain amount of plastic deformation on a micrometer scale.

4. Conclusions

Cyclic butylene terephthalate oligomers were reacted in a ring-opening polymerization with three types of isocyanates: a bifunctional aromatic type, a bifunctional aliphatic type and a polymeric aromatic isocyanate. All reactions took place in a batch mixer. The isocyanate-modified samples showed a considerable torque increase compared to unmodified CBT, suggesting a higher molecular weight. Gel content measurements prior to compression moulding indicated a linear chain structure for the two bifunctional isocyanate-modified samples, whereas the polyfunctional PMDI-modified pCBT exhibited considerable gel formation at higher NCO contents. All compression moulded samples were completely soluble, indicating that the crosslinked structures in pCBT/PMDI samples changed to linear or branched structures during this second melting. Proton NMR analysis showed that the dominant chain extension

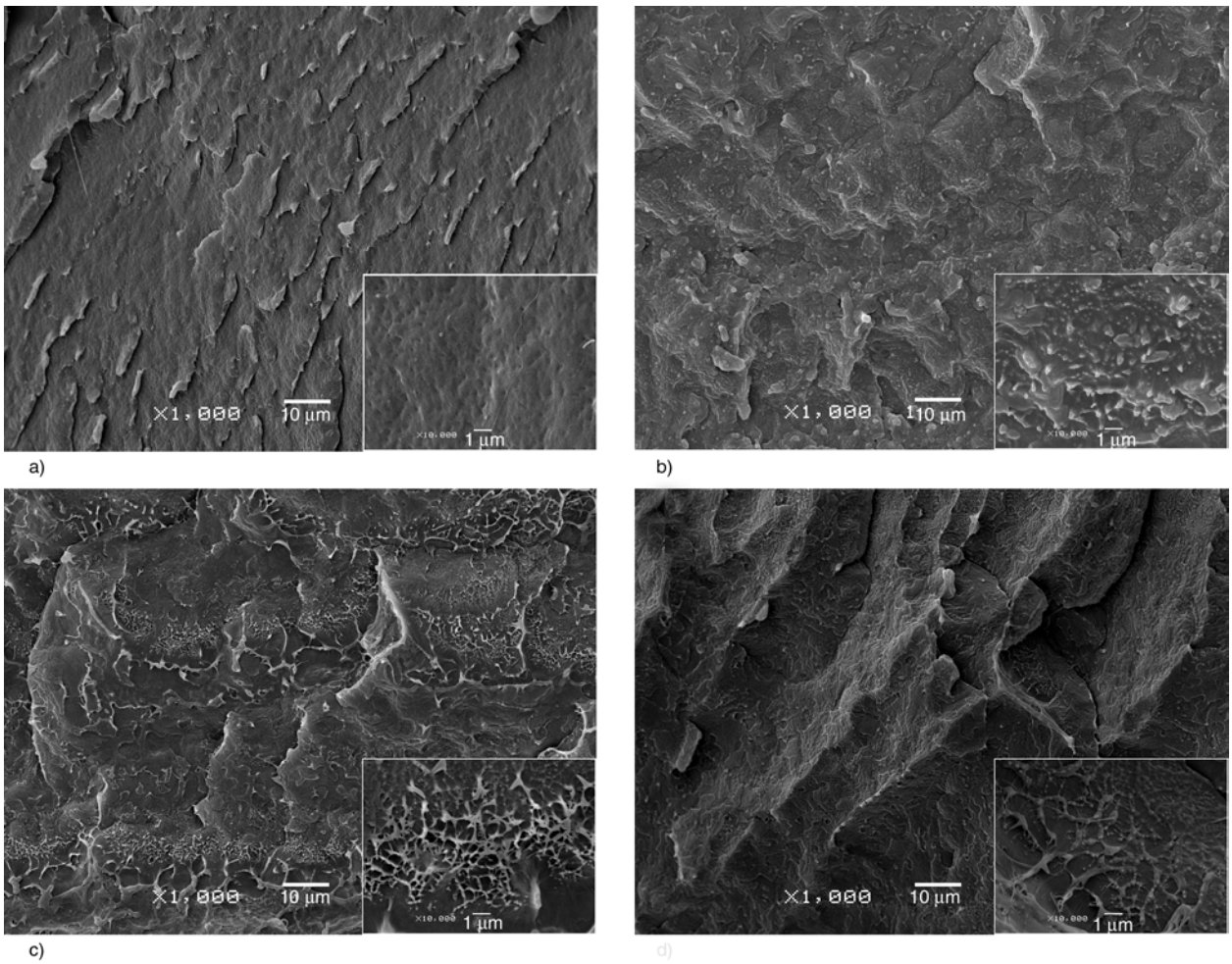

Figure 9. SEM micrographs of compression moulded pCBT (a), pCBT/PMDI 0.75% (b), pCBT/MDI 0.75% (c) and pCBT/HDI 0.75% (d)

reaction mechanism is the formation of thermally stable amide groups. NMR further indicated that pCBT/NCO samples before compression moulding contained more urethane groups, compared to samples after compression moulding. Moreover, the number of hydroxyl end groups and amide groups slightly increased after the compression moulding step. This supports the assumption that the urethane groups dissociated at the processing temperature into isocyanate and hydroxyl end groups, the former subsequently reacted with pCBT carboxyl end groups. DSC analysis revealed a general depression of melting and crystallization temperatures as well as degree of crystallinity. This decrease in crystallinity accounts for the toughening effect of isocyanates. A 22-fold to 28-fold increase in elongation at break was observed in tensile tests when the pCBT contained 0.75 to 1 wt% isocyanate. The highest toughness by means of strain energy was obtained with 0.75 wt% HDI. The most effective toughening agent was PMDI because it showed good toughness from 0.5 to 1 wt% NCO content. Stiffness and strength generally decreased about 10%. The fracture surfaces of isocyanate-modified samples exhibited a network-like fibrillation in a SEM analysis, indicating plastic deformation on a micrometer scale. It can be concluded that a toughened pCBT can be obtained when 0.5 to 1 wt% isocyanate is added to the ring-opening polymerization of CBT.

Acknowledgements

Authors gratefully acknowledge the financial support received from the Spanish Government through the project PSS-370000-2008-13.

References

[1] Brunelle D. J., Bradt J. E., Serth-Guzzo J., Takekoshi T., Evans T. L., Pearce E. J., Wilson P. R.: Semicrystalline polymers via ring-opening polymerization: Preparation and polymerization of alkylene phthalate cyclic oligomers. Macromolecules, **31**, 4782–4790 (1998). DOI: 10.1021/ma971491j

[2] Dion R. P., Bank D. H., Beebe M. C., Walia P., LeBaron P. C., Oelberg J. D., Barger M. A., Paquette M. S., Read M. D.: Polymerized macrocyclic oligomer nanocomposite compositions. U.S. Patent 2005/0059768 A1, USA (2005).

[3] Parton H., Baets J., Lipnik P., Goderis B., Devaux J., Verpoest I.: Properties of poly(butylene terephthatlate) polymerized from cyclic oligomers and its composites. Polymer, **46**, 9871–9880 (2005).
DOI: 10.1016/j.polymer.2005.07.082

[4] Baets J., Dutoit M., Devaux J., Verpoest I.: Toughening of glass fiber reinforced composites with a cyclic butylene terephthalate matrix by addition of polycaprolactone. Composites Part A: Applied Science and Manufacturing, **39**, 13–18 (2008).
DOI: 10.1016/j.compositesa.2007.09.013

[5] Baets J., Godara A., Devaux J., Verpoest I.: Toughening of isothermally polymerized cyclic butylene terephthalate for use in composites. Polymer Degradation and Stability, **95**, 346–352 (2010).
DOI: 10.1016/j.polymdegradstab.2009.11.005

[6] Mäder E., Gao S-L., Plonka R., Wang J.: Investigation on adhesion, interphases, and failure behaviour of cyclic butylene terephthalate (CBT®)/glass fiber composites. Composites Science and Technology, **67**, 3140–3150 (2007).
DOI: 10.1016/j.compscitech.2007.04.014

[7] Mohd Ishak Z. A., Leong Y. W., Steeg M., Karger-Kocsis J.: Mechanical properties of woven glass fabric reinforced *in situ* polymerized poly(butylene terephthalate) composites. Composites Science and Technology, **67**, 390–398 (2007).
DOI: 10.1016/j.compscitech.2006.09.012

[8] Parton H., Verpoest I.: *In situ* polymerization of thermoplastic composites based on cyclic oligomers. Polymer Composites, **26**, 60–65 (2005).
DOI: 10.1002/pc.20074

[9] Baets J., Devaux J., Verpoest I.: Toughening of basalt fiber-reinforced composites with a cyclic butylene terephthalate matrix by a nonisothermal production method. Advances in Polymer Technology, **29**, 70–79 (2010).
DOI: 10.1002/adv.20176

[10] Aurrekoetxea J., Zurbitu J., de Mendibil I. O., Agirregomezkorta A., Sánchez-Soto M., Sarrionandia M.: Effect of superelastic shape memory alloy wires on the impact behavior of carbon fiber reinforced *in situ* polymerized poly(butylene terephthalate) composites. Materials Letters, **65**, 863–865 (2011).
DOI: 10.1016/j.matlet.2010.12.020

[11] Balogh G., Czigány T.: Effect of air humidity on the mechanical properties of *in situ* polymerized cyclic butylene terephtalate matrix composites. Materials Science Forum, **659**, 1–5 (2010).
DOI: 10.4028/www.scientific.net/MSF.659.1

[12] Balogh G., Czigány T.: Effect of low UD carbon fibre content on mechanical properties of *in situ* polymerised cyclic butylene terephtalate. Plastics, Rubber and Composites, **40**, 121–124 (2011).
DOI: 10.1179/1743289811X12988633927871

[13] Yu T., Wu C. M., Chang C. Y., Wang C. Y., Rwei S. P.: Effects of crystalline morphologies on the mechanical properties of carbon fiber reinforcing polymerized cyclic butylene terephthalate composites. Express Polymer Letters, **6**, 318–328 (2012).
DOI: 10.3144/expresspolymlett.2012.35

[14] Karger-Kocsis J., Felhős D., Bárány T., Czigány T.: Hybrids of HNBR and *in situ* polymerizable cyclic butylene terephthalate (CBT) oligomers: Properties and dry sliding behavior. Express Polymer Letters, **2**, 520–527 (2008).
DOI: 10.3144/expresspolymlett.2008.62

[15] Jiang Z., Siengchin S., Zhou L-M., Steeg M., Karger-Kocsis J., Man H. C.: Poly (butylene terephthalate)/silica nanocomposites prepared from cyclic butylene terephthalate. Composites Part A: Applied Science and Manufacturing, **40**, 273–278 (2009).
DOI: 10.1016/j.compositesa.2008.12.003

[16] Baets J., Godara A., Devaux J., Verpoest I.: Toughening of polymerized cyclic butylene terephthalate with carbon nanotubes for use in composites. Composites Part A: Applied Science and Manufacturing, **39**, 1756–1761 (2008).
DOI: 10.1016/j.compositesa.2008.08.004

[17] Romhány G., Vígh J., Thomann R., Karger-Kocsis J., Sajó I. E.: pCBT/MWCNT nanocomposites prepared by *in situ* polymerization of CBT after solid-phase high-energy ball milling of CBT with MWCNT. Macromolecular Materials and Engineering, **296**, 544–550 (2011).
DOI: 10.1002/mame.201000381

[18] Wu F., Yang G.: Synthesis and properties of poly(butylene terephthalate)/multiwalled carbon nanotube nanocomposites prepared by *in situ* polymerization and *in situ* compatibilization. Journal of Applied Polymer Science, **118**, 2929–2938 (2010).
DOI: 10.1002/app.32625

[19] Wu F., Yang G.: Poly(butylene terephthalate)-functionalized MWNTs by *in situ* ring-opening polymerization of cyclic butylene terephthalate oligomers. Polymers for Advanced Technologies, **22**, 1466–1470 (2011).
DOI: 10.1002/pat.1762

[20] Fabbri P., Bassoli E., Bon S. B., Valentini L.: Preparation and characterization of poly (butylene terephthalate)/graphene composites by in-situ polymerization of cyclic butylene terephthalate. Polymer, **53**, 897–902 (2012).
DOI: 10.1016/j.polymer.2012.01.015

[21] Berti C., Binassi E., Colonna M., Fiorini M., Zuccheri T., Karanam S., Brunelle D. J.: Improved dispersion of clay platelets in poly(butylene terephthalate) nanocomposite by ring-opening polymerization of cyclic oligomers: Effect of the processing conditions and comparison with nanocomposites obtained by melt intercalation. Journal of Applied Polymer Science, **114**, 3211–3217 (2009).
DOI: 10.1002/app.30957

[22] Karger-Kocsis J., Shang P. P., Mohd Ishak Z. A., Rösch M.: Melting and crystallization of in-situ polymerized cyclic butylene terephthalates with and without organoclay: A modulated DSC study. Express Polymer Letters, **1**, 60–68 (2007).
DOI: 10.3144/expresspolymlett.2007.12

[23] Lanciano G., Greco A., Maffezzoli A., Mascia L.: Effects of thermal history in the ring opening polymerization of CBT and its mixtures with montmorillonite on the crystallization of the resulting poly(butylene terephthalate). Thermochimica Acta, **493**, 61–67 (2009).
DOI: 10.1016/j.tca.2009.04.004

[24] Tripathy A. R., Burgaz E., Kukureka S. N., MacKnight W. J.: Poly(butylene terephthalate) nanocomposites prepared by in-situ polymerization. Macromolecules, **36**, 8593–8595 (2003).
DOI: 10.1021/ma021364+

[25] Abt T., Sánchez-Soto M., Martínez de Ilarduya A.: Toughening of *in situ* polymerized cyclic butylene terephthalate by chain extension with a bifunctional epoxy resin. European Polymer Journal, **48**, 163–171 (2012).
DOI: 10.1016/j.eurpolymj.2011.10.017

[26] van Rijswijk K., Bersee H. E. N.: Reactive processing of textile fiber-reinforced thermoplastic composites – An overview. Composites Part A: Applied Science and Manufacturing, **38**, 666–681 (2007).
DOI: 10.1016/j.compositesa.2006.05.007

[27] Guo B., Chan C-M.: Chain extension of poly(butylene terephthalate) by reactive extrusion. Journal of Applied Polymer Science, **71**, 1827–1834 (1999).
DOI: 10.1002/(sici)1097-4628(19990314)71:11<1827::aid-app13>3.0.co;2-7

[28] Bahloul W., Bounor-Legaré V., Fenouillot F., Cassagnau P.: EVA/PBT nanostructured blends synthesized by *in situ* polymerization of cyclic cBT (cyclic butylene terephthalate) in molten EVA. Polymer, **50**, 2527–2534 (2009).
DOI: 10.1016/j.polymer.2009.03.055

[29] Tripathy A. R., Chen W., Kukureka S. N., MacKnight W. J.: Novel poly(butylene terephthalate)/poly(vinyl butyral) blends prepared by *in situ* polymerization of cyclic poly(butylene terephthalate) oligomers. Polymer, **44**, 1835–1842 (2003).
DOI: 10.1016/s0032-3861(03)00029-6

[30] Tripathy A. R., MacKnight W. J., Kukureka S. N.: In-situ copolymerization of cyclic poly(butylene terephthalate) oligomers and ε-caprolactone. Macromolecules, **37**, 6793–6800 (2004).
DOI: 10.1021/ma0400517

[31] Wu C-M., Huang C-W.: Melting and crystallization behavior of copolymer from cyclic butylene terephthalate and polycaprolactone. Polymer Engineering and Science, **51**, 1004–1013 (2011).
DOI: 10.1002/pen.21910

[32] Raffa P., Coltelli M-B., Savi S., Bianchi S., Castelvetro V.: Chain extension and branching of poly(ethylene terephthalate) (PET) with di- and multifunctional epoxy or isocyanate additives: An experimental and modelling study. Reactive and Functional Polymers, **72**, 50–60 (2012).
DOI: 10.1016/j.reactfunctpolym.2011.10.007

[33] Torres N., Robin J. J., Boutevin B.: Chemical modification of virgin and recycled poly(ethylene terephthalate) by adding of chain extenders during processing. Journal of Applied Polymer Science, **79**, 1816–1824 (2001).
DOI: 10.1002/1097-4628(20010307)79:10<1816::aid-app100>3.0.co;2-r

[34] Houghton R. P., Mulvaney A. W.: Mechanism of tin (IV)-catalysed urethane formation. Journal of Organometallic Chemistry, **518**, 21–27 (1996).
DOI: 10.1016/0022-328X(96)06223-7

[35] Segura D. M., Nurse A. D., McCourt A., Phelps R., Segura A.: Chemistry of polyurethane adhesives and sealants. in 'Handbook of adhesives and sealants' (ed.: Philippe C.) Elsevier, Amsterdam, Vol 1, 101–162 (2005).
DOI: 10.1016/S1874-5695(02)80004-5

[36] Tang X., Guo W., Yin G., Li B., Wu C.: Reactive extrusion of recycled poly(ethylene terephthalate) with polycarbonate by addition of chain extender. Journal of Applied Polymer Science, **104**, 2602–2607 (2007).
DOI: 10.1002/app.24410

[37] Chen B-K., Shen C-H., Chen S-C., Chen A. F.: Ductile PLA modified with methacryloyloxyalkyl isocyanate improves mechanical properties. Polymer, **51**, 4667–4672 (2010).
DOI: 10.1016/j.polymer.2010.08.028

[38] Yin L., Shi D., Liu Y., Yin J.: Toughening effects of poly(butylene terephthalate) with blocked isocyanate-functionalized poly(ethylene octene). Polymer International, **58**, 919–926 (2009).
DOI: 10.1002/pi.2613

[39] Lapprand A., Boisson F., Delolme F., Méchin F., Pascault J-P.: Reactivity of isocyanates with urethanes: Conditions for allophanate formation. Polymer Degradation and Stability, **90**, 363–373 (2005).
DOI: 10.1016/j.polymdegradstab.2005.01.045

[40] Chattopadhyay D. K., Webster D. C.: Thermal stability and flame retardancy of polyurethanes. Progress in Polymer Science, **34**, 1068–1133 (2009).
DOI: 10.1016/j.progpolymsci.2009.06.002

[41] van Bennekom A. C. M., Willemsen P. A. A. T., Gaymans R. J.: Amide-modified poly(butylene terephthalate): Thermal stability. Polymer, **37**, 5447–5459 (1996).
DOI: 10.1016/S0032-3861(96)00355-2

[42] Tuominen J., Kylmä J., Seppälä J.: Chain extending of lactic acid oligomers. 2. Increase of molecular weight with 1,6-hexamethylene diisocyanate and 2,2′-bis(2-oxazoline). Polymer, **43**, 3–10 (2002).
DOI: 10.1016/S0032-3861(01)00606-1

[43] Zhang Y., Guo W., Zhang H., Wu C.: Influence of chain extension on the compatibilization and properties of recycled poly(ethylene terephthalate)/linear low density polyethylene blends. Polymer Degradation and Stability, **94**, 1135–1141 (2009).
DOI: 10.1016/j.polymdegradstab.2009.03.010

[44] Roulin-Moloney A. C.: Fractography and failure mechanisms of polymers and composites. Springer, London (1989).

eXPRESS Polymer Letters Vol.7, No.2 (2013) 186–198
Available online at www.expresspolymlett.com
DOI: 10.3144/expresspolymlett.2013.17

Influence of microstructure on the crystallization of segmented copolymers constituted by glycolide and trimethylene carbonate units

*E. Díaz-Celorio, L. Franco, J. Puiggalí**

Departament d'Enginyeria Química, Universitat Politècnica de Catalunya, Av. Diagonal 647, E-08028 Barcelona, Spain

Received 25 July 2012; accepted in revised form 11 October 2012

Abstract. Hot and cold non-isothermal crystallization of copolymers having glycolide hard segments and glycolide-co-trimethylene carbonate soft segments was investigated by calorimetry, optical microscopy and synchrotron radiation experiments. The effect of composition and microstructural changes on thermal properties and morphology of crystallized samples was analyzed. Significant differences were found between the nucleation density of spherulites developed during cold crystallization. Crystallizations from the melt were characterized by a lamellar insertion mechanism and a broad distribution of crystal layer widths. By contrast, cold crystallized samples gave rise to practically constant long periods and narrower distributions. Soft segments with high glycolide content were more easily incorporated in the crystalline phase by decreasing the hard segment content of the sample. A significant decrease on the melting point was observed as well as a decrease of the amorphous layer thickness and an increase of the crystalline lamellar thickness when the sample was hot and cold crystallized, respectively.

Keywords: *biodegradable polymers, polyglycolide, surgical sutures, polymer crystallization, synchrotron radiation*

1. Introduction

Segmented copolymers are an interesting class of thermoplastic materials because mechanical properties similar to those of cross-linked elastomers can be achieved. Basically, copolymers are formed by the combination of a 'soft' block comprising units with a random distribution that gives rise to an amorphous phase with a low T_g and a 'hard' block comprising units which can crystallize to form rigid physical crosslinks. Properties are highly dependent on the phase separation induced by crystallization and on the structure of the crystalline phase. In general, reduced hard segment content hinders crystallization and leads to a decrease in the melting temperature.

Typically, hard blocks in segmented copolymers are polyurethanes, poly(butylene terephthalate) or polyamides, with polyethers or aliphatic polyesters acting as the soft blocks [1–4]. Polyurethanes have been intensively studied for several decades, mainly as tissue engineering scaffolds and vascular implants because of their compatibility, elasticity and ease of surface modification.

The use of several soft segments to achieve effective elastomeric and biocompatible properties is being investigated. Specifically, soft segments constituted by trimethylene carbonate units are gaining acceptance5 over more traditional ones based on diisocyanate units due to potential toxicity concerns regarding degradation products of the latter [6–8].

Segmented polymers also play a fundamental role in the development of bioabsorbable monofilament surgical sutures. These sutures have clear advantages over conventional braided sutures (e.g. polyg-

*Corresponding author, e-mail: Jordi.Puiggali@upc.es

lycolide) since they are more resistant to harbor microorganisms and exhibit less resistance to passage through tissue. However, these materials must meet strict requirements concerning mechanical properties (e.g. high flexibility and adequate tensile strength), which can only be achieved by employing copolymers with some elastomeric characteristics. Thus, commercial monofilament sutures are mainly constituted by hard segments based on polyglycolide and soft segments based on trimethylene carbonate, ε-caprolactone and/or *p*-dioxanone units (e.g. Maxon™ with glycolide and trimethylene carbonate [9], Monosyn™ with glycolide, ε-caprolactone and trimethylene carbonate [10], and Biosyn™ with glycolide, *p*-dioxane and trimethylene carbonate) [11]. The main goal of the present work concerns to the study of biodegradable segmented copolymers constituted by polyglycolide (PGL) hard segments and poly(glycolide-*co*-trimethylene carbonate) soft segments. The influence of the hard segment content and composition of the soft segment on the crystallization process will be considered since properties and degradability strongly depend on final morphology and crystallinity.

Phase separation, crystalline morphology and crystallization kinetics of simple block copolymers have been widely studied experimentally as well as theoretically [12–16]. Thus, microstructures that can form from the melt, from solution and for both thin and bulk samples have been extensively reviewed [17, 18], and even some works focus on the production of single crystals of diblock copolymers [19, 20]. By contrast, little research is available on the crystallization behavior of segmented copolymers mainly due to the complexity of their structure [21]. On the other hand, it is well known that polymer morphology has a strong influence on properties and also on degradation mechanisms when samples have bonds susceptible to hydrolytic or enzymatic attack.

Taking into account that polymers are usually processed under non-isothermal conditions, it is also highly important the get insight the understanding of the development of crystal morphology and crystallinity during the non-isothermal crystallization of the proposed segmented copolymers.

2. Experimental section

2.1. Materials

Synthesis of segmented copolymers constituted by glycolide and trimethylene carbonate followed a two-step strategy by which first a soft segment with a theoretically random distribution was prepared by reaction of the two monomers using a difunctional initiator (e.g. diethylenglycol). Then, two hard segments were incorporated at each end of the middle soft segment by subsequent postpolymerization of glycolide (Figure 1). A triblock copolymer was also obtained from a soft segment constituted by trimethylene carbonate only. Synthesis, characterization and evaluation of the basic properties of these samples had previously been performed [22]. Relevant data concerning the samples used in this work are summarized in Table 1. All copolymers are hereafter named as GL-*b*-[TMC-*co*-GL]-*b*-GL *x*–*z*, where *x* and *z* refer to TMC weight percentage in the soft segment and in the final product, respec-

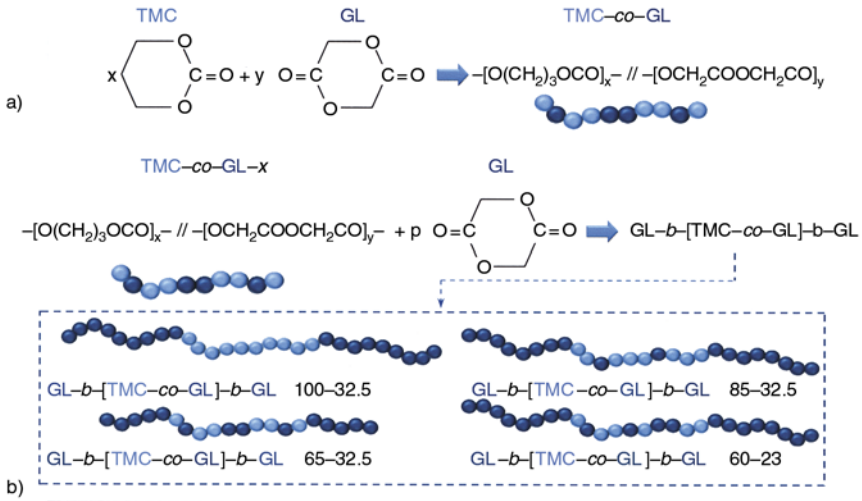

Figure 1. Schemes showing the two-step synthesis of GL-*b*-[TMC-*co*-GL]-*b*-GL *x*–*z* copolymers (a) and the expected microstructure of the studied samples (b)

Table 1. Hard segment content, molecular weight and basic calorimetric data of GL-*b*-[TMC-*co*-GL]-*b*-GL *x–z* samples

Sample		Hard segment [wt%]	M_w[a] [g/mol]	Cooling run		Heating run from quenched samples[b]				
x	z			T_c [ºC]	ΔH_c [J/g]	T_g [ºC]	T_c [ºC]	ΔH_c [J/g]	T_m [ºC]	ΔH_m [J/g]
100	32.5	67.5	51 000	184	49	–17.1	–	–	219.6	55
85	32.5	61.8	65 000	164	43	18.5	74	29	215.7	53
65	32.5	50.0	75 000	140	31	16.0	82	20	194.2	35
60	23.0	61.7	60 000	170	45	21.4	77	31	212.2	50

[a]From GPC data.
[b]At the maximum cooling rate allowed by the equipment.

tively. According to this notation, $x = 100$ corresponds to a triblock copolymer and $x = z$ to a random copolymer. The trimethylene carbonate content of the soft segment and the final copolymer allowed the estimation of the weight percentage of hard polyglycolide segments (*HS*), given by Equation (1), also summarized in Table 1:

$$HS\,[\mathrm{wt\,\%}] = 100\left(1 - \frac{z}{x}\right) \tag{1}$$

2.2. Measurements

Calorimetric data were obtained by differential scanning calorimetry with a TA Instruments Q100 series equipped with a refrigerated cooling system (RCS) operating from –90 to 550°C. Experiments were conducted under a flow of dry nitrogen with a sample weight of approximately 10 mg while calibration was performed with indium. Cooling and heating runs were performed at a rate of 3°C/min from the melt and glass state, respectively. The latter were carried out by cooling a previously melted sample at the maximum rate allowed by the RCS equipment.

Spherulitic morphologies were studied using a Zeiss Axioskop 40 Pol light polarizing microscope equipped with a Linkam temperature control system configured by a THMS 600 heating and freezing stage connected to an LNP 94 liquid nitrogen cooling system. Micrographs were taken with a Zeiss AxiosCam MRC5 digital camera. A first-order red tint plate was employed to determine the sign of spherulite birefringence under crossed polarizers. Spherulites were grown from homogeneous melt-crystallized thin films obtained by melting 1 mg of the polymer over microscope slides. Next, small sections of these films were pressed or smeared between two cover slides and inserted into the hot stage. The thickness of the squeezed samples was in all cases close to 10 μm. Samples were maintained at approximately 10°C above the polymer melting point for 5 minutes to wipe out sample thermal history effects. For hot crystallization experiments, samples were rapidly cooled to a selected temperature, isothermally maintained at this temperature for three minutes for equilibration and then cooled at 3°C/min. Optical microscopy observations revealed that no spherulites formed at the end of this isothermal step. For cold crystallization experiments, the above melted samples were quenched in liquid nitrogen and then heated to the selected crystallization temperature at a rate of 3°C/min.

Simultaneous time-resolved SAXS/WAXD experiments were carried out at the CRG beamline (BM16) of the European Synchrotron Radiation Facility of Grenoble. The beam was monochromatized to a wavelength of 0.098 nm. Polymer samples were confined between Kapton films and then held on a Linkam hot stage with temperature control within ±0.1°C. WAXD profiles were acquired during heating and cooling runs in time frames of 12 s and at rates of 3°C/min. Two linear position-sensitive detectors were used [23]: the SAXS detector was calibrated with different orders of diffraction from silver behenate whereas the WAXD detector was calibrated with diffractions of a standard of an alumina (Al_2O_3) sample. The diffraction profiles were normalized to the beam intensity and corrected considering the empty sample background. WAXD peaks were deconvoluted with the PeakFit v4 program by Jandel Scientific Software using a mathematical function known as 'Gaussian and Lorentzian area' (Pearson VII function). The correlation function and corresponding parameters were calculated with the CORFUNC program [24] for Fiber Diffraction/Non-Crystalline Diffraction, CCP13, provided by the Collaborative Computational Project 13.

3. Results and discussion

3.1. Thermal behavior

Figures 2 and 3 compare the cooling and heating runs from the melt and the glass state, respectively,

of all synthesized samples. Changes in the hot crystallization behavior and thermal properties of melt quenched samples (glass transition temperature, cold crystallization and melting peaks) were clearly observed (Table 1). Thermal history of the as synthesized samples was erased by a former heating run and consequently the reported calorimetric data correspond to samples processed in a similar way. The following observations can be made:

1. Hot crystallization peaks clearly shifted towards lower temperatures for lower *HS* contents (Figure 2 and Table 1). The influence of the *HS* content is noticeable since a decrease from 67.5 to 50% led to a shift of the crystallization peak from 184 to 140°C, respectively. Comparison between samples with the same *HS* content (i.e. GL-*b*-[TMC-*co*-GL]-*b*-GL 60–23 and GL-*b*-[TMC-*co*-GL]-*b*-GL 85–32.5 samples) revealed a slightly lower crystallization peak temperature for the sample with a lower glycolide content in its soft segment (i.e. 164°C, as against 170°C). Hence, crystallization is clearly favored by the increase of the hard segment content and even when the glycolide content of the soft segment is sufficient to allow its incorporation into the crystalline phase. Crystallization enthalpy data (Table 1) are also in full agreement with this conclusion.

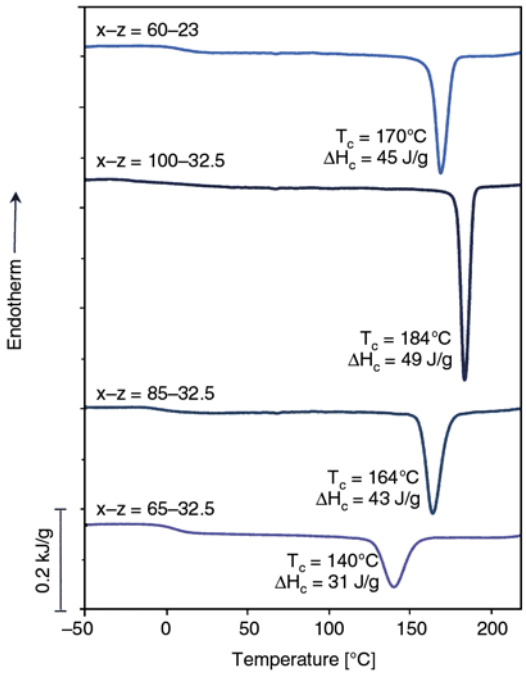

Figure 2. DSC cooling traces (3°C/min) of the indicated samples after being kept in the melt state for three minutes to erase the sample history

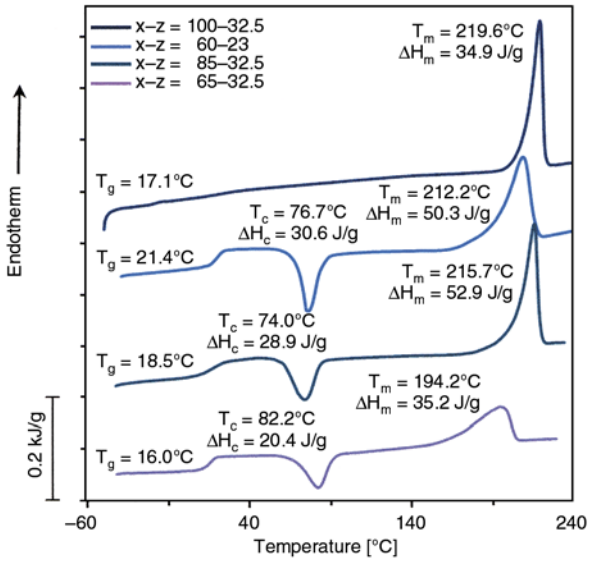

Figure 3. DSC heating traces (3°C/min) of the indicated copolymers after being quenched at the maximum rate allowed by the equipment from the melt

2. The glass transition temperatures of segmented samples having the same trimethylene carbonate content (i.e. GL-*b*-[TMC-*co*-GL]-*b*-GL 85–32.5 and GL-*b*-[TMC-*co*-GL]-*b*-GL 65–32.5) were similar and slightly lower than that of PGL due to their relatively low TMC content (32.5 wt%). This temperature logically increased (from 16.0–18.5 to 21.4°C) with decreasing the TMC content (i.e. from 32.5 to 23 wt%). In any case, it is worth emphasizing that all segmented copolymers had a completely miscible amorphous phase from which crystallization occurred during the subsequent heating process. Note that it was not possible to get completely amorphous samples at the maximum cooling rate allowed by the equipment since the enthalpy of the cold crystallization peak was always lower than the melting enthalpy. Thus, the amorphous phase should have a higher TMC content than expected from the copolymer composition and consequently cautions must be taken into account when T_g is correlated with composition. Logically, the block copolymer GL-*b*-[TMC-*co*-GL]-*b*-GL 100–32.5 had a significantly lower glass transition temperature since its soft segment was only constituted by trimethylene carbonate units.
3. Cold crystallization peaks appeared in a narrow temperature range (74–82°C) but slight differences in temperature and enthalpy were detected. These differences were in full agreement with the expected difficulty to crystallize when the

HS segment content decreased (i.e. the highest temperature and the lowest enthalpy corresponded to GL-*b*-[TMC-*co*-GL]-*b*-GL 65–32.5 sample).

4. Melting temperatures and enthalpies of the synthesized samples increased with *HS* content, indicating the formation of more perfect domains. Interestingly, the melting temperatures of the two samples with the same *HS* content (i.e. GL-*b*-[TMC-*co*-GL]-*b*-GL 60–23 and GL-*b*-[TMC-*co*-GL]-*b*-GL 85–32.5) were significantly different, and specifically a higher value was found when the soft segment was enriched on TMC units. The decrease in the melting temperature was associated with the incorporation of foreign units in the crystalline phase, which should be greater (in agreement with the experimental observation) when the soft segment was able to be incorporated into the crystalline phase due to its higher glycolide content. However, differences in lamellar thickness could also play an important role, and consequently synchrotron experiments appear to be a useful tool to understand the behavior observed.

3.2. Optical microscopy observations on the spherulitic morphologies of hot and cold crystallized samples

Spherulites obtained at the end of cold and hot non-isothermal crystallizations had always a positive birefringence and a fibrilar texture as shown in Figure 4. Spherulites observed in a determined cold crystallization experiment had a similar size, whereas a slightly greater variability (Figure 4d) was detected in the fewer spherulites that formed in the hot crystallized samples. Differences can mainly be attributed to an impingement effect instead of a thermal nucleation where nuclei became progressively active during the cooling rate.

Nucleation density of the studied thin films was in general low and high for hot and cold crystallized samples, respectively (Table 2, Figure 4). It is worth

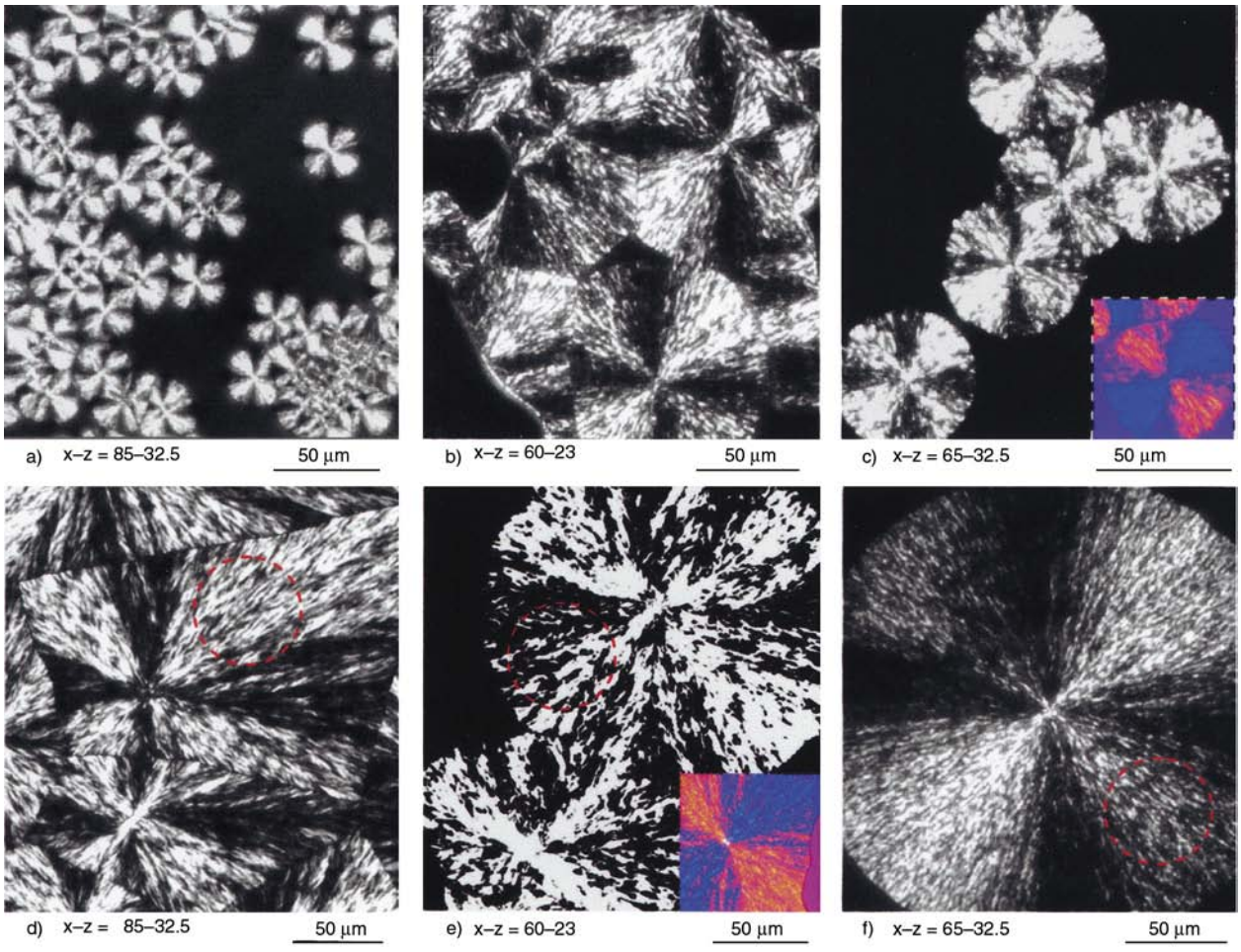

Figure 4. Spherulitic morphologies of GL-*b*-[TMC-*co*-GL]-*b*-GL *x–z* copolymers after being cold (a,b,c) and hot crystallized (d, e, f) at a rate of 3ºC/min from the glass and the melt state, respectively. Insets show details of micrographs taken using a first-order red tint plate

Table 2. Nucleation density of samples at the end of hot and cold non-isothermal crystallizations performed at a rate of 3ºC/min

Sample		Nucleation density [Nuclei/mm^2]	
x	z	Hot crystallization	Cold crystallization
85	32.5	60	1600
65	32.5	15	100
60	23	25	200

pointing out that clear differences were detected among the cold crystallized samples (Figures 4a, 4b and 4c) and consequently physical properties of the studied copolymers should be distinct when processed from the glass state.

It is remarkable that GL-*b*-[TMC-*co*-GL]-*b*-GL 60–23 had a considerable lower nucleation density than GL-*b*-[TMC-*co*-GL]-*b*-GL 85–32.5, although both samples had the same *HS* content. In fact, spherulites of the two samples at the end of crystallization had highly different diameter sizes (i.e. close to 55 and 12 μm). Crystallization may be disfavoured when the copolymer had TMC rich soft segments (e.g. *x*–*z* = 85–32.5) since they were not able to be incorporated in the crystalline structure, and hindered the proper arrangement of hard blocks. Note that soft and hard segments were initially well mixed as a consequence of their partial affinity and the spatial restrictions imposed by chemical linkages. Molecular transport plays a highly important role in low temperature cold crystallization and consequently the diffusion of soft segments far away from the crystal growth surface should be difficult. Crystallization proceeded in this case through the formation of a great number of primary nuclei.

Crystal growth rates (G) can be determined from non-isothermal cold crystallization experiments by measuring the change on the spherulitic radius (R) with temperature (T) during heating runs performed at a constant rate (dT/dt). The plot of the radius versus temperature allows the calculation of its first derivative (dR/dT) at each temperature and the corresponding G value [25, 26], as given by Equation (2):

$$G = \frac{dR}{dt} = \left(\frac{dR}{dT}\right)\left(\frac{dT}{dt}\right) \quad (2)$$

Figure 5 shows the evolution of the spherulitic radius and the crystal growth rate of the three segmented copolymers studied in this work when they were cold crystallized at a heating rate of 3°C/min. The high nucleation of GL-*b*-[TMC-*co*-GL]-*b*-GL 85–32.5 forced that its crystallization data were restricted to a short temperature interval whereas the other samples covered a higher temperature range since spherulites were able to grow to larger dimensions. It is clear that the estimated data corresponded to the left side of typically bell shaped curves and that the average crystal growth rate decreased in the order of *x*–*z* values: 85–32.5 > 60–23 > 65–32.5 (i.e. the lowest rate corresponded to the sample with the lowest polyglycolide hard content).

Spherulites coming from hot crystallization experiments had remarkably bigger diameter sizes (i.e. from 200 to 250 μm) than those above discussed, but in this case scarce differences were found between the different copolymers. Hence, variations on the overall crystallization rates were mainly a consequence of the differences between the crystal growth rates which in this case were mainly influenced by the secondary nucleation constant. Lamellae of copolymers having higher *HS* content had more favourable surfaces to induce secondary nucleation and showed the higher crystallization rates.

Well differentiated amorphous domains should always develop, as will be below explained from the analysis of synchrotron experiments. These domains were probably formed inside the spherulites and affected their optical properties. Note that chain connectivity should lead to crystalline PGL hard segments and amorphous TMC rich soft segments occupying the same spherulite. Black irregular zones in the birefringent spherulite arms (e.g. dashed circle in Figures 4d–4f where big spherulites

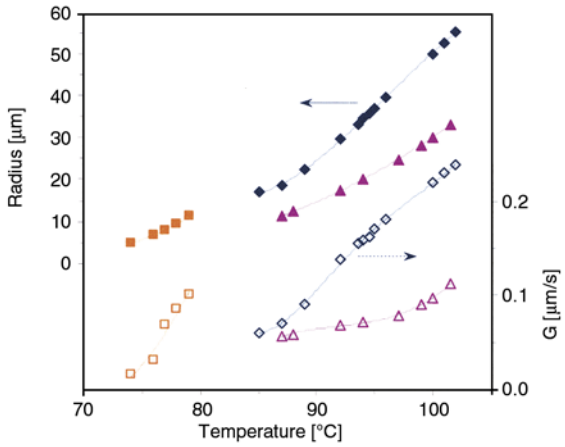

Figure 5. Evolution of the spherulitic radius (full symbols) and the crystal growth rate (empty symbols) during non-isothermal crystallization of GL-*b*-[TMC-*co*-GL]-*b*-GL 85–32.5 (■), GL-*b*-[TMC-*co*-GL]-*b*-GL 65–32.5 (▲) and GL-*b*-[TMC-*co*-GL]-*b*-GL 60–23 (♦) samples

are depicted) appeared and gave rise to a speckled appearance that can be clearly distinguished from usual ringed textures developed at high temperatures. Although, the spherulitic morphology depends on the crystallization temperature, it should be indicated that the indicated irregular textures were always observed independently of the polymer sample and even on the experimental crystallization conditions.

3.3. Study on the non-isothermal hot crystallization of GL-*b*-(TMC-*co*-GL)-*b*-GL samples by time-resolved SAXS/WAXD experiments

Figure 6a shows time-resolved SAXS profiles of the representative GL-*b*-(TMC-*co*-GL)-*b*-GL 85–32.5 sample obtained during a non-isothermal hot crystallization performed at a rate of 3°C/min. A SAXS long period peak is clearly seen at a value of the scattering vector $q = [4\pi/\lambda]\cdot\sin(\theta)$ in the 0.39–0.31 nm^{-1} range after subtraction of the empty sample background observed near the beam stop. This peak can be attributed to the lamellar structure of spherulites and started to appear at a temperature which in general decreased with reducing the *HS* content of the sample. Next, the peak intensity increased significantly with decreasing temperature until reaching a maximum value since a small decrease was subsequently detected. In any case, the SAXS peak reached high intensity, as expected for a large difference in electronic density of the amorphous and the crystalline phases. In fact, polyglycolide crystallizes according to a very tight packing that is peculiar with respect to other aliphatic polyesters [27, 28].

SAXS data were quantitatively analyzed by the normalized one-dimensional correlation function [29], $\gamma(r)$, which corresponds to the Fourier transform of the Lorentz-corrected SAXS profile, as shown by Equation (3):

$$\gamma(r) = \frac{\int_0^\infty q^2 I(q)\cos(qr)\mathrm{d}q}{\int_0^\infty q^2 I(q)\mathrm{d}q} \tag{3}$$

The scattering intensity was extrapolated to both low and high q values using Vonk's model [30] and Porod's law, respectively.

Correlation functions were used to determine the evolution during crystallization of the scattering invariant, Q, associated with the peak intensity and morphological parameters like the long period, L_γ, crystalline lamellar thickness, l_c, and amorphous layer thickness, l_a.

Figure 6b compares the evolution of the scattering invariant, Q, with the temperature for all samples. The resemblance between the scattering invariant profiles of the two samples with the same *HS* content (i.e. the maximum value of the invariant was reached at a relatively similar temperature) is worth noting, although the induction time and the slope of the invariant plot were slightly longer and lower, respectively, for the GL-*b*-[TMC-*co*-GL]-*b*-GL 85–32.5 sample. DSC data (Figure 2) also revealed that the hot crystallization peak of this sample was slightly wider and started to appear at a lower tem-

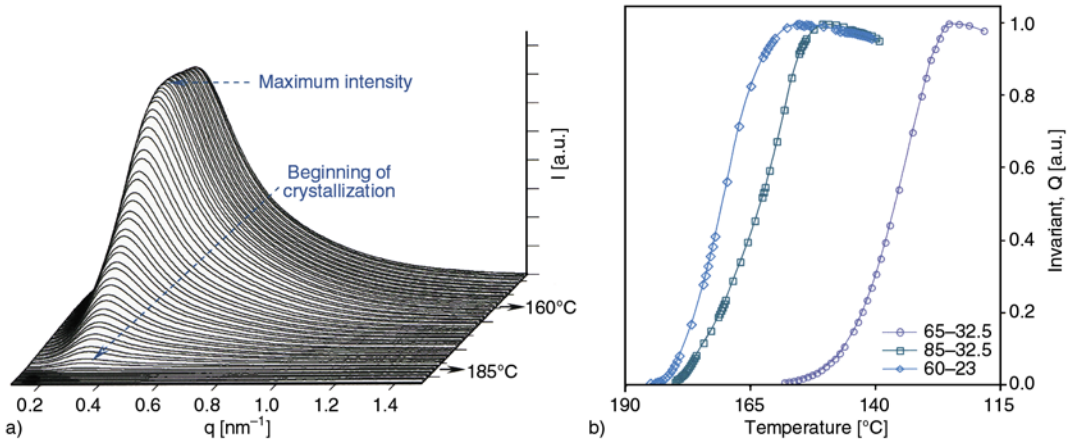

Figure 6. a) Time-resolved SAXS three-dimensional profiles of the GL-*b*-[TMC-*co*-GL]-*b*-GL 85–32.5 sample during the hot crystallization performed at a cooling rate of 3ºC/min. b) Plot of the intensity of the SAXS reflection during cooling for the three studied segmented copolymers

perature. Logically, the sample with the lowest *HS* content (i.e. GL-*b*-[TMC-*co*-GL]-*b*-GL 65–32.5) had the highest induction time and the corresponding invariant increased at the slowest rate, especially during the first crystallization steps.

The final decrease in the SAXS peak intensity, which was always detected, suggests a change in the amorphous phase since this value depends on the degree of crystallinity but also on the difference between the electronic densities of amorphous and crystalline phases. It is clear that on cooling the amorphous interlamellar component should adopt a more compact molecular arrangement.

Time-resolved WAXD profiles of the representative GL-*b*-[TMC-*co*-GL]-*b*-GL 85–32.5 sample obtained during the non-isothermal hot crystallization process can be seen in Figure 7. The initial WAXD profiles show two amorphous halos (inset) whose intensity decreases with crystallization and on which Bragg reflections form. Those most intense appear at 0.400 nm (q = 15.70 nm^{-1}) and 0.310 nm (q = 20.26 nm^{-1}) and can be indexed as the (110) and (020) reflections of the polyglycolide structure, defined by an orthorhombic unit cell having a = 0.522 nm, b = 0.619 nm and c (chain axis) = 0.702 nm [28]. The intensities of these reflections increased significantly at the beginning of crystallization and subsequently at a moderate rate (which should be associated with the secondary crystallization) until reaching an asymptotic value (see dashed lines in Figure 7). The SAXS long period peak and crystal diffractions appeared simultaneously for all samples, as expected for a crystallization process controlled by nucleation and crystal growth.

The evolution of the mass fraction of the crystalline phase in the sample, X_c^{WAXD}, was determined from the deconvoluted WAXD profiles as the ratio between the total intensities of the crystalline reflections I_c and the overall intensity I_T. Values at the end of crystallization ranged between 0.38 and 0.44 depending on the copolymer microstructure and were ordered in complete agreement with DSC observations (i.e. the highest and lowest crystallinities corresponded to samples with *x*–*y* values of 60–23 and 65–32.5, respectively).

Figure 8 plots the values of morphological parameters, scattering invariant and the calculated degree of crystallinity in function of the temperature during the cooling run performed at 3°C/min for GL-*b*-[TMC-*co*-GL]-*b*-GL 85–32.5 as a representative copolymer. A remarkable change in the long period (e.g. from 19.0 to 15.7 nm for the above sample) was detected for the three copolymers. This decrease was mainly due to the contribution of the crystalline lamellar thickness, which diminished in a similar ratio (i.e. from 15.5 to 12.5 nm). This is commonly observed when a lamellar insertion mechanism occurs because of spatial restrictions caused by the thicker lamellae that first crystallize at higher temperatures. As crystallization proceeds, new lamellae should form in the loosely stacked bundles of primary lamellae, leading to thinner defective crystals. Figure 8 also shows that the amorphous layer thick-

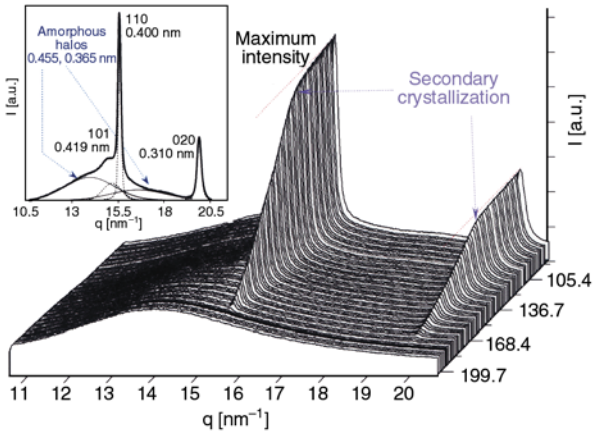

Figure 7. Time-resolved WAXD three-dimensional profiles of the GL-*b*-[TMC-*co*-GL]-*b*-GL 85–32.5 sample during the hot crystallization performed at a cooling rate of 3ºC/min. Inset shows the deconvolution of the X-ray profiles taken at room temperature

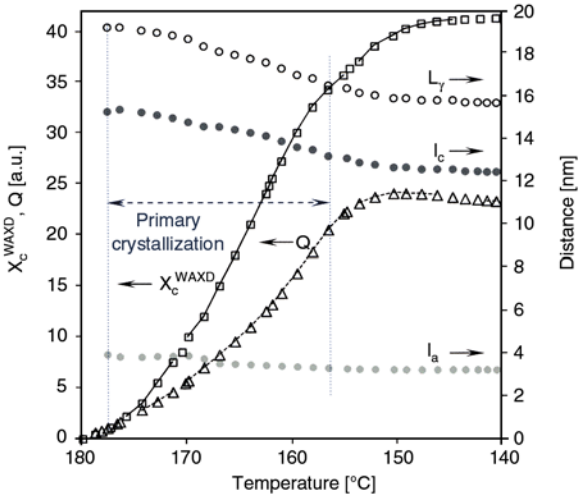

Figure 8. Temperature evolution of the long period, L_γ, crystal thickness, l_c, amorphous thickness, l_a, scattering invariant, Q, and degree of crystallinity X_c^{WAXD}, during a non-isothermal hot crystallization of the GL-*b*-[TMC-*co*-GL]-*b*-GL 85–32.5 sample performed at a cooling rate of 3ºC/min

ness remained practically constant except at the early stages of crystallization, where a slight decrease probably caused by an improved arrangement of the folding surfaces was observed. In fact, the maximum value of the invariant was reached and the main morphological changes had already taken place at the end of the primary crystallization (i.e. spacings remained practically constant or decreased very slightly during the secondary crystallization).

The amorphous and crystalline thicknesses evolved very similarly for the three samples (Figure 9) if the temperature shift associated with the hindered crystallization of the copolymer with the lowest *HS* content (i.e. GL-*b*-[TMC-*co*-GL]-*b*-GL 65–32.5) is considered. Note that all samples had very similar l_c values at the beginning (16–15.2 nm) and even at the end of the crystallization process. It merits attention that a slightly higher l_c value was determined for the sample with the lowest *HS* content during the first crystallization stage despite having the lowest crystallization temperature. This suggests that some TMC units were able to be incorporated into the crystalline lamellar regions, resulting in a clear decrease in amorphous lamellar thickness (Figure 9).

The assignment of l_a and l_c thicknesses was verified from the combined SAXS and WAXD data as it is well known that they could not be distinguished from the analysis of the correlation function [31, 32]. Thus, the ratio between X_c^{WAXD} and X_c^{SAXS} (determined as $l_c/(l_c + l_a)$) is an estimate of the volume-filling fraction of the lamellar stacks, X_S, which should be lower than 1 for a correct assignment. This value ranged between 0.55 and 0.42 for the three copolymers and the given assignment. The lowest volume-filling fraction corresponded to the GL-*b*-[TMC-*co*-GL]-*b*-GL 65–32.5 sample since amorphous phase domains between lamellar stacks were more significant in the samples with a lower *HS* content.

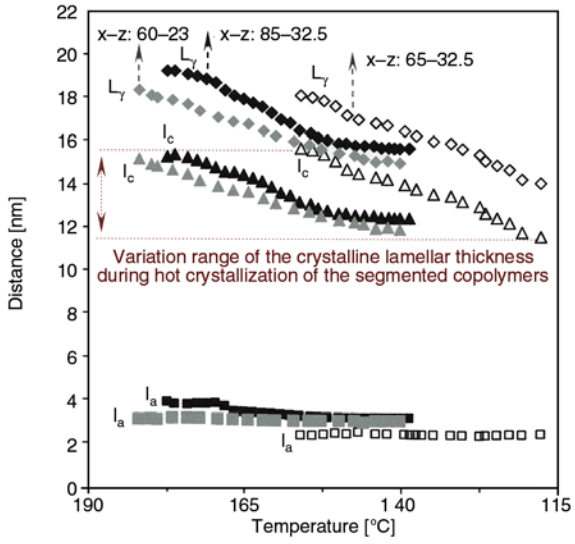

Figure 9. Temperature evolution of L_γ (♦), l_c (▲), and l_a (■) during non-isothermal hot crystallization performed at 3ºC/min with GL-*b*-[TMC-*co*-GL]-*b*-GL 85–32.5, GL-*b*-[TMC-*co*-GL]-*b*-GL 65–32.5 and GL-*b*-[TMC-*co*-GL]-*b*-GL 60–23 samples

Large discrepancies between SAXS and WAXD crystallinities are common in the literature [33] and have been explained by the assumption of the existence of amorphous phase domains. Note also that the given assignment led to a crystalline lamellar thickness, l_c, close to 12 nm, which is a rather typical value of polyester single crystals [34–36]. Moreover, a lamellar thickness of only 2.5–3.2 nm is difficult to combine with the *hkl* reflections detected in the X-ray diffraction patterns due to the expected reduced number of chain repeat units within the lamellae (i.e. lamellar thickness should correspond to four units only). Similarities in crystalline lamellar thicknesses attained for all samples clearly indicate that differences in melting points must be attributed to the incorporation of foreign trimethylene carbonate units into polyglycolide crystals rather than to the existence of lamellar crystals with different thicknesses. Specifically, the high melting point decrease observed for GL-*b*-[TMC-*co*-GL]-*b*-GL 65–32.5 (i.e. more than 20°C with respect to the GL-*b*-[TMC-*co*-GL]-*b*-GL 100–32.5 copolymer was determined in the heating runs performed at 20°C/min with the hot crystallized samples) is only due to the ability of soft segments to become incorporated into the crystalline phase.

Figure 10 compares the correlation functions achieved at room temperature with the three segmented copolymers, including that corresponding to the triblock sample for completeness. It is clear that the most different function was obtained with the GL-*b*-[TMC-*co*-GL]-*b*-GL 65–32.5 copolymer as clearly lower values were reached for the extrapolated l_a value and the spacings associated with the first minimum and maximum of the function.

The L_γ value associated with the most probable distance between the centers of gravity of two adjacent crystals (abscise of the first maximum of the correlation function) is generally greater than the long period determined from twice the abscise value of

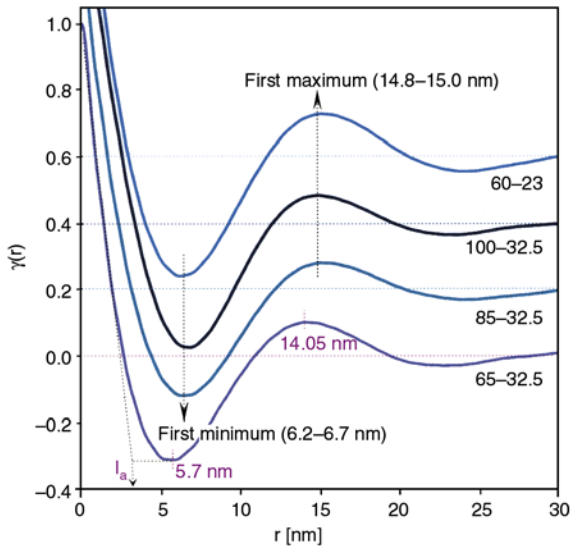

Figure 10. Correlation functions corresponding to the room temperature SAXS profile during cooling runs (3ºC/min) of the triblock and the three studied segmented copolymers

the first minimum of the correlation function, which is interpreted as the most probable distance between the centers of gravity of a crystal and its adjacent amorphous layer. This indicates a broader distribution of the layer widths of the major component [33], which corresponds to the crystal phase. This broadness is clearly higher for the GL-*b*-[TMC-*co*-GL]-*b*-GL 65–32.5 copolymer (i.e. 5.70 and 14.05 nm were determined, as it can be seen in Figure 10), which exhibited the greatest variation in crystalline lamellar thickness during crystallization, and consequently the largest insertion mechanism. Figure 10 also shows that the maximum and minimum of the correlation function were slightly better defined for the copolymer with the highest glycolide content (GL-*b*-[TMC-*co*-GL]-*b*-GL 60–23), suggesting a larger difference in the electronic densities of its amorphous and crystalline phases.

3.4. Study on the non-isothermal cold crystallization of GL-*b*-(GL-*co*-TMC)-*b*-GL samples by time-resolved SAXS/WAXD experiments

SAXS and WAXD profiles taken during cold crystallization of the representative GL-*b*-[TMC-*co*-GL]-*b*-GL 60–23 sample are illustrated in Figure 11. It can be seen that SAXS and WAXD peaks started to appear at practically the same temperature and that intensity increased significantly in the range of a few degrees. The secondary crystallization was slower and involved a larger temperature interval.

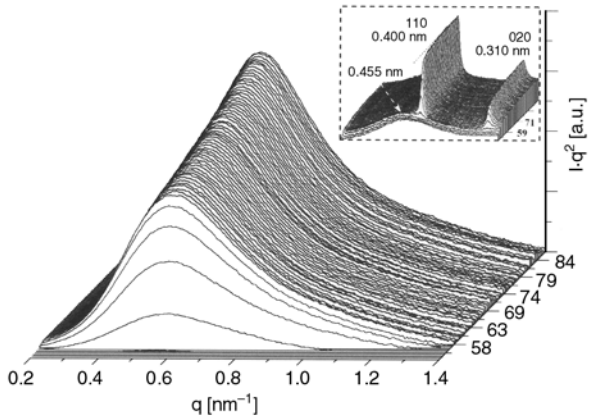

Figure 11. Time-resolved SAXS three-dimensional profiles of the GL-*b*-[TMC-*co*-GL]-*b*-GL 60–23 sample during the cold crystallization performed at a heating rate of 3ºC/min. Inset shows the corresponding time-resolved WAXD profiles

The SAXS peak always increased during crystallization since the effect of densification of the amorphous phase was not produced. Note that the temperature increased during cold crystallization, leading to an expansion of the amorphous phase.

The correlation functions corresponding to the SAXS profile of maximum intensity during hot crystallization and at the end of cold crystallization of the GL-*b*-[TMC-*co*-GL]-*b*-GL 60–23 sample are compared in Figure 12. It is clear that lamellae developed with a smaller thickness and a narrower width distribution during cold crystallization (the distance of the first maximum was practically twice that

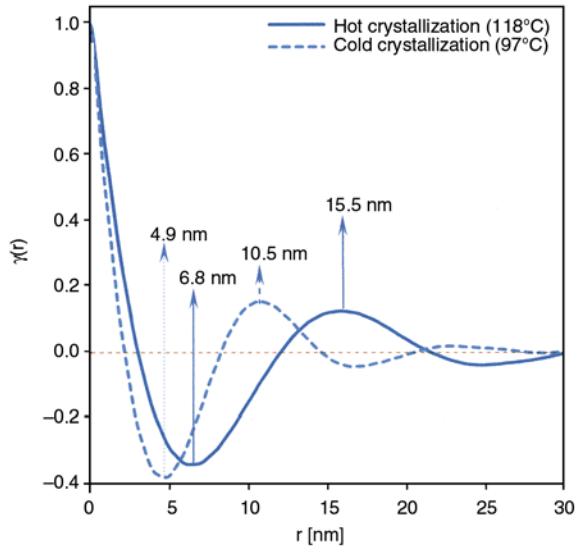

Figure 12. Comparison between correlation functions corresponding to the maximum intensity SAXS profile during hot crystallization (solid line) and at the end of cold crystallization (dashed line) of the GL-*b*-[TMC-*co*-GL]-*b*-GL 60–23 sample

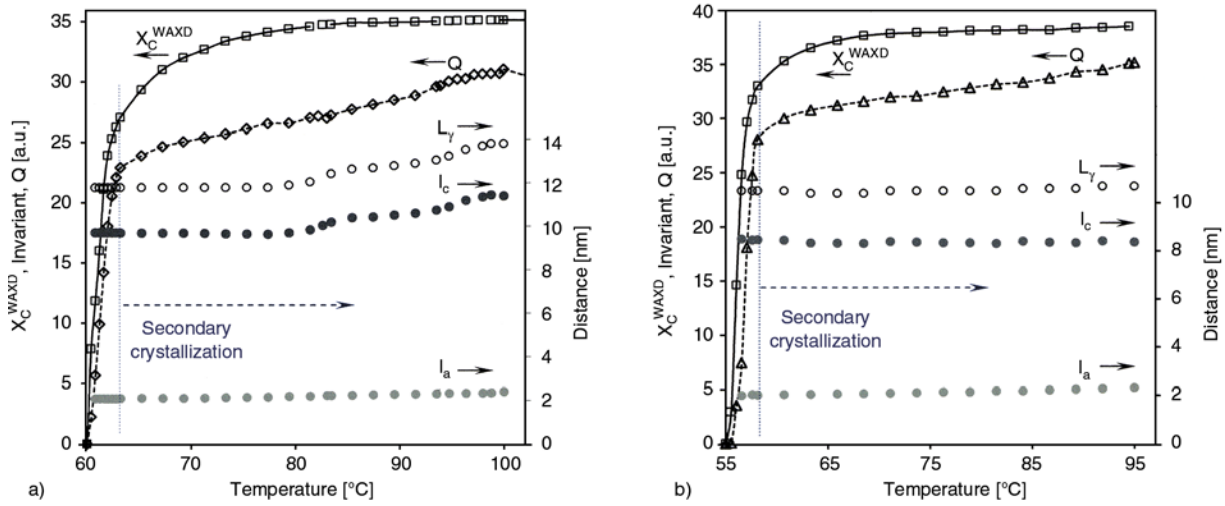

Figure 13. Temperature evolution of the long period, L_γ, crystal thickness, l_c, amorphous thickness, l_a, scattering invariant, Q, and degree of crystallinity X_c^{WAXD}, during a non-isothermal cold crystallization of the GL-*b*-[TMC-*co*-GL]-*b*-GL 65–32.5 (a) and GL-*b*-[TMC-*co*-GL]-*b*-GL 60–23 (b) samples performed at a cooling rate of 3ºC/min.

associated with the first minimum). In addition, minima and maxima were better defined in the correlation function corresponding to the cold crystallized sample, suggesting a larger difference in the electronic densities of amorphous and crystalline phases. The evolution of crystalline parameters, invariant and crystallinity are compared in Figure 13 for the two segmented copolymers with different *HS* content and composition. Both samples showed a rapid and very slow increase in the degree of crystallinity during primary and secondary crystallization, respectively. Final values were logically higher for the sample with higher hard segment content (i.e. 38%, as against 35%) and lower than those obtained after hot crystallization (i.e. 44%, as against 38% for the GL-*b*-[TMC-*co*-GL]-*b*-GL 60–23 sample).

Amorphous layer thickness remained practically constant during cold crystallization, was similar for the two samples and significantly lower than that deduced for the hot crystallized samples (i.e. 2.1–2.2 nm, as against 2.45–3.08 nm). The main distinctive feature between the two cold crystallized samples was the crystalline lamellar thickness, which was significantly higher for the sample with lower polyglycolide hard segment content. Once again, it seems that soft segments were able to be incorporated into the crystal phase, giving rise to more imperfect crystals and a lower melting point (i.e. 194°C, as against 212°C, as indicated in Table 1). Higher segregation of trimethylene carbonate rich sequences was consequently favored for samples with a higher glycolide content and consequently a lower crystalline thickness was attained. In this case, this thickness remained practically constant during crystallization in contrast with the moderate thickening process detected for the second sample (i.e. from 9.7 to 11.5 nm). Calculated SAXS crystallinities were identical than those determined at the end of hot crystallization (i.e. 83 and 79% for the samples with the low and high *HS* content, respectively), but obviously the amorphous phase domains between lamellar stacks were more significant in the cold crystallized samples. Thus, the volume-filling fraction decreased up to 0.42–0.48, the lowest value corresponding again to the sample with the lower *HS* content.

4. Conclusions

Small changes in composition (e.g. from 23 to 32.5 wt% of trimethylene carbonate units) and microstructure (e.g. hard segment content ranging from 50 to 67.5%) of segmented glycolide/trimethylene carbonate copolymers had a great influence on thermal properties, crystallization behavior and morphology of both spherulites and constitutive lamellae.

Spherulites were clearly different for cold crystallized samples; specifically, the highest nucleation rate and the lowest crystal growth rate were characteristic of copolymers having high and low hard segment contents, respectively.

Crystallization from the melt was characterized by a lamellar insertion mechanism whereas lamellar thickness remained practically constant or even increased slightly during cold crystallization. Amorphous phase domains were remarkable between

lamellar stacks and became more significant for cold crystallized samples.

The sample having the lowest hard segment content and a soft segment with a significant glycolide content gave rise to the lowest volume-filling fraction, the most imperfect crystals and the lowest melting temperature. In this case, some trimethylene carbonate units of the soft segment were able to be incorporated into the crystal phase, leading to the highest SAXS crystallinity. Specifically, the highest crystal lamellar thickness and the lowest amorphous layer thickness were attained for cold and hot crystallized samples, respectively. Furthermore, these samples had the broadest lamellar width distribution.

Acknowledgements

This research has been supported by grants from MCYT/FEDER and AGAUR (MAT2009-11503, 2009SGR-1208). We are grateful to Drs. François Fauth and Ana Labrador of the CRG BM16 beamline staff of CELLS (Consortium for the Exploitation of the Synchrotron Light Laboratory). We want also to express our gratitude to B.BRAUN Surgical S. A. for the collaboration and support.

References

[1] Adams R. K., Hoeschele G. K., Witsiepe W. K.: Thermoplastic polyether ester elastomers. in 'Thermoplastic elastomers – A comprehensive review' (eds.: Legge N. R., Holden G., Schroeder H. E.) Hanser, Munich, 163–196 (1987).

[2] Meckel W., Goyert W., Wieder W.: Thermoplastic polyurethane elastomers. in 'Thermoplastic elastomers – A comprehensive review' (eds.: Legge N. R., Holden G., Schroeder H. E.) Hanser, Munich, 13–46 (1987).

[3] Deleens G.: Polyether block amide thermoplastic elastomers. in 'Thermoplastic Elastomers – A comprehensive review' (eds.: Legge N. R., Holden G., Schroeder H. E.) Hanser, Munich, 215–230 (1987).

[4] Rodríguez-Galán A., Franco L., Puiggalí J.: Biodegradable polyurethanes and poly(ester amide)s. in 'Handbook of biodegradable polymers' (eds.: Lendlein A., Sisson A.) Wiley-VCH, Weinheim, 133–152 (2011).

[5] Asplund J. O. B., Bowden T., Mathisen T., Hilborn J.: Synthesis of highly elastic biodegradable poly(urethane urea). Biomacromolecules, **8**, 905–911 (2007). DOI: 10.1021/bm061058u

[6] Tuominen J., Kylmä J., Kapanen A., Venelampi O., Itävaara M., Seppälä J.: Biodegradation of lactic acid based polymers under controlled composting conditions and evaluation of the ecotoxicological impact. Biomacromolecules, **3**, 445–455 (2002). DOI: 10.1021/bm0101522

[7] Guelcher S. A.: Biodegradable polyurethanes: Synthesis and applications in regenerative medicine. Tissue Engineering Part B: Reviews, **14**, 3–17 (2008). DOI: 10.1089/teb.2007.0133

[8] Liow S. S., Lipik V. T., Widjaja L. K., Venkatraman S. S., Abadie M. J. M.: Enhancing mechanical properties of thermoplastic polyurethane elastomers with 1,3-trimethylene carbonate, epsilon-caprolactone and L-lactide copolymers via soft segment crystallization. Express Polymer Letters, **5**, 897–910 (2011). DOI: 10.3144/expresspolymlett.2011.88

[9] Bezwada R. S., Jamiolkowski D. D., Lee I-Y., Agarwal V., Persivale J., Trenka-Bethin S., Erneta M., Persivale J., Suryadevara J., Yang A., Liu S.: Monocryl® suture, a new ultra-pliable absorbable monofilament suture. Biomaterials, **16**, 1141–1148 (1995). DOI: 10.1016/0142-9612(95)93577-Z

[10] Erneta M., Vhora I. A.: Aliphatic polyesters of trimethylene carbonate, epsilon-caprolactone and glycolide. U.S. Patent 5854383, USA (1998).

[11] Rodeheaver G. T., Beltran K. A., Green C. W., Faulkner B. C., Stiles B. M., Stanimir G. W., Traeland H., Fried G. M., Brown H. C., Edlich R. F.: Biomechanical and clinical performance of a new synthetic monofilament absorbable suture. Journal of Long-Term Effects of Medical Implants, **6**, 181–198 (1996).

[12] Muthukumar M., Ober C. K., Thomas E. L.: Competing interactions and levels of ordering in self-organizing polymeric materials. Science, **277**, 1225–1232 (1997). DOI: 10.1126/science.277.5330.1225

[13] Zhu L., Chen Y., Zhang A., Calhoun B. H., Chun M., Quirk R. P., Cheng S. Z. D., Hsiao B. S., Yeh F., Hashimoto T.: Phase structures and morphologies determined by competitions among self-organization, crystallization, and vitrification in a disordered poly(ethylene oxide)-*b*-polystyrene diblock copolymer. Physical Review B, **60**, 10022–10031 (1999). DOI: 10.1103/PhysRevB.60.10022

[14] Ryan A. J., Hamley I. W., Bras W., Bates F. S.: Structure development in semicrystalline diblock copolymers crystallizing from the ordered melt. Macromolecules, **28**, 3860–3868 (1995). DOI: 10.1021/ma00115a016

[15] Schäffer E., Thurn-Albrecht T., Russell T. P., Steiner U.: Electrically induced structure formation and pattern transfer. Nature, **403**, 874–877 (2000). DOI: 10.1038/35002540

[16] Kawai T., Rahman N., Matsuba G., Nishida K., Kanaya T., Nakano M., Okamoto H., Kawada J., Usuki A., Honma N., Nakajima K., Matsuda M.: Crystallization and melting behavior of poly (L-lactic acid). Macromolecules, **40**, 9463–9467 (2007). DOI: 10.1021/ma070082c

[17] Reiter G., Strobl G.: Lecture notes in physics: Progress in understanding of polymer crystallization. Springer, Berlin (2007).

[18] Nandan B., Hsu J-Y., Chen H-L.: Crystallization behavior of crystalline-amorphous diblock copolymers consisting of a rubbery amorphous block. Polymer Reviews, **46**, 143–172 (2006).
DOI: 10.1080/15321790600646802

[19] Chen W. Y., Li C. Y., Zheng J. X., Huang P., Zhu L., Ge Q., Quirk R. P., Lotz B., Deng L., Wu C., Thomas E. L., Cheng S. Z. D.: 'Chemically shielded' poly(ethylene oxide) single crystal growth and construction of channel-wire arrays with chemical and geometric recognitions on a submicrometer scale. Macromolecules, **37**, 5292–5299 (2004).
DOI: 10.1021/ma0493325

[20] Casas M. T., Puiggalí J., Raquez J-M., Dubois Ph., Córdova M. E., Müller A. J.: Single crystals morphology of biodegradable double crystalline PLLA-*b*-PCL diblock copolymers. Polymer, **52**, 5166–5177 (2011).
DOI: 10.1016/j.polymer.2011.08.057

[21] Lee H. S., Yoo S. R., Seo S. W.: Domain and segmental deformation behavior of thermoplastic elastomers using synchrotron SAXS and FTIR methods. Journal of Polymer Science Part B: Polymer Physics, **37**, 3233–3245 (1999).
DOI: 10.1002/(SICI)1099-0488(19991115)37:22<3233::AID-POLB8>3.0.CO;2-J

[22] Díaz-Celorio E., Franco L., Rodríguez-Galán A., Puiggalí J.: Synthesis of glycolide/trimethylene carbonate copolymers: Influence of microstructure on properties. European Polymer Journal, **48**, 60–73 (2012).
DOI: 10.1016/j.eurpolymj.2011.10.014

[23] Rueda D. R., García-Gutiérrez M. C., Nogales A., Capitán M. J., Ezquerra T. A., Labrador A., Fraga E., Beltrán D., Juanhuix J., Herranz J. F., Bordas J.: Versatile wide angle diffraction setup for simultaneous wide and small angle X-ray scattering measurements with synchrotron radiation. Review of Scientific Instruments, **77**, 033904/1–033904/5 (2006).
DOI: 10.1063/1.2182806

[24] Rajkumar G., Al-Khayat H. A., Eakins F., Knupp C., Squire J. M.: The CCP13 *FibreFix* program suite: Semi-automated analysis of diffraction patterns from non-crystalline materials. Journal of Applied Crystallography, **40**, 178–184 (2007).
DOI: 10.1107/S0021889806048643

[25] Chen M., Chung C-T.: Analysis of crystallization kinetics of poly(ether ether ketone) by a nonisothermal method. Journal Polymer Science Part B: Polymer Physics, **36**, 2393–2399 (1998).
DOI: 10.1002/(SICI)1099-0488(19980930)36:13<2393::AID-POLB14>3.0.CO;2-Z

[26] di Lorenzo M. L.: Determination of spherulite growth rates of poly(L-lactic acid) using combined isothermal and non-isothermal procedures. Polymer, **42**, 9441–9446 (2001).
DOI: 10.1016/S0032-3861(01)00499-2

[27] Chatani Y., Suehiro K., Ôkita Y., Tadokoro H., Chujo K.: Structural studies of polyesters. I. Crystal structure of polyglycolide. Makromolekulare Chemie, **113**, 215–229 (1968).
DOI: 10.1002/macp.1968.021130119

[28] Furuhashi Y., Iwata T., Sikorski P., Atkins E. D. T., Doi Y.: Structure and morphology of the aliphatic polyester poly-β-propiolactone in solution-grown chain-folded lamellar crystals. Macromolecules, **33**, 9423–9431 (2000).
DOI: 10.1021/ma001070t

[29] Vonk C. G., Kortleve G.: X-ray small-angle scattering of bulk polyethylene II. Analyses of the scattering curve. Colloid and Polymer Science, **220**, 19–24 (1967).
DOI: 10.1007/BF02086052

[30] Vonk C. G.: A general computer program for the processing of small-angle X-ray scattering data. Journal of Applied Crystallography, **8**, 340–341 (1975).
DOI: 10.1107/S0021889875010618

[31] Hsiao B. S., Gardner K. H., Wu D. Q., Chu B.: Time-resolved X-ray study of poly(aryl ether ether ketone) crystallization and melting behaviour: 1. Crystallization. Polymer, **34**, 3986–3995 (1993).
DOI: 10.1016/0032-3861(93)90658-W

[32] Ikada Y., Jamshidi K., Tsuji H., Hyon S. H.: Stereocomplex formation between enantiomeric poly(lactides). Macromolecules, **20**, 904–906 (1987).
DOI: 10.1021/ma00170a034

[33] Hsiao B. S., Wang Z-G., Yeh F., Gao Y., Sheth K. C.: Time-resolved X-ray studies of structure development in poly(butylene terephthalate) during isothermal crystallization. Polymer, **40**, 3515–3523 (1999).
DOI: 10.1016/S0032-3861(98)00573-4

[34] Gestí S., Almontassir A., Casas M. T., Puiggalí J.: Crystalline structure of poly(hexamethylene adipate). Study on the morphology and the enzymatic degradation of single crystals. Biomacromolecules, **7**, 799–808 (2006).
DOI: 10.1021/bm050860d

[35] Gestí S., Casas M. T., Puiggalí J.: Crystalline structure of poly(hexamethylene succinate) and single crystal degradation studies. Polymer, **48**, 5088–5097 (2007).
DOI: 10.1016/j.polymer.2007.06.057

[36] Gestí S., Zanetti M., Lazzari M., Franco L., Puiggalí J.: Degradable polyoctamethylene suberate/clay nanocomposites. Crystallization studies by DSC and simultaneous SAXS/WAXD synchrotron radiation. European Polymer Journal, **45**, 398–409 (2009).
DOI: 10.1016/j.eurpolymj.2008.10.037

eXPRESS Polymer Letters Vol.7, No.2 (2013) 199–210
Available online at www.expresspolymlett.com
DOI: 10.3144/expresspolymlett.2013.18

An engineering approach to dry friction behaviour of numerous engineering plastics with respect to the mechanical properties

G. Kalácska[*]

[*]Institute for Mechanical Engineering Technology, Faculty of Mechanical Engineering, Szent István University, H-2100 Gödöllő, Hungary

Received 5 August 2012; accepted in revised form 13 October 2012

Abstract. Twenty-one different commercial-grade engineering polymers, including virgin and composite types, were selected for testing, based on mechanical engineering practices. Three groups were formed according to typical applications: 1) Sliding machine element materials; 2) Mechanically load-carrying machine element materials that are often subjected to friction and wear effects; and 3) Additional two amorphous materials used as chemically resistant materials that have rare sliding load properties. The friction running-in state was tested using a dynamic pin-on-plate test rig. During steady-state friction tests, two *pv* regimes (0.8 and 2 MPa·ms^{-1}) were analysed by a pin-on-disc test system. Based on the measured forces on ground structural steel, surface friction coefficients were calculated and analysed with respect to the mechanical effects of friction. The friction results were evaluated by the measured mechanical properties: yield stress, Shore D hardness, Young's modulus and elongation at the break.
The three material groups exhibited different trends in friction with respect to changing mechanical properties. Linear (with varying positive and negative slopes), logarithmic and exponential relationships were observed, and occasionally there were no effects observed. At steady-state friction, the elongation at the break had less effect on the friction coefficients. The dynamic sliding model, which correlates better to real machine element applications, showed that increasing hardness and yield stress decreases friction. During steady-state friction, an increase in *pv* regime often changed the sign of the linear relationship between the material property and the friction, which agrees with the frictional theory of polymer/steel sliding pairs.

Keywords: *material testing, friction of plastics, mechanical properties*

1. Introduction

The effect of friction on the wear of engineering polymers is a complex and intricate consequence of the micro- and macroscopic interactions of surfaces moving against one another. Friction and the resulting wear are not material properties of plastics; therefore, they cannot be reduced to tabular data of material characteristics that can be found in relevant manuals. Determining friction and the resulting wear involves more complex examination because they are characteristics of a frictional contact system where the effects of the entire system are manifest. Precise knowledge of system conditions is essential to evaluate the friction and resulting wear [1]. These materials have system-dependent tribological behaviour; thus, trends can be defined at a given condition, and the materials can be compared. The system approach is well-known from the literature [2,

[*]Corresponding author, e-mail: kalacska.gabor@gek.szie.hu

3] and was published in the former German standard DIN 50322 [4] in the section on wear test categories.

The tribology of polymeric materials involves complicated frictional systems where the deformation and thermal effects of the contact zone, time-dependent stress states, surface energy characteristics, etc., play important roles [5]. Because polymers have gained a more accepted position among industrial materials, plastics are no longer second–class materials. They have become elements of real machines, and the need for tribological knowledge has risen from the many frictional applications now involving plastics. Some general knowledge of polymers and composites has been published summarising global experiences, e.g., wear mechanism and particle detachment, transfer films, and the effects of reinforcements and lubricants [6–8]. Large numbers of papers have addressed a given material family, e.g., polyamides, under different conditions, such as abrasive effects [9–12]. With respect to dry or lubricated conditions of polymer sliding, the principles of some commonly used material families have been tested, and the role of adhesion and surface energy has been discussed [13, 14]. There have been initiatives to find the correlation between the wear behaviour and the mechanical properties of polymers, but difficult or weak correlations have been found, primarily because of the limited condition of the wear systems and the selected material families [15–18]. In recent years, research has focused on the surface-modified engineering polymers and nano-composites because of new technology that enhances the tribological behaviour by changing the molecular or matrix structure to change the surface or bulk properties [19–21].

In the tribological literature of engineering polymers, most of the research is related to materials, material families or operating conditions. Little information is available regarding mechanical engineering applications to compare the different material families and typically applied material groups. The present research investigates the frictional behaviour of several engineering polymers in sliding and mechanical load-carrying applications to determine trends between the mechanical properties and friction.

2. Selected materials and their mechanical properties

The engineering plastic samples tested were machined from commercially available semi-finished stock shapes, namely, from rods. The rods were manufactured by Sustaplast GmbH (Germany), Quadrant EPP (Belgium), Ensinger GmbH (Germany), Teraglobus Ltd. (Hungary) and Quattroplast Ltd. (Hungary), and they were procured from Teraglobus (Hungary) and Quattroplast (Hungary). The mechanical properties were measured according to the appropriate standards (tensile MSZ EN ISO 527-1 and hardness MSZ EN ISO 868: 2003). Then, the mechanical and tribological test samples were machined. After one week of conditioning in the laboratory (23ºC/60% *RH*), mechanical measurements were repeated five times and averaged. The measured data were not equal to the producers' indicative values, not even for the conditioned polyamide-type materials. At Teraglobus Ltd.'s laboratory (Instron 3366 for tensile tests, THS-180 hardness tester for Shore D), the following properties were determined: yield stress (R), Young's modulus (E), elongation at break (A) and

Table 1. Selected materials

Simplified name (code)	Known composition	Simplified name (code)	Known composition
PTFE	PTFE unmodified	PETP	PETP unmodified
PTFE/graphite	PTFE+(graphite)	PETP TF	PETP+(PTFE)
UHMW-PE HD500	UHMW-PE HD500 unmodified l	POM C	POM C unmodified
UHMW-PE HD1000	UHMW-PE HD1000 unmodified	PPS HPV	PPS+(GF+oil)
PA 4.6	PA 4.6 unmodified	PSU	PSU unmodified
PA6E	PA6 Extruded, unmodified	PES	PES unmodified
*PA6G(Mg)	*PA6G(Mg) cast, unmodified	PVDF	PVDF unmodified
*PA6G(Mg)/oil	*PA6G(Mg)+(oil)	PEEK	PEEK unmodified
**PA6G(Na)/MoS_2	**PA6G(Na)+(MoS_2)	PEEK GF	PEEK+(GF)
**PA6G/PE	**PA6G(Na)+(PE)	PEEK Mod	PEEK+(CF+PTFE+graphite)
PA 66 GF30	PA 66+(GF)		

*Mg catalytic casting process
**Na catalytic casting process

Table 2. Material groups and mechanical properties (measured and averaged values)

Simplified name	R [MPa]	A [%]	E [MPa]	H [Shore D]
Sliding materials (Material Group 1)				
PTFE	30.9	384	544.8	55.2
PTFE/graphite	33.1	222	606.5	58.6
UHMW-PE HD500	28.4	585	1350.8	66.0
UHMW-PE HD1000	20.6	298	744.6	62.3
PA6G(Mg)/oil	52.5	58	1808.2	81.5
PA6G(Na)/MoS_2	65.5	53	2020.4	82.1
PA6G/PE	45.1	78	1811.4	77.4
PETP TF	75.3	12	2806.3	82.8
PPS HPV	74.1	8	3712.8	80.1
PEEK Mod	121.5	5	7808.2	85.3
PETP	85.6	19	2991.7	83.3
Load-carrying materials (Material group 2)				
PA 4.6	56.5	106	11288.8	78.5
PA6E	47.2	81	1603.6	79.2
PA6G(Mg)	57.9	69	2034.4	82.3
PA 66 GF30	89.2	19	3900.8	84.7
POM C	74.5	34	2996.4	83.6
PVDF	58.3	30	2110.5	81.4
PEEK	108.4	25	3904.6	87.2
PEEK GF	156.9	5	9688.5	89.1
Other amorphous (Material Group 3)				
PSU	77.8	19	2608.5	83.1
PES	87.1	16	2689.3	82.6

Shore D hardness (*H*). Table 1 shows the materials and the published compositions, while Table 2 shows the measured properties in the three material groups: a) sliding, b) load-carrying and c) other amorphous structural materials. The selected sliding materials are typically used for slide bearings, trust washers, sliding supports and pads, gears and worms, where *pv* (normal load multiplied by sliding speed) is the basis of the construction and the design. The plastics of the second group often face significant mechanical loads in addition to friction effects. The third group (amorphous PES and PSU) is rarely subjected to frictional loads, although it is possible. The target applications for PES and PSU focus mainly on chemical and heat resistance. The knowledge, experiences and suggestions for engineering solutions of the main producers (Quadrant, Ensinger, and Röchling) serve as the basis for the grouping.

3. Experimental design

3.1. Pin-on-disc and dynamic pin-on-plate test systems

To measure the friction in comparative test systems, the pin-on-disc test method and the dynamic pin-on-plate test system are selected, using classical

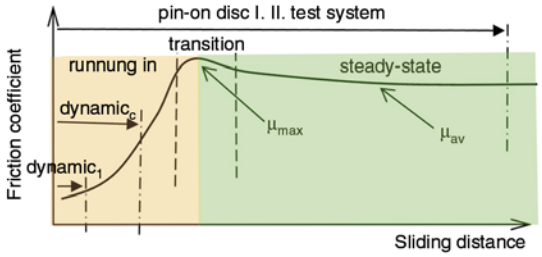

Figure 1. Friction stages between polymer/steel pairs and the placement of pin-on-disc and dynamic pin-on-plate test systems.
dynamic$_1$: 1 cycle of sliding path test within the running-in phase
dynamic$_c$: Complete (5 cycles of sliding path) dynamic sliding test
pin-on-disc I, II test systems: After the running-in period, μmax and μav are measured

(not overloaded) polymer/steel friction processes [1], as shown in Figure 1 [22]. The load and sliding speed values of the test systems correspond to dry slide bearing applications of engineering plastics with high safety factors.

After starting, the friction coefficient increases during the running-in period. During the running-in period, the contact zone is being reformed and restructured (e.g., the topographical and surface layers), strongly influencing the steady-state friction behaviour and the real working lifetime. After the running-in period, a transient zone appears where the maximum coefficient of friction can be measured. During the running-in, a polymeric film forms on the micro-topography of the steel surface. An increasing force is then required to continue the sliding process because of the interfering mechanical cutting and forming of the contact zone and adhesive effects between the materials. As the polymer film forms, the adhesive component of the friction increases from the polymer/polymer contact, which has stronger adhesion than the steel/polymer contact. At the maximum point of friction in the transition zone, the re-adhesion process of the polymer film starts to provide a dynamic balance during further sliding, resulting in what is termed the steady-state of friction (force and coefficient). This phenomenon is shown in Figure 2 [22].

As shown in Figure 1, the pin-on-disc measuring system evaluates the friction process at steady-state in two *pv* regimes, characterising the μ_{max} and μ_{av} (average). The *pv* regimes set for the tests are typical for the normal application of plastic machine elements having a high safety factor. The difference

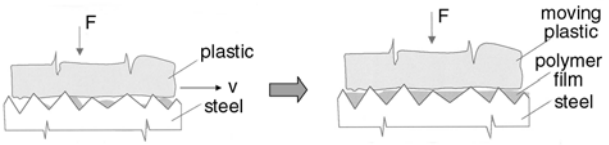

Figure 2. Running-in (left) and steady-state friction (right) with dynamic balance of polymer film adhesion and re-adhesion (μ_{av})

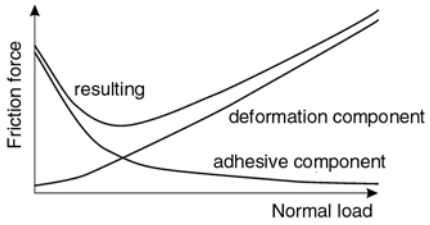

Figure 3. Theory of friction components

between the two systems is the normal load; the sliding speed is held constant. During the evaluation, it is important to know how the change in normal load influences the frictional force and coefficient [1, 22, 23] (Figure 3). According to the theory of friction [5, 23], the dry friction force, F_f, is equal to the sum of the adhesion and the deformation components, $F_f = F_a + F_d$. The special case at low loads, when the deformation component may be orders of magnitude smaller than the adhesion component ($F_a >> F_d$), leads to the relation $F_f \approx F_a$. The research results will show that the set pv-s yields near-optimum (Figure 3) friction values for most of the selected materials.

The dynamic pin-on-plate test system was utilised during the running-in period. Dynamic$_1$ represents one sliding cycle of the programmed sliding path, while dynamic$_c$ refers to the complete dynamic test program, i.e., five repeated cycles of the programmed sliding path. The dynamic modelling method and test rig were developed at Szent István University, where a better laboratory model of the real dynamic effects of the machine elements could be made. The details of the method have been described previously [24].

3.2. Test conditions

Table 3 summarises the test conditions.

The pin-on-disc measurements (Figure 4) were performed according to wear test category VI of the German standard DIN 50322 [4]. The fixed plastic samples, with a diameter of 6 mm and a height of 15 mm, were used as pins for the rotating S235 steel disc, which has a finely ground surface with an average roughness of R_a = 0.05–0.1 μm. The pin was positioned on the disc for each experiment at a radius of 100 mm. During the measurements, the following parameters were simultaneously measured: the coefficient of friction (μ), based on the measured forces (F_x and F_y), and the wear, characterised by the vertical displacement of the pin holder (d) and the temperature close to contact (T). The friction results are presented below.

During the dynamic friction tests (dynamic pin-on-plate), a moving plastic sample pin with a diameter of 4 mm moved along the programmed path (Figure 5) with a dynamic change of normal load and speed values, combined with inertial effects at the bends. The dynamic test completed the full path five times (five cycles) at five average loads and five speeds. During the evaluation, the first cycle is

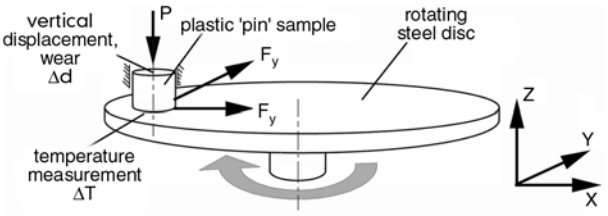

Figure 4. Pin-on-disc setup for steady-state friction measurements

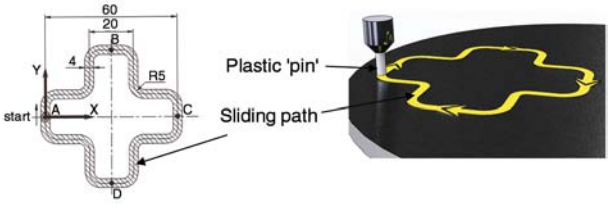

Figure 5. Programmed dynamic sliding path of plastic samples on the fixed steel plate

Table 3. Test conditions

	Pin-on-disc I (pv = 0.8 MPa·ms^{-1})	Pin-on-disc II (pv = 2 MPa·ms^{-1})	Pin-on-plate dynamic tests (pv regime 0–8 MPa·ms^{-1})
Sliding speed [m/s]	0.4	0.4	0–0.4
Period of test [h]	0.75	0.75	1– 5 cycles
Surface load [MPa]	2	5	0–20
Friction path radius [mm]	100	100	Dynamic program path
Disk surface roughness [μm]	R_a 0.05–0.1	R_a 0.05–0.1	R_a 0.05–0.1
Ambient temperature [°C]	23	23	23

illustrated separately (as shown in Figure 1) from the averaged values of the completed five cycles.

4. Results and discussion

4.1. Comparison of the measured friction data

The friction results are summarised in Table 4 (by test system) and illustrated in the graphs in Figures 6–8. In Figure 6, the dynamic pin-on-plate results are summarised. The data show that the short sliding distances result in relatively low friction values, characteristic of the running-in period of friction, as illustrated in Figure 1.

Among the machine element materials, PA6G/PE, PETP and the PETP/PTFE composites experienced a sudden change in friction, implying the rapid formation of a polymer film that changed the properties of the mechanical deformation, mechanical cutting and adhesion in the contact zone.

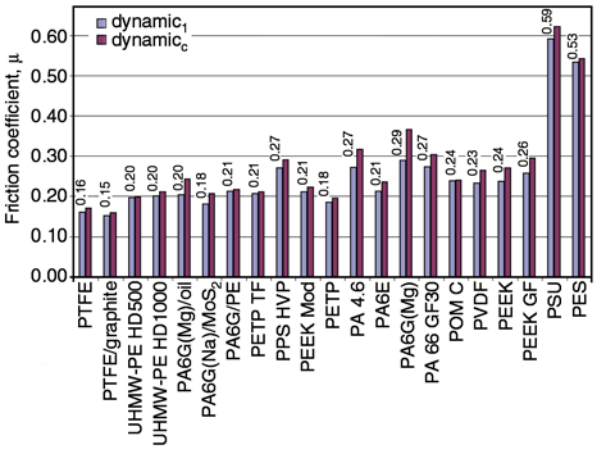

Figure 6. Dynamic pin-on-plate friction results from the sliding cycle 1 and completed full path (the latter values are indicated)

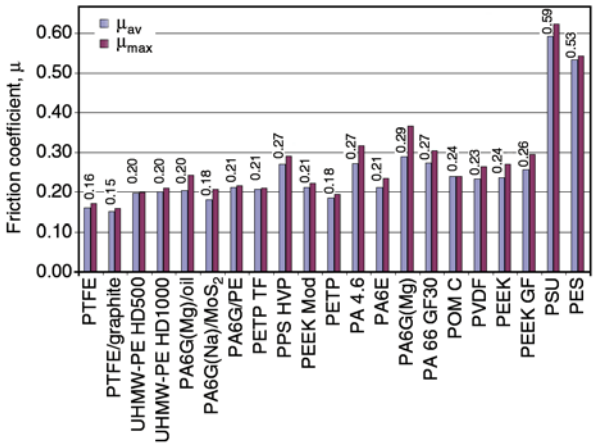

Figure 7. Pin-on-disc results from test system I (pv = 0.8 MPa·ms^{-1}, numbers indicate μ_{av})

Table 4. Measured friction values in different test systems

	Dynamic pin-on-plate		Pin-on-disc I		Pin-on-disc II	
	μ_{av} cycle 1	μ_{av} complete	μ_{av}	μ_{max}	μ_{av}	μ_{max}
Sliding materials (Material Group 1)						
PTFE	0.10	0.13	0.16	0.17	0.17	0.18
PTFE/graphite	0.11	0.13	0.15	0.16	0.18	0.18
UHMW-PE HD500	0.07	0.09	0.20	0.20	0.19	0.20
UHMW-PE HD1000	0.08	0.09	0.20	0.21	0.20	0.20
PA6G(Mg)/oil	0.07	0.10	0.20	0.24	0.16	0.23
PA6G(Na)/MoS_2	0.06	0.10	0.18	0.21	0.17	0.18
PA6G/PE	0.10	0.14	0.21	0.22	0.21	0.22
PETP TF	0.06	0.14	0.21	0.21	0.18	0.18
PPS HPV	0.06	0.09	0.27	0.29	0.24	0.25
PEEK Mod	0.06	0.08	0.21	0.22	0.19	0.19
PETP	0.06	0.13	0.18	0.19	0.18	0.18
Load-carrying materials (Material group 2)						
PA 4.6	0.10	0.11	0.27	0.32	0.30	0.31
PA6E	0.09	0.10	0.21	0.23	0.19	0.23
PA6G(Mg)	0.08	0.10	0.29	0.37	0.25	0.33
PA 66 GF30	0.06	0.09	0.27	0.30	0.21	0.26
POM C	0.07	0.08	0.24	0.24	0.20	0.20
PVDF	0.09	0.10	0.23	0.26	0.28	0.33
PEEK	0.06	0.08	0.24	0.27	0.28	0.29
PEEK GF	0.06	0.08	0.26	0.29	0.29	0.32
Other amorphous (Material Group 3)						
PSU	0.11	0.18	0.59	0.62	0.55	0.65
PES	0.13	0.18	0.53	0.54	0.54	0.58

All the data are valid for dry sliding against a ground S235 steel surface under the defined system characteristics.

The summary of the pin-on-disc I measurements is shown in Figure 7. The relatively low (0.8 MPa·ms^{-1}) *pv* regime resulted in a moderate difference between the material groups, with the exception of the amorphous materials (PES and PSU). The stabilised friction coefficients of material group 1 are 5–10% lower than those of material group 2. In material group 1, the difference between μ_{max} and μ_{av} is generally smaller than it is for the others, indicating a smooth transition zone (see Figures 1 and 2) with an even transfer layer. The results of increased load effects (*pv* = 2 MPa·ms^{-1}) are measured using pin-on-disc measurements and shown in Figure 8.

The pin-on-disc system II (Figure 8) test results, compared to the system I test results (Figure 7), show that most of the materials from category 1 resulted in lower or similar friction with the increased load. For those materials, e.g., PTFE, PETP/PTFE, and PA6G (Mg)/oil, the test systems worked on the left side of the friction optimum point, as shown in Figure 3. This behaviour is in agreement with friction theory [5, 23] and is the result of the lower surface adhesion of sliding-group materials. Many other plastics, e.g., PA4.6 and PEEK, worked on the right side of the optimum point (Figure 3), that is, the increased load resulted in higher friction.

The friction data were evaluated as a function of the measured mechanical properties. The material groups were thus distinguished. PES and PSU were categorized in group 2 but did not follow the group trendlines, most likely because PES and PSU differ from the other tested materials not only in molecular structure but also in friction behaviour.

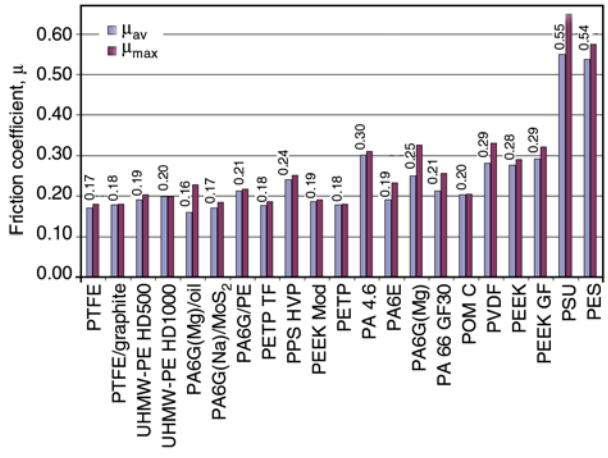

Figure 8. Pin-on-disc results from test system II (*pv* = 2 MPa·ms^{-1}, numbers indicate μ_{av})

4.2. Friction coefficients and yield stress

The relationship between the friction values and yield stress is shown in Figure 9.

During the running-in period, when the dynamic changes of speed and load temporarily reach the highest load (*pv* = 8 MPa·ms^{-1}), the friction decreases with increasing yield stress (Figure 9a). A power-function curve is an estimate for the first cycle of the dynamic test, but the complete program (five cycles) results in too much scatter to perform a curve-fit. This trend can be explained by the role of the still-weak effects of the generated frictional heat and also by the actual size of the contact area.

Each test system shows that the group of sliding machine element materials (material group 1) offers lower friction coefficients compared to the structural and load-carrying plastics (material group 2). In the pin-on-disc test systems, the '*R*' property has little effect on friction. At the lower *pv* regime (pin-on-disc I test system, *pv* = 0.8 MPa·ms^{-1}), '*R*' does not influence the friction in the case of material group 2. For material group 1, except during the running-in period, the friction increases slightly with increasing '*R*' as a result of deformation and adhesion because of the varying adhesion forces occurring in the dynamic balance of the polymer film formation with respect to the minimal deformation at low loads (Figure 9b). The elevated load in the pin-on-disc II test system affects the result. '*R*' has no effect on material group 1, but for material group 2, higher '*R*' values cause a slight increase of friction (Figure 9c).

4.3. Friction coefficients versus the elongation at the break

Figure 10 shows the friction coefficients versus the elongation at the break. For the first cycle of the dynamic test system (Figure 10a), the relationship is logarithmic and linear. Higher '*A*' values result in increased friction, even for material group 2. This behaviour relates to the role of adhesion: higher strain can cause higher deformation, enlarging the actual contact area. Based on the pin-on-disc test system results, the elongation at the break ('*A*') has a weak effect on friction. At lower loads (Figure 10b), an increase in '*A*' causes a negligible decrease of friction for material group 1 and a slight increase of friction for material group 2.

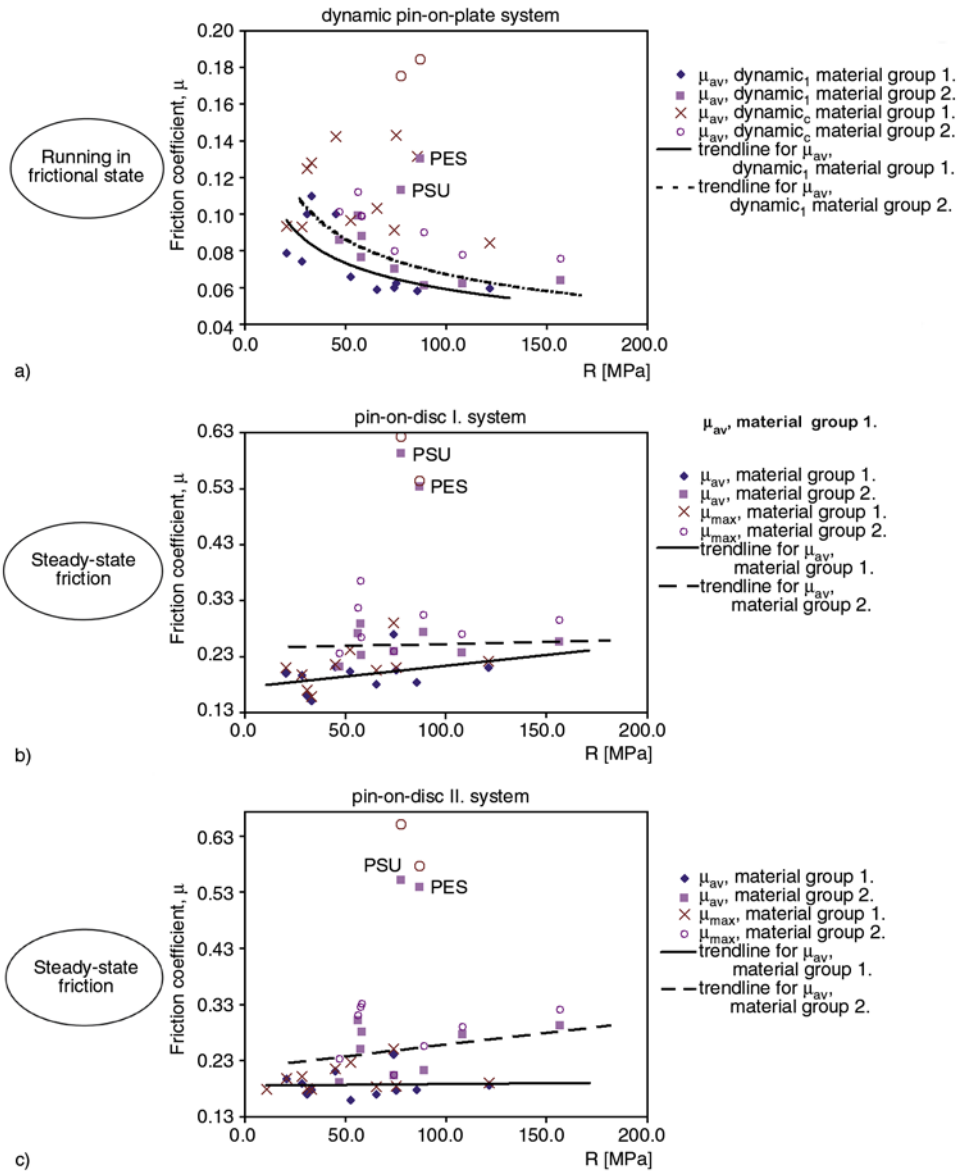

Figure 9. Friction coefficients versus yield stress, R [MPa]. (a) dynamic pin-on-plate, cycle 1 and completed program, μ_{av} values, (b) pin-on-disc I (pv = 0,8 MPa·ms^{-1}), μ_{max} and μ_{av} values, (c) pin-on-disc II (pv = 2 MPa·ms^{-1}), μ_{max} and μ_{av} values.

With the elevated loads (pin-on-disc II), no effect of '*A*' on friction was observed (Figure 10c).

4.3. Friction coefficients in the function of modulus of elasticity

Figure 11 shows the friction coefficients versus Young's modulus. During the running-in period, there were similar results for the dynamic pin-on-plate test for both material categories. An optimum '*E*' value is shown for sliding and load-carrying plastics in cycle 1. In the test system, the optimum '*E*' is approximately 5000–6000 MPa. This value is system-dependent as it depends on the surface roughness, the metallic composition of the mating surface and other system features (e.g., temperature). The test system was designed using typical engineering solutions. After five cycles, near the transition, the scatter in the data (Figure 11a) is too large to define any specific trend.

During steady-state friction, the pin-on-disc measurements primarily show a linear relationship between the friction and Young's modulus ('*E*'). The relationship changes with the load level of the systems. For pin-on-disc I, an increase in '*E*' causes a larger increase in friction for material group 1 than for material group 2 (Figure 11b). At low load levels, this phenomenon may be due to adhesive effects from the higher surface energy, in accordance with the adhe-

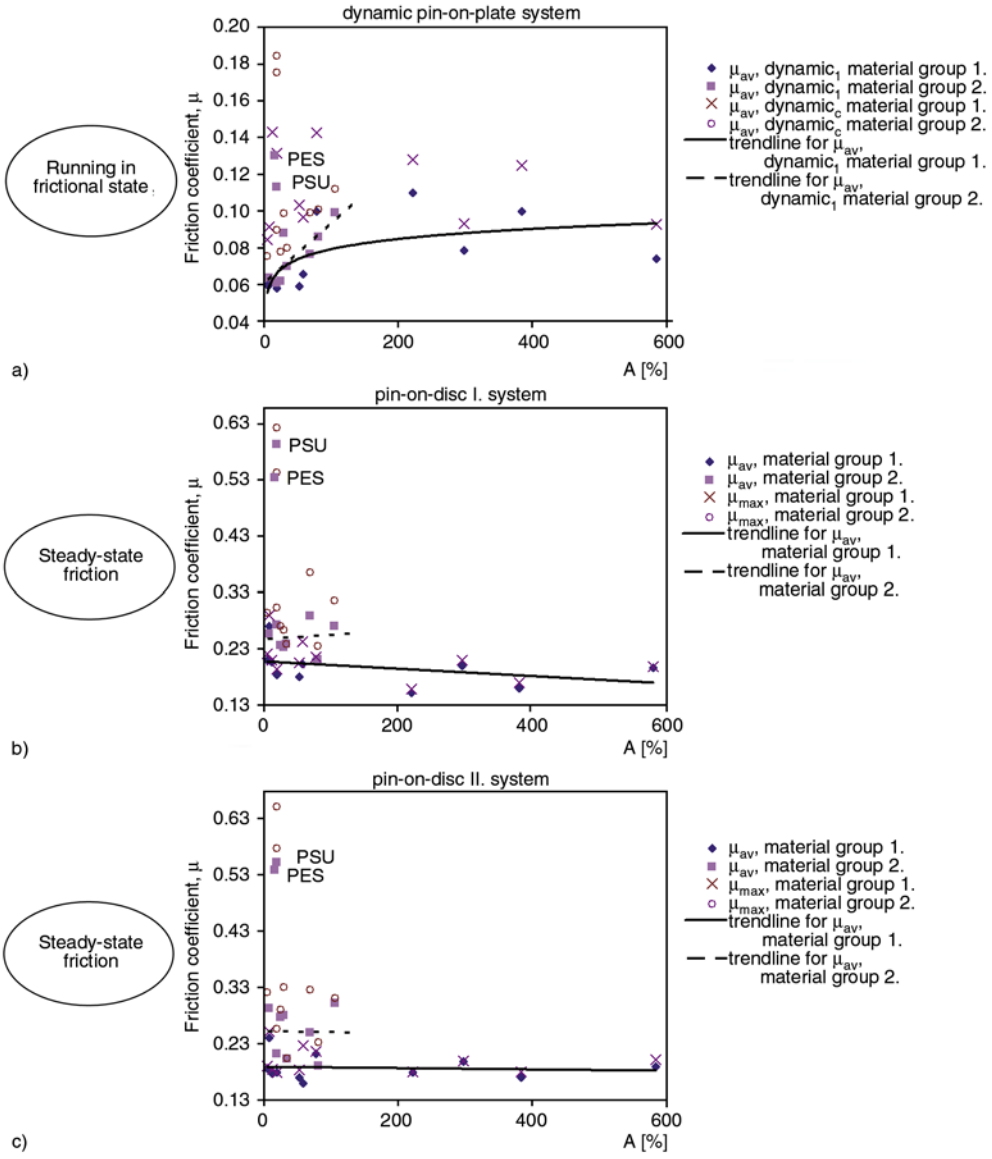

Figure 10. Friction coefficients versus elongation at break, A [%]. (a) dynamic pin-on-plate, cycle 1 and completed program, μ_{av} values, (b) pin-on-disc I (pv = 0,8 MPa·ms^{-1}), μ_{max} and μ_{av} values, (c) pin-on-disc II (pv = 2 MPa·ms^{-1}), μ_{max} and μ_{av} values.

sive theory of friction [5, 23]. It is known that in PEEK or PEEK composites, both the 'E' value and the surface energy are higher than in other materials, such as UHMW-PE. The increased load level in the pin-on-disc II tests shows different trends between friction and 'E', as well (Figure 10c). The deformation and adhesion work together to form the resulting friction changes for material group 2 but provide no significant change for material group 1.

4.5. Friction coefficients plotted against Shore D hardness

Figure 12 shows the relationship between the Shore D hardness and friction. The dynamic tests show that during the early stage of friction, the increased hardness is advantageous and results in lower friction in both material groups because of lower deformation and smaller actual contact area, resulting in lower mechanical and adhesive forces. Nearing the transition zone (Figure 1) during the complete dynamic test, the forming polymer layer and its adhesive effect change the dynamic, and the scatter in the data (Figure 12a) is too large to indicate a trend.

The steady-state friction measurements revealed that the role of the surface hardness changes. At lower loads (Figure 12b), the hardness has no significant effect on the observed friction in material group 2, but a slight increase of friction with hardness in material group 1 reflects the different adhe-

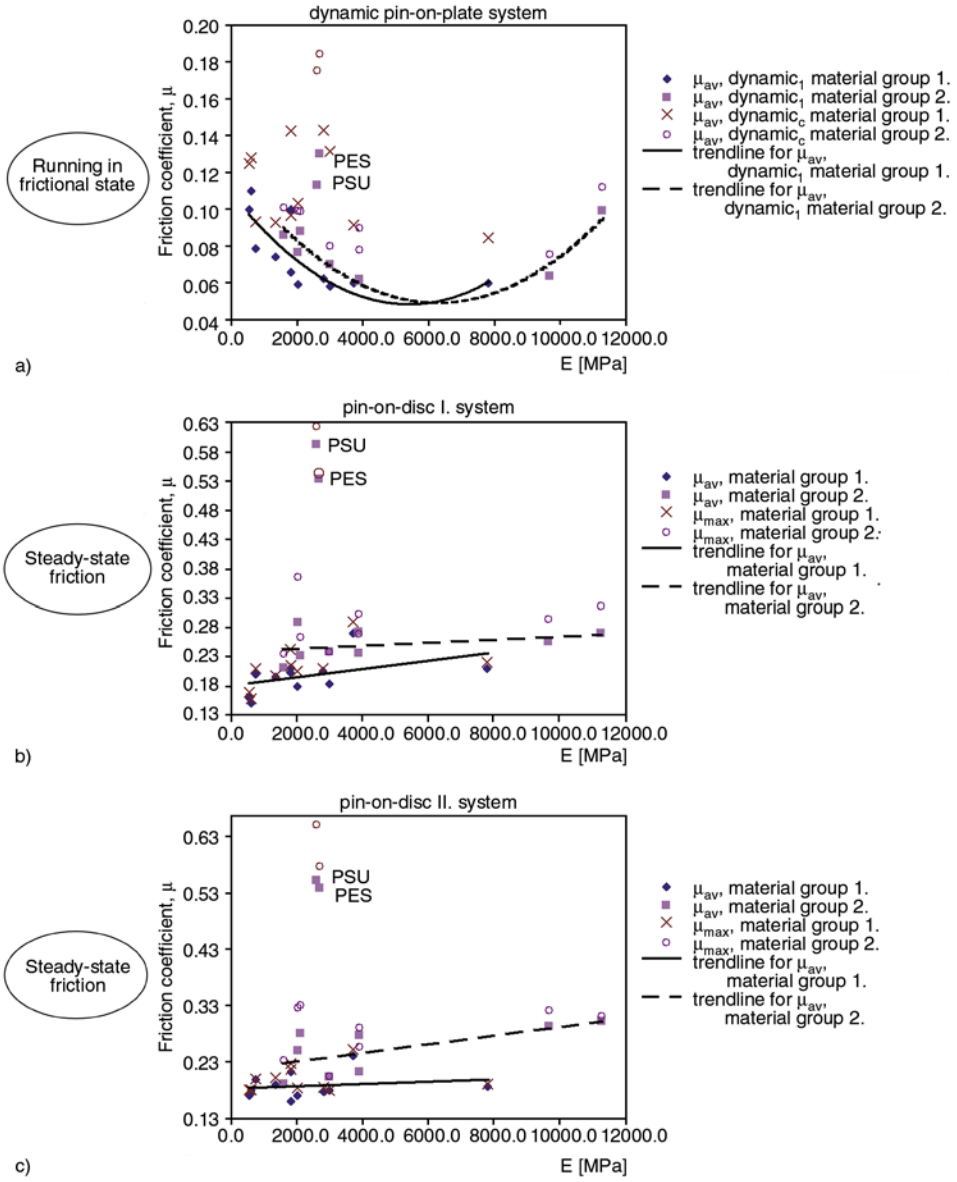

Figure 11. Friction coefficients versus Young's modulus, E [MPa]. (a) dynamic pin-on-plate, cycle 1 and completed program, μ_{av} values, (b) pin-on-disc I (pv = 0,8 MPa·ms^{-1}), μ_{max} and μ_{av} values, (c) pin-on-disc II (pv = 2 MPa·ms^{-1}), μ_{max} and μ_{av} values.

sion and surface energy of the plastics. Increasing the load (pin-on-disc II) modifies the effect (Figure 12c) of the hardness on the friction. In the case of material group 1, the plastics having a Shore D hardness of 80 or higher exhibited lower friction; those materials in the pin-on-disc I system worked in the zone to the left of the optimum point of friction (according to the friction theory in Figure 3), but at higher loads, they worked in the zone closer to the optimum point. This was not the case for material group 2. Those plastics worked around the optimum point or in the zone to the right of the optimum point (in Figure 3) in the pin-on-disc I system, and at higher loads, they moved away from the optimum point to higher values.

5. Conclusions

Twenty-one different engineering polymers separated into three groups (semi-crystalline materials of sliding machine elements, semi-crystalline materials of load-carrying machine elements, and amorphous engineering plastics) were tested during both the running-in period and steady-state friction, and dynamic effects and different load levels (pv = 0.8 and 2 MPa·ms^{-1} at steady state friction) were applied according to plastic engineering practices. Using

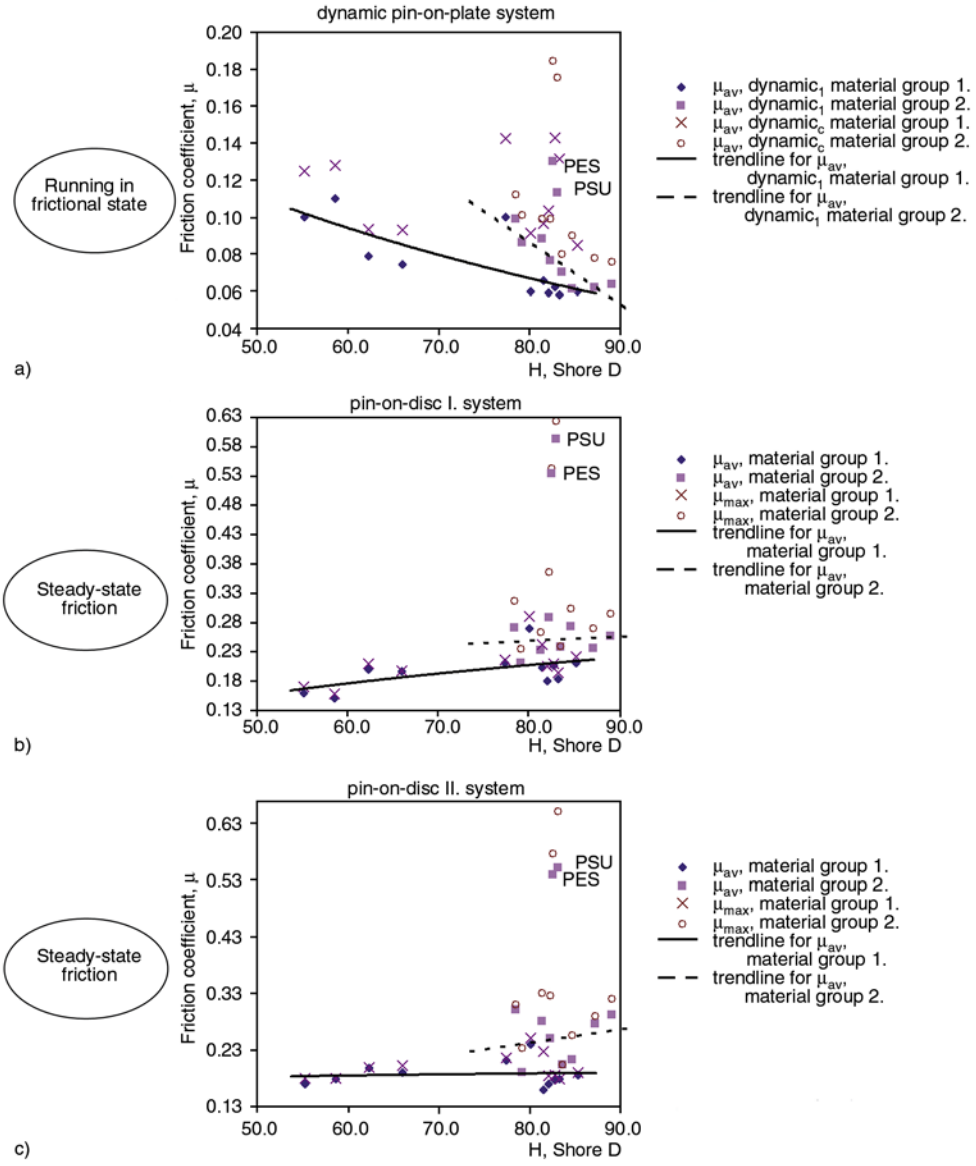

Figure 12. Friction coefficients versus Shore D hardness. (a) dynamic pin-on-plate, cycle 1 and completed program, μ_{av} values, (b) pin-on-disc I (pv = 0,8 MPa·ms^{-1}), μ_{max} and μ_{av} values, (c) pin-on-disc II (pv = 2 MPa·ms^{-1}), μ_{max} and μ_{av} values.

pin-on-plate and pin-on-disc test rigs, the dry friction coefficient against a ground structural steel surface was determined. The data were evaluated as a function of various mechanical properties. In the test systems (engineering modelling applications), the following relationships were found:

– During the running-in period, the friction coefficient decreased with increasing yield stress and Shore D hardness. Friction increased with higher elongation at the break. μ had an optimum point (minimum) as a function of Young's modulus.
– During steady state friction under the lower load value the following relationships were found:
  • Friction increased with increasing yield stress, Young's modulus, Shore D hardness, and the effect of the mechanical properties on friction was stronger for material group 1 (sliding materials) than for material group 2.
  • Friction decreased with increasing elongation at break for the sliding material group, but no significant effect was found for the load-carrying material group.
– At the elevated load level (pv = 2 MPa·ms^{-1}) in the pin-on-disc system, the following friction changes resulting from the effects of the deformation and adhesion components were observed:
  • In the sliding material group, the mechanical properties showed no significant effects on friction.

- In the load-carrying material group, the elongation at the break had no effect on friction, while increasing the yield stress, Young's modulus and the Shore D hardness increased friction.

– The results from the amorphous PES and PSU materials showed poor friction performance. These materials cannot be compared to the semi-crystalline engineering plastics and are not recommended as structural materials supporting a frictional load.

Acknowledgements

Many thanks to L. Zsidai, R. Keresztes, M. Andó for their laboratory assistance and to Quattroplast Ltd. for supporting this research work.

Abbreviations

μ	Friction coefficient [–]
F_x, F	Measured friction force component [N]
R	Yield stress [MPa]
H	Shore D hardness [–]
A	Elongation at break [%]
E	Modulus of elasticity [MPa]
pv	Data of friction system design of thermoplastics [MPa·ms^{-1}]
P	Normal load [N]
R_a	Surface roughness [μm]
PTFE	Unmodified Polytetrafluoroethylene
PTFE/graphite	Polytetrafluoroethylene/graphite composite
UHMW-PE HD500	Unmodified Ultra-high-molecular-weight polyethylene, grade HD500
UHMW-PE HD1000	Unmodified Ultra-high-molecular-weight polyethylene, grade HD1000
PA 4.6	Unmodified Polyamide 4.6
PA6E	Unmodified extruded Polyamide 6
PA6G(Mg)	Unmodified Magnesium catalytic cast Polyamide 6
PA6G(Mg)/oil	Magnesium catalytic cast Polyamide 6/oil composite
PA6G(Na)/MoS_2	Potassium catalytic cast Polyamide 6/MoS_2 composite
PA6G/PE	Potassium catalytic cast Polyamide 6/Polyethylene composite
PA 66 GF30	Polyamide 66/glass fibre composite
PETP	Unmodified Polyethylene terephthalate
PETP TF	Polyethylene terephthalate/Polytetrafluoroethylene composite
POM C	Unmodified Polyoxymethylene copolymer
PPS HPV	Polyphenylene sulphide/glass fibre, oil composite
PSU	Unmodified Polysulfone
PES	Unmidufued Polether sulfone
PVDF	Unmodified Polyvinylidene fluoride
PEEK	Unmodified Polyether ether ketone
PEEK GF	Polyether ether ketone/glass fibre composite
PEEK Mod	Polyether ether ketone/carbon fibre, Polytetrafluoroethylene, graphite composite

References

[1] Bhushan B.: Modern tribology handbook. Vol. 1–2. CRC Press, Boca Raton (2001).

[2] Zum Gahr K-H.: Microstructure and wear of materials. Elsevier, Amsterdam (1987).

[3] Hutchings I. M.: Tribology: Friction and wear of engineering materials. Edward Arnold, London (1992).

[4] DIN 50322: Wear. Wear testing categories (1986).

[5] Yamaguchi Y.: Tribology of plastic materials. Elsevier, Amsterdam (1990).

[6] Böhm H., Betz S., Ball A.: The wear resistance of polymers. Tribology International, **23**, 399–406 (1990). DOI: 10.1016/0301-679X(90)90055-T

[7] Czichos H., Klaffke D., Santner E., Woydt M.: Advances in tribology: The materials point of view. Wear, **190**, 155–161 (1995). DOI: 10.1016/0043-1648(96)80014-7

[8] Santner E., Czichos H.: Tribology of polymers. Tribology International, **22**, 103–109 (1989). DOI: 10.1016/0301-679X(89)90170-9

[9] Rajesh J. J., Bijwe J., Tewari U. S.: Abrasive wear performance of various polyamides. Wear, **252**, 769–776 (2002). DOI: 10.1016/S0043-1648(02)00039-X

[10] Tewari U. S., Bijwe J., Mathur J. N., Sharma I.: Studies on abrasive wear of carbon fibre (short) reinforced polyamide composites. Tribology International, **25**, 53–60 (1992).
DOI: 10.1016/0301-679X(92)90121-3

[11] Keresztes R., Kalácska G., Zsidai L., Eberst O.: Abrasive wear of polymer-based agricultural machine elements in different soil types. Cereal Research Communications, **36**, 903–907 (2008).

[12] Arribas A., Bermúdez M-D., Brostow W., Carrión-Vilches F. J., Olea-Mejía O.: Scratch resistance of a polycarbonate + organoclay nanohybrid. Express Polymers Letters, **3**, 621–629 (2009).
DOI: 10.3144/expresspolymlett.2009.78

[13] Unal H., Findik F.: Friction and wear behaviours of some industrial polyamides against different polymer counterparts under dry conditions. Industrial Lubrication and Tribology, **60**, 195–200 (2008).
DOI: 10.1108/00368790810881542

[14] Byett J. H., Allen C.: Dry sliding wear behaviour of polyamide 66 and polycarbonate composites. Tribology International, **25**, 237–246 (1992).
DOI: 10.1016/0301-679X(92)90061-Q

[15] Kato K.: Wear in relation to friction – A review. Wear, **241**, 151–157 (2000).
DOI: 10.1016/S0043-1648(00)00382-3

[16] Khan M. S., Franke R., Gohs U., Lehmann D., Heinrich G.: Friction and wear behaviour of electron beam modified PTFE filled EPDM compounds. Wear, **266**, 175–183 (2009).
DOI: 10.1016/j.wear.2008.06.012

[17] Myshkin N. K., Petrokovets M. I., Kovalev A. V.: Tribology of polymers: Adhesion, friction, wear, and mass-transfer. Tribology International, **38**, 910–921 (2005).
DOI: 10.1016/j.triboint.2005.07.016

[18] Xu D., Karger-Kocsis J., Schlarb A. K.: Rolling wear of EPDM and SBR rubbers as a function of carbon black contents: Correlation with microhardness. Journal of Materials Science, **43**, 4330–4339 (2008).
DOI: 10.1007/s10853-008-2637-7

[19] Khan M. S., Lehmann D., Heinrich G., Gohs U., Franke R.: Structure-property effects on mechanical, friction and wear properties of electron modified PTFE filled EPDM composite. Express Polymers Letters, **3**, 39–48 (2009).
DOI: 10.3144/expresspolymlett.2009.7

[20] Brostow W., Dutta M., de Souza J. R., Rusek P., de Medeiros A. M., Ito E. N.: Nanocomposites of poly (methyl methacrylate) (PMMA) and montmorillonite (MMT) Brazilian clay: A tribological study. Express Polymers Letters, **4**, 570–575 (2010).
DOI: 10.3144/expresspolymlett.2010.71

[21] Kalácska G., Zsidai L., Keresztes R., Tóth A., Mohai M., Szépvölgyi J.: Effect of nitrogen plasma immersion ion implantation of polyamide-6 on its sliding properties against steel surface. Wear, **290–291**, 66–73 (2012).
DOI: 10.1016/j.wear.2012.05.011

[22] Keresztes R.: Tribology research of polymer/steel gear pairs. PhD thesis (in Hungarian). Szent István University, Gödöllő (2009).

[23] Bowden F. P., Tabor D.: Friction and lubrication of solids. Oxford University Press, London (1954).

[24] Samyn P., Kalacska G., Keresztes R., Zsidai L., De Baets P.: Design of a tribotester for evaluation of polymer components under static and dynamic sliding conditions. Proceedings of the Institution of Mechanical Engineers Part J: Journal of Engineering Tribology, **221**, 661–674 (2007).
DOI: 10.1243/13506501JET266